

PHOTONIC CONTROL OVER
LIGHT ABSORPTION AND EMISSION
IN PHOTOVOLTAICS

Photonic control over light absorption and emission in photovoltaics

Ph.D. Thesis, University of Amsterdam, April 2022

Tom Veeken

ISBN: 978-94-6421-732-2

Cover design: *Simulated (front and back: left side) and measured (back: right side) angular emission profile of luminophores embedded in TiO₂ nanocylinder arrays, as studied in Chapter 4.*

The work described in this thesis was performed between September 2017 and March 2022 at NWO-Institute AMOLF, Science Park 104, 1098 XG Amsterdam, The Netherlands.

This work is part of the Dutch Research Council (NWO).

A digital version of this thesis is available at:
<https://ir.amolf.nl> and <https://www.lmpv.nl/Theses/>.

Printed by <https://www.proefschriften.nl>

Copyright © 2022 by Tom Veeken

PHOTONIC CONTROL OVER
LIGHT ABSORPTION AND EMISSION
IN PHOTOVOLTAICS

ACADEMISCH PROEFSCHRIFT

ter verkrijging van de graad van doctor

aan de Universiteit van Amsterdam

op gezag van de Rector Magnificus

prof. dr. ir. K.I.J. Maex

ten overstaan van een door het College voor Promoties ingestelde commissie,

in het openbaar te verdedigen in de Agnietenkapel

op woensdag 11 mei 2022, te 10.00 uur

door Thomas Petrus Nicolaas Veeken

geboren te Alkmaar

Promotiecommissie

<i>Promotor:</i>	prof. dr. A. Polman	Universiteit van Amsterdam
<i>Copromotor:</i>	dr. J. van de Groep	Universiteit van Amsterdam
<i>Overige leden:</i>	prof. dr. P. Schall	Universiteit van Amsterdam
	prof. dr. E.C. Garnett	Universiteit van Amsterdam
	prof. dr. W.C. Sinke	Universiteit van Amsterdam
	prof. dr. I.P. Staude	University of Jena
	dr. R. Saive	University of Twente

Faculteit der Natuurwetenschappen, Wiskunde en Informatica

Contents

1	Introduction	1
1.1	Energy	2
1.2	Photovoltaics	3
1.2.1	The potential of solar power	4
1.2.2	The spectrum of sunlight	5
1.2.3	Detailed-balance solar cell efficiency limit	6
1.3	Photonics for photovoltaics	9
1.3.1	Photonic light management	10
1.4	Motivation	12
1.5	Outline of the thesis	16
2	Directional quantum dot emission by soft-stamping on silicon Mie resonators	19
2.1	Introduction	21
2.2	Nanophotonic design	22
2.3	Fabrication: soft-stamping of QDs onto nanostructures	26
2.4	Photoluminescence measurements	27
2.5	Photoluminescence lifetimes	30
2.6	Conclusions	32
2.7	Methods	32
2.8	Supplementary information	35
3	Unlocking higher power efficiencies in luminescent solar concentrators through anisotropic luminophore emission	39
3.1	Introduction	41
3.2	Results and discussion	44
3.2.1	Thermodynamics of anisotropic LSC devices	44
3.2.2	Emitters with steplike anisotropy	47
3.2.3	Emitters with dipolelike anisotropy	50
3.2.4	Emitters with forwardlike anisotropy	50
3.2.5	Enhancing the efficiency of the record LSC	52
3.2.6	Loss mechanisms within anisotropic LSCs.	53
3.3	Conclusions and future work	55
3.4	Computational methods	55
4	Anisotropic luminophore emission for enhanced light trapping in luminescent solar concentrators	57
4.1	Introduction	59
4.2	Nanophotonic angular emission control	61
4.3	Nanocylinder array fabrication	64
4.4	Spatial photoluminescence measurements	64
4.5	Angle-resolved photoluminescence	65
4.6	Conclusions	69
4.7	Methods	70
4.8	Supplementary information	73

5	Passive radiative cooling of silicon solar modules with silica microcylinder arrays	77
5.1	Introduction	79
5.2	Passive radiative cooling	81
5.3	Photonic design	84
5.4	Fabrication	86
5.5	Hemispherical reflection measurements	87
5.6	Conclusions	89
5.7	Methods	90
6	Application and validity of the effective medium approximation to the optical properties of nano-textured silicon coated with a dielectric layer	95
6.1	Introduction	97
6.2	Methods	99
6.2.1	Generation of random surfaces	99
6.2.2	Summary of EMA simulation	101
6.2.3	Effective medium theory	101
6.2.4	Extraction of volume fraction for an individual element	102
6.2.5	Details of numerical FDTD calculation	103
6.3	Results	105
6.3.1	Effective medium approximation for bare silicon	105
6.3.2	Electric field intensity distributions of light incident on the nanotexture	106
6.3.3	Effective medium approximation for silicon coated with a dielectric	108
6.3.4	Proposed criteria for approximating electromagnetic theory by the effective medium approximation	108
6.4	Conclusions	111
7	Plasma focused ion beam tomography for accurate characterization of black silicon validated by full-wave optical simulations	113
7.1	Introduction	115
7.2	Experimental methodology	117
7.3	Results and discussion	121
7.4	Conclusion	127
	Bibliography	129
	List of publications	151
	Summary	153
	Samenvatting	157
	Acknowledgements	163
	Curriculum Vitae	171

1

Introduction

*“If you don't change direction,
you will end up where you are heading”*
— Lao Tzu

Light is at the very heart of life as we know it on earth, as light from the sun heats our planet and provides the energy necessary for animated life forms. The earth is situated at a sweet spot in the solar system, close enough to the sun for the average temperature to be above the freezing point of water and far enough from the sun for the temperature to be below the boiling point of water. For this reason, we have plenty of liquid water on earth, the main ingredient supporting our organic life forms.

Light also has a central role in our perception of the world around us because of our sight. Humans use their eyes in conjunction with their other senses to survive and thrive, though arguably sight is the most versatile of the senses. Across human length scales of millimeters to kilometers, light travels practically instantaneously, providing information at an instant. Our concepts of beauty, color, and vibrancy are due to the astounding capability of our eyes to discern between different wavelengths, intensity, and point of origin of the light it receives. Moreover, we have evolved to interpret the world based on what we see, ranging from discerning edible from inedible food to obtaining social cues through non-verbal communication.

Besides the obvious role light plays in everyday life, light is also central to modern human society. With the advances in electrical lighting, we are no longer bound to the rhythm of day and night for work or social activities. More recently, light also revolutionized our communication and information systems, as it is used as information carrier in optical fibers that serve as the backbone for telecommunication and the internet [1]. Lasers, used for many applications ranging from precise distance measurements to cutting steel, and medical technologies such as endoscopes or optical tomography are also based on light. Finally, optical detection systems continue to revolutionize our world. The first accounts of magnification date back almost 2000 years, and lenses were studied already in the late 1200s [2]. This resulted in the first practical eyeglasses around that time, the first telescopes in the early 17th century, and the development of microscopes by Hooke and Van Leeuwenhoek shortly after

[2]. The consequent development of optical telescopes and microscopes has increased our understanding of the macro and micro parts of our world enormously. Also, over the past few decades, our daily lives have been revolutionized by the advent of photography, personal computers, mobile phones, light-emitting diodes (LEDs), and displays. Even today, research and development of image recognition, optical computing, and biometric sensing continues to shape our future modern world.

Light also plays a key role in the revolution of renewable energy generation. In this thesis, we study how detailed light management can improve the conversion efficiency of sunlight into electricity in photovoltaic cells. Empowered by recent developments in micro- and nanotechnology, we structure materials at the scale of the wavelength to control the flow of light. In this first chapter, we discuss the fundamental properties of light and of energy conversion. We then investigate the potential of solar energy conversion on earth, the fundamental limits of energy conversion by solar cells, and the impressive decrease of the costs of solar power generation over the past decades. The majority of this thesis concerns the use of well-defined nano- or microstructures to control the reflection, transmission, absorption, and emission of light. Therefore, we provide a short overview of the different light management geometries that are commonly used to improve solar cell technologies. We conclude with a motivation and outline of the thesis.

1.1 Energy

Light is a form of energy. Textbooks such as ‘The Feynman Lectures on Physics’ teach us about many kinds of energy: “gravitational energy, kinetic energy, heat energy, elastic energy, electrical energy, chemical energy, radiant energy, nuclear energy, mass energy.” [3] Conversion of one type into another type of energy is oftentimes possible but mostly not 100% efficient. Yet, as far as we know, energy is never lost. Energy is a conserved quantity, which means that it is never created nor destroyed. Instead, one type of energy can be converted into a combination of other types while the grand total is constant. It is a simple fact we observe in our universe, but at the same time a marvelous fact — Feynman pointed it out quite cleverly:

The law is called the conservation of energy. It states that there is a certain quantity, which we call energy, that does not change in the manifold changes which nature undergoes. That is a most abstract idea, because it is a mathematical principle; it says that there is a numerical quantity which does not change when something happens. It is not a description of a mechanism, or anything concrete; it is just a strange fact that we can calculate some number and when we finish watching nature go through her tricks and calculate the number again, it is the same.

...

It is important to realize that in physics today, we have no knowledge of what energy is. We do not have a picture that energy comes in little blobs of a definite amount. It is not that way. However, there are formulas for calculating some numerical quantity, and when we add it all together it gives ... always the same number. It is an abstract thing in that it does not tell us the mechanism or the reasons for the various formulas [3].

Besides different types of energy, we can also discern between sustainable and unsustainable energy sources. Energy from the sun (radiant), wind and hydro (kinetic), and geothermal (heat) are sustainable because they are continuously replenished. In contrast, the use of fossil fuels such as coal, oil, and natural gas (chemical), and nuclear energy are unsustainable; they

can be used only a single time (the time scales for replenishment are orders of magnitude larger than the average human lifetime). Moreover, the fossil fuel industries and the waste produced upon use endanger all forms of life on earth as we know them.

The United Nations list energy as their 7th Sustainable Development Goal (SDG), but recently recognized that practically all other 16 SDGs are linked to energy [4]. For example, Poverty and Hunger (SDGs 1 and 2) can be reduced significantly by access to cheap energy for heating, light, and cooking. Moreover, cheap and clean energy can revolutionize Global Health and access to Clean Water (SDGs 3 and 6), amongst others by providing climate control and water purification. A few other examples are the improvement of Global Education (SDG 4) by internet access, Responsible Consumption and Production (SDG 12) by conversion of traditional to sustainable energy generation, and Decent Work, Sustainable Cities, and Peace (SDGs 8, 11 and 16) by local, independent generation of renewable energy.

Electricity is an important factor in the transition to sustainable energy production and is an important ingredient in our modern living standards. The electrification of global energy use is well underway because of the high conversion efficiency between electricity and other forms of energy, the advances in battery technology, and the increasing use of renewable energy sources. Between 1973 and 2019, the fraction of global energy consumption in the form of electricity rose from 9.5% to 19.7% [5]. However, only 26.5% of that electricity is generated by sustainable energy sources. To meet the global greenhouse gas emission targets, which were agreed upon to limit global warming to well below 2 degrees Celsius compared to pre-industrial levels due to the manifold adverse effects associated with it, we need to replace fossil fuels with renewable energy sources [6, 7]. Solar energy conversion by photovoltaics is one of the renewable energy technologies that is well-suited to replace fossil fuels and has already begun to do so. In the next sections, we will touch upon the tremendous potential of solar energy conversion and the achievements made by photovoltaics until today.

1.2 Photovoltaics

The direct conversion of solar light (radiative energy) to electricity (electrical energy) is called photovoltaic energy conversion [8]. A photovoltaic system makes use of the photovoltaic effect: the excitation of an electron from a lower to a higher energy state in a material due to absorption of a photon. Typically, the photovoltaic effect is employed in a semiconductor material, where the photon excites an electron from the valence band (bound state) to the conduction band (unbound state). The energy difference between the highest valence band energy and the lowest conduction band energy is called the bandgap energy (or bandgap in short). An electron can only be excited to the conduction band if the photon has energy equal to or greater than the bandgap. After excitation, the photon's energy has been converted into electric potential energy, stored in the semiconductor material by the separation of the negatively charged electron and the positively charged 'hole' left behind in the valence band.

After a certain amount of time (the 'life-time'), the electron will decay to its initial lower energy state in the valence band, and it has several pathways to get there. A prominent first path is called thermalization: after the electron is excited up into the conduction band, it quickly relaxes to the bottom of the conduction band and transfers its energy to the surrounding atomic lattice in the form of phonons (lattice vibrations; heat). This is one of the reasons that a solar cell heats up when it is illuminated, even though it is designed to convert light into electricity instead of heat. If the electron remains at the bottom of the conduction band, the typical consecutive pathway is called recombination. During recombination, the electron relaxes back to the valence band by recombining with the hole. In the case of radiative

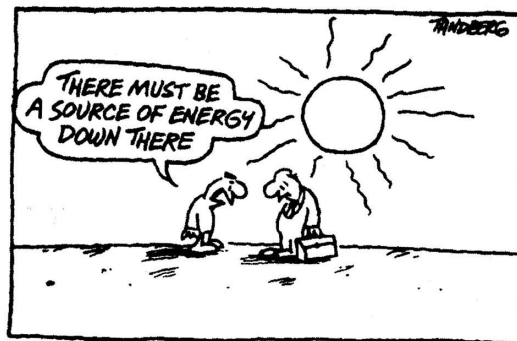
recombination, the electron-hole pair gives up its energy by the emission of a photon with energy equal to the bandgap — this is the mechanism by which a light-emitting diode (LED) generates light. Alternatively, the energy is released as additional heat, in which case we speak of non-radiative recombination. In the case of photovoltaics, we want to convert the chemical potential of the electron-hole pair into an electrical potential before it undergoes recombination. This pathway is enabled by contacting the conduction and valence bands of the semiconductor with electrical contacts. Now, the electron can travel through the contacts back to the valence band and give up its energy in the form of an electrical potential, typically over an electrical resistance between the contacts. The precise engineering of the energy levels in solar cell semiconductor materials and contacts is of tremendous importance to promote the efficient collection of electron-hole pairs [9].

Besides conversion into electricity, solar energy can also be converted into thermal energy, for example, by solar thermal collectors that convert sunlight into hot water. Solar energy is also converted into chemical energy, using either solar photons, solar thermal energy, or solar electricity to produce synthetic fuels (solar fuels). Throughout this thesis, we focus on the improvement of photovoltaic systems. To understand why photovoltaic energy conversion is a candidate for future global-scale renewable energy production, we first look at the potential of solar energy conversion and the fundamental limitations of photovoltaic systems.

1.2.1 The potential of solar power

The total amount of solar power received by the earth is astounding. Given the luminosity of the sun and the distance to the earth, we can calculate the intensity of solar light reaching the earth: 1361 Wm^{-2} . By multiplying the intensity with the area of the earth as seen from the sun, we obtain the total solar power that reaches the earth: 173 petawatt (10^{15} W)!

A number with this many zero's is quite incomprehensible, so let's put it in perspective. The International Energy Agency (IEA) reports a world total energy supply in 2019 of 606.6 exawatt (10^{18} W), which corresponds to 19.2 terawatt (10^{12} W) [5]. That is over 9000 times less than the amount of solar energy received by the earth. In other words, if we could harvest only 0.011% of the solar energy that reaches earth, we would have enough to power the entire planet. Given the nearly inexhaustible power that the sun provides and the fact that it will continue to shine as it does for about another 5 billion years [10], energy from the sun is an ideal source for renewable energy production. In this thesis we study photovoltaic energy conversion of sunlight, however, technically renewable energy sources such as wind, tidal, wave, and hydro energy are also powered by the sun.



1.2.2 The spectrum of sunlight

The energy of the sun reaches the earth as electromagnetic radiation, with wavelengths ranging from the ultra-violet (UV) to the visible, near-infrared (NIR), and infrared (IR). Part of that light is reflected back into space by the atmosphere, clouds, and the earth's surface. Another part is absorbed in the atmosphere, thereby heating it, or scattered by atmospheric particles, which explains the typical blue color of the sky and the red color of the sun at sunrise and sunset. Finally, a spectrum of wavelengths reaches the earth's surface, which fluctuates over time due to changes in the atmosphere, the orbit of the earth, and solar activity. For practical analysis purposes, the typical solar spectrum reaching the earth has been standardized as the AM0 (air mass zero) and AM1.5G (air mass 1.5 global) spectra [11]. The AM0 spectrum corresponds to the light that reaches the top of the earth's atmosphere, for which we calculated a total power of 1361 Wm^{-2} in the previous section. The AM1.5G spectrum represents the typical irradiance at noon, at an average latitude, clear sky, and including both direct and diffuse illumination. The integrated power is set to 1000 Wm^{-2} by definition. Figure 1.1 shows the spectral intensity of the AM1.5G spectrum (black). Most of the intensity is emitted in the visible, 400-700 nanometer (nm), and near-infrared (700-1400 nm) wavelength ranges.

Given the AM1.5G spectrum, we can calculate the maximum power conversion efficiency of a single-junction solar cell, called the detailed-balance (DB) limit [12]. Based on the bandgap of the solar cell and assuming 100% radiative efficiency, the DB model calculates what fraction of the energy in the solar spectrum can be converted to electricity. For a single-junction solar cell, this limit is at 33.7% for a bandgap energy of 1.34 eV ($\lambda = 925 \text{ nm}$) [13]. A silicon solar cell (bandgap 1.12 eV; $\lambda = 1107 \text{ nm}$) has almost the same limit, 33.4%. The fraction of the AM1.5G spectrum that a single-junction silicon solar cell could convert is plotted in Fig. 1.1a in orange. The inset in Figure 1.1a shows a schematic of the semiconductor valence and conduction bands discussed before, with the bandgap that matches the energy of the photon indicated by the green arrow. The elementary charge times the open-circuit voltage, qV_{oc} , is slightly lower than the bandgap, which we will discuss in the next section. Light with energy below the silicon bandgap cannot be absorbed (red arrow), thus beyond 1107 nm wavelength, the conversion is zero in Fig. 1.1a. Furthermore, light with energy greater than the bandgap excites the valence electron higher up into the conduction band (blue arrow), where it quickly

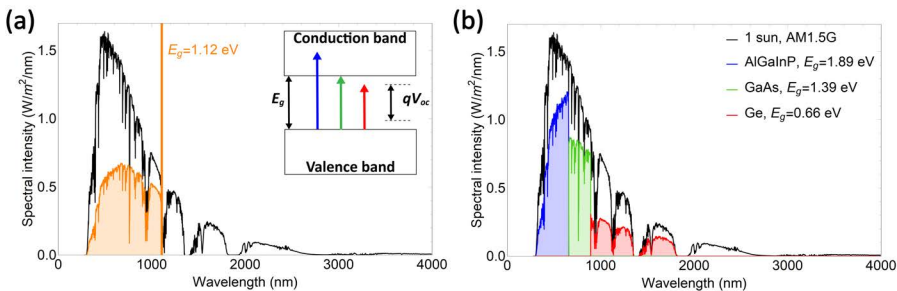


Figure 1.1: AM1.5G solar irradiation spectrum (black) and the energy utilization spectrum (a) for an ideal silicon solar cell (bandgap: 1.12 eV, detailed-balance efficiency limit: 33.4%) and (b) for an ideal multi-junction solar cell (bandgaps: 1.89/1.39/0.66 eV, detailed-balance efficiency limit: 51.6%).

thermalizes to the bottom of the conduction band, losing its energy as heat. Thus, photons with a shorter wavelength than 1107 nm do not convert all of their energy in the silicon solar cell — this is the reason that the orange curve is well below the AM1.5G intensity in Fig. 1.1a. A maximum efficiency of 33.7% might seem rather low at first sight, but the typical electricity conversion efficiency of a coal or natural gas power plant in the United States in 2020 was similar: 32% and 44%, respectively [14].

One of the efforts to decrease the losses from thermalization and lack of absorption in a solar cell is the use of two or more absorber materials with different bandgaps in a single device. Such a device is called a multi-junction or tandem solar cell. Each of the subcells efficiently converts the part of the solar spectrum that matches its bandgap. Figure 1.1b shows the DB conversion limit for a triple-junction solar cell made of compound materials AlGaInP and GaAs, and germanium (Ge). Scaling from a single-junction to a triple-junction solar cell increases the DB conversion limit from 33.7% to 51.6%. This increases the potential of photovoltaics tremendously, both for large-scale cost-competitive tandem devices [15] and ultra-high efficiency tandem devices for niche applications such as vehicle-integrated PV [16] or solar power harvesting in space [17] that can permit higher costs.

Many other approaches to solar energy conversion beyond the DB limit are being explored. A notable example is that of bifacial silicon solar cells, which is a typical silicon solar cell with metal wire contacts on the back rather than a full metal contact. This allows light to also enter from the back, adding to the generated power because there is more than ‘1-sun illumination’. This type of solar cell already had a market share of 20% in 2020 and this share is expected to increase up to 70% by 2030 [18]. Another approach is that of multiple exciton generation: exciting multiple low-energy charges with one high-energy photon. Up- and down-conversion of sunlight is also explored, converting a high-energy photon into multiple low-energy photons or vice versa. Limiting the radiative emission angles to raise the output voltage also poses significant potential [19]. Finally, in concentrating photovoltaics, light is focused onto a solar cell to increase its output power. Typically, large-scale optics such as mirrors and lenses are used to increase the solar flux, boosting mainly the current density, which requires direct illumination and actively maintaining orientation towards the sun.

In the next two sections, we summarize the progress that has been made on the power conversion efficiency for several single-junction solar cells. We also address the photovoltaic systems that could exceed the single-junction detailed-balance limit.

1.2.3 Detailed-balance solar cell efficiency limit

In Figure 1.1a, we calculated the fraction of the solar spectrum that could be converted for a single material, in this case, silicon with a bandgap at 1.12 eV. If we calculate this fraction for a range of bandgaps, we obtain the black curve plotted in Figure 1.2a: the detailed-balance efficiency limit for bandgaps between 0.5 eV ($\lambda \approx 2480$ nm) and 1.95 eV ($\lambda \approx 635$ nm). As we noted before, we find the maximum for a bandgap of 1.34 eV and a second peak around 1.12 eV, marking the trade-off between the absorption of lower-energy photons and the efficient conversion of higher-energy photons. If we decrease the bandgap further, the DB efficiency quickly decreases: although more sunlight can overcome the bandgap energy barrier, more energy is lost due to thermalization (red fraction in Figure 1.1b). If we increase the bandgap beyond 1.34 eV, the DB efficiency also drops: now less energy is lost due to thermalization (blue fraction in Figure 1.1b), but less light is absorbed. The DB efficiency curve marks the ideal bandgap range for photovoltaic energy conversion and allows for comparison between different solar cell types. The semiconductor bandgaps of different materials depend on their building blocks (atoms, molecules, nanocrystals) and their arrangement (crystal, amorphous,

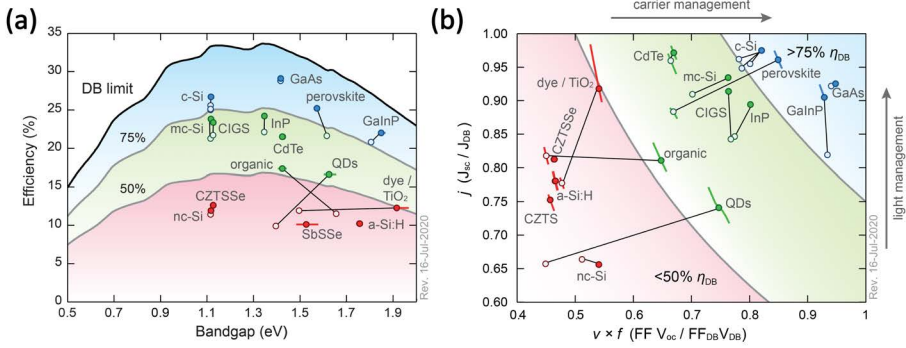


Figure 1.2: Fraction of the detailed-balance (DB) limit for record-efficiency solar cells of 15 different materials. The open symbols show the record values from April 2016, the solid symbols show the values in July 2020. Figures from references [13] and [20], which are continuously updated with data from new record-efficiency solar cells and made available at <https://www.lmpv.nl/DB/> (a) Fraction of the DB efficiency limit (black line) as a function of the bandgap. Gray lines show 75% and 50% of the limit. (b) Fraction of the DB current density (j) versus the fraction of the DB voltage times fill factor ($v \times f$), corresponding to the efficiencies in panel (a).

host-material, passivation, and spacer layers). As we will see, there is a remarkable breadth of materials with different or even tunable bandgaps and corresponding record efficiencies.

The power conversion efficiency of solar cells has been improved upon for over half a century. In 1954, the first practical solar cell was demonstrated at Bell Labs, a crystalline silicon solar cell with 6% efficiency [21]. A vast global research effort ensured a steady increase in efficiency over time, and in 2017, the newest world-record efficiency for a silicon solar cell was set at 26.7% [22]. Besides silicon, many more material systems have been successfully explored for photovoltaics. Figure 1.2a shows the current world-record efficiencies for 15 of the most commonly used materials, plotted against their bandgap and the DB limit we discussed in the previous section. Over the past several years, we have continuously updated these Figures that were first published in 2016 by Polman et al. [13]. The updated Figures are publicly available at <https://www.lmpv.nl/DB/>.

In 2020, we published the updated Figures in a review paper looking back at the progress over the previous 4 years [20]. The open and closed data points in Figure 1.2a show this progress between 2016-2020, for each material system. The blue, green, and red shaded backgrounds indicate the performance as a fraction of the DB limit, respectively >75%, >50%, and <50%. Above 75%, we find ultrahigh-efficiency mono-crystalline materials such as Si, GaAs, GaInP, and more recently also perovskite. On the other hand, we see the most impressive efficiency increases for QD and organic solar cells. The plethora of materials used in photovoltaics nowadays and their continued advancement makes for a robust industry, offering many options for many different mainstream and niche applications [15].

There are several reasons why even record solar cells do not come much closer than 75% of the DB limit. We can understand them by looking at the components that make up the generated electrical power at the maximum power point P_{mp} :

$$P_{mp} = V_{oc} \times J_{sc} \times FF = V_{mp} \times J_{mp}. \quad (1.1)$$

Here, V_{oc} is the open-circuit voltage, the output voltage of the solar cell when the circuit is not closed: the electrical resistance is infinite and no current flows. J_{sc} is the short-circuit current density, the current that the solar cell generates when the electrical resistance is zero, and thus, the voltage is zero. Finally, FF is the fill factor, which accounts for all nonidealities in the cell. Expressed as $FF = (V_{mp}J_{mp})/(V_{oc}J_{sc})$, the FF indicates how well the voltage and current density approach their maximum values at the maximum power point. Fundamentally, the FF cannot become unity because the resistance in the circuit cannot be zero (short-circuit) and infinite (open-circuit) at the same time. Moreover, a finite load is needed to harvest the energy because both V and J need to be nonzero for the power (P) to be nonzero. V_{mp} and J_{mp} are defined as the voltage and current density that together generate the maximum amount of power and stipulate the ideal electrical resistance in the circuit. With the specified maximum generated power, we can calculate the efficiency of the solar cell according to:

$$\eta = \frac{P_{mp}}{P_{AM1.5G}}, \quad (1.2)$$

with η the power conversion efficiency and $P_{AM1.5G}$ the power in the AM1.5G solar spectrum, which is defined as 1000 W m^{-2} .

Now that we have separated the voltage and current density components in the generated power, we can specify the implications of a few notable nonidealities in a solar cell. First and foremost, a realistic solar cell does not absorb all incident sunlight in the active layer. Instead, fractions of the light are lost due to reflection, incomplete absorption, or parasitic absorption in other layers, which lowers the generation rate of carriers (electron-hole pairs). This mainly lowers the J_{sc} . Incomplete collection of the generated carriers can further lower the J_{sc} . The V_{oc} is decreased by phenomena such as Auger recombination, band tail recombination, and recombination in the bulk, and at interfaces and surface defects [13]. Finally, nonidealities such as electrical resistance and contact losses are captured in the FF. Combined, these are the reasons why the record-efficiency solar cells in Figure 1.2 are below the DB limit.

Figure 1.2b shows the fraction of the DB limit of the voltage, FF, and current density according to Equation (1.1), corresponding to the record efficiencies shown in Figure 1.2a. As discussed in the previous paragraph, now we can understand that the current density axis indicates to what degree the light management is the limiting factor (incomplete absorption), while the voltage \times FF axis indicates the limitation by charge carrier management (recombination). Interestingly, the ultrahigh-efficiency materials show either near-perfect light management (Si and perovskite) or near-perfect carrier management (GaAs and GaInP). Similarly, the CIGS and dye records advanced mainly by increased light management, while the organic and QD records advanced mostly by improved carrier management. This indicates that both light management and carrier management are very active areas of photovoltaics research and development.

Improving carrier management requires understanding and control over the recombination mechanisms in a solar cell [13]. This is mostly a materials science challenge, with a focus on the quality of materials and interfaces. The focus of this thesis is on the improvement of light management, which requires control over the propagation and absorption of light inside the cell. Although light management also benefits from material quality, the main challenge is to achieve absorption in the active layer. It is a dynamic game, where the goal is to simultaneously reduce the reflection, transmission, and parasitic absorption of light with energies above the solar cell bandgap, and decrease heating from below-bandgap light. Photonic concepts offer a plethora of possible light management techniques for several different applications. The bulk of this thesis is concerned with *photonics for photovoltaics*, so in the next section we will explore this field of study in more detail.

1.3 Photonics for photovoltaics

Light is an amazing phenomenon. We understand it as a quantized packet of energy that has a momentum but no mass and can therefore travel at the maximum speed in our universe — the speed of light. As we describe light in more detail, we find that it behaves either as a particle or as a wave, depending on its environment: the famous particle-wave duality. In the particle description, light behaves like objects we know from ordinary life: a ball will either bounce back from a solid wall or move through a hole in that wall. Similarly, a light particle, called a photon, will reflect from a mirror or transmit through a hole in that mirror. The analogy is almost perfect, except for the fact that a photon has a probability associated with reflection, transmission, or absorption by a material, while the ball will bounce from the wall with 100% certainty. Thus, even in the particle description of light, we describe the propagation of a photon with probabilities (relating to the quantum mechanic nature of light). When we have a large number of photons, for instance, when we measure the number of photons reflected by and transmitted through a window, we find back the probabilities in the statistics of reflected or transmitted photons. When the features of the environment are much larger than the wavelength of the light, we can model light with geometric (ray) optics. This model, which we use in **Chapters 3 and 6**, describes light propagation as rays moving in straight lines that behave according to the statistics described before. However, to explain the full behavior of light, we have to describe it as a wave.

In the wave description, light behaves much like a wave on the ocean: it has a certain distance between the tops (called the wavelength), travels at a certain speed, and the amplitude of the wave can be interpreted as the number of photons. In contrast to the particle description, we can describe the phenomenon of light interference in the wave description. In daily life, we know of the interference of water waves, for example, when we throw two stones next to each other in a pond: each stone creates a circular water wave by its impact. When the two waves meet, they interfere: crests in the waves add up to higher peaks; troughs in the waves add up to lower depths; and a crest and a trough dampen each other. Effects such as interference become dominant when we shrink down the material that we illuminate down to the size of the wavelength. For visible light, the wavelength lies roughly between 400 and 700 nm (ultraviolet - red), which corresponds to 0.0004 - 0.0007 millimeter (mm). When we talk about nanotechnology or the nanoscale, we refer to materials with features with this length scale and smaller (1 - 1000 nm). Nanoscale materials have been used for centuries because of their special interaction with light, for example, the use of gold nanoparticles that cause the colors in stained glass windows and the famous Lycurgus Cup [23]. However, the advances made over the past few decades in micro- and nanoscale fabrication, (nano)photonic light management, and powerful electromagnetic simulation methods have sparked a rich field of research on photonic light management.

1.3.1 Photonic light management

Typically, light travels in straight lines and undergoes reflection, transmission, refraction, and absorption when it interacts with a material. The strength of reflection and refraction at an interface is dictated by the refractive index of the materials. The imaginary part of the refractive index, the extinction coefficient, dictates the absorption of light in a material (Beer-Lambert law) and thereby the transmission. For a high-efficiency solar cell, the challenge is to maximize the absorption of light in the active layer (the semiconductor layer where charges can be extracted). This implies that the reflection of incident light must be minimized, and all other layers must transmit the light to be absorbed in the active layer. To absorb all the light, the active layer of a conventional solar cell must be ‘optically thick’. Because the strength of the extinction coefficient varies strongly between different semiconductor materials, this thickness varies from a few micrometers (μm) for direct-bandgap materials such as gallium arsenide (GaAs) to several hundreds of micrometers for indirect-bandgap materials such as Si. A large optical thickness poses a dilemma for conventional solar cells because the use of a thicker solar cell increases light absorption but also increases the losses in extraction and recombination. Photonic design can help increase the absorption of incident light, thereby enabling the use of a thinner solar cell.

For a silicon solar cell, incident light experiences a large contrast of refractive index at the air-silicon interface of about a factor 4. This impedance mismatch for an electromagnetic wave traveling in air or silicon causes strong reflection at the interface (given by Snell’s law). This mismatch can be reduced by placing a material in between the air and silicon that has a refractive index between that of air and silicon. A commercial solar cell has several of these materials, such as the silica module glass, a transparent conductive oxide (TCO) contact, and/or an anti-reflection layer such as silicon nitride (Si_3N_4). Alternatively, nanoscale structuring of the material can also reduce reflection. In the simplest case, the structuring is much smaller than the wavelength, such that the light propagates as if it was in a single material with an effective refractive index. The validity of this effective medium approximation is discussed in **Chapter 6**. Figure 1.3a shows this effect in a schematic: the top surface of the solar cell (light blue) is structured to enhance light propagation into the solar cell.

When we increase the size of the features on top of the solar cell in Figure 1.3a to the scale of the wavelength, we enter a regime of resonant light-matter interaction. In this case, the interaction is enhanced because the wavelength matches the length scale of the material and the energy of light is temporarily stored inside the nanostructure. In daily life, we know this effect from the sound of a guitar string (the wavelength matches the length and material of the string) or from the tuning of a radio (the radio antenna resonates at the radio frequency).

When light interacts with a material that is structured at the nanoscale, this can cause several resonant effects, depending on the material properties, such as Fabry-Pérot constructive or destructive interference [24], or the coupling to Mie-like resonances (dipolar or multipolar polarization of the material) [24–26], plasmon resonances (localized excitations or propagating modes on the surface of a metal) [27], or waveguide modes (propagation confined to one or two dimensions) [28].

Fabry-Pérot type resonances were discussed above as the typical flat, thin-film anti-reflection layers of a solar cell. Mie-like resonances are discussed in detail in **Chapter 2**. In Figure 1.3, Mie-like resonances in panel (a) cause forward scattering of light under an enhanced angular range into the solar cell to achieve light-trapping. In Figure 1.3(b), Mie-like resonators are designed for infrared light to achieve enhanced cooling of the cell — this concept of passive radiative cooling is discussed in **Chapter 5**. In panels (c), (e), and (f), Mie-like resonators are used to control the reflection and transmission of light at interfaces

depending on their wavelength. In panel (c), high-energy light is reflected back into the top subcell of a tandem solar cell, while low-energy light is transmitted into the bottom cell. In panel (f), the same effect is pursued and dynamically adapts to the performance of the subcells (for example, to improve current-matching). In panel (e), light of a specific wavelength is reflected to “color” a solar cell (structural color), while most light is transmitted into the cell for conversion (not drawn). Panel (d) shows the effects of up- or down-conversion of light, as discussed earlier. In down-conversion, high-energy photons (blue) are converted into multiple low-energy photons (red), which reduces thermalization losses; up-conversion does the inverse, enabling conversion of light with energy below the bandgap. These types of conversion are achieved by absorption and subsequent emission of light — control over these processes with nanophotonic structures is discussed in **Chapters 2 and 4**.

The concepts of light management in photovoltaics were first explored with plasmonic resonances, as reviewed in references [27, 29]. It was found that parasitic absorption caused by the metal building blocks made the use of plasmonics in solar cells challenging. Many of the concepts first shown with plasmonics were then pursued with all-dielectric nanophotonic resonances such as those discussed above [13, 30–32]. In this thesis, we focus on the use of all-dielectric nanostructures that can be used to enhance photovoltaic energy conversion.

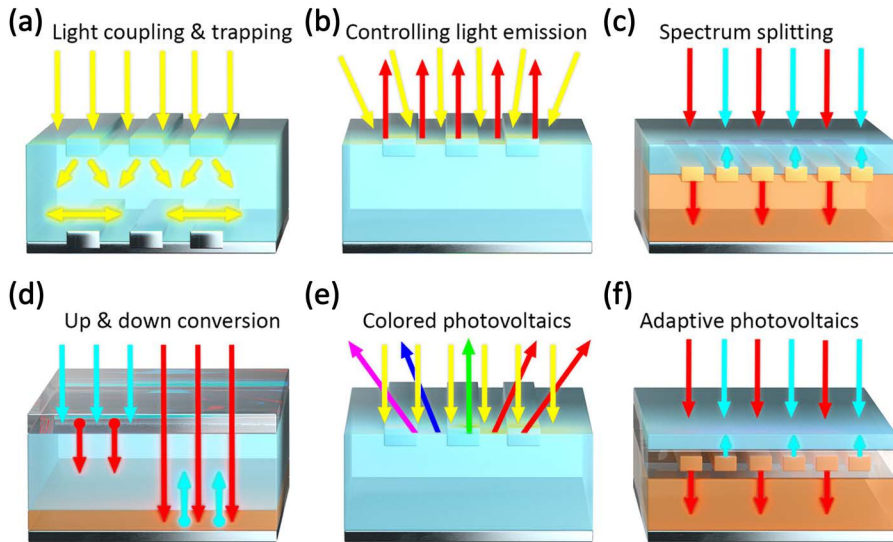


Figure 1.3: Schematic of photonic light management geometries to optimize photovoltaics. Figure from ref. [32].

1.4 Motivation

In the previous sections, we have seen that an enormous amount of solar energy reaches the earth, that photovoltaics is a mature technology that can convert this energy to electricity, and that photonics can improve both conventional and new types of photovoltaic systems. Yet, even after decades of research and technological advancements, there are two key challenges that remain to be overcome. The first is to further reduce the cost of solar electricity generation to enable it as one of our main energy sources, and the second is the integration of solar electricity generation into buildings, landscapes, and infrastructures. We briefly discuss them both as the motivation to this thesis.

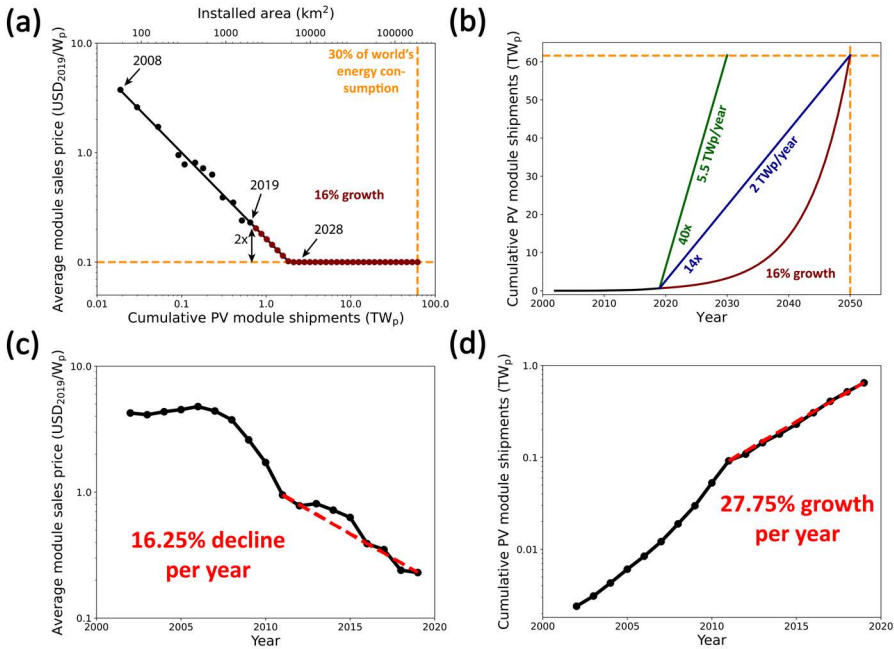


Figure 1.4: Cost reduction and PV installation growth. (a) Average sales price of Si solar modules normalized by the generated power under standardized conditions (W_p) as a function of total installed capacity since 2008. Data from the ITRPV report [18]. Red data points are extrapolations of the 22% annual cost reduction at a yearly 16% growth of installed capacity, assuming that module prices will saturate at a price of 0.1 US\$/W_p. (b) Historic realization (black) and 16% annual fixed growth scenario (red) of installed PV capacity. The linear curves correspond to increased PV installation rates (14/40× compared to ~0.1 TW_p/year in 2019, to reach a 60 TW_p target in 2050/2030). Panels (a) and (b) from ref. [32]. Panels (c) and (d) plot the historic data of the average module sales price and the cumulative module shipments, respectively, versus the corresponding years (2002-2019). It shows essentially the same data as the black lines in panels (a) and (b) but visualizes the exponential decline in price over time and the simultaneous exponential growth of the installed capacity over time.

Given the disparity between a finite amount of fossil fuels and near-infinite solar energy supply, one might conclude that solar is an obvious choice and bound to replace fossil fuels. Yet, even by the year 2040, fossil fuels are expected to still supply more than half our global energy supply [5]. The fossil fuel industry supplies many jobs and is a key economic driving force of our modern society, but most of all it supplies very inexpensive energy. Where (global) policy can surely impact the transition to renewable energy use, lowering the cost of PV-generated power will certainly accelerate the transition. Figure 1.4a shows the historic price data from 2008 until 2019 in black: the average module sales price vs. the cumulative PV module shipments (global installed area). The curve shows an exponential decline in the average price (Fig. 1.4c) and an exponential increase in the installed area (Fig. 1.4d). This power law relation is very impressive, sustaining an installed-capacity growth of 16% per year, mainly fueled by economy of scale as the production capacity increases [13]. In Figure 1.4a, Garnett et al. assumed a saturation at a price of 0.1 dollar (USD) per watt-peak (W_p). This is a fair assumption for the current market that is dominated by silicon technology, where the costs of the raw materials of the cell and module cannot scale down forever. If we could sustain this 16% growth until the year 2050 (red dots), this would yield an estimated 30% share in the world energy consumption ($\sim 60 \text{ TW}_p$ installed capacity). Here, we assume the global primary energy supply would grow from 18 TW in 2019 to 23.5 TW in 2050 [33]. To generate an average of 7.05 TW (30% of 23.5 TW) with PV, assuming a global PV capacity factor of 8.5, we obtain the estimated $\sim 60 \text{ TW}_p$ installed capacity.

However, such exponential growth of the installed capacity has the most impact in the final years, as is clearly visible in Figure 1.4b: the black line is the historic installed capacity on a linear scale; the red line the projected exponential increase at 16% per year. In the exponential projection, only about a quarter of the $\sim 60 \text{ TW}_p$ is installed by the year 2040. Alternatively, also two linear projections are plotted that start in 2019, which need an abrupt $14/40\times$ increase in the added module shipments per year, and need to sustain that pace until 2030/2040. Evidently, the linear cases will not be met, but it does demonstrate the upscaling of the solar panel manufacturing that is needed. Polman et al. have put in perspective how much area actually would be needed to power the world with solar energy only, indicating that it is not impossible:

“Assuming a modest module efficiency of 20%, a system capacity factor of 15%, an average ground cover ratio of 50%, and 50% losses related to storage and secondary conversion, 1.6% of Earth’s land area would be required to produce an amount of energy equal to the current primary supply (18 TW in 2019). Although in absolute terms this is a very large number, it is not unrealistic. To put this in perspective, this area is less than 5% of the area used for agriculture worldwide. Also, note that substantial land areas are already used today for production of fossil fuels and various types of biofuel. Finally, by drastically increasing the efficiency of solar modules, by integrating PV into buildings and other objects, and by combining PV technology with other renewable sources such as solar thermal energy and wind energy, a much smaller land area would be needed.” [13]

To power our world with clean, renewable, and at least climate-neutral energy, we need to replace fossil fuels, with solar energy playing a major role. To meet the global greenhouse gas emission targets [6, 7], we have to accelerate the energy transition beyond the current exponential growth. This can be done by making solar modules even cheaper. This can mean either producing the same module at a lower price or producing a higher-efficiency module at the same price, which indicates the need for further research and development of PV. However, accelerating the growth can also be achieved by producing entirely different types of PV: for

example, by producing flexible, thin-film PV at half the efficiency but more than two times cheaper, or a tandem device at the same price but higher efficiency. These technologies are not commercially available yet but are potentially disruptive.

The second challenge, the integration of solar electricity generation into the environment, concerns where we install different kinds of PV systems. Solar power plants typically deploy high-efficiency, flat panel solar modules covering large land areas. Especially countries with high population densities, such as The Netherlands, necessitate the further development of high-efficiency PV in landscapes. The use of PV with somewhat lower efficiency (e.g., 15-20%) at a very low cost might be a viable option for certain cases or regions that are not limited by the physical area. Complementary to installing PV in landscapes, it can be installed in buildings and infrastructures. Building-integrated photovoltaics (BIPV) covers many different types of PV technologies, ranging from conventional silicon solar cells integrated into roofs [34] or walls [35], colorful solar cells [36, 37], or even semi-transparent PV. In **Chapters 3 and 4**, we present our efforts to enhance the efficiency of luminescent solar concentrators as semi-transparent BIPV. Photonic concepts are particularly important for these emerging types of PV, for example, to engineer the color of the photovoltaic, ensure light trapping in thin, lightweight, and flexible PV, or combine semi-transparency with efficient power generation in windows.

To conclude this motivation, we take a look at the estimated area of PV we would need in the Netherlands to generate 50% of the primary energy consumption in 2019. Here, we consider a typical solar panel of 300 W_p per 1.5 m², the solar capacity factor in the Netherlands of 11.3, and the energy consumption of 0.13 TW, both in 2019. Figure 1.5 shows the estimated area of 60 × 60 = 3600 km², almost 9% of the land area of the country, amounting to ~735 GW_p installed PV capacity. As mentioned before, it might be impossible to cover 9% of the land area with PV. Estimating the installation of PV in landscapes to be limited to 3%, we have a need for large-scale integration of PV into buildings, infrastructure, and possibly even PV on water. The necessary area also decreases by increasing the efficiency of the PV; in **Chapters 5, 6, and 7**, we investigate the use of radiative cooling and the reduction of reflection losses to increase the efficiency of solar cells.



Figure 1.5: Map of the The Netherlands. The yellow square indicates the area needed for photovoltaics to power 50% of the estimated primary energy consumption of the Netherlands in the year 2050.

1.5 Outline of the thesis

The absorption and emission of light can be controlled using photonic structures. In the first part of this thesis, we investigate the use of resonant nanophotonic structures to control the angular distribution of luminophore emission (quantum dots or nanoplatelets). In the second part of the thesis, we investigate the use of micro- and nanostructures in silicon solar cells to enhance infrared emission for radiative cooling and to reduce reflection of visible and near-infrared light.

Part I: resonant nanophotonic structures for directional emission

In **Chapter 2**, we present a soft-stamping method to selectively print a homogeneous layer of CdSeTe/ZnS core-shell quantum dots (QDs) on top of an array of Si nanocylinders with Mie-type resonant modes. Using this new method, we gain control of the QD's angular emission through engineered coupling of the QDs to these resonant modes. We show enhanced upward or downward QD emission depending on the cylinder size, as well as enhanced absorption of laser light due to the cylinder array.

In **Chapter 3**, we employ Monte Carlo ray-trace modeling to evaluate the conversion efficiency of luminescent solar concentrators (LSC) using anisotropic luminophore emission as a function of photoluminescence quantum yield, waveguide concentration, and geometric gain. By spanning the full LSC parameter space, we define a roadmap towards high LSC conversion efficiency. An analytical function is derived for the dark radiative current of an LSC to calculate the conversion efficiency from ray-tracing results. We provide design parameters for optimized luminescent solar concentrators with practical geometrical gains of 10. Using luminophores with strongly anisotropic emission and high (99%) quantum yield, we conclude that conversion efficiencies beyond 28% are achievable.

In **Chapter 4**, we demonstrate anisotropic luminophore emission that can be used to enhance light trapping in the LSC waveguide. By embedding semiconductor nanoplatelet emitters into high-index TiO₂ nanocylinders, we alter their angular emission profile to increase emission into total internal reflection (TIR) angles. The emission direction can be controlled by tweaking Mie-like multipolar resonances in the individual nanocylinders (form factor) and the interaction with the lattice (structure factor). Angle-resolved photoluminescence measurements on the fabricated nanocylinders arrays corroborate this understanding. By optimizing the cylinder shape and lattice spacing, we show an increase in light trapping from 75% (isotropic emission) to 83.5%.

Part II: resonant nanophotonic structures for directional emission

In **Chapter 5**, we investigate the use of passive radiative cooling (PRC) to dissipate excess heat from a solar cell into or through the earth's atmosphere. For a silicon solar cell, the challenge is to enhance PRC while simultaneously retaining transparency for sunlight above the silicon bandgap. We fabricate a hexagonal array of microcylinders that can be integrated on top of the solar cell module glass. We show very good comparison between simulations and measurements of the infrared spectra while retaining transparency for above-bandgap light.

Textured silicon solar cells that achieve ultra-low reflectance are called black silicon (BSi) because of their black appearance. The diversity and complex surface structures of BSi make it challenging to commercialize BSi devices. Modeling and simulation are commonly used in the semiconductor industry to better understand the material properties, predict the device performance, and provide guidelines for optimizing fabrication parameters. In **Chapter 6**,

we model three BSi nanotextures, each with a distinct random geometry, with an effective medium approximation (EMA). We validate the use of EMA with full-wave optical simulations. We propose criteria for the validity of different optical simulation techniques for a set of industrial photovoltaic textures. This analysis reveals a region within which neither geometric optics nor EMA are adequate for calculating the reflectivity of a textured surface, and hence full-wave optical simulations are required.

Finally, in **Chapter 7**, we investigate the accurate characterization of BSi textures. We compare 3D models of challenging BSi textures obtained by atomic force microscopy (AFM) and plasma focused ion beam (PFIB) tomography techniques. Hemispherical reflection measurement results are compared to full-wave optical simulated results to test the reliability and consistency of the tomography models. Our results provide strong evidence that PFIB tomography is a better substitute to the AFM for highly roughened surface topographical characterization such as BSi, which provides surface 3D models with better reliability and consistency.

Overall, this thesis provides new insights into multiple light management strategies to improve photovoltaic systems. Many of these insights are more generally applicable to other optoelectronic devices, including photodetectors, light-emitting diodes, and displays.

2

Directional quantum dot emission by soft-stamping on silicon Mie resonators

We present a soft-stamping method to selectively print a homogeneous layer of CdSeTe/ZnS core-shell quantum dots (QDs) on top of an array of Si nanocylinders with Mie-type resonant modes. Using this new method, we gain accurate control of the quantum dot's angular emission through engineered coupling of the QDs to these resonant modes. Using numerical simulations we show that the emission into or away from the Si substrate can be precisely controlled by the QD position on the nanocylinder. QDs centered on a 400 nm diameter nanocylinder surface show 98% emission directionality into the Si substrate. Alternatively, for homogeneous ensembles placed over the nanocylinder top-surface, the upward emission is enhanced 10-fold for 150 nm diameter cylinders. Experimental PL intensity measurements corroborate the simulated trends with cylinder diameter. PL lifetime measurements reflect well the variations of the local density of states at the QD position due to coupling to the resonant cylinders. These results demonstrate that the soft imprint technique provides a unique manner to directly integrate optical emitters with a wide range of nanophotonic geometries, with potential applications in LEDs, luminescent solar concentrators, and up- and down-conversion schemes for improved photovoltaics.

This chapter is based on:

Directional quantum dot emission by soft-stamping on silicon Mie resonators

Tom Veeken¹, Benjamin Daiber¹, Harshal Agrawal¹, Mark Aarts¹, Esther Alarcón-Lladó¹, Erik C. Garnett¹, Bruno Ehrler¹, Jorik van de Groep², and Albert Polman¹

Nanoscale Advances **4**, pp. 1088-1097, 2022.

<https://doi.org/10.1039/D1NA00630D>

¹Center for Nanophotonics, NWO-Institute AMOLF, Science Park 104, 1098 XG Amsterdam, The Netherlands

²Van der Waals-Zeeman Institute, Institute of Physics, University of Amsterdam, Science Park 904, 1098 XH Amsterdam, the Netherlands

Author contributions:

Tom, Benjamin, Bruno, and Albert conceived the project. Tom performed the FDTD simulations, PL measurements, data analysis, and wrote the original draft. Benjamin and Tom performed the TCSPC measurements. Benjamin fitted the lifetimes. Harshal and Tom developed and performed the stamping procedure, under the supervision of Erik. Harshal, Benjamin and Tom performed the SEM imaging. Mark performed the AFM measurements, under the supervision of Esther. Bruno and Albert supervised the project. Jorik and Albert reviewed and edited the manuscript. All authors provided feedback and contributed to the manuscript.

2.1 Introduction

Accurate control over the angular distribution of light emission is of great importance in many technological applications. In light-emitting diodes (LEDs) for example, controlling the angular distribution of light emission inside the semiconductor into the escape cone optimizes the output power [38, 39]. In solid-state lighting systems, tailored visual appearances can be achieved by controlling the angular distribution of light emission [40, 41]. And in photovoltaic systems, control over the directionality of emission can improve the efficiency of luminescent solar concentrators [42, 43] and enhance the efficiency of up- and down-conversion schemes [44–47].

Resonant nanostructures can help tailor the emission of dipole-like point emitters by controlling the coupling between the resonant modes and the emitter. The spectrum, polarization, and angular distribution of the emission are then determined by the coherent superposition of the scattered fields of the electric and magnetic multipoles and their coupling to the emitter's dipole moment. Initial work in this area focused on coupling noble-metal nanoparticles to optical emitters, where the spectrum and polarization were controlled by coupling emitters to selected plasmonic modes [48, 49] and directional emission was achieved with nanoparticle antenna's [50–53]. More recently, all-dielectric resonant nanostructures have received great interest because of their strongly reduced optical losses and the larger variation of multipoles that can be excited [54–57]. This offers more degrees of freedom to design the resonant interaction with the emitter. Moreover, optical emitters can be placed directly inside the resonant nanostructures [41, 58]. Vice versa, nanostructures can be directly placed on top of emitters, as recently shown for resonant silicon (Si) nanowires on monolayers of MoS₂ [59], to create directional forward and backward emission depending on the complex interplay of the nanowire resonances. In these pioneering first experiments, there was only limited control on the exact placement of emitter with respect to the nanoresonator [60–62]. However, to leverage all benefits of the dielectric resonator-emitter coupling, precise control over the placement and coupling between the emitter and resonant nanostructure is of great importance. Selective coating of nanostructures with uniform monolayers of emitters, in particular, would be highly desirable for applications in e.g. LEDs and luminescent concentrators.

Here, we introduce a new method to achieve selective control over the placement of optical emitters on resonant nanostructures using a soft stamping technique [63]. As a demonstration, we fabricate arrays of Si nanocylinders that exhibit strong optical Mie resonances using standard electron-beam lithography (EBL) and reactive-ion etching (RIE) techniques. Then, using a PDMS rubber stamp we selectively place luminescent quantum dots (QDs) on top of nanophotonic structures only in a controlled manner. By directly spin-coating the QDs on the PDMS stamp, we realize a single-step stamping process that is simplified compared to existing pick-and-place stamping techniques [64–67]. Using photoluminescence (PL) mapping spectroscopy and lifetime measurements in combination with numerical modeling, we show evidence of strong directional emission of the QDs coupled to the nanoresonators. Our results contribute towards novel routes for improved efficiencies of quantum dot applications in LEDs, wide spectrum emission, and enable up and down-conversion schemes in photovoltaics. The resonant directional light emission demonstrated in this chapter is generic and can be applied to a wide range of emitters, including semiconductor quantum wells, fluorescent molecules, and perovskite films.

2.2 Nanophotonic design

The angular emission intensity distribution in the far-field of an optical emitter depends on the local density of optical states (LDOS), given the position and orientation of the emitter and the (near-field) coupling to the available optical modes. The LDOS varies strongly with position near an interface, and the modal density in the far-field is linearly proportional to the refractive index [68]. As a result, an optical emitter in a low-index medium close to a high-index substrate (Fig. 2.1a) shows strongly anisotropic emission towards the higher index medium [69]. For distances on the order of the wavelength, back-action between the dipole and its emitted light reflected at the interface leads to strong modulation of the anisotropic emission with distance from the interface, as first shown by Drexhage [70]. In Fig. 2.1c, the azimuthal angular emission profile is shown for an electric dipole placed 5 nm above a Si substrate, obtained from an analytical Green's function model [68]. To emulate the profile of an ensemble of dipoles with a random orientation distribution, as is often the case experimentally, the emission profile in Fig. 2.1c is the average of the three orthogonal transition dipole moments, x , y , and z . The results in Fig. 2.1c show that the strong index contrast at the Si/air interface results in 93.5% of the emission being directed into the Si substrate. For photovoltaic applications, this 6.5% loss is significant and therefore requires enhancing the downward emission even further. On the contrary, for light-emitting applications, the anisotropy caused by a high index substrate calls for enhancing the upward emission. Both these effects are addressed in this paper.

To control the emission anisotropy, high-index resonant nanostructures are placed in the near-field of the emitter, as depicted in Fig. 2.1b. Silicon structures with dimensions in the few-100-nm range support an electric dipole (ED), magnetic dipole (MD), and higher-order multipoles [54, 71]. The coupling of the emitter to these multipolar modes alters the angular emission pattern through interference of the scattered light in the far-field. The shape and size of the resonator determines the strength of the multipolar modes at the emission wavelength, and as such, acts as a control for the direction of emission. We first use Finite-Difference Time-Domain (FDTD) simulations to calculate the coupling between the emitter and the nanostructure, using known optical constants for Si and a dipole emitting at $\lambda = 760$ nm placed 5 nm above the center of a Si cylinder. In Fig. 2.1e, the fraction of radiation emitted into the top hemisphere is plotted as a function of Si cylinder diameter for different heights (see Fig. 2.7 for corresponding emission profiles). The upward emission is defined as the total radiation emitted into the upper hemisphere, by a single dipole on top of a single cylinder. The dashed line in Fig. 2.1e indicates the reference value of 6.5% for the case of a substrate without resonator. We find that for small cylinder diameters between 50 and 250 nm, the upward radiation away from the substrate is enhanced, whereas the downward radiation is enhanced in the range of 250-500 nm. Beyond a diameter of 500 nm, the upward emission approaches the reference; here, the Si cylinder has many resonant modes at the emitter wavelength, but none with significant strength, such that the coupling is similar to that for a planar film. The maximum fraction of downward radiation is achieved for a cylinder diameter of 400 nm and height of 125 nm, at a value of 98%. The corresponding azimuthal angular emission profile is shown in Fig. 2.1d.

To assess which Mie-like multipolar modes are excited in the Si cylinder, we calculate the normalized scattering cross-section Q_{scat} using FDTD simulations, defined as the scattering cross-section normalized to geometrical cross-section for a normal-incident plane wave [54]. Figure 2.1f shows Q_{scat} as a function of wavelength and cylinder diameter. Many Mie-like resonances are visible for the cylinder without substrate (top), some of which can be attributed to single multipole resonances such as the ED, MD, toroidal dipole (TD), electric quadrupole

(EQ), and magnetic quadrupole (MQ). When the substrate is introduced under the cylinder (Fig. 2.1f, bottom), the lineshape of the multipolar resonances broadens significantly due to strong radiative leakage from the resonant mode into the substrate. However, the Q_{scat} remains well above unity, indicating the strong resonant character of the cylinder.

The broad range of Mie-like modes in a Si cylinder is shown in Fig. 2.1g, for the cylinder with maximum emission downwards but without the substrate. To obtain insight into which modes contribute to the strongly directional radiation pattern, we use a multipole decomposition to extract the relative contribution of a set of multipolar resonances: ED and toroidal dipole (TD), MD, EQ, MQ, and the electric octupole (EOC) [71]. Clearly, all five components attribute to the Q_{scat} over a broad range of wavelengths, and notably quite evenly at the target wavelength of 760 nm. Therefore, we attribute the enhanced downwards emission to a combination of multipolar modes in the cylinder and direct emission of the dipole into the far-field. Note that the multipolar resonances we find here are those that can be excited by the normal-incident plane wave. A dipole-like point emitter placed in the near-field of the nanocylinder can couple to the resonant modes with different relative amplitudes, and also excite modes with symmetric modal field profiles that cannot be excited a plane wave. Despite this, the multipole analysis provides valuable insight in the complex combination of multipolar resonances that collectively give rise to strong broadband light scattering.

So far, we analyzed the emission of a dipole placed at the center of the cylinder's top surface. Now, we investigate the angular emission for an ensemble of dipoles homogeneously distributed over the nanocylinder surface. We use FDTD to calculate the angular emission distribution for different radial positions on the nanocylinder surface, as shown in Fig. 2.1h for the cylinder diameter of 400 nm (which showed the highest downward emission in Fig. 2.1e). Subsequently, we average these simulation results, weighted by their radial area, to determine the upward emission fraction for the ensemble, which is shown in Fig. 2.1i. The result shows that the average upward directionality is always higher than that for the flat reference, i.e., the upward emission can be tuned. Similar to the calculation for the single emitter at the center, the curves converge to the reference for large diameter, but there is no cylinder geometry where the emission reaches below the reference. This means that emitters placed in the outer perimeter of the nanocylinder surface couple well to multipolar resonances that promote upward emission (see Fig. 2.8). Figures 2.1h,i indicate that the placement of quantum dots on the nanocylinders strongly controls the directional emission.

Figure 2.1: Directional dipole emission by nanophotonic engineering. (a,b) Schematics of a dipole above a Si surface in air and on top of a Si nanocylinder. (c,d) Calculated azimuthal angular dipole emission patterns corresponding to the cases depicted in (a,b) on a logarithmic radial axis. 98% downward emission is achieved for a dipole on top of a cylinder with optimized dimensions. (e) Calculated fraction of upward emission at $\lambda = 760$ nm as a function of cylinder diameter (x-axis) for different heights for a single dipole at the center of the cylinder. (f) Calculated Q_{scat} (color) as a function of wavelength and cylinder diameter for a cylinder in air (top) and a cylinder on a Si substrate (bottom). (g) Q_{scat} (dashed black) corresponding to the dashed line in (f) and its multipole decomposition (legend). (h) Calculated fraction of upward emission, similar to (e), but now as a function of dipole position on top of the 400 nm diameter cylinder. (i) Calculated fraction of upward emission, similar to (e), but now averaged over a homogeneous distribution of dipole positions on top of the cylinder. For all Figures throughout the paper, the distance between the dipole and the Si surface is kept constant at 5 nm, and the dipole emission intensity is averaged over all polarizations. The dashed line indicates the reference case for a dipole on a flat Si surface.

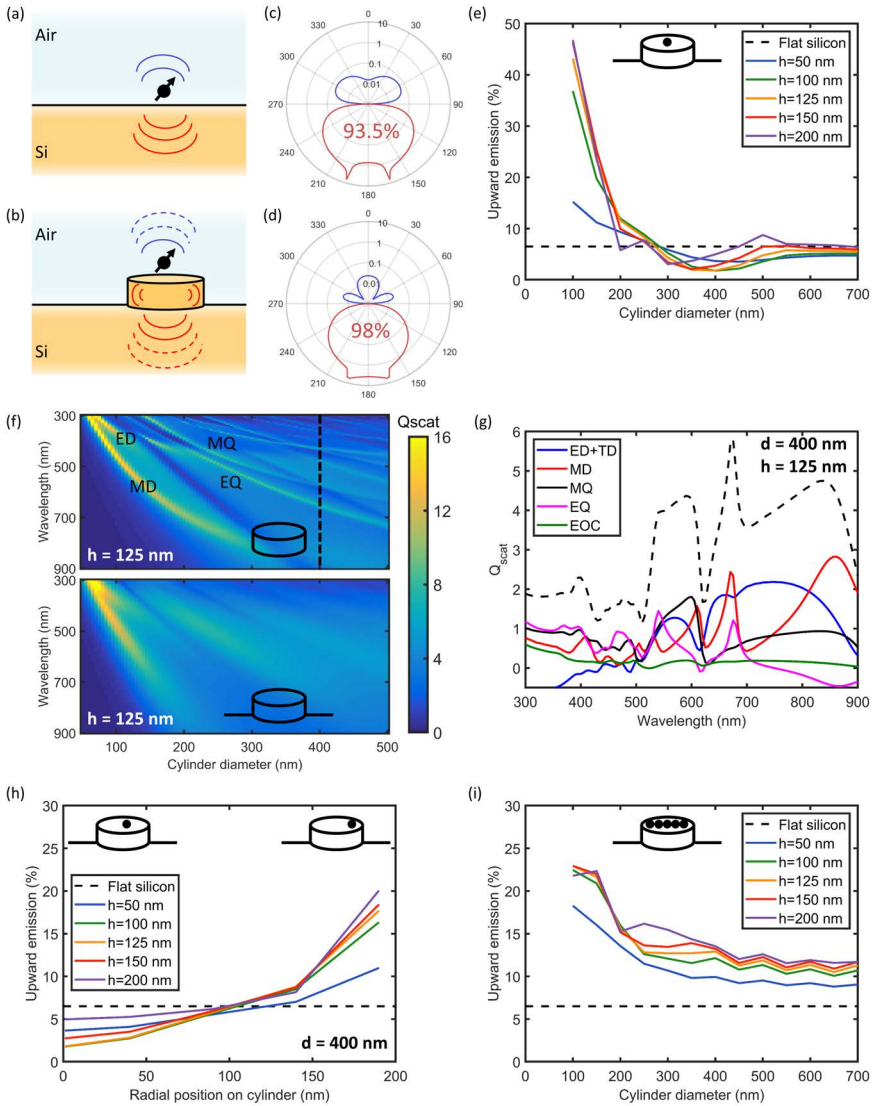


Figure 2.1: Directional dipole emission by nanophotonic engineering.

2.3 Fabrication: soft-stamping of QDs onto nanostructures

To experimentally demonstrate the nanophotonic control over QD directional emission, we fabricated the structures designed above. Silicon nanocylinders were patterned into the top surface of a Si substrate by EBL. A negative tone resist, hydrogen silsesquioxane (HSQ), was spin-coated on top of a polished Si(100) substrate (500 μm thick). Square arrays of disks were exposed in the HSQ with the electron beam. After development, only the exposed HSQ remained, which was subsequently used as an etch mask during the RIE step. A scanning electron microscopy (SEM) image of the resulting Si cylinder arrays is shown in Fig. 2.2a for a target diameter of 425 nm, height of 145 nm, and pitch of 1275 nm. This design differs slightly from the optimal design in Fig. 2.1e because fabrication was based on designs at a different target emission wavelength.

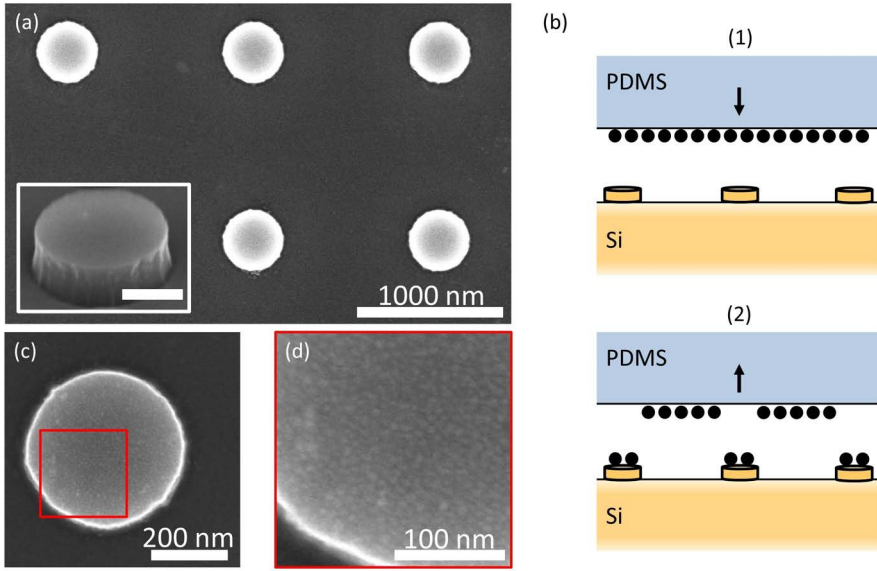


Figure 2.2: Nanocylinder fabrication and selective QD stamping. (a) SEM micrograph of Si cylinders on a Si substrate fabricated with EBL and RIE. Inset: SEM micrograph under an angle, showing straight sidewalls (scale bar is 200 nm). (b) Schematic representation of the stamping procedure; (1) QDs are spin-coated on a silanized PDMS stamp and pressed down on the nanostructured Si substrate; (2) after pressing for 10 minutes at 3 N force and 40 °C, the stamp is retracted, leaving behind the QD layer that came into contact with Si. (c,d) High-resolution SEM micrograph of Si cylinders after QD stamping showing a complete and conformal layer of QDs on the surface.

Subsequently, QDs were selectively placed on top of the Si cylinders using our novel one-step soft stamping procedure as depicted in Fig. 2.2b. We used CdSeTe/ZnS core-shell QDs (Qdot 800, ThermoFisher) dispersed in octane. First, a layer of QDs was directly spin-coated on top of a silanized PDMS stamp. The Si nanocylinder sample surface was activated with a UV-ozone treatment. Then, the PDMS stamp was mounted above the Si sample in a soft printing machine, face down. The stamp was brought into contact with the sample and pressed down with a force of 3 N. Once in contact, the sample was heated to 40 °C for 10 min, after which the stamp was withdrawn. The stamping was implemented with motorized controls. The flexible nature of PDMS facilitates a conformal contact with the substrate, which printed a uniform film of QDs on the sample. Figure 2.2c shows a representative SEM image of the top surface of a cylinder after stamping, showing the homogeneous coverage. In the zoomed-in image (Fig. 2.2d), the individual QDs can be recognized with a diameter of ~10 nm on the cylinder surface. The QD print on the cylinder and the clean Si surface besides the cylinder in Fig. 2.2c confirm that the stamping method printed completely and selectively on top of the tallest nanostructured surface.

2.4 Photoluminescence measurements

To characterize the directionality of the QD emission, we use a WITec confocal microscope in reflection mode. Figure 2.3a shows an optical image of the edge of a cylinder array using a 100x magnification and a broadband LED illumination source. The dark area on the left is the flat Si surface covered by a film of QDs. On the right, the dark dots correspond to the cylinders with a QD layer on top, while the bare Si substrate in between shows a brighter reflection.

Figure 2.3b shows a photoluminescence (PL) intensity map at $\lambda = 760$ nm of the same region imaged in Fig. 2.3a. A PL spectrum was measured under excitation of a $\lambda = 532$ nm laser at each position on the map. The measured PL intensity in the upwards direction is defined by the collection of the objective, i.e. up to angles of ~64 degrees (NA = 0.9) from the confocal collection spot of 1 μm . Clear QD emission is observed on top of the cylinders, and strong emission is also observed from QDs printed on the Si wafer next to the nanopatterned region. The latter directly results from the use of a flexible stamp that conformally coats the surface. In contrast, in between the cylinders, the signal is low. In Fig. 2.3c, the PL spectra for three characteristic positions are plotted: on the flat Si surface, on top of a cylinder, and in between four cylinders. The characteristic wide-band QD emission spectrum is observed in all three cases. We attribute the emission observed in the map between the cylinders to the fact that the tail of the laser (diffraction-limited spot size ~300 nm) excites QDs on top of the cylinders when the spot is centered in between cylinders and indirect excitation by light scattered from small roughness on the etched Si surface.

The PL data in Fig. 2.3 have been obtained for a rather thick QD layer printed on the sample. This results in a strong signal in the PL map in Fig. 2.3b and strong contrast between the cylinders and the surface, enabling direct imaging of QDs on top of the cylinders. Atomic force microscopy (AFM) measurements of the printed layer are shown in Fig. 2.4a. The printed layer is not completely conformal: the top surface of the Si cylinder is clearly visible (dark orange), with the inhomogeneous QD coverage in brighter colors, up to a height of 100 nm. To perform optical experiments on a thinner and more homogeneous QD layer and to enable a comparison with our simulation results, we repeated the printing process with a QD monolayer spin-coated on the PDMS stamp. An AFM map of the resulting QD coverage is shown in Fig. 2.4b, showing a homogeneous thin film of QDs on the cylinder surface. This imprint of a thin film of QDs corresponds to the SEM images in Fig. 2.2b,c.

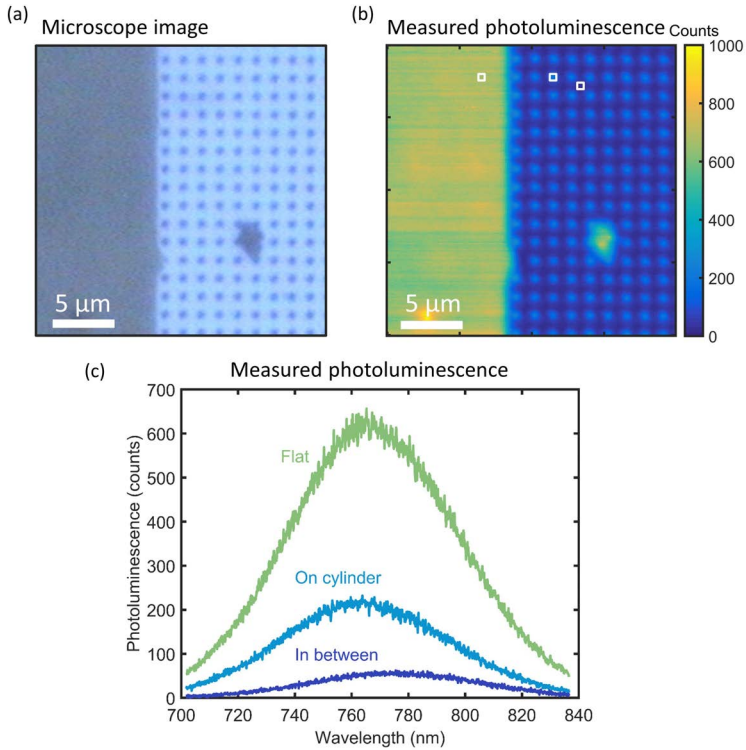


Figure 2.3: Photoluminescence mapping after thick QD print. (a) Microscope image of the Si substrate (blue) with a thick QD layer on top of flat Si and the Si cylinder array (gray). (b) PL map of the area depicted in (a). Color scale depicts the intensity at 760 nm wavelength. (c) PL spectra of three typical positions on the sample, indicated by the squares in (b): on the flat Si (green), in the middle of a cylinder (light blue), and in between four cylinders (dark blue).

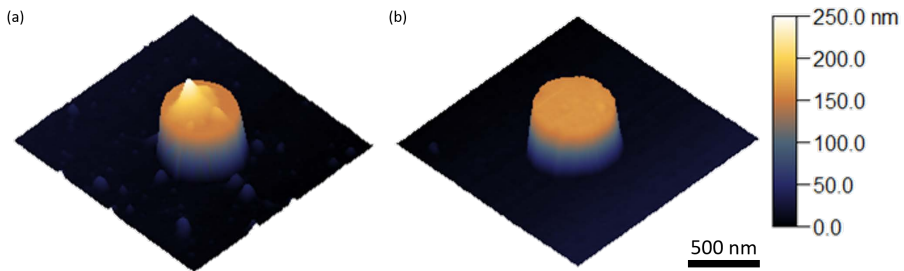


Figure 2.4: AFM height mapping; $1.5 \times 1.5 \mu\text{m}^2$ maps. (a) AFM image of a single cylinder with a thick layer of QDs stamped on top. The print is non-uniform and incomplete. (b) AFM image of a single cylinder with a uniform and complete monolayer of QDs stamped on top.

Figure 2.5a shows the PL map for the same cylinder array as in Fig. 2.3, with 425 nm diameter and 1275 nm pitch, but now with a QD monolayer on top. The emission from the individual cylinders is not distinguishable here because of the smaller 20x magnification. To compare the QD emission from the cylinder array with the flat Si beside it, we correct the emission counts for the ratio of the unit cell area to the cylinder top area, assuming that the cylinders are covered with QDs and that there are no QDs between the cylinders. We find that the upward emission intensity from the QDs on the cylinders, as collected by the microscope, is enhanced by a factor 2.6 ± 0.2 relative to the flat Si reference.

To compare the measured results with simulations, we have to account for resonant enhancement of the quantum dot by the cylinders. To do this, we derive the excitation enhancement by using FDTD to obtain the electric field enhancement above the cylinder at the laser wavelength (see Methods and Fig. 2.9). The electric field intensity above the cylinder is then used to weigh the contribution to the upward emission intensity of each position on the cylinder's top surface. From this analysis, we find an upward emission enhancement by a factor 1.8, close to the experimental value found above from Fig. 2.5a. This confirms that the FDTD simulations accurately predict the coupling between the emitter and the nanostructure in the near-field and the resulting far-field emission.

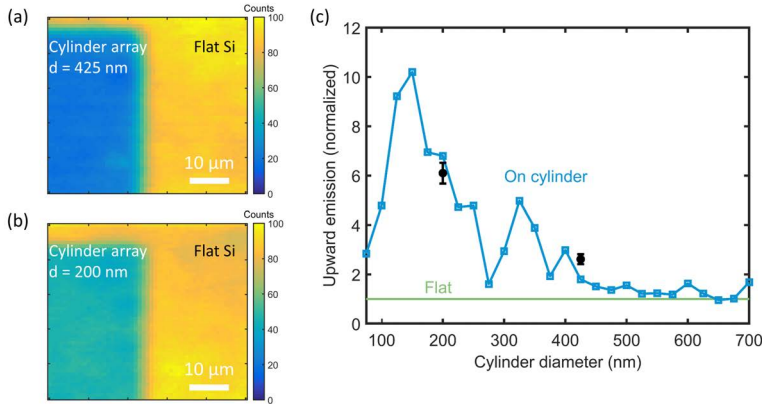


Figure 2.5: Photoluminescence mapping after monolayer QD print. (a,b) PL maps of the boundary area between a cylinder array and flat Si, for diameters of 425 and 200 nm, respectively. The color scale depicts the intensity at $\lambda = 760$ nm. (c) Calculated upward emission intensity (blue) as a function of cylinder diameter at the experimental cylinder height (145 nm), averaged over the cylinder surface. Calculations are corrected for resonant excitation enhancement of the QDs at the cylinder surface at the laser wavelength and normalized to the flat Si reference case (green) to emulate experimental conditions. Experimental data points (black) corresponding to measurements in (a,b) are in good agreement with the predictions.

We now use FDTD to calculate the upward QD emission intensity as a function of cylinder diameter, normalized to the flat Si reference simulation (Fig. 2.5c). A strong dependence on cylinder diameter is observed, with a ten-fold enhancement for 150-nm diameter cylinders. To test this experimentally, we measured a PL map for a cylinder diameter of 200 nm and pitch of 600 nm (Fig. 2.5b). The same analysis as for Fig. 2.5a yields an enhancement factor

for upward emission of 6.1 ± 0.4 , consistent with the upward trend for smaller diameter shown in the simulations of Fig. 2.5c, but below the calculated value of 6.8. We explain the discrepancies by small differences in geometry between experiment and calculation. Overall, the experimentally observed enhanced upward emission is well explained by the combination of resonant directional emission and enhanced excitation obtained from simulations. Figure 2.5c doesn't compare to the results of Figure 2.1 due to the correction for the excitation enhancement; separate curves for the simulated upward emission and excitation enhancement can be found in Fig. 2.11.

2.5 Photoluminescence lifetimes

To corroborate the role of resonant coupling to optical modes in the nanocylinders in the emission directionality, we study the PL emission lifetime. PL lifetime measurements are conducted using a time-correlated single-photon counting (TCSPC) setup with 485 nm excitation wavelength (see Methods). Figure 2.6a,b shows the decay traces for measurements on the 425-nm and 200-nm cylinder arrays, respectively, and on the flat Si substrate directly beside it. Clearly, QD emission on the 200-nm cylinder decays faster than that on the flat Si beside it, while the decay for the 425-nm cylinder is nearly identical to that for the flat Si. The decay traces were fitted with a sum of two exponentials, shown as the line through measured the data points in Fig. 2.6a,b. The lifetime values obtained from this fitting procedure are detailed in Table 2.1. We assign the faster decay for the 200 nm diameter cylinders to the enhanced LDOS due to the strongly modified nanophotonic environment provided by the cylinders.

To analyze this in more detail, we use the FDTD simulations of the angular emission profiles to calculate the PL emission rate (see Methods). Figure 2.6c shows the simulated PL radiative lifetime for a dipole on a Si cylinder, normalized to the lifetime of a dipole on a flat Si substrate and averaged over all possible dipole positions. Here we also correct for the excitation enhancement by the laser on the cylinder (see Fig. 2.11), to ensure that the simulations emulate the experimental conditions. A strongly varying dependence of cylinder diameter is observed, and the measured decay rates (black) correspond well with the simulations: for the 200 nm diameter cylinder, the lifetime is significantly shorter than for the flat Si reference case, while the lifetime of the 425 nm diameter case is just above that for the reference. The variations in the simulated lifetime are almost entirely due to the simulated excitation enhancement (see Fig. 2.12), which further corroborates the necessity of the correction.

Finally, we investigate the Purcell factor and LDOS as a function of cylinder diameter. The PL lifetime curve in Figure 2.6c results from the convolution of the calculated LDOS enhancement and laser excitation enhancement, which corresponds to the measurement conditions and compares well with the results. In Figure 2.6d, we leave out the correction for the laser excitation enhancement and plot only the calculated emission enhancement as a function of the cylinder diameter (but still averaged over polarization and cylinder surface). The left and right y-axes values are the Purcell factor and absolute LDOS, respectively, which directly follow from the FDTD calculations and the free-space LDOS at the emission wavelength (see Methods). We find an increase of the Purcell factor of about 10% for almost all diameters compared to the flat Si reference. The dashed lines in Figure 2.6d depict the downward emission fraction for the cylinder and reference case. Comparing the total LDOS to the downward LDOS and both reference values, we can conclude that the enhanced upward emission (Fig. 2.1i) is due to an increase in the upward LDOS – the downward LDOS is almost

equal to the reference. For diameters of 150 nm and smaller, the LDOS increases significantly while simultaneously the upward emission fraction increases, detailing that the cylinder modes increase the upward LDOS more strongly. The LDOS as a function of dipole position on the cylinder is detailed in the Supplementary Information (Fig. 2.13), which shows a strong radial dependence. Preferential upward or downward emission can thus further be controlled by placing QDs selectively on the center or edge of the cylinder.

Table 2.1: PL lifetimes corresponding to the fitted curves in Figures 2.6a,b.

	Flat silicon		On cylinder	
	Fast lifetime	Slow lifetime	Fast lifetime	Slow lifetime
d = 425 nm	1.11 ns	20.1 ns	1.22 ns	21.7 ns
d = 200 nm	0.91 ns	18.8 ns	0.69 ns	21.3 ns

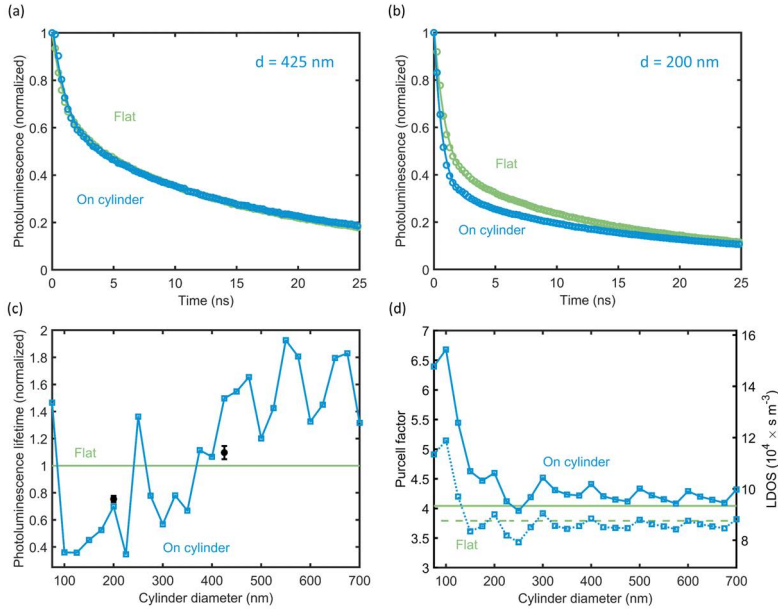


Figure 2.6: PL lifetime measurements after monolayer QD print. (a,b) Measured (circles) and fitted (lines) PL decay traces on a cylinder array (blue) and on flat Si (green), for cylinder diameters of 425 and 200 nm, respectively. (c) Calculated PL radiative lifetime (blue) as a function of cylinder diameter at the experimental cylinder height (145 nm), averaged over the cylinder surface. Average calculations account for the resonant excitation enhancement of the QDs due to the cylinders at the laser wavelength and are normalized to the flat Si reference (green) to emulate experimental conditions. Experimental data points (fast decay components, black) from the measurements in (a,b) are in good agreement with the calculations. (d) Calculated Purcell factor (left y-axis) and corresponding LDOS values (right y-axis) as a function of cylinder diameter, averaged over the cylinder surface (blue). Flat Si reference case (green) is indicated, as well as the downward emission fractions (dashed lines).

2.6 Conclusions

In conclusion, we demonstrate accurate control over the directional emission of luminescent quantum dots selectively placed on top of resonant Si nanocylinders on a Si substrate. The QDs are placed on the silicon nanostructures using a novel soft-stamp method that selectively prints on the top surface of the nanostructures. The angular distribution of the QD emission is controlled through controlled coupling with Mie-like resonances in the cylinders. By varying the position of quantum dots on the cylinders and by engineering the cylinder diameter, the ratio of upward and downward emission can be strongly controlled. Placing QDs only in the center of the nanocylinder enhances downward emission into the Si substrate, while a homogeneous distribution over the surface creates a strongly enhanced upward emission away from the substrate. The relative ratio of upward or downward emission is dictated by far-field interference of direct emission from the dipoles and resonantly excited cylinder modes and is reflected in consistent changes in LDOS that are probed with the lifetime measurements. The experimental PL intensity and lifetime measurements are in good agreement with FDTD simulation results. Our soft-stamping method for QDs onto nanostructures provides a way to integrate optical emitters with nanophotonic structures, with potential applications in emission control of LEDs, LSCs, and in up- and down-conversion for photovoltaics.

2.7 Methods

Green's function calculations

The angular dipole emission pattern for a dipole above a Si substrate was calculated using the far-field Green's function formalism according to Appendix D of *Principles of Nano-Optics* by Novotny and Hecht [68].

FDTD simulations

The fractions of dipole upward and downwards emission and the angular dipole emission pattern for dipoles above Si cylinders were calculated using finite-difference time-domain (FDTD) calculations performed in Lumerical FDTD Solutions [72]. Perfectly Matched Layer (PML) boundary conditions were used in three dimensions. A single, monochromatic electric dipole source was used for each simulation, with a polarization axis along either the X, Y, or Z-axis. A "scat_ff" power monitor box was used to collect the electric and magnetic field components surrounding the nanocylinder and dipole. Convergence was found at a uniform mesh size of 5 nm, a distance of 250 nm from the structure to each FDTD box boundary, and conformal mesh refinement. To convert the simulated near-fields to far-field radiation intensities, we used the open-source RETOP tool [73]. The real value of the optical constants of Si was used (the imaginary part was set to zero) [74].

The multipole decomposition as in Figure 2.1g was performed by calculating the electric field inside the nanocylinder according to the method by Evlyukhin et al. [71].

Radiative lifetime simulation results were obtained from the same dipole emission simulations by keeping a fixed electric dipole amplitude in each simulation. In this fashion, the total emitted power at constant dipole amplitude is directly proportional to the Purcell factor and the LDOS [68]. In turn, the inverse of the total emitted power is a measure for the experimental radiative lifetime. Direct comparison of simulated and measured results was possible because the flat Si reference case normalizes both. The absolute values for the LDOS

in Figure 2.6d were obtained by multiplying the calculated Purcell factor by the free-space LDOS at the emission wavelength:

$$\rho_0 = \frac{\omega^2(\lambda = 760\text{ nm})}{\pi^2 c^3} = 2.31 \times 10^4 \text{ s m}^{-3}. \quad (2.1)$$

The excitation rate enhancement due to resonant coupling at the pump wavelength was simulated, and the results were used to normalize the experimental photoluminescence intensity and lifetime results. For both laser wavelengths, the electric field intensity above the nanocylinder was determined. We used a monochromatic plane-wave source above a nanocylinder, employing periodic boundary conditions in the substrate plane to mimic the array in the experiment and PMLs in the lateral directions. Using a field monitor, we obtained the field intensity 5 nm above the cylinder surface (see Figures 2.9 and 2.10). Again, normalization to the flat Si reference case allowed for direct comparison with measurements.

PDMS chemicals

Elastosil RT 601 A/B (RTV-2 Silicone Rubber) polydimethylsiloxane (PDMS) was bought from Wacker Chemie. Octadecyltrichlorosilane (ODTS) and 1H,1H,2H,2H-Perfluorooctyltrichlorosilane were purchased from Sigma Aldrich.

PDMS stamp preparation

The PDMS stamp was made via mixing the prepolymer and curing agent in a ratio of 9:1. A plastic rod was used to mix the liquid thoroughly. The viscous liquid was kept in vacuum for 30 min to eliminate the air bubbles trapped due to mixing. A 1 mm thick Viton spacer (made by Speedy 400 laser machine from Trotec Laser B.V.), which defines the final PDMS dimensions, was kept on a fluorosilanized (see below) regular microscopic glass slide. The liquid mixture was poured into the center of the spacer. A UV-ozone activated (45 min in a UV Ozone ProCleaner (BioForce Nanosciences) square glass piece with 15 mm in length and 1 mm in thickness was pressed on the liquid mixture. This assembly was cured in an oven at 80 °C for 24 hours.

PDMS silanization

For silanization, the sample was activated with oxygen plasma for 10 s. Then the sample was placed beside the desired silane molecule solution in a Teflon boat at a controlled temperature in a Vacucenter VC20 vacuum oven from Salvis LAB, at 50 mbar for a well-defined time. For fluorosilanization of a microscopic glass slide, 10 μL of 1H,1H,2H,2H-perfluorooctyltrichlorosilane was used and placed in the oven at 50 °C for 1 hour. The treatment formed a self-assembled monolayer (SAM) of fluorinated silane chains on the glass slide's surface and rendered it highly hydrophobic. This facilitated peeling off the cured PDMS. For the silanization of cured PDMS, 10 μL of ODTS was used and placed in the oven at 100 °C for 3 hours. This treatment formed SAMs of ODTS on the surface of the PDMS. The layer of ODTS improved the wetting of octane, forming an even layer of QDot 800 via spin coating, and prevented swelling of PDMS.

QD printing

The purchased QDot 800 particles were dispersed in decane. A 100 μL QD solution was mixed with 100 μL of isopropanol and centrifuged at 8000 RPM for 10 min. to form a solid precipitate of particles at the bottom of the centrifuging tube. The supernatant was discarded completely, and fresh octane was added to disperse the precipitate: 25 μL for the thick QD print (Fig. 2.4a) and 100 μL for the thin QD print (Fig. 2.4b). This solution was spin-coated on the silanized PDMS at 2500 RPM with 650 RPM/s for 120 s.

The printing experiments were performed with a Universal Testing System model 5965 with 50 kN force capacity from INSTRON. The Si substrate with cylinders was activated for 10 min by UV-ozone treatment. Both the stamp and the substrate were mounted via vacuum on the printing machine.

Atomic force microscopy

AFM images were obtained with a ScanAsyst-AIR probe (Bruker, nominal tip radius 2 nm), operated in PeakForce Tapping mode using a Bruker Dimension Icon AFM.

Photoluminescence measurements

For the photoluminescence (PL) measurements, a WITec alpha300 RS confocal microscopy setup was used in reflection mode with 20 \times and 100 \times magnification, air objectives. The QDs were excited with a 532 nm excitation wavelength continuous-wave laser, 10 mW power, and ~ 1 μm -diameter spot size. Spectra were collected using the fiber-connected WITec UHTS spectrometer, where the collection by the fiber acts as the confocal pinhole. Given a fiber core of 100 μm in diameter, we calculate collection spots of 5 (20 \times) and 1 (100 \times) μm using $\text{FWHM} = d_{\text{fiber}}/M$, with M the magnification of the objective [75].

TCSPC measurements

The time-resolved PL traces were measured using a home-built time-correlated single-photon counting (TCSPC) setup with a laser at 485 nm excitation wavelength (PicoQuant LDH-D-C-485). The laser repetition rate was 1 MHz. The laser was focused with a Nikon 60 \times water immersion objective (PlanAPO VC 60x A/1.2 WI) onto the sample. The TCSPC map was created by scanning the sample in a 10 by 10 μm^2 window with a scanning piezo-electric stage (PI-P-733.3CL). The PL was then collected through the same objective, and the laser excitation was filtered with a 488 nm notch filter and a 500 nm long-pass filter. The detectors are silicon-single photon avalanche detectors (Micro Photon Devices, MPD-5CTD) controlled by a PicoQuant HydraHarp 400 event timer.

Lifetime fitting

We used Wolfram MATHEMATICA 12 [76] to fit a sum of 2 exponential functions to the data, using the built-in NonlinearModelFit function.

2.8 Supplementary information

As is the case for all plots in the main text, in the following supplementary Figures the distance between the dipole and the Si surface is kept constant at 5 nm, and the emission intensity is averaged over all polarizations.

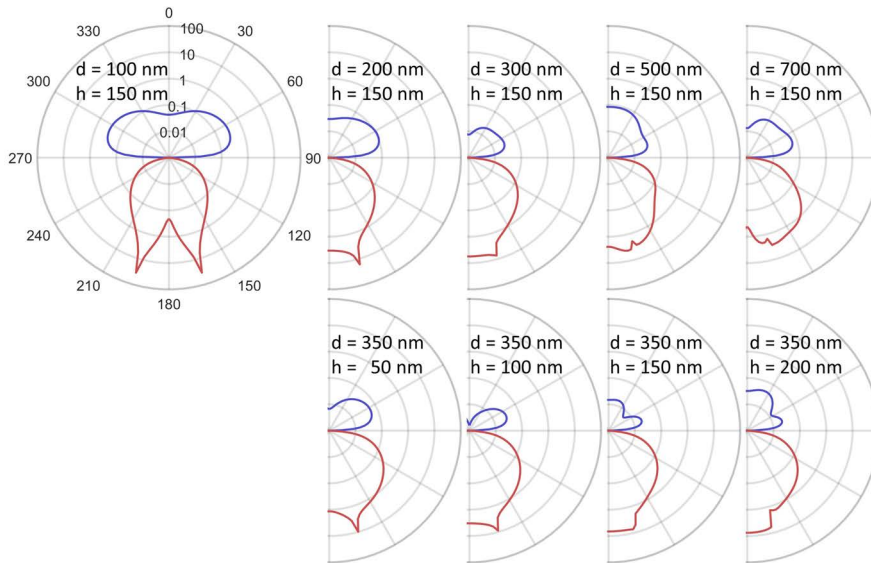


Figure 2.7: Calculated azimuthal angular dipole emission patterns for several combinations of cylinder dimensions on a logarithmic radial axis.

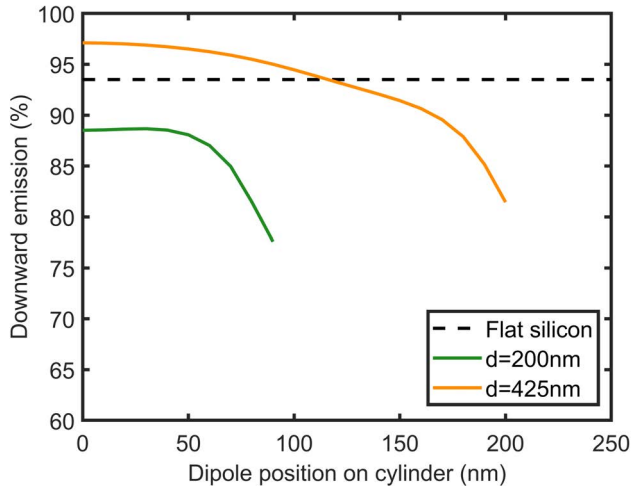


Figure 2.8: Similar to Fig. 1h: Downward emission percentage as a function of dipole position on the cylinder (0 is at the center of the cylinder).

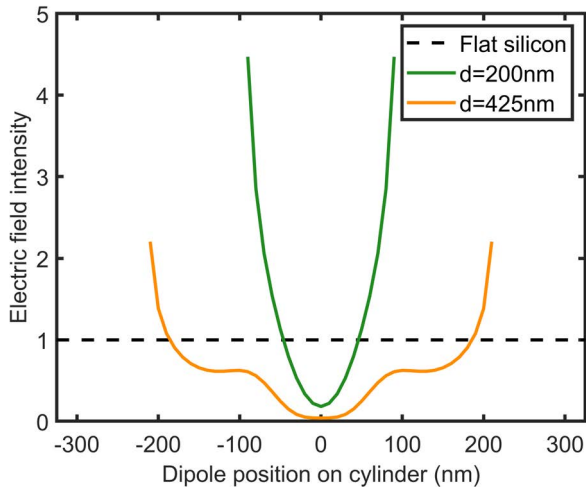


Figure 2.9: Excitation enhancement at 532 nm laser wavelength, as a function of dipole position on the cylinder (0 is at the center of the cylinder).

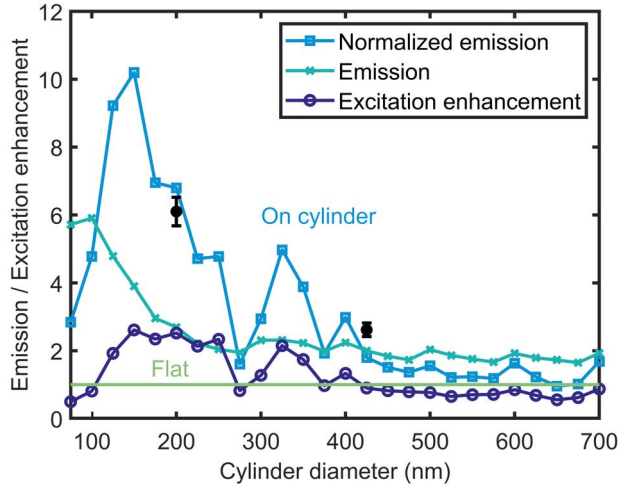


Figure 2.10: Similar to Fig. 5c: Calculated upward emission intensity (blue) as a function of cylinder diameter at the experimental cylinder height (145 nm), averaged over the cylinder surface. Calculations are corrected for resonant excitation enhancement of the QDs at the cylinder surface at the laser wavelength and normalized to the flat Si reference case (green) to emulate experimental conditions. The emission (light blue, cross) and excitation enhancement (dark blue, circle) curves are plotted for reference, showing that the oscillation in the normalized emission curve is mostly due to the excitation enhancement correction.

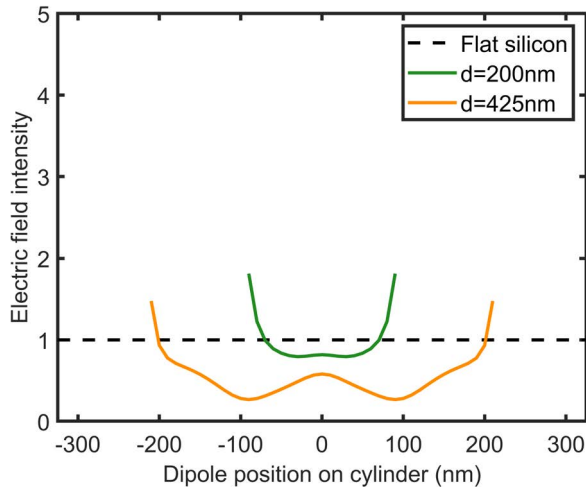


Figure 2.11: Excitation enhancement at 485 nm laser wavelength, as a function of dipole position on the cylinder (0 is at the center of the cylinder). Cylinder height is 145 nm.

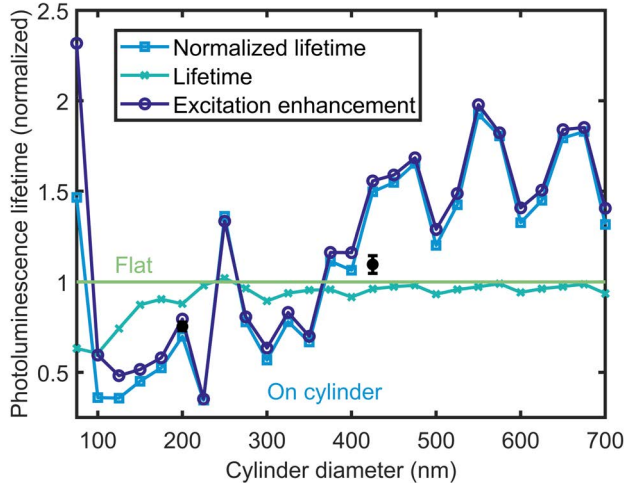


Figure 2.12: Similar to Fig. 6c: Calculated PL radiative lifetime (blue) as a function of cylinder diameter at the experimental cylinder height (145 nm), averaged over the cylinder surface. Average calculations account for the resonant excitation enhancement of the QDs due to the cylinders at the laser wavelength and are normalized to the flat Si reference (green) to emulate experimental conditions. Experimental data points (fast decay components, black) from the measurements in Fig. 6a,b are in good agreement with the calculations. The emission (light blue, cross) and excitation enhancement (dark blue, circle) curves are plotted for reference; the oscillation of the normalized lifetime is mostly due to the excitation enhancement correction.

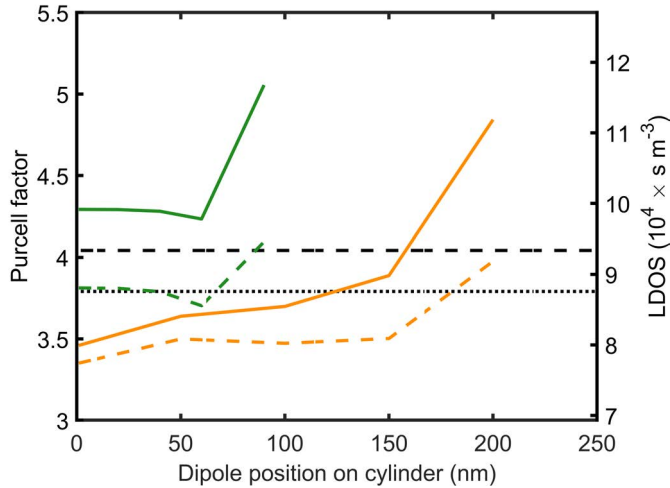


Figure 2.13: Similar to Fig. 6d: Calculated Purcell factor and corresponding LDOS values as a function of dipole position on the cylinder (0 is at the center of the cylinder). Flat Si reference case (black) is indicated, as well as the downward emission fractions (dashed lines).

3

Unlocking higher power efficiencies in luminescent solar concentrators through anisotropic luminophore emission

The luminescent solar concentrator offers a potential pathway for achieving low-cost, fixed-tilt light concentration. Despite decades of research, conversion efficiency for luminescent concentrator modules has fallen far short of that achievable by geometric concentrators. However, recent advances in anisotropically-emitting nanophotonic structures could enable a significant step forward in efficiency. Here, we employ Monte Carlo ray-trace modeling to evaluate the conversion efficiency for anisotropic luminophore emission as a function of photoluminescence quantum yield, waveguide concentration, and geometric gain. By spanning the full LSC parameter space, we define a roadmap towards high LSC conversion efficiency. An analytical function is derived for the dark radiative current of an LSC to calculate the conversion efficiency from ray-tracing results. We show that luminescent concentrator conversion efficiency can be increased from the current record value of 7.1% to 9.6% by incorporating anisotropy. We provide design parameters for optimized luminescent solar concentrators with practical geometrical gains of 10. Using luminophores with strongly anisotropic emission and high (99%) quantum yield, we conclude that conversion efficiencies beyond 28% are achievable. This analysis reveals that for high luminescent solar concentrator performance, waveguide losses are as important as the luminophore quantum yield.

This chapter is based on:

Unlocking Higher Power Efficiencies in Luminescent Solar Concentrators through Anisotropic Luminophore Emission

Julia S. van der Burgt^{1*}, David R. Needell^{2*}, Tom Veecken^{1*}, Albert Polman¹, Erik C. Garnett¹, Harry A. Atwater²

ACS Applied Materials & Interfaces **13**, pp. 40742–40753, 2021.

<https://doi.org/10.1021/acsami.1c12547>

*Julia, David, and Tom contributed equally to this work.

¹Center for Nanophotonics, NWO-Institute AMOLF, Science Park 104, 1098 XG Amsterdam, The Netherlands

²Department of Applied Physics and Materials Science, California Institute of Technology, Pasadena, California 91125, United States

Author contributions:

David, Tom, Albert and Harry conceived the project. David and Harry developed the Monte-Carlo model and the open-circuit calculations. Julia, David, and Tom performed the Monte-Carlo simulations, data analysis, and wrote the original draft. Erik, Albert, and Harry supervised the project and edited the manuscript.

3.1 Introduction

Despite outpacing other forms of renewable energy [77], solar photovoltaics still occupies a limited fraction of the worldwide energy portfolio — with just 580 TWh of solar electricity generated in 2019 compared to over 23,000 TWh of total electricity consumed [78]. Given the disparity between solar generation and worldwide consumption, tremendous research effort is underway to spur further adoption. Building-integrated photovoltaics is one such area, and aims to incorporate solar generation into residential and commercial building components (e.g., envelopes [35, 79, 80], roofs [34], windows [81–83], greenhouses [84–88]). The decreasing cost of solar modules and the proportionate increase in balance of system and soft costs [89] motivates integration of photovoltaics into buildings to minimize overall system and installation expenses [80].

First introduced in the mid-twentieth century for scintillation counting applications [90], the luminescent solar concentrator (LSC) offers unique advantages for building-integrated devices. An LSC consists of a dielectric waveguide containing suspended luminophore particles at a given concentration (i.e., optical density). Upon illumination of the waveguide top surface, the embedded luminophores absorb photons within their absorption band and re-emit energetically down-shifted photoluminescence (PL) at a radiative efficiency given by the luminophore PL quantum yield (PLQY). The spectral and angular PL emission profiles of the luminophore, along with the index of refraction contrast between the waveguide and surrounding media (often polymer and air, respectively), determine the amount of PL trapped in the waveguide through total internal reflection (TIR). For photovoltaic applications, solar cells can be optically coupled to the waveguide edges. Figure 3.1a illustrates the fundamental operating principles and components of a general, single-edged photovoltaic LSC device.

Thermodynamically, an LSC holds distinct advantages over both traditional geometric concentrator modules as well as conventional, nonconcentrating photovoltaic systems. As has been shown, the Stokes shift (spectral separation between luminophore absorption and emission) sets the maximum achievable concentration limit [91]. Unlike traditional passive concentrators whose limit depends upon the acceptance angle [92], LSCs can absorb and concentrate off-angle and diffuse irradiance [93, 94]. Consequently, LSC photovoltaic cells maintain lower operating temperatures than both geometric concentrators and non-concentrated, flatplate photovoltaics owing to decreased thermalization of high-energy photogenerated excitons of the collection cell [95].

Economically, LSCs offer potential system-level-cost reductions owing to the flexibility of these devices into building-integrated photovoltaic designs [96, 97]. The ratio of top surface waveguide area to the net solar cell area, termed the geometric gain (GG), sets the amount of the photovoltaic material required per LSC module. The optical density of luminophores suspended within the waveguide, as well as the luminophore absorption and emission spectral profiles, determines the visible transparency and color tinting of the LSC [98]. Thus, LSCs can be aesthetically tuned to meet the need(s) of building-integrated photovoltaic designs. The LSC aesthetic tunability also compels such devices for myriad façade components and end-uses [99, 100]. Beyond such applications, previous studies have also investigated routes toward high-efficiency photovoltaic applications as a promising area for LSC research — exploring, for example, LSC–LSC [101] and LSC–Si [102–105] tandem structures.

The concentration mechanism for an LSC introduces a large number of design and performance parameters [106]. Among these include the luminophore PLQY, optical density of luminophores, GG of the LSC system, Stokes shift of the luminophore absorption/PL profiles, trapping efficiency of the emitted PL, reabsorption probability by the luminophore species, attenuation and bulk/surface scattering by the host waveguide, and the quantum

efficiency of the photovoltaic cell collector [107]. Previous studies have highlighted the most important parameters for LSC optical and conversion efficiency; PLQY, PL trapping, optical density, and GG are observed to be highly influential for a given LSC and luminophore system type [108–112]. While some parameters need to be maximized (e.g., PLQY) or minimized (e.g., attenuation in the waveguide), others attain optimal values that strongly depend on the entire LSC design, complicating the process (e.g., optical density, GG) [113, 114]. In addition, there exist numerous pathways for photon loss intrinsic to the LSC design. Consequently, the single-junction LSC conversion efficiency remains limited to below 10%, with the current record achieving 7.1% under 1 sun illumination [115].

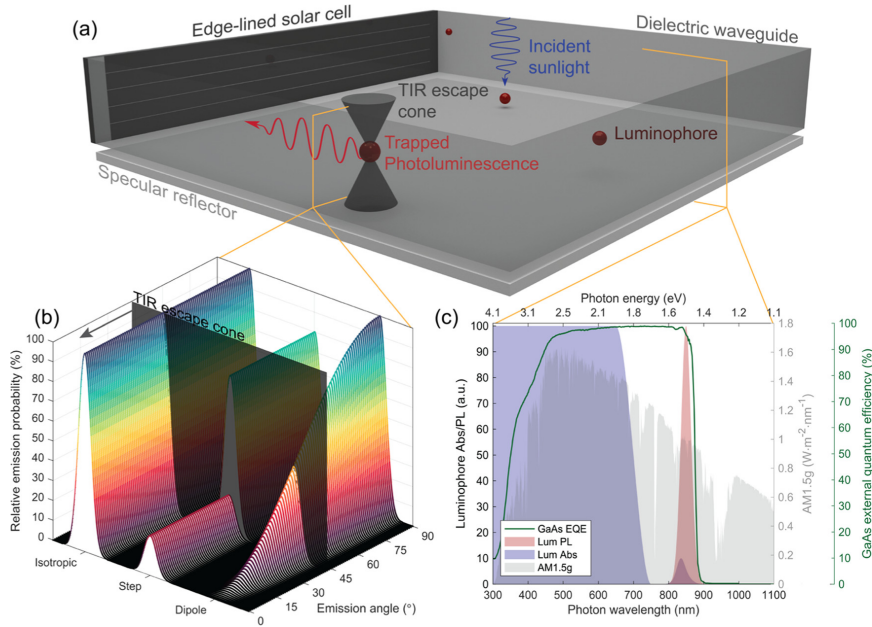


Figure 3.1: (a) 3D rendering of a rectangular luminescent solar concentrator coupled to an edge-lined solar PV cell. Incident sunlight strikes embedded luminophores within the optical, dielectric waveguide where, given the luminophore radiative efficiency (i.e., PLQY), down-shifted PL is emitted. Given the waveguide's index of refraction, a portion of PL emits into the TIR escape cone, while a portion occupies TIR angles. In this work, we assume a waveguide with a broadband specular reflector cladding the bottom surface, as shown here. (b) Three examples of luminophore PL profiles (arbitrary wavelength) given the emission angle relative to the top waveguide surface normal. Here, we show the relative PL emission probability for the case of an isotropic luminophore with equal probability of PL across all angles; a step function like luminophore with a probability, P_{esc} , of emitting into the escape cone and a complementary probability, P_{TIR} , of emitting into TIR angles; and a dipole emission pattern showing a continuous anisotropic profile. (c) Spectral profile that we assume for this model, where we assume a luminophore with an absorption edge up to 700 nm (left y-axis), a PL center of 800 nm with an FWHM of 20 nm (left y-axis), and a GaAs cell whose external quantum efficiency (EQE) we show in green (far right y-axis). We plot against the AM1.5G spectrum (right y-axis) for reference.

Among the many parameters that can be tuned for highly efficient LSCs, the methods by which the waveguide layer traps and guides PL to the optically coupled solar cells remain an active field of research. Common rectangular LSC waveguide materials (e.g., polymer or glass) trap under 75% of the isotropically emitted luminescence radiation by TIR [90, 116]. To decrease the waveguide losses through the escape cone, methods for trapping have addressed either cladding the top/bottom LSC surfaces with Bragg mirrors to reflect a portion of the PL emitted within the escape cone [117–119] or employing luminophore materials or structures that preferentially emit outside of the escape cone [120–127]. This significant body of research has detailed the effects of LSC parameters on cladding losses (i.e., external dichroic mirrors and photonic crystal structures) as well as anisotropically emitting luminophores. With recent advances in the angular control of luminescence radiation using nanophotonic structures, however, this has become a key focus area for research in LSCs [50]. Together with semiconductor quantum dots whose emission efficiencies can extend beyond 99% [128], nanophotonic-luminophore designs open new directions for improved LSC efficiency. Unlike previous works, here we quantify the effects of luminophore anisotropic emission for a variety of profiles, for a common edge-lined LSC structure, while covarying the device parameters of interest to unveil the pathway to achieving high power conversion efficiency devices.

In this work, we compare the effects of several types of anisotropic emitters on LSC conversion efficiency. Figure 3.1b illustrates different emission patterns for an arbitrary PL spectrum. An isotropic emitter has an equal probability of emission into any angle, as shown on the left of Figure 3.1b. To quantify the effects of angular emission, we model luminophores with a step-function anisotropic profile, as illustrated in the center of Figure 3.1b. While useful in its analysis, such a step-function emission profile is unphysical. As such, we next discuss and analyze the consequences of more realistic, continuous emission probabilities, like that of the nanophotonic dipole emitter shown on the right-hand side of Figure 3.1b. We assume that the embedded luminophore particles do not anisotropically scatter incident photons below the absorption bandgap. Thus, Figure 3.1b displays the PL profiles of example luminophores for photons with energies greater or equal to the absorption bandgap, as given by Figure 3.1c. Further, unlike the absorption cross section of certain luminescent dyes that depend on their physical orientation and the angle of incidence, we assume isotropically absorbing luminophores regardless of the tilt angle within the waveguide (e.g., two-dimensional transition-metal dichalcogenide heterobilayer absorption/emission [129] or all-dielectric resonant nanostructures coupled to quantum emitters [58, 61]).

We quantify the effects of luminophore PL anisotropy in a rectangular planar LSC waveguide, employing four high-efficiency GaAs cells optically coupled to each edge of a polymer matrix. We apply an experimentally validated Monte Carlo ray-trace model to uncover the conversion efficiency performance for such an LSC employing an ideal luminophore. By evaluating the performance of the LSC with respect to power conversion efficiency (rather than, for example, concentration factor), we ensure area-agnostic comparisons across devices of differing GGs. Figure 3.1c highlights the external quantum efficiency (EQE) of the GaAs cell, the ideal absorption/PL spectral profiles of the luminophore, and the simulated AM1.5G irradiance assumed to strike the device at normal incidence. We include a thorough discussion of the Monte Carlo ray-trace computational method and the implementation of luminophore anisotropy within such a model. In addition, we provide a thorough physical picture of the radiative limit for such LSCs. We discuss the impact of luminophore anisotropy on LSC performance and its covariation with PLQY, GG, and optical density. We then model the impact of luminophore PL anisotropy on the current record LSC. Finally, we end with a detailed thermodynamic breakdown of the loss mechanisms for a variety of LSCs with anisotropically emitting luminophores.

3.2 Results and discussion

Here, we discuss the effects of anisotropy on conversion efficiency using Monte Carlo modeling. To unveil the conversion efficiency performance with respect to luminophore anisotropy, we begin with a discussion on the LSC system detailed balance, quantifying the dark radiative current thermodynamics. Next, to consider how LSC parameters for anisotropic luminophores affect conversion efficiency, we simultaneously vary the geometric gain from 1 to 100, luminophore optical density at 750 nm from 0 to 3, and the luminophore quantum yield from 75 to 100%. We introduce the case of a steplike emission pattern and its effect on this conversion efficiency, where we vary the luminescence fraction trapped in TIR modes continuously from 75 to 100%. Finally, we analyze the LSC performance given dipole and forward emitter anisotropy profiles.

3.2.1 Thermodynamics of anisotropic LSC devices

To elucidate the conversion efficiency behavior of an arbitrary LSC device, we must quantify both the resulting short-circuit current (J_{sc}) and open-circuit voltage (V_{oc}). We can model the resulting short-circuit current density given the high accuracy Monte Carlo ray-trace methods, as described in the Computational Methods section. However, to calculate the open-circuit voltage, we first define the radiative limit case and subsequently include the GaAs cell external radiative efficiency nonidealities. [130, 131] Beginning with the radiative limit equation [12], we have

$$V_{oc}^{rad} = \frac{kT}{q} \ln \left(\frac{J_{sc}}{J_0^{rad}} \right) \quad (3.1)$$

where k , q , and T are the Boltzmann constant, electronic charge constant, and temperature of the LSC (assumed to be at 300 K), respectively. As stated, J_{sc} gives the total exciton generation under direct illumination by the sun (i.e., the short-circuit current), while J_0^{rad} gives the exciton generation under no direct illumination but instead in the ambient, Blackbody background at temperature T for purely radiative recombination and generation.

In thermodynamic equilibrium, the total absorption by the LSC system from the Blackbody background (J_0^{abs}) must equal the total emission by the LSC into free space (J_0^{emit}), as illustrated in Figure 3.2a. Therefore, when solving for J_0 , we can choose either the absorption or emission picture [132]. Let us assume that $X\%$ of luminophore PL and $Y\%$ of GaAs PL enter the escape cone and radiate into free space. Here, $X\%$ can be calculated via the specific luminophore radiance profile — as described later in this study — and $Y\%$ by the waveguide index of refraction [90], assumed here to be a constant 1.49 across PL wavelengths ($Y\% \cong 25\%$). Starting with the emission picture, we can distinguish the resulting LSC dark current into the contribution from the luminophore ($J_0^{emit,lum}$) and GaAs cell ($J_0^{emit,pv}$) into free space

$$J_0^{rad} = J_0^{emit} = J_0^{emit,lum} + J_0^{emit,pv} \quad (3.2)$$

Figure 3.2a-c conceptually illustrates this dark current term in both the emission and absorption settings. Given the $X\%$ and $Y\%$ fractions, we can rewrite Equation 3.2 to include the total amount of the luminophore and cell emission rather than emission solely into the escape cone and thereby back into free space. Doing so, we have

$$J_0^{rad} = X\% \cdot J_{total}^{emit,lum} + Y\% \cdot J_{total}^{emit,pv}, \quad (3.3)$$

where $J_{\text{total}}^{\text{emit,lum}}$ and $J_{\text{total}}^{\text{emit,pv}}$ give the total amount of PL by the luminophores and GaAs cells, respectively. Given that total absorption into the luminophores or GaAs cells must equal total emission out of the luminophores or GaAs cells, respectively, we can rewrite Equation 3.3 in the context of the absorption profiles, as shown by Figure 3.1c

$$J_0^{\text{rad}} = X\% \cdot J_{\text{total}}^{\text{abs,lum}} + Y\% \cdot J_{\text{total}}^{\text{abs,pv}}. \quad (3.4)$$

As shown in Figure 3.2b, we know that the total GaAs cell absorption ($J_{\text{total}}^{\text{abs,pv}}$) must be a sum of both the trapped luminophore PL (i.e., $1 - X\%$) and photons entering the waveguide and striking the edge-lined cell directly from the Blackbody spectrum at ambient temperature, T — where the GG gives this amount of incident light reaching the edge-lined cell. We assume, given the absorption profile of the luminophores and the fact that GaAs PLQYs are significantly lower than that of the luminophores, that the TIR-trapped GaAs PL contributes a negligible amount of the total absorption of the luminophores. Therefore, we can write

$$J_0^{\text{rad}} = X\% \cdot J_{\text{total}}^{\text{abs,lum}} + Y\% \cdot ((1 - X\%) \cdot J_{\text{total}}^{\text{abs,lum}} + \frac{1}{GG} \cdot J_0^{\text{abs,pv}}). \quad (3.5)$$

Where, as shown in Equation 3.5, we distinguish between $J_{\text{total}}^{\text{abs,lum}}$ and $J_0^{\text{abs,pv}}$, where the former gives the total amount of absorption by the luminophore species — which must equal the total amount of PL — while the latter indicates the amount of irradiance absorbed by the GaAs cells exclusively from free space, Blackbody radiation and not by luminophore PL. We can now define each of these terms given our known absorption profiles and the Planck spectrum

$$J_0^{\text{rad}} = [X\% + Y\%(1 - X\%)] \cdot \int_{\omega} \int_{\Omega} A_{\text{lum}}(\omega) \cdot \Phi_{\text{bb}}(\omega) d\Omega d\omega \\ + Y\% \cdot \frac{1}{GG} \cdot \int_{\omega} \int_{\Omega} A_{\text{pv}}(\omega) \cdot \Phi_{\text{bb}}(\omega) d\Omega d\omega, \quad (3.6)$$

where A_{lum} and A_{pv} are the absorption profiles of the luminophore and GaAs cell, respectively, Φ_{bb} is the Planck spectra at 300 K, ω is the frequency of the photon, and Ω is the solid angle (2π steradians for this case of background radiation). With this expression and our simulated photocurrent term from the Monte Carlo ray-trace model, we can fully define the LSC open-circuit voltage in the radiative limit. Given Equation 3.6, we can conceptually understand the effect of luminescence trapping within a waveguide in terms of spectral shifting of the GaAs cell, highlighted by Figure 3.2d-f. In the limit where the geometric gain is large and the luminophores exhibit perfect PL trapping within the waveguide (i.e., $X\% = 0$), the dark radiative current is given by that of the luminophore absorption profile (that is, electronic bandgap). In this limit, the LSC open-circuit voltage is limited by the bandgap of the luminophore and not the photovoltaic cell.

As shown in Figure 3.2d, if we assume general luminophore and GaAs cell absorption and emission profiles — where the luminophore absorption and PL are separated by a certain Stokes shift energy — we can qualitatively observe the impact of trapping on PL of the GaAs cell. As seen in Figure 3.2e, partial trapping will yield blue-shifted cell PL, while full trapping (Figure 3.2f) shows how the effective cell open-circuit voltage saturates to the luminophore bandgap for the limit of high GG. To include nonradiative effects of the GaAs cell, we apply an explicit form of the GaAs external radiative efficiency, as well as approximate fill factor calculations, as described in the Computational Methods section.

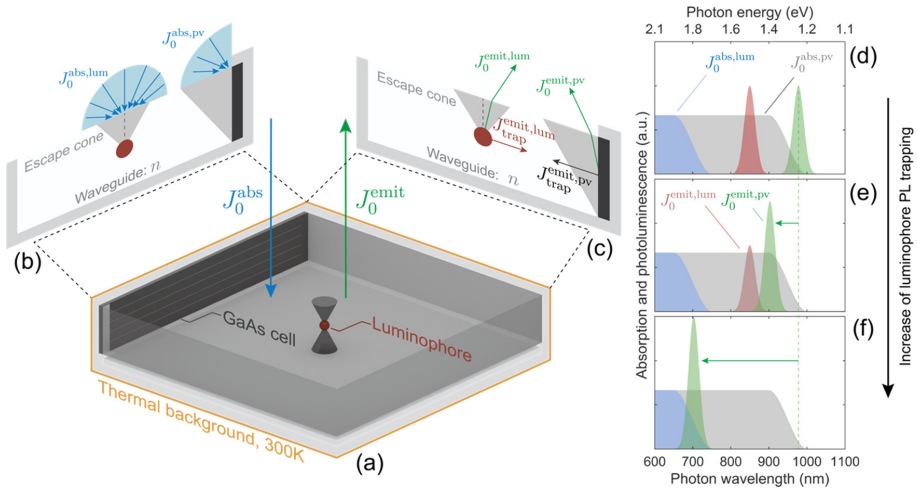


Figure 3.2: Conceptualization of the LSC system when in thermal equilibrium with the ambient Blackbody background at 300 K. In this case, we know that absorption into and emission out of the LSC system must be equal as shown in (a). Therefore, we can choose to analyze the system in either the absorption (b) or emission (c) pictures. (d), (e), and (f) conceptually illustrate the spectral consequence to outgoing, free space PL via the GaAs cell as the luminophore PL trapping increases. (d) depicts the case of no photoluminescence trapping, where the luminophore absorption (blue) and luminescence (red) are shown to be separated by the Stokes shift energy, and there is some spectral width to the cell PL (green) for an arbitrary cell absorption (gray). (e) and (f) show how varying the amount of luminophore PL trapping affects the spectral location of the cell emission — where, as shown in (f), complete trapping yields the highest open-circuit voltage condition, which is given by the luminophore absorption bandgap.

3.2.2 Emitters with steplike anisotropy

To begin, we assume a steplike luminescence angular emission distribution, as shown in Figure 3.3a,b. We vary the luminescence intensity fraction, P_{TIR} , emitted at TIR angles, and assume this angular distribution to be symmetric about the z-axis (i.e., normal to the waveguide plane). By representing the luminophore anisotropy with a single variable, we can uncover the relationship between anisotropic emission, GG, optical density, and PLQY. First, we vary the luminescence quantum yield and P_{TIR} of the luminophores, assuming a high optical density of 3, such that 99.9% of the incident light is absorbed in a single pass and a modest geometric gain of 20. As shown in Figure 3.3c, the optimal conversion efficiency occurs for unity PLQY and P_{TIR} , where for this luminophore/cell system, we observe a global maximum of approximately 29% under 1 sun illumination — approaching the detailed balance limit with respect to the luminophore absorption and reabsorption bandgaps, including nonradiative effects within the GaAs cell. In contrast, the isotropic case ($P_{\text{TIR}} = 75\%$) falls short of 5%.

Within Figure 3.3c, we plot contours of the product ($\text{PLQY} \cdot P_{\text{TIR}}$) for constant values of 0.60, 0.70, 0.80, 0.90, 0.95, and 0.99, finding qualitative agreement between these contours and the simulation results. This agreement can be understood from the fact that the product of luminescence quantum yield and P_{TIR} sets the probability that a trapped photon survives an absorption event by a luminophore and is guided to the solar cell. Whether the photon is lost through nonradiative recombination (for low PLQY) or by escaping the waveguide (low P_{TIR}) is irrelevant for the resulting efficiency. Significantly, increasing P_{TIR} is as important as increasing the luminescence quantum yield.

To examine the relationship between PL trapping, PLQY, GG, and optical density, Figure 3.3d,e shows stacked contour maps for TIR-limited and ideal trapping cases, respectively. As seen in Figure 3.3d, there exists a global optimum optical density for all PLQY and GG values of approximately 0.50 for PLQYs between 75 and 100%. As GG increases for PLQYs at or below 99%, we observe a steep and monotonically decreasing conversion efficiency at constant optical density. However, importantly, we find that for ideal emitters (near-unity PLQY and unity trapping) lower GG limits the maximum concentration of the system thereby constraining the open-circuit voltage to the GaAs electronic bandgap. As the GG increases for this high PLQY and trapping cases, the system bandgap tends toward the luminophore absorption bandgap yielding higher overall performance.

We find a similar trend with a global optimum optical density near 1.0 for cases where the PLQY falls below 95%. However, for higher PLQYs, we observe a shift in maximum conversion efficiency with respect to optical density — in the case of unity PLQY, higher optical density yields a higher conversion efficiency. Only in the case of unity trapping and unity PLQY do we observe that conversion efficiencies remain nearly constant with increasing GG. Figure 3.3c,e demonstrates the importance of achieving both near-unity PLQY and PL trapping.

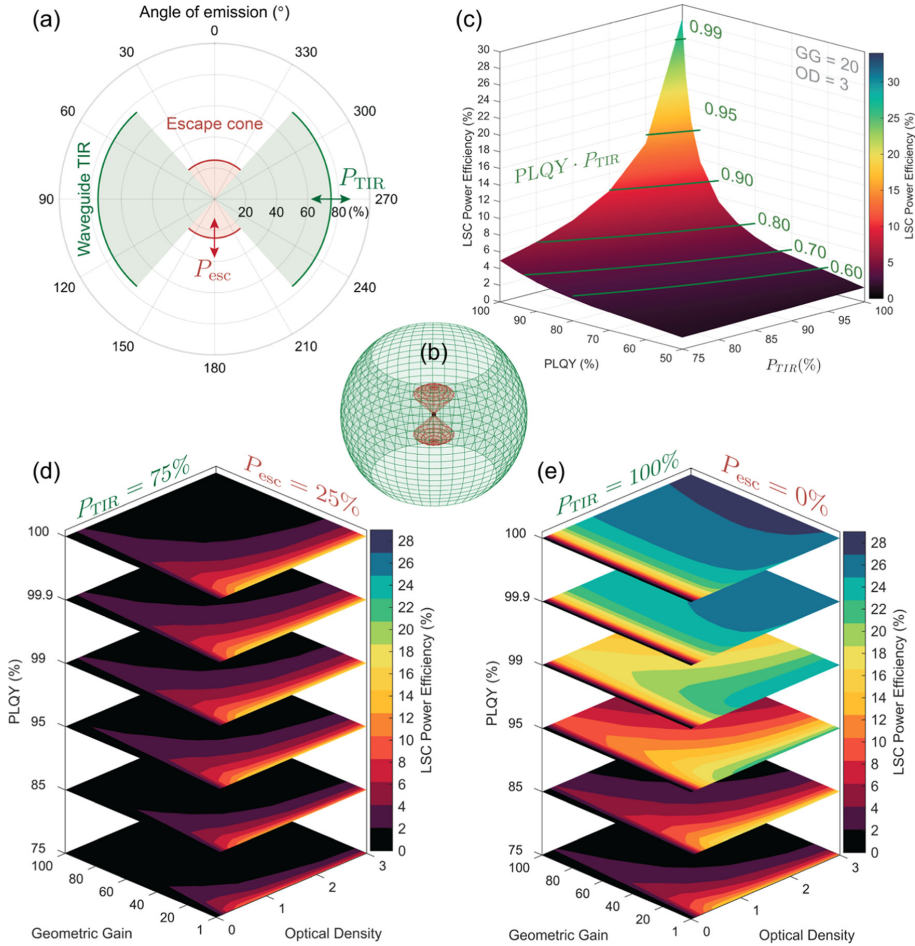


Figure 3.3: (a) Two-dimensional (2D) polar plot of the step-function emitter profile, illustrating how the TIR escape cone probability (P_{esc}) and TIR trapping probability (P_{TIR}) affect the overall luminescence angle of emission probability. As shown in (c), we assume symmetry about the polar angle (i.e., about the z-axis). (b) Effects of luminophore anisotropy on the conversion efficiency of an LSC. Here, we vary the PLQY and amount of TIR emitted radiation by the luminophore, assuming a geometric gain (GG) of 20 at a waveguide optical density of 3. The analytical predictions for the waveguide efficiency (green contours) show close matching with the Monte Carlo results. (d, e) Monte Carlo ray-trace simulations for the conversion efficiency of an LSC with luminophores that emit 75% into TIR angles (i.e., anisotropic) vs 100% into TIR angles (i.e., anisotropic) as a function of GG, optical density, and PLQY.

To more closely quantify the role of optical density and GG, Figure 3.4a,b examines how various $(PLQY, P_{TIR})$ pairs impact conversion efficiency. As seen in Figure 3.4a, the optimal luminophore optical density depends strongly upon the waveguide trapping and luminophore radiative efficiency. Since this density determines both the amount of absorbed sunlight as well as the amount of PL reabsorption within the waveguide, a poor $PLQY$ and P_{TIR} results in detrimental nonradiative recombination and high escape cone losses for the absorbed incident and re-emitted PL photons. As the $(PLQY, P_{TIR})$ product increases, the drawback of reabsorption diminishes while the advantage of increased sunlight absorption remains, thereby increasing the optimal optical density. Figure 3.4b illustrates the difficulty in achieving a high conversion efficiency for the increasingly large waveguide to cell area ratios for products less than unity. In all but the ideal case, efficiency monotonically decreases with increasing GG. Even in this special case of unity $PLQY$ and P_{TIR} , increasing the GG beyond a certain value yields higher likelihood of photoluminescence scattering inside the escape cone, resulting in lowered conversion efficiencies. For efficiencies above 15% at GGs above 10, the $(PLQY, P_{TIR})$ product must be greater than 85%. Having demonstrated the upper performance limits of the LSC with a steplike emission profile, we can readily observe the interplay between the various LSC parameters as well as quantify how to reach increased power conversion efficiencies. However, to understand the limitations of more experimental anisotropic profiles, we next discuss several more realistic emission patterns.

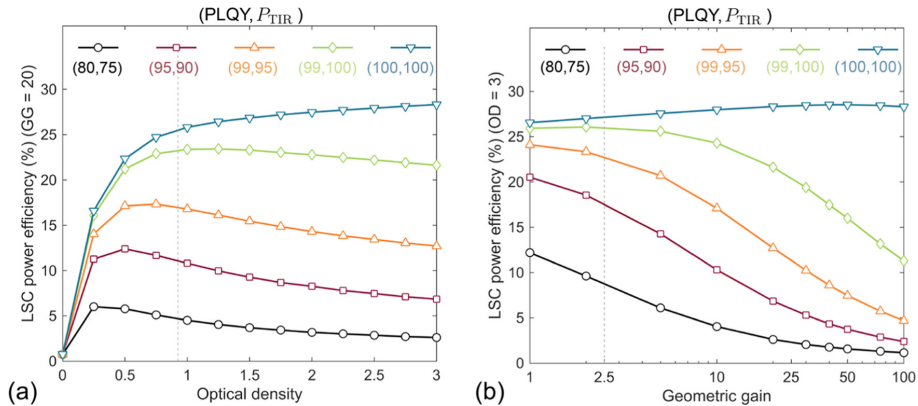


Figure 3.4: (a) LSC power efficiencies as a function of optical densities for several $(PLQY, P_{TIR})$ pairs, illustrating how an increase in the $(PLQY, P_{TIR})$ enables higher efficiencies and shifts the optimum OD to higher values. Here, we assume a GG of 20. (b) LSC power efficiencies as a function of GG for the same $(PLQY, P_{TIR})$ pairs as (a), assuming an OD of 3. We observe monotonically decreasing efficiencies with increasing GG, regardless of the $PLQY$ and P_{TIR} due to the unavoidable surface and bulk scattering by the waveguide. The dotted lines in both (a) and (b) correspond to the OD and GG for the current record LSC with a conversion efficiency of 7.1%, respectively.

3.2.3 Emitters with dipolelike anisotropy

For a more realistic approximation of a luminescent concentrator employing anisotropic emission, we model a system comprised of dipolelike emitters. Figure 3.5a,b illustrates the polar and 3D plots of the far-field dipole emission pattern, where we again observe symmetry about the z-axis. We find upon integration that approximately 91% of the generated luminescence is emitted into TIR angles. Varying the PLQY, GG, and optical density, we find that — similar to our previous analysis for nonunity (PLQY, P_{TIR}) pairs — there exist optimal optical densities. A PLQY of 95% and GGs below 60 yield optimal optical densities of approximately 0.67. We find maximum conversion efficiency of approximately 25% for the case of unity PLQY, an optical density of 3, and GG of 1. For a GG of 10, a geometry of practical experimental interest, the maximum conversion efficiency is approximately 18.5% for unity PLQY and an optical density of 0.75.

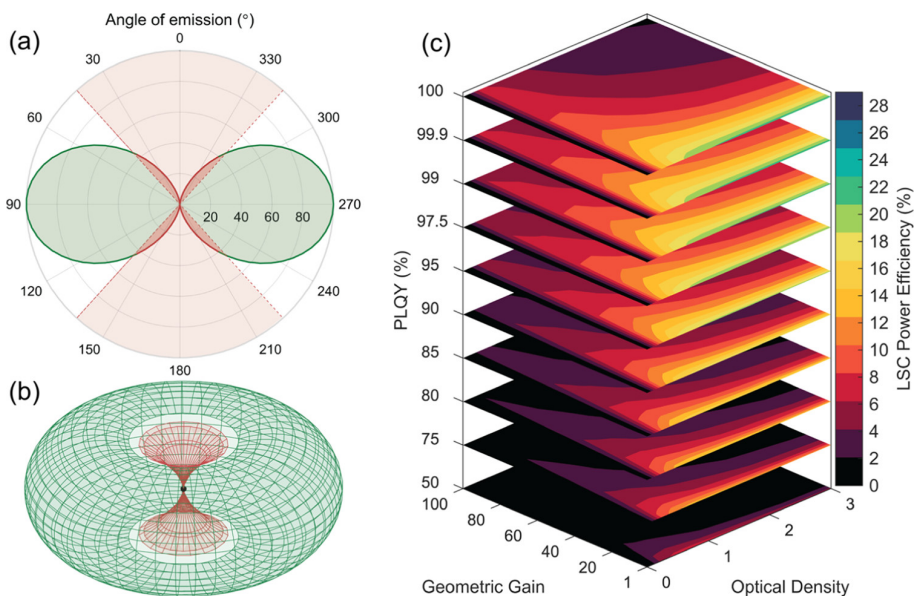


Figure 3.5: Monte Carlo ray-trace results for the dipolelike emission pattern, where (a) shows a polar 2D plot of the simulated PL profile with respect to the azimuthal angle and (b) illustrates the polar angle symmetry (i.e., about the z-axis). (c) Conversion efficiency of the LSC module with respect to GG, optical density, and PLQY.

3.2.4 Emitters with forwardlike anisotropy

Thus far, our analysis has employed anisotropic emitters with far-field radiation symmetric about the z-axis. We now turn attention to optical structures that exhibit strong emission in a single direction, breaking this symmetry. In the case of emission systems symmetric about the z-axis, photons perform random walks throughout the waveguide. By contrast, forward-emitting luminophores exhibit a decreased mean free path for photon propagation to the collector cells. As detailed in the Methods section, we simulate forward-emitting

luminophores consisting of spherical absorbing/emitting nanoparticles embedded within a nanocone. For such a forward-emitting luminophore, Figure 3.6a-c highlights the polar radiation plot, spatial radiation profile, and nanocone structure. Integrating the luminescence intensity, we observe that approximately 88% of the intensity from such structures couples into the TIR waveguide angles — slightly less than for the dipole emitter.

As shown in Figure 3.6d, the dependence of forward emitter conversion efficiency on optical density, GG, and PLQY closely parallels that of the dipole emitter case. However, even though the forward emitter is 33% more likely to emit photons into the escape cone relative to dipole structures, we observe a maximum conversion efficiency of 24%, approximately 96% of the dipole emitter maximum. We find fewer luminescence reabsorption events for forward emitters compared to their dipole emitter counterparts, suggesting that breaking this z-axis symmetry enables shorter luminescence mean free paths within the waveguide. This shorter path almost completely compensates the increased escape cone loss. Further, we observe that for a GG of 10, the maximum conversion efficiency reaches 17.3% for the case of unity PLQY and an optical density of 0.75.

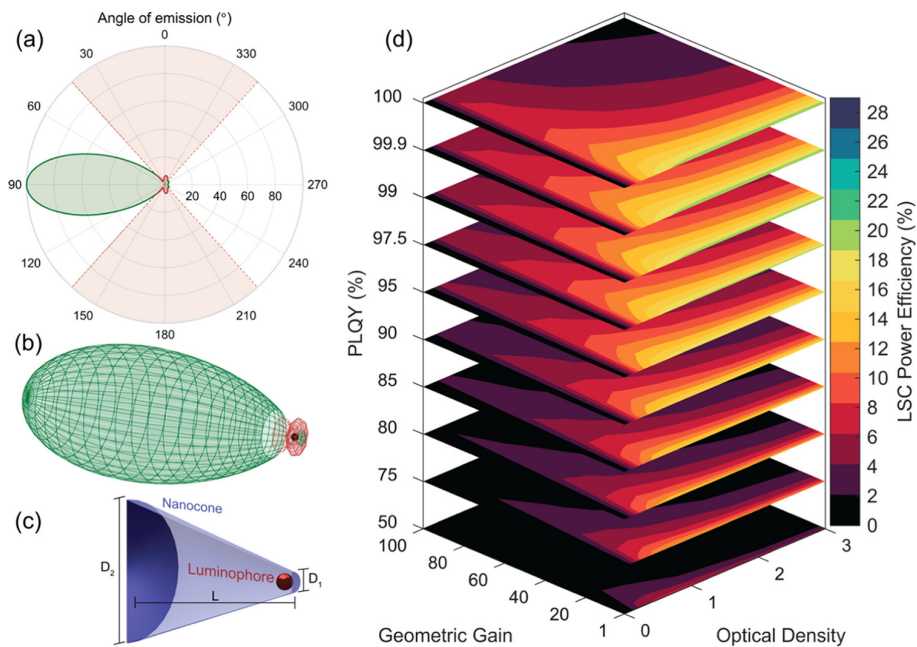


Figure 3.6: Monte Carlo ray-trace results for the forward, nanocone emission pattern, where (a) shows a polar 2D plot of the simulated PL profile with respect to the azimuthal angle and (b) illustrates the polar angle asymmetry of the forward emitter, where the structure preferentially emits into angles along a single direction of the horizontal x-axis. (c) 3D rendering of a cross section of the forward-emitting structure, consisting of the luminophore (red sphere) at the narrow end of the cone (D_1) of length L with a final, large diameter of D_2 . (d) Conversion efficiency of the LSC module with respect to GG, optical density, and PLQY.

3.2.5 Enhancing the efficiency of the record LSC

While the dipole and forward emission cases correspond to physically realizable emitters, the LSC structure itself assumes certain idealities. Specifically, we thus far have assumed record GaAs PV cells coupled to ideal luminophore emitters with a narrow PL profile matched to the GaAs bandgap (as shown in Figure 3.1c). Additionally, our simulated LSC waveguide matrix assumes a constant index of refraction for generated PL. To illustrate how anisotropic emission can significantly benefit less idealized systems, we model the current record conversion efficiency LSC fabricated by Slooff et al. [133] As shown in Figure 3.7a, this device employs two luminophore species: Lumogen Red and Fluorescence Yellow dyes, with peak optical densities of 0.71 and 2.36, and luminescence quantum yields of 87 and 98%, respectively. With a square waveguide side length of 5 cm and an overall thickness of 0.50 cm, the fabricated LSC yields an overall GG of 2.5. Figure 3.7a displays the refractive index of the waveguide polymer matrix material, poly(methyl methacrylate), as well as the external quantum efficiency of the GaAs solar cell. Finally, a diffuse Lambertian-scattering back reflector is coupled to the bottom surface of the waveguide, with approximately 97% averaged reflectance at PL wavelengths.

We first simulate this record efficiency LSC and validate our model by obtaining conversion efficiencies equal to the experimental measurement. As a next step, we systematically vary the luminescence fraction emitted into TIR angles in the waveguide. As shown in Figure 3.7b, the isotropic emission case (i.e., P_{TIR} of 75%) attains the experimentally measured conversion efficiency value of 7.1% under 1 sun illumination. However, upon increasing the anisotropic luminescence fraction, we find a monotonic increase in performance up to 9.6% in the ideal case of unity P_{TIR} — a relative increase of 35%. The observed conversion efficiency enhancement resulting from luminophore anisotropy underscores the crucial role waveguide trapping plays in enabling high conversion efficiency.

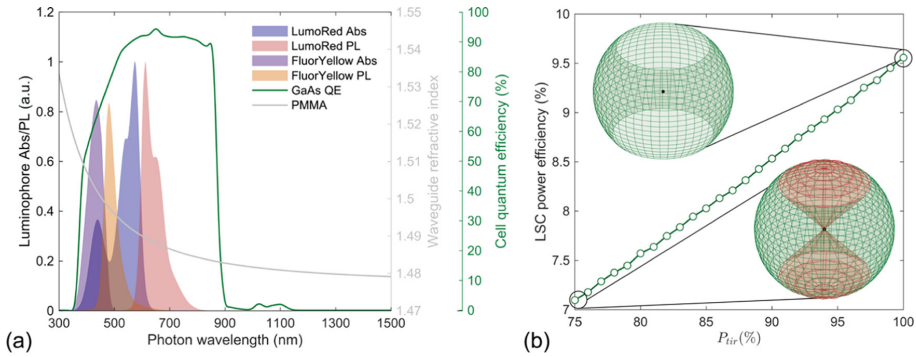


Figure 3.7: (a) Spectral characteristics of the current record LSC device, consisting of two luminophores within the waveguide (Lumogen Red, Fluorescence Yellow) (left y-axis), four edge-lined GaAs cells (cell quantum efficiency at far right y-axis), and a PMMA waveguide matrix (refractive index at right y-axis). (b) Monte Carlo ray-trace simulations showing the impact of anisotropy on the conversion efficiency for the current record device. At the isotropic limit (P_{TIR} of 75%), we observe close matching between measured and modeled efficiencies (7.1% measured and 7.096% modeled). At the anisotropic limit, power efficiencies reach 9.6%, a relative increase of approximately 35%.

3.2.6 Loss mechanisms within anisotropic LSCs.

As discussed in the Methods section, we track photons collected as well as photons lost. For the luminescent concentrator, we categorize losses into five thermodynamic mechanisms. Figure 3.8a-c illustrates these losses as a function of the luminophore optical density at an LSC GG of 20, assuming PLQY of 95%. For each of the three emitter types (step, dipole, and forward), losses can be understood as either: (i) nonabsorbed incident photons, either due to sub-bandgap photon energy or low luminophore optical density; (ii) thermalization, i.e., energetic relaxation of photogenerated excitons to the luminophore bandgap energy; (iii) waveguide escape cone loss; (iv) subunity PLQY loss; and (v) loss from the photovoltaic cell itself, owing to thermalization from the luminophore emission energy to the cell bandgap, subunity collection efficiencies (i.e., EQE), fill factor, and cell contact resistance.

Figure 3.8a-c illustrates the trade-off between optical density and maximum conversion efficiency (black). Although a higher optical density minimizes the nonabsorbed incident light (blue), waveguide escape cone loss (yellow) and luminophore nonradiative recombination (orange) adversely affect the overall performance for the dipole and forward emitters. For the perfect step emitter, we observe that increased luminophore optical density yields substantially higher amounts of luminophore nonradiative recombination (orange). As expected, we observe lower escape cone loss in the dipole emitter case compared to that of the forward emitter. However, the forward emitter loses comparatively less power through luminophore nonradiative recombination compared to the dipole case given shorter mean free PL path lengths, as previously discussed.

Figure 3.8d compares four nonideal systems to an ideal case of unity PLQY and P_{TIR} , a high optical density of 3, and a GG of 20 (yielding a maximum conversion efficiency of approximately 29%). For isotropic emission (i.e., P_{TIR} of 75%) at a PLQY of 95%, the dominant loss mechanism is PL coupling into the escape cone. We also observe that for dipole, forward, or perfect step emission and PLQY of 95%, the primary loss mechanism is luminophore nonradiative recombination. In the ideal case of complete PL trapping and perfect luminophore radiative efficiency, the LSC conversion efficiency reaches the detailed balance limit of a photovoltaic system whose bandgap is given by the luminophore absorption spectra rather than the GaAs bandgap. This can be understood given that incident light with energies greater than the bandgap of the cell, but less than the luminophore absorption edge, will not be absorbed by either the luminophore or waveguide matrix — assuming a dielectric waveguide with an arbitrarily large bandgap (i.e., insulator). As demonstrated by previous studies [134, 135], LSCs can retain the detailed balance limit only if this condition holds where the dark radiative saturation current is not scaled with the short-circuit current.

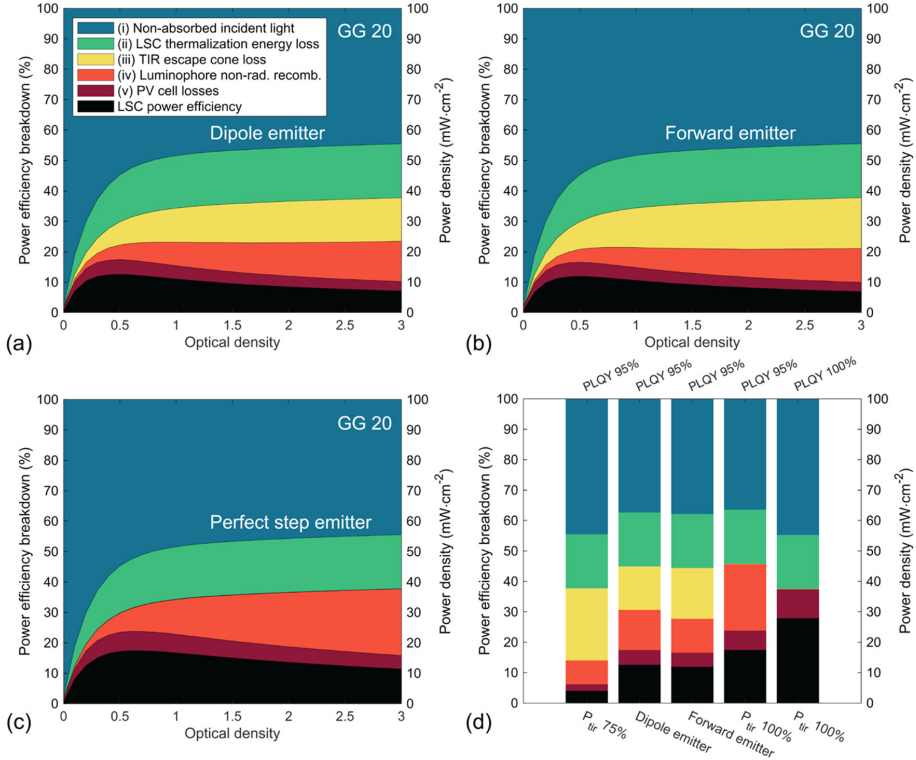


Figure 3.8: Overall conversion efficiency loss mechanisms of an LSC with respect to the optical density of the luminophores within the optical waveguide for the case of the dipole emitter (a), forward emitter (b), and perfect anisotropic step emitter (c). (a), (b), and (c) assume a PLQY of 95%. Here, we define the losses as (i) incident irradiance not absorbed by the LSC, limited by both the absorption spectrum of the luminophore and, for lower optical densities, the amount of in-band luminophore absorption; (ii) LSC thermalization energy loss, owing to the thermalization of photogenerated excitons within the luminophore that relax to the PL band; (iii) TIR escape cone loss of the PL, which can result from emitted PL coupling into the cone from an emission event or a scattering event by the waveguide; (iv) luminophore nonradiative recombination of photogenerated excitons given nonunity PLQYs; and (v) PV cell losses, which include parasitic absorption, given the limited internal quantum efficiency of the coupled cell material and thermalization from the PL emission wavelength to the bandgap of the cell. (d) Comparison of five cases at optimal OD given the emitter and GG of 20 for (from left to right): a PLQY of 95% and TIR-limited PL trapping, the dipole emitter at 95% PLQY, the forward emitter at 95% PLQY, a PLQY of 95% and perfect PL trapping, and the upper performance limit of unity PLQY and perfect PL trapping.

3.3 Conclusions and future work

In this chapter, we investigate the role that anisotropy plays in improving LSC conversion efficiency. Through Monte Carlo simulations, we illustrate the importance of maximizing the waveguide trapping efficiency, P_{TIR} , in addition to the luminophore radiative efficiency, PLQY. By systematic variation of critical design parameters, we explore the role of anisotropic luminophore emission for ideal step, dipole, and forward emitters on LSC conversion efficiency. We find that for the experimental luminophores and LSC design used for the present record LSC (conversion efficiency 7.1%), the upper anisotropic emission limit ($P_{\text{TIR}} = 100\%$) increases this efficiency to 9.6%. Our model also shows that a modest geometrical gain ($GG = 10$) can be realized with a conversion efficiency of greater than 15% via anisotropic luminophore emission ($P_{\text{TIR}} = 95\%$) with a luminescence quantum yield of 99%. Notably, a conversion efficiency above 25% is achievable for PLQY = 99% and full light trapping ($P_{\text{TIR}} = 100\%$) at such a geometric gain. The recent demonstration of luminophores with ultrahigh luminescence quantum yield, combined with well-developed nanophotonics design and fabrication methods for anisotropic scatterers, can open the door to previously unreachable LSC conversion efficiencies.

3.4 Computational methods

We employ a Monte Carlo ray-trace model to evaluate LSC conversion efficiency for varying GG, luminophore optical density, PLQY, and PL emission patterns. Previous studies have validated this model both with experimental data and also LSCs reported in the literature [42]. The Monte Carlo stochastically traces individual photons throughout each layer of the LSC. We initialize a constant grid matrix across the waveguide top surface area of 150 by 150 for all GGs, simulating photon wavelengths between 300 and 1200 nm in steps of 10 nm. Following the previous methods [136], we model approximately 2×10^6 photons for each LSC module type to achieve statistically reliable results. We adopt an ideal luminophore absorption and PL profile with a Stokes shift of approximately 200 nm from the absorption edge (750 nm) to the PL center (950 nm). Each luminophore exhibits reabsorption, as shown in Figure 3.1c. We base the luminophore absorption band tail and PL full width at half maximum archetype core/shell quantum dot structures.

We track the photon's previous and current positions (x, y, z), previous and current velocity vectors (v_x, v_y, v_z), and original and current wavelengths (λ_0, λ). Photons propagate through the LSC in discrete steps of 5 μm , where the current velocity determines the resulting direction. To determine the probability of luminophore absorption, we apply the Beer-Lambert law, given the optical density constant of that particular LSC for a given simulation step. To determine reflection and refraction angles at LSC layer interfaces, we apply Fresnel and Snell laws, respectively, for an assumed waveguide with a refractive index of 1.49 at the PL emission wavelengths, approximately 800-900 nm. We model current record high-efficiency Alta Devices' GaAs cells and simulate the photon-cell interaction through the measured reflectance and internal quantum efficiency, where we assume 2.5% of the cell surface area to be entirely reflective, representative of the front metal contact area. We assume GaAs edge-lined cells to optically couple to each of the four perimeter edges of 100 μm thick LSC waveguides, where we set the edge length according to the GG (GG of 1 corresponds to a 400 μm perimeter). We assume a perfect specular back reflector optically coupled to the bottom surface of the LSC to evaluate escape cone loss for only the top waveguide surface.

For each photon striking the LSC, we mark whether the photon is collected by one of

the four edge-lined GaAs cells or lost via a particular mechanism. If collected, we weigh the original incident photon wavelength by the AM1.5G solar spectrum to calculate the resulting photocurrent density of a given GaAs cell. We assume the four GaAs cells to be connected in parallel. Once all photons are simulated and determined, collected or lost, we calculate the open-circuit voltage and fill factor. To calculate the former, we assume an arbitrarily large dielectric waveguide electronic bandgap, such that any contribution from the waveguide matrix to the radiative dark saturation current of the GaAs cell is negligible. We then calculate the radiative limit open-circuit voltage given the absorption spectra of the luminophore — scaling by the luminophore optical density and the emission out of the waveguide and into the escape cone. We also consider the contribution to the radiative dark current via background spectra photons reaching the GaAs cells directly — scaling by the system GG and emission out of the waveguide given by the refractive index. To account for cell nonradiative combination of photogenerated excitons, we apply an explicit approximation within such GaAs cells, as given by Equation 3.7 [131]. Finally, we calculate the fill factor given previous explicit models that have shown close experimental matching and apply series and shunt resistances to match the diode behavior for current, record GaAs cells [137].

$$V_{oc}^{nonrad} = \frac{kT}{q} \ln \left(\frac{2.5}{1 + 1/J_{sc}} \right) \quad (3.7)$$

To vary the angular distribution of emission for embedded luminophores, we generate a probability distribution function for each radiation pattern (i.e., a steplike, dipolelike, and forwardlike emission). We assume a uniform alignment of all luminophore emitters within the waveguide. The step emission profile, as depicted in Figure 3.1b, assumes a constant probability of emission for angles inside the escape cone for a waveguide refractive index of 1.49. We employ a dipole emission profile following previous studies of the emission angle [124].

Finally, we model directional forward radiation to evaluate the LSC performance for a luminophore whose angular distribution is anisotropic in both the azimuthal and polar directions. Here, we assume a nanocone structure of a refractive index 2.5 hosting an embedded spherical luminophore. We performed full-wave electromagnetic simulations using the finite-difference time-domain (FDTD) method to model the far-field radiation pattern. In the full-wave simulations, we varied the nanocone central axis length, front and end radii, and emitter position along the central axis. We implemented a particle swarm optimization routine within this four-dimensional design space (i.e., axis length, front radius, end radius, emitter position) to probe the optimal performing structure, where the fraction of emission into the forward direction is taken as the figure of merit. The champion structure has an 887 nm axis length and radii of 180 and 1367 nm.

4

Anisotropic luminophore emission for enhanced light trapping in luminescent solar concentrators

Building-integrated photovoltaic (BIPV) technologies integrate photovoltaic energy generation into the design of semi-transparent and opaque building envelopes. The photovoltaic luminescent solar concentrator (LSC) is an example of such a technology and offers the potential for low-cost, passive concentration of direct and diffuse light. Recent advances in the emission efficiency of semiconductor luminophores could significantly reduce parasitic losses, but efficient light trapping remains elusive to achieve high conversion efficiency LSCs. Here, we demonstrate anisotropic luminophore emission to enhance light trapping in the LSC waveguide. By embedding semiconductor nanoplatelet emitters into high-index TiO_2 nanocylinders, we alter their angular emission profile to increase emission into total internal reflection (TIR) angles. The emission direction can be controlled by tweaking Mie-like multipolar resonances in the individual nanocylinders (form factor) and the interaction with the lattice (structure factor). Angle-resolved photoluminescence measurements on the fabricated nanocylinders arrays corroborate this understanding. By optimizing the cylinder shape and lattice spacing, we show an increase in light trapping from 75% (isotropic emission) to 83.5%. This novel approach to the integration of nanoscale photonic structures and emitters paves the way for enhanced emission control in photovoltaic systems, as well as in solid-state lighting and smart displays.

This chapter is based on:

Anisotropic luminophore emission for enhanced light trapping in luminescent solar concentrators

Tom Veeken¹, Kyra Orbons¹, Nelson de Gaay Fortman¹, Aurelio A. Rossinelli², David J. Norris², A. Femius Koenderink¹, and Albert Polman¹
in preparation

¹Center for Nanophotonics, NWO-Institute AMOLF, Science Park 104, 1098 XG Amsterdam, The Netherlands

²Optical Materials Engineering Laboratory, Department of Mechanical and Process Engineering, ETH Zurich, 8092 Zurich, Switzerland

Author contributions:

Kyra, Tom, and Albert conceived the project. Kyra developed the nanocylinders fabrication protocol with embedded emitters and drew the sketches. Kyra and Tom performed the FDTD simulations, ellipsometry, SEM and PL measurements, and the data analysis. Tom performed the AFM measurements and wrote the original draft. Nelson and Tom performed the Fourier measurements. Femius and Tom performed the RCWA simulations. Aurelio synthesized the nanoplatelets, under the supervision of David. Albert supervised the project. Femius and Albert reviewed and edited the manuscript. All authors provided feedback and contributed to the manuscript.

4.1 Introduction

The amount of energy from the sun that reaches the earth's surface is practically inexhaustible and free, providing a staggering 1.5 billion TWh annually [138]. This is about 9 thousand times our annual primary energy production of 168 thousand TWh [5]. Solar photovoltaics (PV) currently makes up about 0.3% of the world's energy production, or 3% of electricity production [139], and is growing at a high pace (20% in 2020). To sustain this growth, a large global research effort is well underway to develop further several PV technological families [15, 20]. Besides the continued deployment of solar farms, where economies of scale push the installed capacity up by decreasing costs [32], many other complementary PV technologies have emerged [140]. Building-integrated photovoltaics (BIPV) is a set of such a technologies, integrating solar power generation into the built environment: e.g. building envelopes [35, 37], roofs [34], windows [82, 83, 98, 141], greenhouses [84, 87], public spaces [96], and art [142]. BIPV receives much attention because of their potential to minimize the use of land for PV systems, decrease the overall system and installation costs due to its multifunctional use, and make PV systems more aesthetically appealing. Moreover, local generation in combination with local consumption and storage of electricity is of benefit to a future energy grid with large proportions of variational renewable energy sources [143].

The photovoltaic luminescent solar concentrator (LSC) is a BIPV device that consists of a dielectric waveguide with embedded luminophores and integrated solar cells along the edges or in a matrix (see Figure 4.1a). Part of the incident sunlight is absorbed by the luminophores, given by their absorption band and particle concentration (optical density). The luminophores subsequently emit photoluminescence (PL) at lower energy, set by the Stokes shift. The photoluminescence quantum yield (PLQY) indicates the efficiency of emission after absorption. A fraction of the PL is trapped in the waveguide by total internal reflection (TIR). The angular range of TIR is determined by the index of refraction contrast between the waveguide and air. The spectral profiles and intensity of the absorption and emission of the luminophores determine the opacity and color of the LSC, i.e., the average visible transparency (AVT) [144]. Thus, using the LSC as a facade or roof component offers additional aesthetic options due to its variable semi-transparent and/or colored surface.

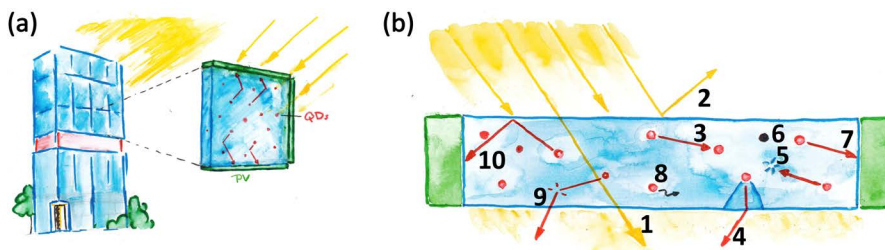


Figure 4.1: (a) Schematic representation of a luminescent solar concentrator as a building-integrated photovoltaic device. (b) An overview of the optical pathways in an LSC: 1) represents light that is not absorbed by a luminophore, 2) reflection at the surface, 3) reabsorption, 4) escape cone loss, 5) parasitic absorption by the waveguide 6) long-term luminophore instability, 7) parasitic losses in the solar cell, 8) limited photoluminescence quantum efficiency, 9) internal scattering, and 10) total internal reflection [106]. Sketches drawn by Kyra Orbons.

Photovoltaic LSCs exhibit several features that set them apart from other photovoltaic devices. Compared to conventional flat photovoltaic cells, LSCs offer superior mechanical flexibility, lower operating temperatures [95], and use less active photovoltaic material. Geometric concentrating photovoltaic systems also use less active material but typically operate at higher temperatures. Moreover, geometric concentrator systems have limited acceptance angles and therefore require sun-tracking, whereas LSCs are passive concentrators that absorb both direct and diffuse irradiance [93]. Finally, the combination of distinct absorption spectra and developments in ultra-high PLQY luminophores make the LSC a promising candidate for future tandem devices [101, 102, 104].

Many device parameters can be tuned when designing an LSC, many of which affect each other [106, 145]. Among these are the aforementioned luminophore PLQY, optical density (OD), and index of refraction of the dielectric waveguide, as well as the luminophore absorption and emission spectra. The refractive index sets the critical angle for TIR inside the waveguide, while the Stokes shift between luminophore absorption and emission imposes the maximum achievable concentration [91, 146]. Moreover, the absorption onset of the PV should be aligned with the luminophore emission spectrum to minimize carrier thermalization in the PV. The ratio between the top surface area of the waveguide and the active PV material surface area of the LSC is termed the geometric gain (GG) – a larger GG implicates a larger average optical path from the emitter to the PV cell, amplifying loss pathways.

Despite several decades of LSC research, interplaying loss mechanisms still limit its potential [106]. Novel luminophores, such as highly emissive perovskites and colloidal quantum dots [147, 148], have largely replaced the traditional organic dye molecules that suffered from limited spectral coverage, low emission efficiency (i.e., PLQY), and small Stokes shifts leading to strong reabsorption losses [149]. Yet, the record power conversion efficiency of 7.1%, for a GG of 2.5 and 1 sun illumination, is still reported for a dye-based LSC [115]. Figure 4.1b shows all the possible optical pathways in an LSC. These include reflection, absorption, and transmission of incident sunlight; emission, reabsorption, and recombination by the luminophore; parasitic losses by the waveguide and solar cell; scattering and escape cone loss; and total internal reflection [106]. The emission of photons through the escape cone is a major loss channel, accounting for over 25% of all emitted photons. This is a direct consequence of the typical isotropic luminophore emission in the waveguide matrix and the critical angle of a glass/plastic waveguide in air that sets the single-pass trapping by TIR at 75%.

Much computational and experimental research has aimed to reduce the escape cone losses in LSCs. For instance, by selectively reflecting light at the luminophore emission wavelength with Bragg mirrors placed on the top and bottom surface of the LSC [42, 117, 118]. Using a proper dichroic mirror, this approach completely eliminates PL escape cone and scattering losses at the cost of the additional (expensive) mirror component and a significantly altered AVT for the waveguide. Partially limiting escape cone emission angles with Bragg mirrors has also been proposed for an LSC with an external PV [150]. An alternative approach is to alter the angular emission profile of the luminophore to emit more into TIR angles, for example, by adjusting the luminophore shape [43, 151], orientation [152], or nanophotonic environment [123]. In Chapter 3, we systematically evaluated the effect of anisotropic luminophore emission on the power conversion efficiency. Using a Monte Carlo ray-tracing model, the impact of anisotropic emission was evaluated for a wide variety of LSC parameter combinations. The results imply that strong anisotropic emission into TIR angles in combination with ultra-high PLQY [128] unlocks power conversion efficiencies towards the single-junction detailed-balance limit [145].

In this chapter, we present and demonstrate a novel nanophotonic approach to anisotropic luminophore emission for LSCs. By directly embedding luminophores into

high-index TiO_2 nanocylinder arrays, we increase emission into TIR angles. The shape and size of the cylinder arrays are optimized such that the Stokes-shifted luminophore emission is resonantly directed in-plane, while (sun)light with energy higher than the luminophore bandgap is resonantly absorbed in the out-of-plane direction. We use finite-difference time-domain (FDTD) simulations to find the optimal nanostructure. The simulations predict that the escape cone losses at the single resonator level (form factor) are reduced from 25% to 14.7% in the optimized design. Subsequently, rigorous coupled-wave analysis simulations are performed to find the optimal lattice constant for the array of cylinders (structure factor), predicting reduced escape cone losses of 16.5%.

We fabricated arrays of TiO_2 nanocylinders on top of a glass substrate with integrated highly-emissive CdSe-CdZnS core-shell nanoplatelets, according to the optimized design. Spatially resolved photoluminescence measurements show that the luminophores are only located inside the cylinders as designed. Angle-resolved photoluminescence microscopy measurements show strong anisotropic emission. To emulate the incorporation of the cylinder array inside an LSC waveguide, we use an immersion-oil objective, which also enables the collection of luminophore emission beyond the critical angle of a glass waveguide in air. We show excellent agreement between the simulated and measured angle-resolved emission profiles that result from the single-particle Mie resonances (form factor) and photonic crystal modes of the cylinder array (structure factor).

4.2 Nanophotonic angular emission control

Nanophotonic angular emission control of dipole-like emitters [153] is considered a promising route to improve various photovoltaic systems and has thus been studied extensively [19, 32]. Unidirectional emission was first demonstrated by placing QDs in the vicinity of plasmonic nanoantennas [48, 50]. The coupling of QD emission with the photonic modes in a plasmonic resonator alters the angular emission profile. Directional emission control is achieved by controlling the photonic modes, which depend on the resonator material and shape, and the coupling of the modes with the dipole-like emitter, which depends on its position relative to the resonator [154]. By employing an array of resonators, the emitter also couples to diffractive lattice modes [49, 155]. Complementary to the plasmonic resonators, directional emission was demonstrated by coupling emitters to all-dielectric nanophotonic resonators [156]. Notable examples are QDs coupled to a leaky-antenna [157], QDs dispersed in glass Mie-like resonators [58], rare-earth ions coupled to dielectric metasurfaces [158], and monolayer MoS_2 coupled to silicon nanowires [59]. Lasing from semiconductor nanocrystals has also been demonstrated by coupling them to plasmonic [159, 160] and dielectric nanoparticle arrays [161]. In Chapter 2, we have shown directional emission of semiconductor QDs by soft-stamping them onto silicon nanocylinders, modifying the angular emission profile due to near-field coupling of the QD transition dipole with Mie-like multipolar resonances in the high-index nanocylinder [162].

Here, we directly embed colloidal CdSe-CdZnS core-shell nanoplatelets [163] in high-index TiO₂ nanocylinder arrays. The nanoplatelets (NPLs) have a reported center emission wavelength of 655 nm and a full-width half-maximum (FWHM) linewidth of 19.5 nm. In this system, we avoid enhanced parasitic absorption losses typical of plasmonic or absorbing dielectric systems, control the precise location of the emitters with respect to the TiO₂ resonator, control the shape of the TiO₂ cylinders, and fabricate arrays composed of tens of thousands of resonators – a novel combination of features.

The photonic building block we use is a dielectric nanocylinder. These structures exhibit multipolar Mie-like resonances [25, 164] when their size is on the order of the effective wavelength, i.e., the free-space wavelength divided by their refractive index. Our material of choice is TiO₂ due to its relatively high refractive index (~ 2.3 at 650 nm wavelength) and simultaneous low extinction coefficient (below 0.003 beyond 400 nm wavelength) – see Figures 4.7 and 4.8 in the Supplementary Information for the experimental complex refractive index data. This refractive index gives sufficiently high contrast in a typical glass/plastic LSC waveguide environment to support Mie-like resonances.

With the ingredients introduced above – dielectric TiO₂ nanocylinders in a glass-like environment (refractive index: $n = 1.475$) – we optimize for the shape with the best response. Vaskin et al. separated the single unit cell response (form factor) from the lattice response (structure factor) [153]. Using this description, we first design the form factor, i.e., the response of the single nanocylinders, where the figure of merit is emission into TIR angles. The structure factor is taken into account separately in the next section. To find the optimal size of the individual nanocylinder, we perform finite-difference time-domain (FDTD) simulations (see Methods for details). We start with a single, monochromatic ($\lambda = 650$ nm, similar to the experimental peak emission wavelength) dipole source in the center of the cylinder (Fig. 4.2a) and optimize its height and diameter. As a result, we obtain a maximum of 93.7% emission into TIR angles for a diameter of 450 nm and height of 150 nm. Fig. 4.2b shows the corresponding angular emission profile as calculated by FDTD (blue), averaged over the three orthogonal dipole moments: x, y, and z oriented. The black line shows the reference case of isotropic emission with unity normalized intensity. In the reference case, 75% of the emission is within the TIR angular range, indicated by the red dashed line (42.7 degrees from normal incidence). The intensity of the optimized emission profile in blue is normalized by the isotropic case. This enables us to calculate the simulated LDOS enhancement at the center of the cylinder to be 4.25 (see Methods for details).

From an implementation perspective, multiple luminophores are needed per cylinder to achieve reasonable absorption in an LSC. Moreover, a layer of luminophores instead of a single one also enables a layer-by-layer fabrication protocol. Therefore, we extend our design to that of a TiO₂ nanocylinder with a center layer of luminophores (Fig. 4.2c). The optimization now involves the simulation of dipole sources at several radial and axial positions and subsequently a weighted incoherent summation over positions and dipole orientations to emulate a full sampling of all source positions in the layer. The single dipole source optimization proves a good initial indicator because the optimal shape remains similar: a diameter of 500 nm and height of 150 nm, now with a centered luminophore layer of 30 nm in thickness. Figure 4.2d shows the resulting angular emission profile (blue) for the ensemble of luminophores positions, again averaged over the three dipole moments, yielding 85.3% emission into TIR angles. The corresponding LDOS enhancement is 3.5. Thus, the lower efficiency than for the dipole in the center above is attributed to a change in the coupling between the off-center dipoles and the nanocylinder Mie-like modes. The position-dependent coupling alters the LDOS enhancement slightly, from 4.25 to 3.5, but this does not explain the change in the emission profile within escape cone angles. This change indicates that off-center dipoles

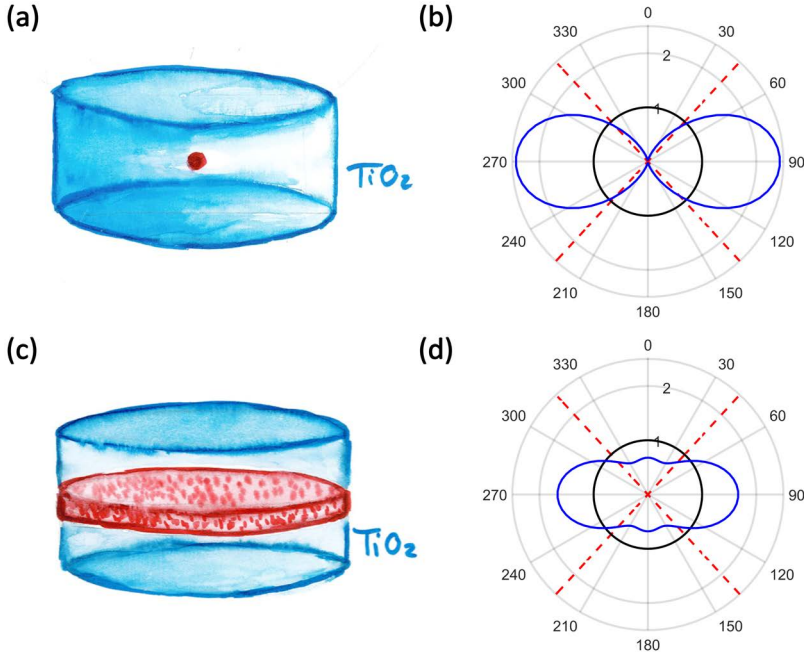


Figure 4.2: (a) A single dipole-like emitter (red) embedded in the center of a TiO₂ nanocylinder and (b) its corresponding, optimized directional emission profile (blue) at a diameter of 450 nm and height of 150 nm. (c) A layer of emitters (red) embedded in the nanocylinder at center height and (d) its corresponding, optimized directional emission profile (blue) at a diameter of 500 nm and height of 150 nm. Emission profiles are calculated with FDTD, averaged over the three orthogonal dipole moments. The black line shows the reference case of isotropic emission, with 75% emission into TIR angles (red dashed line indicates the critical angle for TIR). The intensity of the optimized emission profiles in blue are normalized by the isotropic case. Sketches drawn by Kyra Orbons.

excite the Mie-like modes with different strengths than the center-dipoles, and the total interference causes stronger emission into escape cone angles.

The Stokes shift allows for the decoupling of the absorption and emission probabilities that otherwise are coupled through reciprocity. This makes it possible to maximize emission into TIR angles without reducing the absorption of light coming from outside the waveguide. In fact, the optical cross-section of the nanocylinders for wavelengths below the absorption onset of the luminophores can be designed to enhance absorption. Here, however, we have not considered the luminophore absorption as a figure of merit during the design. With the optimized cylinder design, we proceed to the fabrication of TiO₂ nanocylinder arrays with embedded luminophores on a glass substrate (Fig. 4.3a).

4.3 Nanocylinder array fabrication

We fabricate the designed structures using a top-down approach, similar to that reported by Ha et al. [165]. First, a layer of 60 nm TiO_2 was deposited on a borosilicate glass substrate (500 μm thick) using electron-beam physical vapor deposition (EBPVD). Then a 30 nm layer of CdSe-CdZnS core-shell nanoplatelets (NPLs) was spin-coated, and a final 60 nm TiO_2 layer was evaporated on top. Electron-beam lithography (EBL) and reactive-ion etching were then used to pattern the triple layer on glass into an array of cylinders. A negative tone resist, ma-N 2400, was used as the EBL mask. After EBL exposure and development of the resist, a combination of CHF_3 and O_2 gases was used to etch the structures with RIE (see Methods section for details). On a single substrate, several fields of $100 \times 100 \mu\text{m}$ cylinder arrays were fabricated by raster scanning of EBL. While EBL gives full control over the shapes and sizes of the arrays, which is particularly useful for prototyping but makes the patterning rather slow, upscaling of this nanostructuring technique is fully feasible with stamping technologies such as soft conformal imprint lithography (SCIL) to obtain large-area RIE masks [166]. Figure 4.3b shows an atomic force microscopy (AFM) map of the resulting nanocylinder array for target dimensions of 500 nm diameter and 1400 nm pitch. Given the initial height of 150 nm for the triple layer, the sample has certainly been over-etched. However, the fact that we etched into the glass is not a problem for our experiment because our design considers a homogeneous glass surrounding, and measurements are performed with index-matching fluid covering the cylinder arrays. A scanning electron microscopy (SEM) image is also shown in Fig. 4.9 for a nominally identical nanocylinder array but fabricated on a silicon substrate for reference.

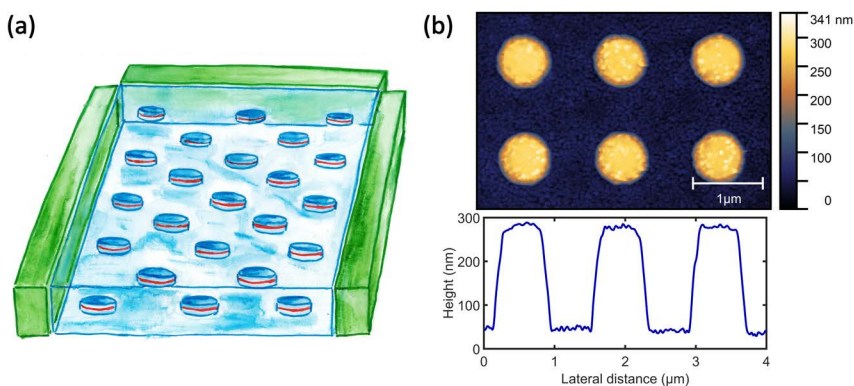


Figure 4.3: (a) Sketch of the implementation of the nanocylinders array inside an LSC. (b) AFM height map of the TiO_2 nanocylinder array with embedded nanoplatelets. Sketch drawn by Kyra Orbons.

4.4 Spatial photoluminescence measurements

Before turning to directional photoluminescence measurements, we measured the photoluminescence of the embedded NPLs as a function of position on the nanocylinders array. Figure 4.4a shows a microscope image taken in a confocal microscope in reflection. In Figure 4.4b, we plot the photoluminescence intensity at $\lambda = 650 \text{ nm}$ as a function of position,

corresponding to the area marked by the red square in Fig. 4.4a. Bright PL is observed when the laser is positioned on top of a cylinder, confirming that the NPLs remain bright emitters after going through all of the fabrication stages. Moreover, most cylinders display similar PL intensity, showing that a homogeneous sample was fabricated, and subsequent angle-resolved photoluminescence measurements can be collected from an extended area by exciting multiple cylinders. In Figure 4.4c, two representative PL spectra are plotted corresponding to the data in Fig. 4.4b: on top of a cylinder (green) and in between four cylinders (purple). We attribute the nonzero intensity when the laser is positioned in between the cylinders to emission from NPLs in the surrounding cylinders, which were excited by a combination of the tails of the diffraction-limited laser spot, light scattered by small roughness on the etched glass substrate, and light funneled towards the cylinders due to their increased optical cross-section at the laser wavelength [164].

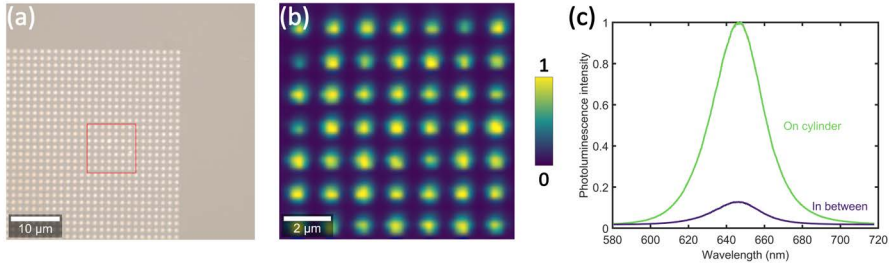


Figure 4.4: (a) Optical microscopy image of the corner of the TiO_2 nanocylinder array with embedded nanoplatelets. (b) Photoluminescence intensity map of the marked area in (a), indicating emission is confined to the nanocylinders. Color scale depicts the normalized intensity at 650 nm wavelength; pixels have been smoothed with a moving-average filter (original data are shown in Fig. S4). (c) Photoluminescence spectra corresponding to two positions in (b): on top of the cylinder and in between four cylinders.

4.5 Angle-resolved photoluminescence

Following the spatial PL measurements shown above, we measured the PL as a function of angle with a Fourier microscopy setup (see Methods). First, we measured on a nanocylinder array with 800 nm pitch, illuminating several hundreds of cylinders with the laser excitation spot. Figure 4.5a shows the obtained angle-resolved PL intensity image as a function of normalized parallel wavevector. The white dashed lines correspond to $\text{NA} = 1$ (critical angle from glass substrate to air) and $\text{NA} = 1.45$ (maximum for the objective), respectively. The observed high-intensity curves set the result apart from the simulated results for single resonators in Figure 4.2. To understand the origin of these curves, we must include the photonic modes of the array in the description: the angular emission profile is determined by the convolution of the structure factor given by the array and the form factor given by the single cylinder. We can understand the structure factor as the modes of a square lattice photonic crystal, which supports in-plane waveguide modes. The photonic crystal waveguide modes are described by dispersion relations that relate the locus of allowed wave vectors $(k_x, k_y)_{\text{wg}}$ to frequency. In a qualitative picture, where the cylinder-layer can be viewed as an effectively homogeneous slab with a weak periodic perturbation, the locus of wave vectors

is just a circle concentric around $k = 0$, with radius depending inversely on the wavelength, and determined by the guided mode index. Emitters predominantly radiate into these guided modes. The periodic perturbation makes these guided modes accessible to free space light by virtue of grating diffraction, which in k -space expresses as repetition of the dispersion relation of the waveguide at each reciprocal lattice point [61, 153]. The data in Figure 4.5a are well described by concentric circles repeated on a square lattice: we observe vertical and horizontal oval shapes resulting from parts of large displaced circles.

To model the full angular emission profile of the nanocylinder array, we perform rigorous coupled-wave analysis (RCWA) simulations using the open-source software package S^4 by Liu and Fan [167] (see Methods). Similar to the FDTD simulations, we model the structure with experimentally obtained optical constants for TiO_2 , but now we place the nanocylinder in periodic boundary conditions. Thus, the results from these simulations contain both the form factor and structure factor. We use reciprocity, according to which far-field emission patterns from sources in the structure can be predicted from the local absorption generated by far-field plane wave incidence (see Methods). To this end, we model the structure in RCWA, and insert absorption (imaginary part of the refractive index, $k = \sqrt{0.1} = 0.316$) exactly in the NPL layer inside the TiO_2 cylinders. At the target wavelength of 650 nm, we calculate the absorption in the center layer as a function of azimuthal and polar angle. Figure 4.5b shows the result for a pitch of 800 nm, normalized and plotted on the same axis as the experimental values in Fig. 4.5a. The experimental and simulated results show clear similarities: a horizontal and vertical shape is present with double bands, and the center shows a cross and diamond shape. However, bands do not appear at quite the same normalized k_x, k_y values, which we attribute to differences between the nanocylinder shape in the simulation and measurement. In general, the high-intensity bands remain within the inner dashed white circle, corresponding to the glass-air escape cone, so enhanced TIR light trapping is not achieved at this pitch.

The measurement and simulation are repeated for nanocylinder arrays with a larger pitch of 1000 nm, 1200 nm, and 1400 nm; the results are shown in Figures 4.5c-h. Again, we find a good comparison between the high-intensity features in the measured and simulated data. Moreover, the comparison becomes better as the pitch increases. For the largest pitch of 1400 nm, the desired emission profile is obtained where emission into TIR angles is stronger than within the escape cone. The pitches are chosen between 800 and 1400 nm to ensure the lattice supports waveguide modes at the emission wavelength.

The combination of higher and lower intensity features in Figures 4.5b,d,f,h are understood as many photonic crystal waveguide modes that are overlaid by their copies, repeated over the reciprocal lattice. The locations of the maxima are fully determined by the lattice, which we call the structure factor. The intensity distribution of this structure factor is modified by the angular emission profile of the individual cylinder, which we call the form factor. We observe that the photonic crystal bands in the center have lower intensity than the bands at higher wavevectors. This follows precisely our design, combining a form factor with strong emission into TIR angles and photonic crystal bands that also lie in the TIR angular range.

Many broader features in the simulation results are actually a combination of two separate modes, as can be seen at some locations in Fig. 4.5b,d. These two modes are waveguide modes for orthogonal polarization, parallel or perpendicular to the photonic crystal, which we will refer to as S and P polarization, respectively. Figure 4.11 in the Supplementary Information shows the same polarization averaged result as in Figures 4.5b,d,f,h, as well as individual S and P polarization results. The figures clearly show the two separate modes at similar locations, indicating a slightly different mode index for the orthogonal polarizations. The differences in the intensity and lineshape of the S and P polarization figures reveal that the coupling efficiency is significantly higher for the S polarization waveguide modes.

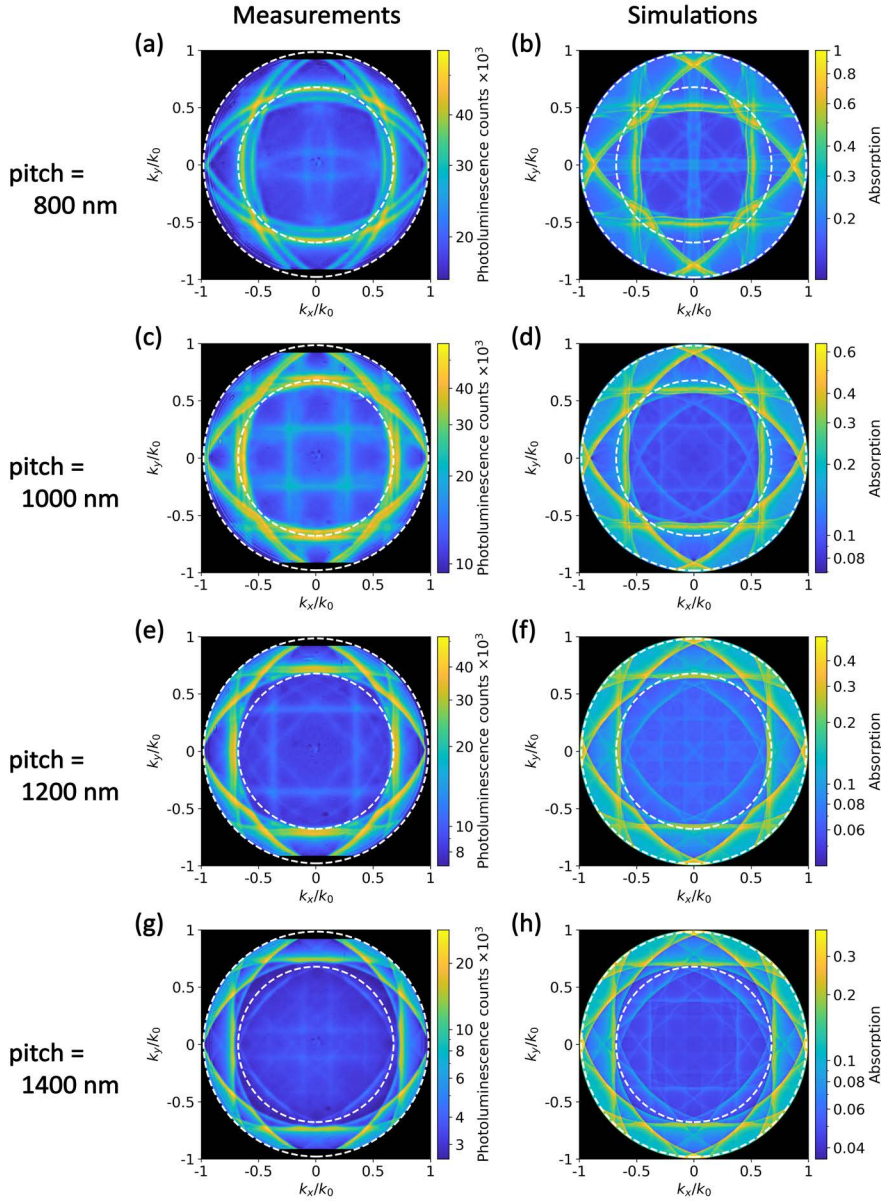


Figure 4.5: Angle-resolved photoluminescence measured on and simulated for a (a,b) 800 nm, (c,d) 1000 nm, (e,f) 1200 nm, and (g,h) 1400 nm pitch array. The measured results correspond well with the simulated photonic crystal bands. For the largest pitch of 1400 nm, 83.5% of the emitted light is trapped under TIR angles. The white dashed lines correspond to $NA = 1$ (critical angle from glass substrate to air) and $NA = 1.45$ (maximum for the objective), respectively. All data are averaged over S and P polarization.

Extending upon the repeated rings in the k_x, k_y plane, we can obtain a Fourier plane image at several frequencies (wavelengths) of the emitted light. This three-dimensional dataset describes the dispersion of the photonic crystal waveguide modes as the frequency and corresponding wavevector is changed. The rings are extended to cones in 3D, as described in reference [153]. Instead of slicing the dataset along a certain wavelength to obtain subsets as shown in Figure 4.5, we now slice along the $k_y = 0$ plane to depict the dispersion along k_x , revealing the photonic crystal bands as a function of wavelength in Figure 4.6. The red dashed line indicates a wavelength of 650 nm. In panel (a), we find two bands with high intensity that correspond to the high-intensity oval shapes in Fig. 4.5a. Upon increasing the array pitch (Fig. 4.6b-d), the bands move outwards to higher wavevectors for equal wavelength. The slope of the bands remains similar, indicating that the mode indices remain similar upon expanding the array pitch. Given the similar mode index, we explain the movement of the bands to higher wavevectors by the decrease of the reciprocal lattice vector due to the increasing pitch.

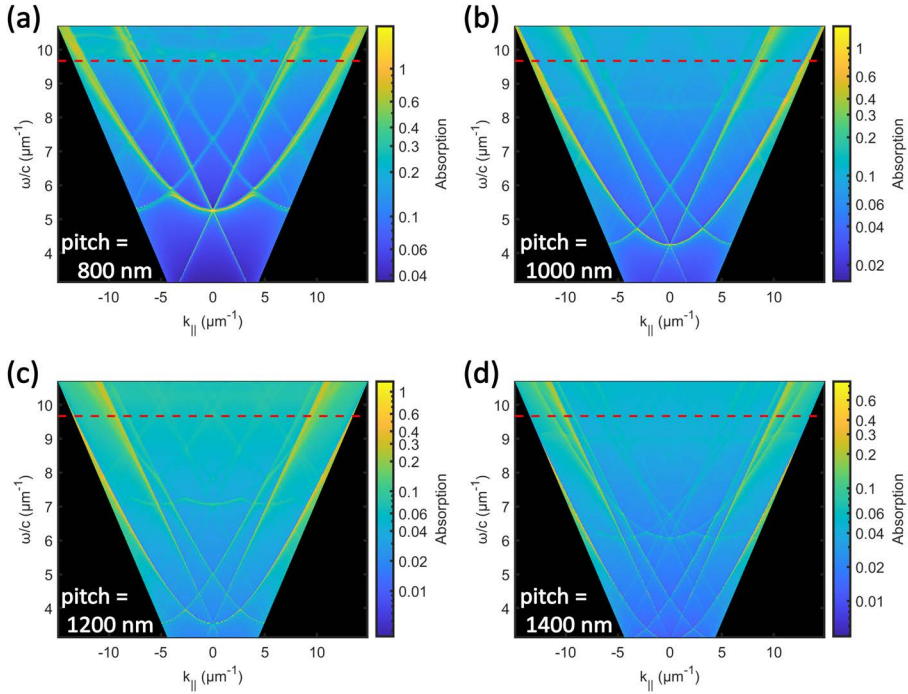


Figure 4.6: Calculated dispersion diagrams for a (a) 800 nm, (b) 1000 nm, (c) 1200 nm, and (d) 1400 nm pitch array, averaged over S and P polarization, along the $k_{par} = k_x$ axis and as a function of normalized frequency ($2\pi/\lambda$). The red dashed line indicates the target wavelength of 650 nm, corresponding to a horizontal cut through the plots in Figure 4.5 at $k_y = 0$. As we already observed in Figure 4.5 and 4.11, the photonic crystal bands are displaced outwards with increasing array pitch, which is attributed to a decrease in the reciprocal lattice constant.

Finally, we calculate the emission fraction into TIR angles based on the simulated results in Figure 4.5. For the 800 nm pitch array, the TIR emission fraction is 68.5%, which is actually lower than the isotropic reference case of 75%. This suggests that the same design procedure described here could be employed to increase the fraction of light emitted into the escape cone, for example, to increase the yield of LEDs or displays. Emission into TIR angles increases steadily from 68.5% (800 nm) to 75.9%, 81%, and 83.5%, for 1000, 1200, and 1400 nm pitch, respectively. Calculation of the TIR fractions for the measured results is not readily possible because the objective does not collect light emitted beyond the NA, and thus, we do not obtain the emission for grazing angles between ~ 79.4 and 90 degrees. Nevertheless, we can see in Figures 4.5g,h that the experiment and simulation compare very well, many fine features and relative intensity variations are well reproduced, and their logarithmic color scales span about one order of magnitude.

4.6 Conclusions

In conclusion, we have demonstrated anisotropic to enhance light trapping in an LSC waveguide. By embedding CdSe-CdZnS nanoplatelets into an array of TiO_2 nanocylinders, we alter their angular emission profile to increase emission into the angular range of total internal reflection (TIR). First, we optimized the dimensions of a single nanocylinder with an embedded layer of dipole-like emitters to maximize emission into TIR angles of a typical LSC waveguide. Changing the diameter and height of the cylinder alters the multipolar Mie-like modes it sustains, as well as their strength, and the coupling of the emitters with these photonic modes alters their angular emission profile. Subsequently, we designed and fabricated a square lattice of nanocylinders such that emission into lattice modes occurs at angles outside the escape cone. Angle-resolved photoluminescence measurements are in good agreement with simulated emission profiles, corroborating our understanding of the coupling between the emitters and the photonic structures. Finally, we show an increase in light trapping from 75% (isotropic emission) to 83.5%, which could significantly increase LSC conversion efficiencies. This novel approach to directive emission, by embedding emitters in dielectric nanostructures, can pave the way towards enhanced emission control in photovoltaic systems, as well as solid-state lighting and smart displays.

4.7 Methods

FDTD simulations

The angular emission profiles for dipoles embedded in a single TiO₂ nanocylinder were calculated using finite-difference time-domain (FDTD) calculations performed in Lumerical FDTD Solutions [72]. Perfectly Matched Layer (PML) boundary conditions were used in three dimensions. A single, monochromatic electric dipole source was used for each simulation, with a polarization axis along either the X, Y, or Z-axis. A “scat_ff” power monitor box was used to collect the electric and magnetic field components surrounding the nanocylinder. Convergence was found at a uniform mesh size of 5 nm, a distance of 250 nm from the structure to each FDTD box boundary, and conformal mesh refinement. To convert the simulated near fields to far field radiation intensities, we used the far field projection function from Lumerical FDTD Solutions. The complex experimental optical constants of TiO₂ as determined by ellipsometry (see Methods on Ellipsometry) were used.

By keeping a fixed electric dipole amplitude in each simulation, the total emitted power is proportional to the LDOS (and Purcell factor) [68]. Thus, for the two optimized cases in Fig. 4.2, the LDOS enhancement is calculated as the emitted power divided by the emitted power in free space (weighted by incoherent summation over positions and dipole orientations).

RCWA simulations

To simulate the angle-resolved emission intensities, we used the open-source software package S⁴: the Stanford Stratified Structure Solver by Liu and Fan [167]. The rigorous coupled-wave analysis (RCWA) software simulates the propagation of electromagnetic waves through 3D structures with 2D periodicity. Identical to the FDTD simulations, we simulate a TiO₂ nanocylinder, but now in periodic boundary conditions. The real part of the refractive index of TiO₂ is set to $n = 2.32$, according to the measured refractive index at $\lambda = 650$ nm. The extinction coefficient is set to $k = 0.316$ ($\text{Im}(\epsilon) = 0.1$) for the center layer of 30 nm; the rest of the cylinder is considered lossless.

The emission intensity results are obtained by performing the reciprocal simulation: according to the Helmholtz reciprocity principle, absorption of light at a certain position that is incident from the far-field at a certain angle and polarization is reciprocal with emission of light from the same position towards the far-field at the same angle and polarization. In contrast to the FDTD simulations, this allowed us to calculate the absorption at all emitter positions in a single simulation. The simulation was performed for a wide range of combinations of wavelength, polarization, azimuthal angle, and polar angle.

The number of components used in the Fourier series (NG) and the extinction coefficient were tested for convergence – the results are shown in Figure 4.13, showing convergence for NG = 101 and $k = 0.1$. To find convergence, we calculate the angle-resolved emission with S4 for several NG values, $\sigma(i)$, and determine the weighed difference between subsequent results, $\Delta\sigma(i)$ and $\Delta\sigma_N(i)$, according to:

$$\Delta\sigma(i) = \frac{\int(\sigma_i - \sigma_{i-1})^2 dr}{\int(\sigma_i)^2 dr}, \quad \Delta\sigma_N(i) = \frac{\int(\sigma_i - \sigma_N)^2 dr}{\int(\sigma_i)^2 dr} \quad (4.1)$$

where r represents the variable of integration, in this case, the points on the k_x, k_y plane, and N is the most accurate result in the convergence test, in our case NG = 161. The curve for $\Delta\sigma(i)$ indicates the difference between subsequent steps in the convergence test along the variable, while the $\Delta\sigma_N(i)$ curve indicates the difference between a step and the final step.

Electron-beam physical vapor deposition

The Ti_3O_5 precursor was evaporated by electron-beam heating and precipitated onto the substrate. The base pressure of the chamber was 10^{-7} mbar and was raised to 2.5×10^{-5} mbar by flowing O_2 gas into the chamber. The oxygen flow partially determines the final material stoichiometry. The deposition rate was maintained at 2 Å/s.

Spin coating of CdSe-CdZnS core-shell nanoplatelets

CdSe-CdZnS core-shell nanoplatelets with a graded shell [163] were dispersed in a hexane solution with a concentration of 10 mg NPLs per 1 ml hexane. The solution is spin-coated on top of the first TiO_2 layer at 2000 RPM with 500 RPM/s for 60 s, followed by a curing step on a 60 °C hot plate for 10 min.

Electron-beam lithography and reactive ion etching

Ma-N 2403, a negative tone resist, was used as an EBL mask. First, hexamethyldisilazane (HMDS), a resist adhesion promotor, is spin-coated on the sample at 4000 RPM with 1000 RPM/s for 35 s, followed by a curing step on a 150 °C hot plate for 1 min. Then, the undiluted ma-N 2403 solution is spin-coated at 4000 RPM with 1000 RPM/s for 35 s and cured at 90 °C for 4 min. The resulting ma-N mask thickness is 365 nm. When fabricating nanostructures on an insulating substrate like glass, a final layer of Electra 92 is spin-coated to help dissipate the e-beam charge, at 2000 RPM, 400 RPM/s for 40 s. When using a silicon substrate, no additional charge-dissipation layer is necessary.

A Raith Voyager EBL system was used to write the patterns in the mask, operating in 50 keV LC60 mode, write field of 500 μm and dose $\sim 250 \mu\text{C}/\text{cm}^2$.

The mask was then developed in ma-D 525 resist developer for 50 s, rinsed twice in H_2O for 30 s, and blow-dried under a nitrogen gun.

Finally, the sample was etched in a Oxford Instruments Plasmalab 80 Plus reactive ion etcher for 40 minutes. Flowing 50 sccm of CHF_3 and 1 sccm O_2 gases, we used a single TiO_2 etch recipe based on ref. [165] – the NPL layer was also properly etched, without significant over or under etching. The ma-N mask was removed with a 15 min oxygen plasma etch in the same etcher, using a 10 s plasma strike at the start and otherwise 0 W forward power.

Ellipsometry

We used a variable-angle spectroscopic ellipsometer (VASE) from J.A. Woollam Co. to measure the angle- and polarization-dependent reflection spectra of a TiO_2 thin film on a silicon and glass substrate. Using a Cody-Lorentz oscillator in CompleteEASE software, we fitted the complex refractive index of the TiO_2 thin film with a mean squared error (MSE) of 4 (n,k values are plotted in Fig. 4.7). We corroborated the fitted n,k values by measuring reflection and absorption from the TiO_2 thin film, showing excellent agreement with calculated reflection and absorption spectra based on the fitted n,k values (see Fig. 4.8).

Atomic force microscopy

AFM images were obtained with a ScanAsyst-AIR probe (Bruker, nominal tip radius 2 nm), operated in PeakForce Tapping mode using a Bruker Dimension Icon AFM.

Spatial photoluminescence measurements

For the photoluminescence measurements, a WITec alpha300 RS confocal microscopy setup was used in reflection mode with a 100 \times magnification, 0.9 NA, air objective. The NPLs were excited with a 532 nm excitation wavelength continuous-wave laser, 1 mW power, and diffraction-limited ~ 300 nm-diameter spot size. Spectra were collected using the fiber-connected WITec UHTS spectrometer, where the collection by the fiber acts as the confocal pinhole. Given a fiber core of 100 μm in diameter, we calculate a collection spot of 1 μm using $\text{FWHM} = d_{\text{fiber}}/M$, with M the magnification of the objective [75]. Given the 0.9 NA, angles up to ~ 64 degrees are collected.

Angle-resolved photoluminescence measurements

Angle-resolved photoluminescence measurements were conducted in a Fourier microscopy setup, where we illuminated the sample with a 515 nm wavelength pulsed laser, with a repetition rate of 1 MHz and a power of 1.39 mW. The sample is placed facing down in the focus of an inverted microscope immersion oil objective (Plan Apo λ 100 \times NA = 1.45 oil). We illuminate the sample in epi-mode by focusing the pump beam on the back-focal plane (BFP) of the objective to achieve a collinear spot of ~ 40 μm diameter in the sample plane (25 cylinders across for 800 nm pitch; 14 cylinders for 1400 nm pitch). To image angle-resolved photoluminescence from the sample on the detector, we place a lens (Fourier lens) on a flip mount in the focus of the BFP of the objective, via a 1:1 telescope, as is done in ref [168]. We remove the pump from the PL signal with a combination of 514 nm dichroic and 550 nm long-pass filters. Given the refractive index of the glass substrate and immersion oil ($n = 1.475$), we collected angles up to ~ 79.4 degrees.

4.8 Supplementary information

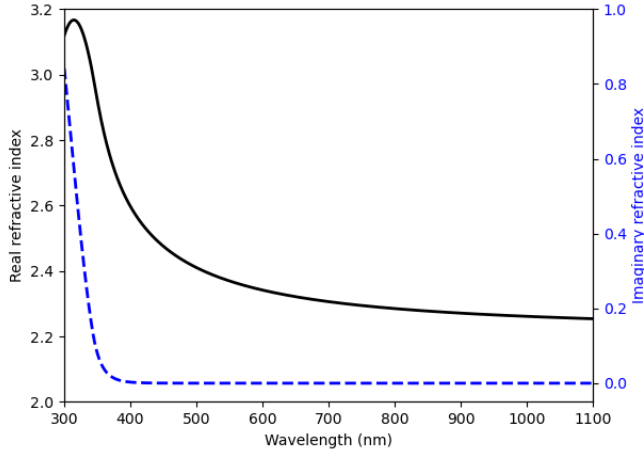


Figure 4.7: Real (black) and imaginary (blue dashed) parts of the refractive index of a TiO_2 thin film as fitted from ellipsometry measurements. A Cody-Lorentz oscillator model was used, yielding a mean squared error (MSE) of 4.

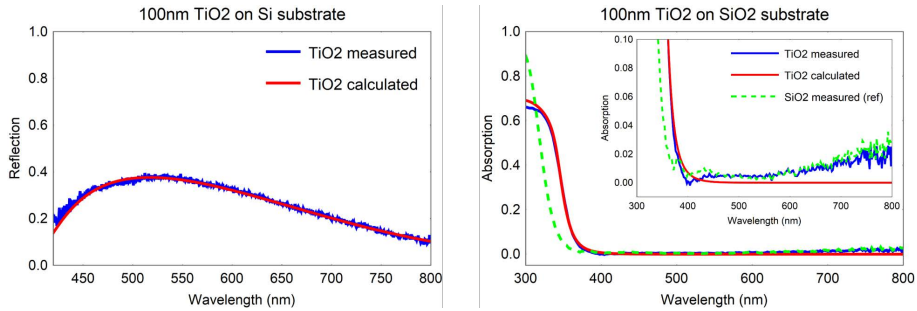


Figure 4.8: Reflection (absorption) from a 100 nm TiO_2 thin film on a silicon (glass) substrate, measured in an integrating sphere setup and calculated using the n, k values obtained from ellipsometry. The excellent agreement corroborates the fitted values. The nonzero absorption for longer wavelengths is attributed to scattering by the glass substrate. The TiO_2 thin film was evaporated with EBPVD on the silicon and glass substrates simultaneously.

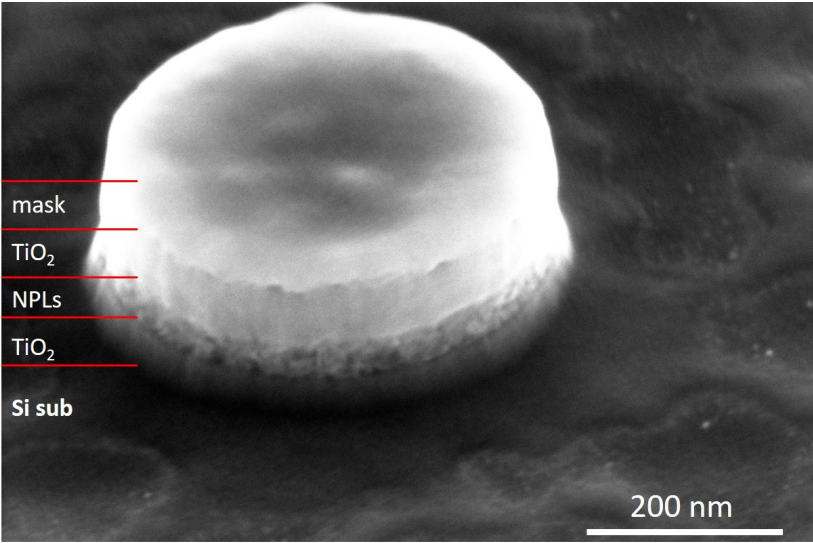


Figure 4.9: Scanning electron microscopy (SEM) image of a TiO₂ nanocylinder with embedded NPLs, fabricated for reference on a silicon substrate. The image is taken under a 45 degree angle. The silicon substrate facilitates charge dissipation in the SEM, enabling us to obtain this high-resolution image, which is typically not possible on an insulating glass substrate. In contrast to the homogeneous TiO₂ layer on top, the NPL layer shows many features on its surface. The ma-N e-beam resist mask is still on top of the cylinder.

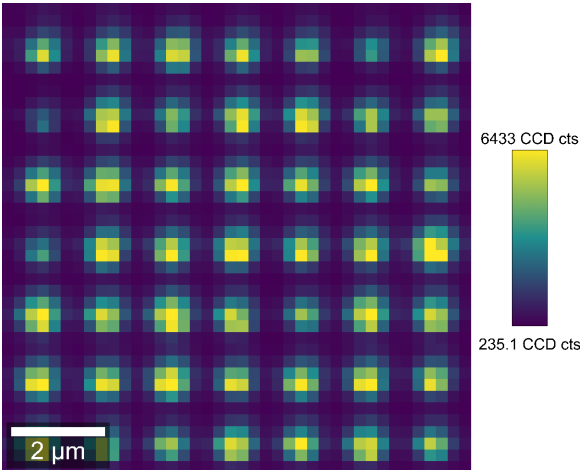


Figure 4.10: Identical to the data presented in Fig. 4b, but without smoothing the data: Photoluminescence intensity map of the marked area in Fig. 4a, indicating emission is confined to the nanocylinders. Color scale depicts the intensity at the target wavelength of 650 nm, in counts per pixel per second, for 1 mW input power of the 532 nm CW laser.

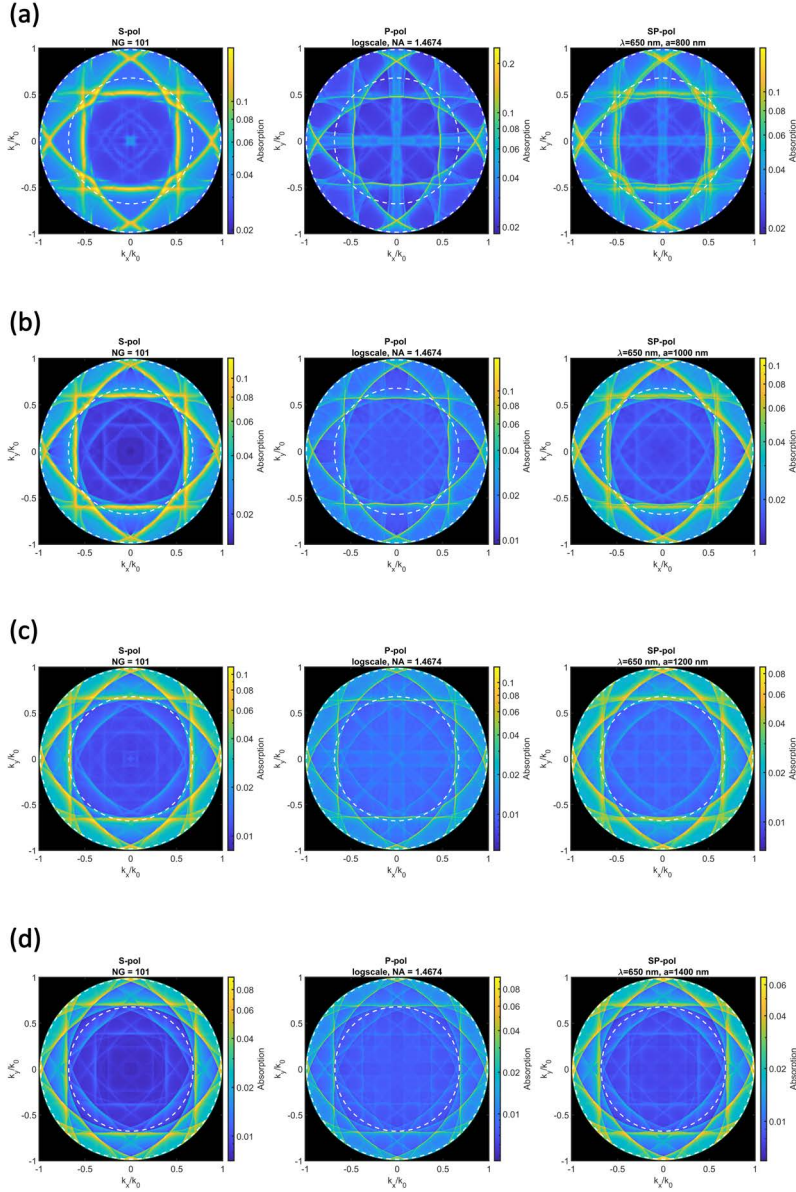


Figure 4.11: Angle-resolved photoluminescence simulated for a (a) 800 nm, (b) 1000 nm, (c) 1200 nm, and (d) 1400 nm pitch array. The left and middle plots on each row correspond to the S and P polarization, whereas the right plot shows the averaged polarization, identical to the simulated plots in Figure 4.5 of the main text. The white dashed lines correspond to $NA = 1$ (critical angle from glass substrate to air) and $NA = 1.45$ (maximum for the objective).

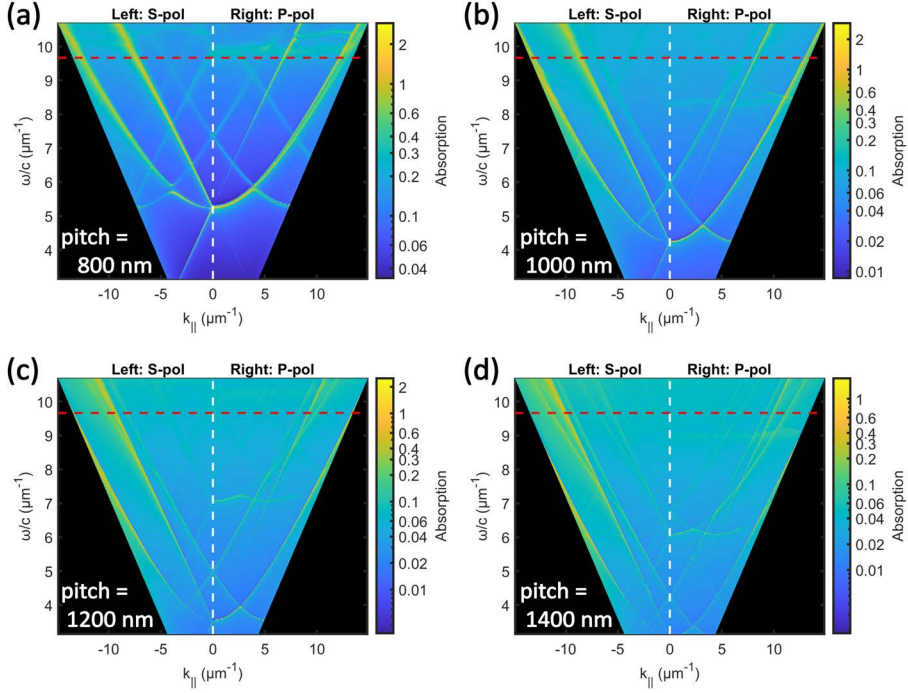


Figure 4.12: Calculated dispersion diagrams for a (a) 800 nm, (b) 1000 nm, (c) 1200 nm, and (d) 1400 nm pitch array. The left and right sides of the graphs show the S and P polarized emission, along the $k_{par} = k_x$ axis and as a function of normalized frequency ($2\pi/\lambda$). The white dashed line indicates the border between the S and P polarized data. The red dashed line indicates the target wavelength of 650 nm, corresponding to a horizontal cut through the plots in Figure 4.11 at $k_y = 0$. As we already observed in Figures 4.5 and 4.11, the photonic crystal bands are displaced outwards with increasing array pitch.

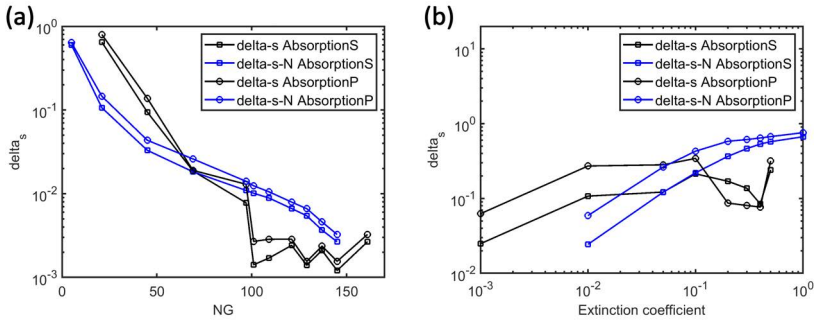


Figure 4.13: S4 calculation convergence testing for (a) the number of Fourier series components (NG) and (b) the extinction coefficient ($\text{Im}(\epsilon)$) of the absorbing center layer. Convergence was found at NG = 101, which is used in the extinction simulations, where convergence was found for $\text{Im}(\epsilon) = 0.1$. See methods for definition of $\Delta\sigma$ (delta-s) and $\Delta\sigma_N$ (delta-s-N).

5

Passive radiative cooling of silicon solar modules with silica microcylinder arrays

Passive radiative cooling (PRC) is a method to dissipate excess heat from a material into or through the earth's atmosphere by the spontaneous emission of infrared (IR) thermal radiation. Photovoltaic systems can benefit from PRC by lowering the system's operating temperature. In particular, for a (silicon) solar cell, the challenge is to enhance PRC while simultaneously retaining transparency for sunlight above the (silicon) bandgap. Here, we propose a hexagonal array of cylinders etched into the top surface of the solar cell module glass to enhance PRC. We use FDTD simulations to optimize the cylinder geometry to enhance the emissivity in the IR spectral range. Multipolar Mie-like resonances in the cylinders are shown to cause anti-reflection effects in the IR, which results in enhanced IR emissivity. Next, the optimized structures are fabricated by UV-lithography and reactive ion etching. Using integrating sphere Fourier transform infrared (FTIR) spectroscopy, we measure the emissivity of the silica cylinder array, and find good correspondence to the simulated results. The fabricated microstructure increases the average emissivity between $\lambda = 7.5 - 16 \mu\text{m}$ from 84.3% to 97.7%, without reducing visible light transmission. Our design procedure offers a PRC structure for any photovoltaic device, with or without module glass encapsulation, and any other outdoor device that benefits from a lower operating temperature.

This chapter is based on:

Passive radiative cooling of silicon solar modules with silica microcylinder arrays

Evelijn Akerboom^{*1}, Tom Veeken^{*1}, Chris Hecker², Jorik van de Groep³, and Albert Polman¹
in preparation

^{*}Evelijn and Tom contributed equally to this work.

¹Center for Nanophotonics, NWO-Institute AMOLF, Science Park 104, 1098 XG Amsterdam, The Netherlands

²Department of Earth Systems Analysis, Faculty of Geo-Information Science and Earth Observation (ITC), University of Twente, Hengelosestraat 99, 7500 AA Enschede, The Netherlands

³Van der Waals-Zeeman Institute, Institute of Physics, University of Amsterdam, Science Park 904, 1098 XH Amsterdam, the Netherlands

Author contributions:

Tom and Albert conceived the project. Evelijn fabricated the microcylinder arrays, and performed the transfer matrix model calculations and the data analysis. Evelijn and Tom performed the FDTD simulations and visible-NIR hemispherical reflection measurements. Evelijn and Chris performed the infrared hemispherical reflection measurements. Tom wrote the original draft. Albert supervised the project. Jorik and Albert reviewed and edited the manuscript. All authors provided feedback and contributed to the manuscript.

5.1 Introduction

Over the past few decades, significant effort has been put into improving the power conversion efficiency of solar cells [15]. The detailed balance limit [12] calculates a fundamental efficiency limit of 29.7% for silicon-based solar cells [169], not far from the current record efficiency of 27.6% [170]. Solar cell efficiency measurements are performed at standardized testing conditions, e.g., 1 sun illumination at an operating temperature of 25 °C. However, due to hot-carrier cooling and non-radiative recombination, a silicon solar cell typically reaches operating temperatures of 60 °C under direct sunlight, and even as high as 80 °C [171]. Elevated operating temperatures reduce the power conversion efficiency and the operating lifetime of the cell. This efficiency reduction is mainly attributed to a decrease in the open-circuit voltage due to increased recombination rates [172]. An average relative efficiency drop of -0.45% has been shown for every 1 °C temperature rise of mono- and poly-crystalline silicon solar modules [173]. A temperature increase from 25 to 60 °C amounts to a significant -15.75% efficiency drop. Even though the effects of elevated operating temperatures on the operating lifetime of a silicon solar module have not been isolated [174], it is expected to negatively impact all degradation modes [175, 176]. These adverse temperature effects emphasize the need for a method to cool Si solar modules. Here, we investigate the enhancement of passive radiative cooling (PRC) to decrease the operating temperature of a Si solar cell. The concept of PRC leverages the thermal emission of an object to dissipate heat to lower its temperature. According to thermodynamics, two objects with different temperatures will exchange heat via thermal radiation until an equilibrium temperature is reached. The Stefan-Boltzmann law states that the amount of heat emitted as thermal radiation scales with the temperature of an object as $\propto T^4$, so effectively, heat is transferred from the warmer object to the colder object. Thus, to cool a hot object with thermal emission, a colder object is needed to function as the heat sink. Outer space is the perfect heat sink due to the temperature of about 3 K and the immense volume, which makes it a heat sink with practically infinite capacity. The concept of emitting thermal radiation into outer space is the core principle of PRC.

During the last two decades, interest in PRC has grown for several applications [177], from dew collection in remote and dry places [178] to the cooling of buildings [179]. In 2014, Raman et al. showed a 4.9 °C sub-ambient daytime cooling using a thin-film multilayer to optimize the radiative properties of the structure [180]. The multilayer was designed to enhance PRC while simultaneously excluding heating by reflecting incident solar radiation. However, the high reflectance of this geometry in the visible spectral range makes it particularly unsuitable for solar cells applications. A solar cell absorbs light with photon energy larger than the bandgap energy, including visible wavelengths.

Over the past years, several different materials and methods have been explored to cool solar cells with PRC: multilayers [181, 182], 2D structures [183–188], a combination of a multilayer and 2D structures [189, 190], or an effective medium approach [191–193]. Table 5.1 lists the calculated (*italic*) or fabricated (**bold**) material systems of a few notable works, and their reported temperature reduction: calculated values are in *italic*, measured values in **bold** font. To enable comparison of the achieved temperature reductions, it is important to specify the reference material system. This is particularly important since bare silicon exhibits practically no PRC while a standard glass cover achieves significant PRC. Jaramillo-Fernandez et al. demonstrated the largest temperature reduction, both with respect to a bare silicon substrate and silicon covered with silica glass [184]. They placed a self-assembled monolayer of silica spheres on top of the silicon and silicon-silica reference samples and measured an average temperature reduction of 14 and 9 °C, respectively. Although the layer of spheres performs well, it may suffer from structural degradation in outdoor conditions.

Here, we propose resonant microstructures to enhance the PRC of a silicon solar module by etching them into the module glass. The design enhances the cooling power while keeping the structure transparent in the visible and near-infrared wavelength range. First, we theoretically derive a general condition for the ideal optical properties to achieve maximum PRC in a silicon solar module. Then, we use numerical finite-difference time-domain (FDTD) simulations to design a microcylinder array on top of a quartz silica module glass to enhance PRC compared to the flat silica reference. We fabricate the optimized design by UV photolithography and reactive ion etching. Hemispherical reflection measurements in the IR are performed to obtain the experimental emissivity spectra, which correspond very well to the simulated results. The average emissivity between $\lambda = 7.5 - 16 \mu\text{m}$ is increased from 84.3% (silica reference) to 97.7%, which results in a calculated reduction of 3 K in the equilibrium temperature. Finally, we show that the silica substrate with a microcylinder array remains transparent in the visible and near-infrared (NIR) wavelength ranges.

Table 5.1: *Advances of passive radiative cooling for solar cells. The PRC structure, the reference sample, and the calculated (italic) or measured (bold) temperature reduction are listed.*

First Author (year) [reference]	Passive radiative cooling structure	Reference sample	Temperature reduction (K)
Zahir (2021) [182]	Multilayer: <i>TiO₂/BK7</i>	Si solar cell Si + SiO ₂	<i>18.4</i> <i>5.4</i>
Perrakis (2021) [183]	<i>2D structure: SiO₂ square micro grating with nanopillars on top</i>	Si Si + SiO ₂	<i>5.8</i> <i>0.2</i>
Jaramillo-Fernandez (2019) [184]	<i>2D structure: self-assembly of SiO₂ spheres</i>	Si Si + SiO ₂	14 9
Long (2019) [185]	<i>2D structure: SiO₂ square lattice of micro-cylinders</i>	Si Si + SiO ₂	<i>20</i> 2
Zhu (2015) [188]	<i>2D structure: lattice of air holes in SiO₂</i>	Si Si + SiO ₂	13 1
Zhao (2018) [190]	Multilayer+2D structure: <i>TiO₂/SiO₂ with a lattice of air cylinders</i>	Si solar cell Si + SiO ₂	<i>12</i> <i>8.3</i>
Chen (2021) [192]	<i>Effective medium: polymer matrix with embedded SiO₂ nanoparticles</i>	Si solar cell	5
Akerboom (2022) [this work]	<i>2D structure: SiO₂ microcylinder array</i>	Si Si + SiO ₂	<i>21</i> <i>3</i>

5.2 Passive radiative cooling

The concept of passive radiative cooling (PRC) is based on the thermal balance of a solar cell. In Figure 5.1a, a schematic representation of the energy balance of a solar cell is shown, indicating the four main power terms that determine the equilibrium temperature of the cell: the absorbed radiation coming from the sun (P_{sun}), the absorbed thermal radiation from the atmosphere (P_{atm}), the thermal radiation the solar cell is emitting (P_{rad}), and the power lost or gained by convection (P_{conv}). Here we assume that heat conduction via connection to the rooftop is negligible. The total cooling power is given by the sum of the four main powers,

$$P_{\text{cool}} = P_{\text{rad}} + P_{\text{sun}} + P_{\text{atm}} + P_{\text{conv}}. \quad (5.1)$$

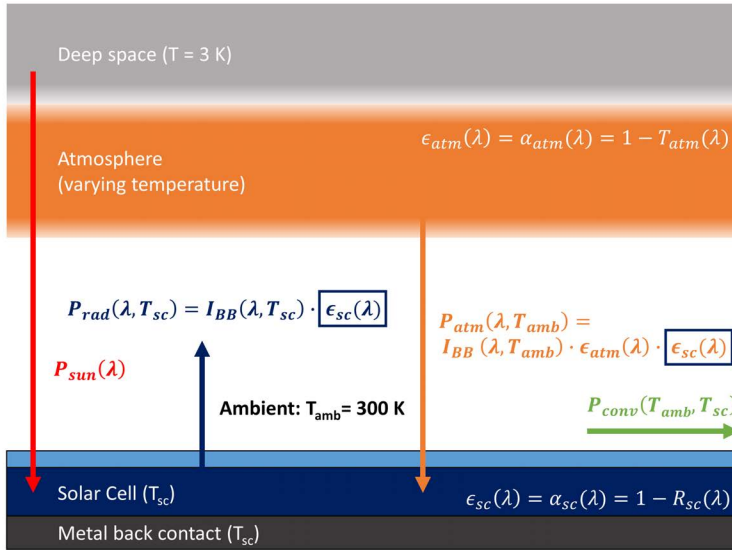


Figure 5.1: Schematic representation of the incoming and outgoing power flows that govern the equilibrium temperature of a solar cell (T_{sc}). The solar cell reaches its equilibrium temperature when the power from the sun (P_{sun}) and the thermal radiation from the atmosphere (P_{atm}) are in balance with the thermal radiation emitted by the solar cell (P_{rad}) and the power flow by convection and conduction (P_{conv}).

When the total cooling power is zero, there is no net heat flux, and the solar cell has reached equilibrium temperature. A positive cooling power will effectively reduce the temperature, while a negative cooling power indicates the solar cell is heating up. Figure 5.1 shows a schematic representation of the power flows in Eq. (5.1) — a detailed analysis of the interplay is provided in the Methods section. For a constant incident solar power (P_{sun}) (Fig. 5.2a) and (P_{conv}), we find that the cooling power depends on:

$$P_{\text{cool}}(T_{\text{sc}}, T_{\text{amb}}) \propto \int (I_{\text{BB}}(\lambda, T_{\text{sc}}) - I_{\text{BB}}(\lambda, T_{\text{amb}}) \epsilon_{\text{atm}}(\lambda)) \epsilon_{\text{sc}}(\lambda) d\lambda. \quad (5.2)$$

Here, T_{sc} and T_{amb} are the temperatures of the solar cell and ambient, respectively, I_{BB} is the intensity of the blackbody spectrum, ϵ_{atm} is the emissivity of the atmosphere, and ϵ_{sc} the emissivity of the solar cell.

Figure 5.2b shows the ideal blackbody spectra at ambient temperature (300 K) and a typical solar cell operating temperature (340 K). The spectrum of a non-ideal blackbody is obtained by multiplying the ideal spectrum by the emissivity. By photonic engineering of the emissivity, we can explore the effect of an emissivity spectrum on the resulting equilibrium temperature. First, we consider the upper temperature bound of zero emissivity for energies above the solar cell bandgap, plotted in Fig. 5.2c in red. Calculating the cooling power with Eq. (5.1), we obtain the red curve in Fig. 5.2d and an equilibrium temperature of 366.5 K. Second, we consider an emissivity window that is unity only in the main atmospheric transmission window between 8 - 14 μm , as shown in Fig. 5.2c in green. This is the ideal emissivity spectrum for a solar reflector, enabling it to cool below ambient temperature by radiating through the atmosphere while keeping heat from the sun and atmosphere out. However, when used for a solar absorber material like a silicon solar cell, the resulting PRC is sub-optimal with an equilibrium temperature of 341.5 K, as shown in Fig. 5.2d in green. Third, we consider a solar absorber at a temperature higher than ambient. Due to this higher temperature, it emits more blackbody radiation than it receives from the atmosphere — see the intensity difference plotted in Fig. 5.2b. Therefore, a solar absorber can achieve higher PRC by setting its emissivity to 1 throughout its entire blackbody radiation spectrum, from 3 - 30 μm , as plotted in blue in Fig. 5.2c. Below 3 μm , the blackbody radiation at 340 K is negligible; thus, we set the emissivity to 0 between the silicon bandgap and 3 μm . This emissivity spectrum achieves the minimum equilibrium temperature at 330.5 K. We color the background of Fig. 5.2d purple to indicate the attainable equilibrium temperatures to be used as a reference for the final results. In the next section, we look at the PRC of a silicon solar cell stack and improve the PRC with a photonic cylinder array.

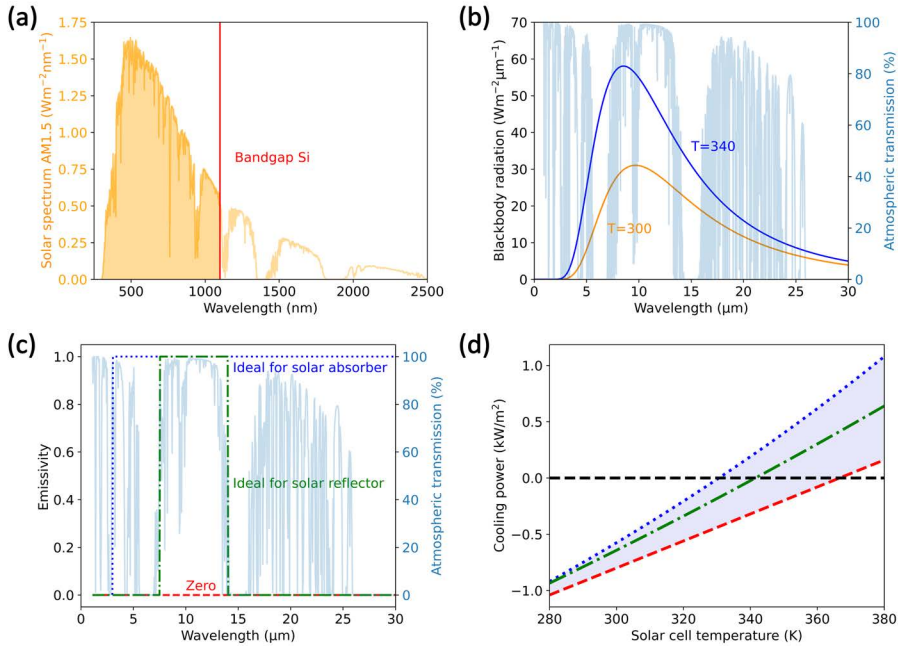


Figure 5.2: (a) AM1.5G solar irradiation spectrum (yellow line) as a function of wavelength, the bandgap of silicon (red line), and the part of the solar spectrum that can be absorbed by silicon (yellow surface). (b) Blackbody radiation spectra for an object at 300 K (orange) and 340 K (blue), and the atmospheric transmission (light blue). (c) Step function of three emissivity spectra: zero emissivity (red), a non-zero emissivity only in the main atmospheric transmission window (green), and the ideal emissivity for a body at 340 K (blue). (d) The calculated cooling power versus solar cell temperature (Eq. (5.1)), corresponding to the emissivity spectra in (c). The equilibrium temperature is reached when the cooling power is zero.

5.3 Photonic design

In the previous section, we have derived a condition for the ideal emissivity of a solar cell: unity emissivity for wavelengths larger than $3\text{ }\mu\text{m}$. The silicon solar cell itself has zero absorptivity (extinction coefficient) throughout the IR wavelength range (see Fig. 5.6 in the Methods section), and thus zero emissivity (the reciprocity between absorptivity and emissivity according to Kirchoff's law is described in the Methods section). Therefore, we need to add a material to the solar cell to improve its PRC capacity, which is in thermal equilibrium with the solar cell. A typical solar module has a glass cover on top of the silicon, making it an obvious choice. Figure 5.6 also shows the absorptivity of quartz silica (SiO_2), borosilicate glass, and soda-lime glass (SLG). Beyond $7.5\text{ }\mu\text{m}$, their extinction coefficient is non-zero, making them much more suitable materials for PRC than silicon.

We use a transfer matrix model (TMM, see Methods for details) to calculate the reflectivity of a solar module geometry consisting of a silicon substrate with a gold coating on the backside (solar cell back contact) and a quartz silica substrate on the top. The gold coating eliminates any transmission of light through this stack, and thus we can compute the emissivity as $1-R_{\text{sc}}$, as shown in Fig. 5.3a in red. The emissivity of the silica-on-silicon stack is much higher than the reference without silica, which is only slightly above zero due to parasitic absorption in the Au back coating (Fig. 5.3a in green). The dip in the emissivity spectrum of the silica-on-silicon stack at $9\text{ }\mu\text{m}$ wavelength is caused by enhanced reflection at the air-silica interface. The enhanced reflection is a direct consequence of the strong fluctuation of the complex optical constants of silica in this spectral range, which is attributed to the asymmetric stretching vibration of Si-O-Si bridges [194]. Even though we defined the ideal emissivity as unity until $\lambda = 30\text{ }\mu\text{m}$ in the previous section, we carried out simulations until $\lambda = 16\text{ }\mu\text{m}$ because this was the range of the experimental emissivity data.

In Table 5.1, we have already seen that significant calculated and measured temperature reductions have been achieved with 2D structures for enhanced PRC. However, only Zhu et al. made use of the solar cell module glass for their experimental PRC results, which would be ideal for practical reasons. They enhanced PRC by etching deep hollow cylinders, improving anti-reflection due to the gradual refractive index change [188]. While this does enhance PRC, this approach does not include optimization for specific wavelengths. Therefore, we propose direct integration of a thinner 2D microstructure in the module glass, which we can optimize thoroughly. The microstructures should minimize the reflection between 7.5 and $16\text{ }\mu\text{m}$ wavelength (to minimize the dip in the red curve in Fig. 5.3a) and simultaneously retain transparency for sunlight with photon energies above the silicon bandgap. To achieve anti-reflection, we design a hexagonal array of silica microcylinders on the silica substrate. These structures exhibit Mie-like resonances when their size is on the order of the wavelength [164]. These types of resonant structures have received much attention in the field of nanophotonics [195, 196]. For photovoltaics, in particular, Mie-like resonant structures have been used to enhance light trapping [197], design solar cells with structural colors [36], and achieve anti-reflection for incident sunlight [24, 26]. Here, we design cylinders of several micrometers in size to achieve resonant anti-reflection for IR instead light. We use finite-difference time-domain (FDTD) simulations to optimize the dimensions of the hexagonal cylinder array (see Methods for technical details). We varied the cylinder diameter, height, and array pitch to minimize the reflection in the $4 - 16\text{ }\mu\text{m}$ wavelength range, finding the optimum for a diameter of $3.5\text{ }\mu\text{m}$, a height of $2.25\text{ }\mu\text{m}$, and a $6.125\text{ }\mu\text{m}$ pitch in a hexagonal array. The calculated emissivity is plotted in Fig. 5.3a in blue, showing a significant increase compared to flat silica.

To gain an understanding of the resonant anti-reflection effect of the microcylinder array, we analyze the modal scattering contribution to the reflection spectrum. We attribute

the anti-reflection effect to forward scattering of incident light by the multipolar Mie-like modes in the cylinders. According to the (generalized) Kerker condition, forward scattering is typically achieved by the interference of at least two different Mie-like modes according to the (generalized) Kerker condition [198, 199]. Figure 5.3b shows the contributions of several Mie-like modes to the extinction cross-section of a single microcylinder, decomposed using the method outlined by Evlyukhin et al. [71]. The decomposition shows that the main broad contribution comes from the electric and toroidal dipoles (ED+TD). The magnetic dipole (MD) and electric quadrupole (EQ) contributions are slightly detuned from each other. When we consider the coherent excitation of these multipolar modes by a normal-incident plane wave, the modes oscillate in phase with each other. The symmetry of the modes leads to constructive interference between the ED and MD/EQ in the forward direction (transmission) and destructive interference in the backward direction (reflection). A ‘pure’ Kerker condition of zero backscattering is achieved when the amplitude between the ED and MD/EQ are equal — this condition is typically only met for distinct wavelengths. Here, we achieve enhanced forward scattering by imperfect destructive interference of the ED and MD+EQ over a broad wavelength range. Further improving the destructive interference due to a better balance of the mode’s amplitudes might be possible by changing the shape of the resonator. However, deviating from a radially symmetric shape also yields a polarization-dependent response. Moreover, destructive interference due to the interaction of multiple resonators or lattice modes is challenging with thermal sources [200], as we discuss next.

In general, interference between modes such as the Mie-like modes discussed above relies on a coherent phase-relation between them. However, the thermal emission that we consider as the source has only limited spatial coherence, typically on the order of $\lambda/2$ [201]. Between 8 - 16 μm wavelength, the coherence length would be 4 - 8 μm , which is larger than the size of the designed cylinder. That suggests that single-particle resonances such as the Mie-like modes, and their interference within the same particle, can be excited by thermal emission.

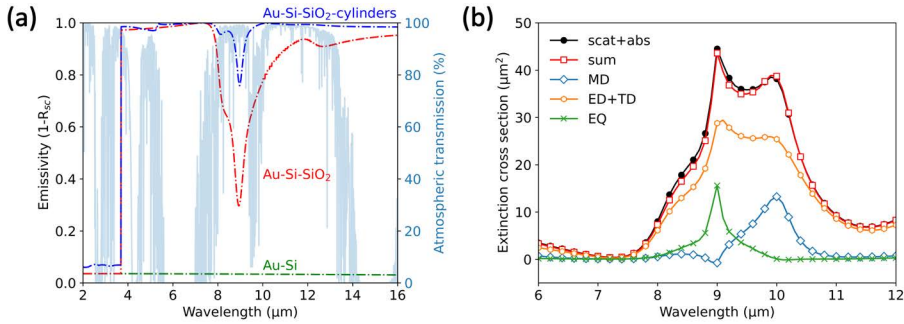


Figure 5.3: (a) Calculated emissivity of a stack of double-side polished silicon coated with gold (Au-Si), with a silica layer on top (red) and a silica layer (blue) with the optimized geometry of silica cylinders (radius of 1.75 μm , height of 2.25 μm and a pitch of 6.125 μm). Atmospheric transmittance is shown in light blue. The patterned module glass reduces and narrows the emissivity dip of glass at 9 μm , improving the radiative cooling of the stack. (b) Multipole decomposition for a silica cylinder (radius 1.75 μm , height 2.25 μm), where the contribution of several resonances to the total extinction cross-section is shown. The silica cylinder exhibits a broadband electric- (ED) and toroidal dipole (TD), in combination with a narrower magnetic dipole (MD) and electric quadrupole (EQ).

5.4 Fabrication

Based on the theory and simulations of the previous section, we fabricate the hexagonal microcylinder array on top of a silica substrate. A double-side polished (DSP) silicon wafer with a gold coating on the back (see Methods) is placed under the silica to replicate a simple solar absorber (see Fig. 5.4a). We used UV photolithography and subsequent reactive ion etching to realize the microcylinder array on top of a silica substrate (see Methods for details). An optical micrograph of the finalized array covering a $24 \times 24 \text{ mm}^2$ silica substrate is shown in Fig. 5.4b, showing a uniform cylinder array and homogeneous color. Figure 5.4c shows a scanning electron microscope (SEM) image of a crosscut of the microcylinders, from which we determine a diameter of $3.65 \text{ }\mu\text{m}$ and height of $2.20 \text{ }\mu\text{m}$, almost identical to the target dimensions of $3.50 \text{ }\mu\text{m}$ (+4%) and $2.25 \text{ }\mu\text{m}$ (-2.5%), respectively. The pitch is precisely $6.125 \text{ }\mu\text{m}$ as designed. High transparency of the sample for visible light is visually demonstrated in Fig. 5.4d, which shows a photograph of the sample on top of the AMOLF logo.

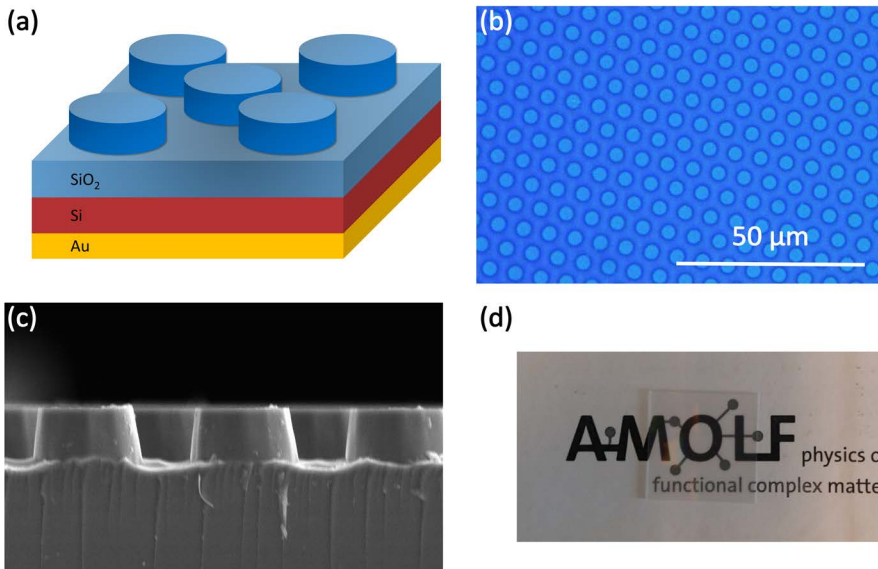


Figure 5.4: (a) Schematic representation of the hexagonal silica microcylinder array on top of a solar module stack. (b) Optical microscopy image of the array. (c) An SEM image of a crosscut of the fabricated microcylinders, revealing straight and slightly slanted sidewalls. (d) Photograph of the microcylinder array sample ($24 \times 24 \text{ mm}^2$) on top of the AMOLF logo, showing high transparency in the visible spectral range.

5.5 Hemispherical reflection measurements

To characterize the IR emissivity of the fabricated microcylinder array sample, we measure the hemispherical reflectance in a Fourier-transform infrared (FTIR) spectrometer (see Methods). Figure 5.5a shows the calculated emissivity spectra (dashed, shown before in Fig. 5.3a) and the experimentally obtained spectra (solid). The reference case of a bare double-side polished silicon substrate with a gold coating on the back is plotted in green. The calculated spectrum is almost zero ($\sim 3.5\%$) because the extinction coefficient of Si is zero beyond $\lambda = 1150$ nm. However, the measured emissivity is significantly higher beyond $\lambda = 9$ μm , which we attribute to intraband transitions in the slight n-type doped silicon substrate [202]. This small discrepancy does not influence our subsequent results because any IR light transmitted into the silica substrate is already absorbed before reaching the silicon substrate underneath. Thus, we can model the silicon to be non-absorptive in the IR.

The measured emissivity of a flat silica substrate on top of a silicon substrate is shown in Fig. 5.5a in red. An air gap between the silica and silicon substrates was avoided by adding a layer of immersion oil in between for the optical measurements. Beyond $\lambda = 5$ μm , the experimental emissivity is almost identical to the calculated spectrum. This result validates the experimental setup and the optical constants of silica that were used in the calculation. Moreover, this also validates that the thermal light source has the required coherence to excite the designed resonant modes: while we do not measure blackbody radiation, the excitation source is a thermal Globar source. The discrepancy between the calculated and experimental spectra in the range of 2 - 5 μm is attributed to a slight mismatch between the optical constants used for the calculation and the actual optical constants of the silica substrate. The absorption onset is quite abrupt for the literature values, just below 4 μm , while the actual values seem to gradually increase between 2 - 5 μm and exhibit more spectral features.

The measured emissivity of the silica substrate with the microcylinder array on top also resembles very well the calculated spectrum, as shown in Fig. 5.5a in blue. Over a broad range from 7.5 to 16 μm , a significant increase in the emissivity was found, precisely as designed. The dip in the emissivity spectrum at 9 μm wavelength is reduced from 30% to 70%. Moreover, the average emissivity between 7.5 and 16 μm is increased from 84.3% to 97.7%.

Based on the experimental emissivity spectra, we now calculate the total cooling power as a function of operating temperature. Figure 5.5b shows three cooling power curves corresponding to the measurements in Fig. 5.5a. The purple-colored background indicates the theoretical area between the upper and lower temperature bounds, as calculated in Fig. 5.2d. At zero cooling power, we find the equilibrium temperature. As expected, we find that the silicon substrate with only the gold coating performs very poorly with an equilibrium temperature of 360 K, close to the maximum of 366.5 K. The addition of the flat silica substrate moves the curve closer to the minimum equilibrium temperature. The optimized silica microcylinder substrate pushes the equilibrium temperature even further towards the theoretical minimum. The flat silica stack and microcylinder silica stack reach equilibrium temperatures of 339 and 336 K, respectively, close to the minimum of 330.5 K. Interestingly, the flat silica substrate already achieves high PRC performance due to its near-ideal optical constants, realizing a cooling potential of 21 K compared to the bare silicon reference. The microcylinders decrease the equilibrium temperature by another 3 K. Assuming a 0.45% increase in efficiency per degree cooling, this temperature reduction would result in a relative efficiency increase of 1.35 – 10.8%, depending on the PRC capability of the reference module cover. These values overestimate the equilibrium temperatures because they are based on experimental emissivity data up to $\lambda = 16$ μm (Fig. 5.5a). In contrast, the theoretical maximum is based on unity emissivity until $\lambda = 30$ μm (Fig. 5.2c).

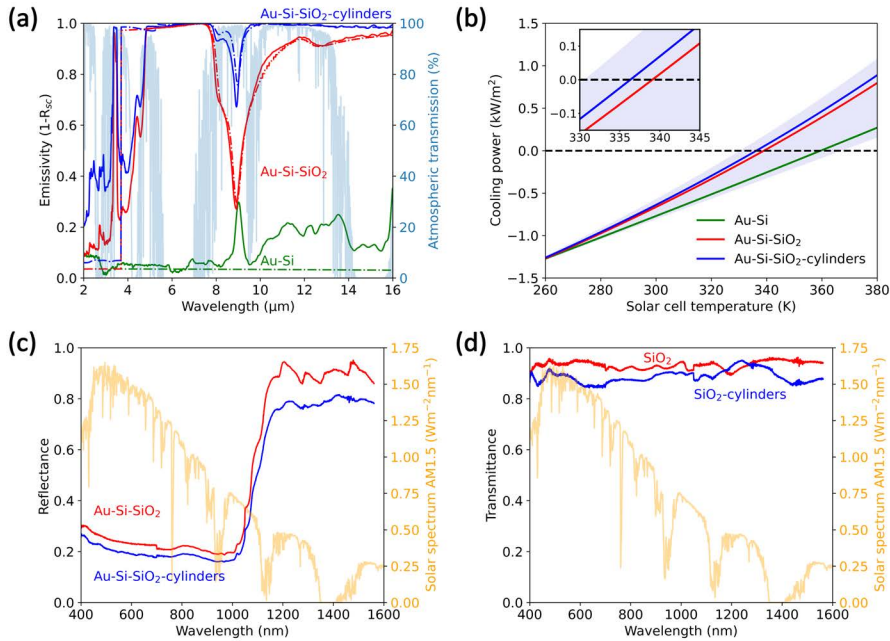


Figure 5.5: (a) Measured (solid) and calculated (dashed) IR emissivity of silicon without module glass (green), with flat silica module glass (red), and with microcylinder module glass (blue). The microcylinder array significantly increases the emissivity in the main atmospheric transmission window (light blue, 7.5 - 14 μm). (b) Calculated cooling power versus solar cell operating temperature corresponding to the measured emissivity in (a). The purple-colored background indicates the theoretical bounds as calculated in Fig. 3b. The inset shows a zoom-in of the calculated equilibrium temperatures (zero cooling power) for comparison with the theoretical minimum equilibrium temperature. (c) Measured visible to near-infrared hemispherical reflectance of silicon with flat silica module glass (red) and microcylinder module glass (blue). (d) Measured visible to near-infrared hemispherical transmittance of the flat silica module glass (red) and microcylinder module glass (blue). The results in (c,d) show that the silica substrate remains transparent for wavelengths smaller than the silicon bandgap after adding the microcylinder array on top and even slightly improves absorption in the silicon substrate due to light trapping.

The calculated equilibrium temperature corresponds well with the range of values listed in Table 5.1. An exact comparison of the reported temperature reductions is not possible because the calculation methods are not identical: the exact wavelength span and the optical constants vary. However, the results do show that choosing a proper module cover impacts the equilibrium temperature significantly. This is important for flat pane (silicon) solar cells, as discussed here, and concerns the development of flexible thin-film solar cells that use thin plastic module covers.

Finally, we perform hemispherical reflectance and transmittance measurements in the visible to near-infrared (NIR) spectral range to verify that the fabricated microcylinder arrays do not adversely affect the transmission of sunlight into the solar cell for energies above

the Si bandgap. Figure 5.5c shows the experimental reflectance for the two silicon-silica stacks. The reflectance is around 20% up to the silicon bandgap, mostly due to reflection at the silica-silicon interface. Beyond 1100 nm, the reflectance is higher because the gold coating at the back reflects most NIR light. This is significantly higher than the reflection of commercial solar modules, which achieve only a few percent reflection due to anti-reflection coatings and/or textures. The comparison in Fig. 5.5c shows that the microcylinders slightly decrease the reflection of light for wavelengths smaller than the silicon bandgap. We attribute this to the trapping of light that is scattered by the array into the Si. Figure 5.5d shows the experimental transmittance for the same two silica substrates without the silicon substrate. The flat silica substrate shows transmission of about 90%, typical of transmission through two silica-air interfaces. The microcylinder array shows slightly lower transmittance than the flat silica substrate over almost the entire wavelength range. This difference is again explained by light trapping: light is scattered by the microcylinders and trapped in the silica substrate by total internal reflection, reducing the transmission. When the silicon substrate is placed in contact, this scattered light does not undergo total internal reflection but instead transmits into the silicon, adding to the absorption and thus a lower reflection, as seen in Fig. 5.5c.

5.6 Conclusions

This work shows that the passive radiative cooling (PRC) power of a silicon solar module can be enhanced by placing an array of microcylinders on top of the module glass. Photonic Mie-like resonances in the silica cylinders reduce infrared (IR) light reflection at the silica-air interface through engineered destructive interference of the resonant multipolar modes. By reciprocity, this improved anti-reflection effect increases the IR emissivity of the silica module glass. First, we studied the optimal emissivity profile for a typical silicon solar module that operates at elevated temperatures. By examining the thermal balance of a solar cell at $T = 340$ K, we found quartz silica to be the ideal module glass material due to its broad extinction coefficient in the $\lambda = 3 - 30$ μm spectral range. Subsequently, we designed a microcylinder array etched into the silica and optimized the dimensions for enhanced emissivity with FDTD simulations. The cylinder array is optimized to reduce the emissivity dip around $\lambda = 9$ μm that is caused by strong reflection at the silica-air interface.

Next, the microstructures were fabricated by UV photolithography and reactive ion etching into a silica substrate. To mimic a silicon solar module, we placed the microstructured silica substrate on a silicon substrate with a gold coating on the back. This stack has zero transmittance throughout the visible and IR wavelength ranges. The measured hemispherical IR reflectance compares very well to the simulated results, demonstrating the designed PRC enhancement. The fabricated microstructure increased the average emissivity between $\lambda = 7.5 - 16$ μm from 84.3% to 97.7%. Moreover, the microstructured silica substrate shows a slight increase in the transmittance in the spectral range where the Si solar cell absorbs. In conclusion, the flat silica substrate already achieves high PRC due to its near-ideal optical constants, realizing a cooling potential of 21 K compared to the bare silicon reference. The microcylinders decrease the equilibrium temperature by another 3 K. Assuming a 0.45% increase in efficiency per degree cooling, this would result in a relative efficiency increase of 1.35 – 10.8%, depending on the PRC capability of the reference module cover. This insight is also relevant for the development of light weight photovoltaics that do not use a glass cover.

These results highlight the opportunities of thermal management for photovoltaic applications by considering the module glass as an integral part of the photonic design. Our design concepts are general and applicable to all solar cell designs as well as module glass materials.

5.7 Methods

Passive radiative cooling calculation

In Figure 5.1, a schematic representation of the energy balance of a solar cell is shown, indicating the four main power terms that determine the cooling power of the cell:

$$P_{cool} = P_{rad} + P_{sun} + P_{atm} + P_{conv}. \quad (5.3)$$

Here, P_{sun} is the absorbed radiation coming from the sun, P_{atm} the absorbed thermal radiation from the atmosphere, P_{rad} the thermal radiation the solar cell is emitting, and P_{conv} the power lost or gained by convection. We assume that heat conduction via connection to the rooftop is negligible. The primary energy input is the irradiation from the sun, which is for normal incidence given by:

$$P_{sun} = - \int I_{AM1.5G}(\lambda) \alpha_{sc}(\lambda) d\lambda, \quad (5.4)$$

with $I_{AM1.5G}$ the solar irradiation within AM1.5G [11] and $\alpha(\lambda)$ the absorptivity of the solar cell. In Figure 5.2a, the AM1.5G solar spectrum is shown, and the silicon bandgap energy is indicated. The AM1.5G solar spectrum has an integrated power of 1000 Wm^{-2} , but silicon does not absorb light with energies below its bandgap. Therefore, for further calculations, P_{sun} is set to 808 Wm^{-2} , which is the integrated power in the AM1.5G solar spectrum for energies above the silicon bandgap (the yellow surface in Fig. 5.2a). The power input from the sun is completely independent of the infrared emissivity that is tuned to improve PRC. Therefore, this factor influences the absolute equilibrium temperatures but not the slope of the temperature curves in Figures 5.2d and 5.5b, nor the distance between different curves. For this comparative study, the precise value of P_{sun} is thus unimportant. This also allows us to neglect the fact that a solar cell converts about 20% of the incoming solar power into electricity rather than heat.

Secondly, heat can be exchanged between the solar cell and its environment through convection, given by the product of the non-radiative heat transfer coefficient (h_c) and the temperature difference between the solar cell and the ambient environment:

$$P_{conv}(T_{sc}, T_{amb}) = h_c (T_{sc} - T_{amb}). \quad (5.5)$$

We set the non-radiative heat transfer coefficient to $6 \text{ Wm}^{-2}\text{K}^{-1}$, corresponding to a wind speed of 1 m/s [187].

The solar cell radiates as a non-ideal blackbody, so its emitted radiative power is given by:

$$P_{rad}(T_{sc}) = \int I_{BB}(\lambda, T_{sc}) \epsilon_{sc}(\lambda) d\lambda, \quad (5.6)$$

which is the product of the emissivity of the solar cell ($\epsilon_{sc}(\lambda)$), a number between zero and one that determines the quality of the solar cell as a blackbody, and the black body radiation according to Planck's law [203]:

$$I_{BB}(\lambda, T) = \frac{2hc^2}{\lambda^5} \frac{1}{e^{\frac{hc}{\lambda kT}} - 1}. \quad (5.7)$$

The atmosphere also radiates as a non-ideal blackbody. The radiative power from the atmosphere that is absorbed by the solar cell is given by:

$$P_{atm}(T_{amb}) = - \int I_{BB}(\lambda, T_{amb}) \epsilon_{atm}(\lambda) \alpha_{sc}(\lambda) d\lambda, \quad (5.8)$$

which is the product of the blackbody radiation from the atmosphere, the emissivity of the atmosphere ($\epsilon_{atm}(\lambda)$), and the solar cell absorptivity ($\alpha_{sc}(\lambda)$). The blackbody spectrum of the atmosphere depends on the ambient temperature, T_{amb} , just as the blackbody spectrum of the sun depends on the temperature of its surface.

Then we use Kirchhoff's law for a body in thermal equilibrium, which states that the emissivity equals the absorptivity at every wavelength:

$$\epsilon(\lambda) = \alpha(\lambda). \quad (5.9)$$

Substituting the absorptivity for the emissivity in Eq. (5.8), we find that the cooling power depends on the balance between incoming radiation from the atmosphere and the outgoing blackbody radiation from the cell:

$$P_{cool}(T_{sc}, T_{amb}) \propto \int (I_{BB}(\lambda, T_{sc}) - I_{BB}(\lambda, T_{amb})\epsilon_{atm}(\lambda))\epsilon_{sc}(\lambda)d\lambda. \quad (5.10)$$

Here, the emissivity of the atmosphere at normal incidence [187] is given by:

$$\epsilon_{atm}(\lambda) = 1 - T_{atm}(\lambda), \quad (5.11)$$

where $T_{atm}(\lambda)$ is the atmospheric transmittance [204, 205].

Both terms in Eq. (5.10) depend on the emissivity spectrum of the solar cell, $\epsilon_{sc}(\lambda)$, which is the most important parameter to tune to achieve PRC. The integrand in Eq. (5.10) scales linearly with $\epsilon_{sc}(\lambda)$, so the radiative cooling power can readily be optimized by calculating the integrand for each wavelength λ_i , at a given solar cell and ambient temperature. If the integrand is positive, i.e., at λ_i the solar cell emits more radiation than it receives from the atmosphere, the ideal emissivity $\epsilon_{sc}(\lambda_i) = 1$:

$$\begin{aligned} I_{BB}(\lambda_i, T_{sc}) - I_{BB}(\lambda_i, T_{amb})\epsilon_{atm}(\lambda_i) &\geq 0; & \epsilon_{sc}(\lambda_i) &= 1, \\ I_{BB}(\lambda_i, T_{sc}) - I_{BB}(\lambda_i, T_{amb})\epsilon_{atm}(\lambda_i) &< 0; & \epsilon_{sc}(\lambda_i) &= 0. \end{aligned} \quad (5.12)$$

In the case of a solar reflector, a body with a temperature equal to the ambient temperature ($T_{sc} = T_{amb}$), this criterion sets $\epsilon_{sc}(\lambda_i) = 1$ only for low atmospheric emissivity. This ideal curve is plotted in Figure 5.2c in green, where the emissivity is 1 only in the main atmospheric transmission window between 8 - 14 μm .

In the case of a solar absorber like a silicon solar cell, the operating temperature is higher than the ambient temperature ($T_{sc} > T_{amb}$). Figure 5.2b shows the atmospheric transmission with the blackbody spectra at temperatures 300 K and 340 K, corresponding to ambient temperature and the approximated temperature of an operating solar cell, respectively. Thus, the solar absorber emits more blackbody radiation than it receives from the atmosphere, independent of the atmospheric emissivity. Therefore, the ideal emissivity of a solar absorber is unity between $\lambda = 3 - 30 \mu\text{m}$, as plotted in blue in Fig. 5.2c. Below 3 μm , there is negligible blackbody radiation at 340 K, so we set the ideal solar absorber emissivity to 0 between $\lambda = 3 \mu\text{m}$ and the solar cell bandgap.

The emissivity of the solar cell also equals its absorptivity (Kirchhoff's law, Eq. (5.9)), which can be determined by:

$$\epsilon_{sc}(\lambda) = \alpha_{sc}(\lambda) = 1 - R_{sc}(\lambda) - T_{sc}(\lambda), \quad (5.13)$$

with $R_{sc}(\lambda)$ the reflection and $T_{sc}(\lambda)$ the transmission of the solar cell. Maximizing the IR emissivity of the solar cell thus equals minimizing the reflection and transmission.

Transfer matrix model

We use a transfer matrix model based on the Fresnel equations to calculate the reflection and transmission of planar multilayer stacks. In particular, we use the Python implementation written by Steven J. Byrnes [206]. Literature values for the optical constants of Si and SiO₂ (Fig. 5.6) were used from ref. [74] and for Au from ref. [207].

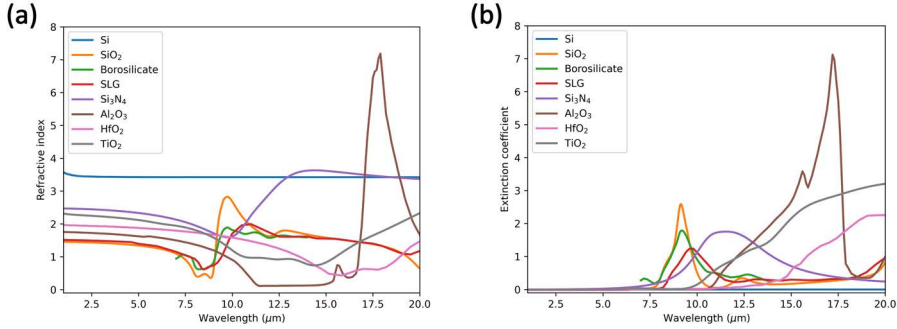


Figure 5.6: (a) The refractive index and (b) the extinction coefficient of the most prevalent materials in photovoltaics.

5

FDTD simulations

The optimization of the microcylinder array was performed by finite-difference time-domain (FDTD) calculations using Lumerical FDTD Solutions [72][48]. The single-pass IR reflection was minimized for a hexagonal array of silica cylinders at the interface of a semi-infinite silica substrate and air superstrate. Minimizing the reflection led to maximizing the cooling power (see calculation above), assuming that all IR light transmitted into the silica substrate is absorbed. The cylinder array was simulated in periodic boundary conditions. Convergence was found for a uniform 25 nm mesh size, conformal mesh refinement, and 10^{-7} auto shutoff value. The results of the optimization procedure are shown in Figure 5.7. The figure of merit is the radiative part of P_{cool} , according to Eq. (5.10), integrated between $\lambda = 2 - 16 \mu\text{m}$. In Figure 5.7a, we find a maximum for the pitch equal to 3.5 times the radius and height (equal). In Figure 5.7b, the pitch is constant at 3.5 times the radius, and we find the maximum for radius = $1.75 \mu\text{m}$ and height = $2.25 \mu\text{m}$.

The multipole decomposition in Figure 5.3b was performed by calculating the electric field inside the microcylinder according to the method outlined by Evlyukhin et al. [38].

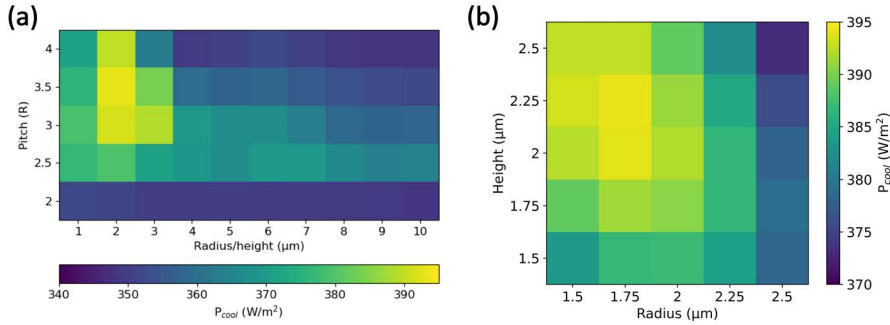


Figure 5.7: Optimization of the hexagonal microcylinder array. (a) Pitch optimization as a function of radius and height (equal); maximum at pitch = $3.5 \times$ radius. (b) Radius and height optimization, using optimal pitch found in (a). Optimal geometry was found at radius = $1.75 \mu\text{m}$, height = $2.25 \mu\text{m}$, and pitch = $3.5 \times 1.75 = 6.125 \mu\text{m}$. Color scaling is calculated according to Eq. (5.1).

Electron-beam physical vapor deposition

A double-side polished (DSP) silicon wafer (WRS Materials, lightly phosphorus n-type doped, resistivity 1 - $20 \Omega\text{m}$) with a thickness of $500 \mu\text{m}$ was used as the absorber substrate. Electron-beam physical vapor deposition was used to deposit an 80 nm gold layer on one side of $24 \times 24 \text{ mm}^2$ DSP Si substrates at a deposition rate of 0.5 \AA/s .

UV photolithography and reactive ion etching

As a photolithography mask, a negative photoresist, ma-N 1420, was spin coated onto a 4 inch silica wafer of $500 \mu\text{m}$ thickness. A hexamethyldisilazane (HMDS) resist adhesion promotor was spin-coated on the wafer at 4000 RPM with 1000 RPM/s for 35 s, followed by a curing step on a 150°C hot plate for 1 min. A $2 \mu\text{m}$ thick layer of ma-N 1420 was spin coated at 2000 RPM with 500 RPM/s for 30 s and cured at 100°C for 2 min.

The photoresist was illuminated ($\lambda = 365 \text{ nm}$) in a UV mask aligner (Süss MicroTec MABA6) through a quartz substrate with a chrome mask (commercial, Delta Mask BV). Unwanted interference due to reflection from the bottom silica-air interface is decreased by placing an absorptive tape on the back. The resist was developed by immersing the wafer into ma-D 533/S photoresist developer for 75 s; the wafer was then rinsed in H_2O for 30 s (twice) and blow-dried using a nitrogen gun.

The microstructured photoresist was used as a reactive ion etching (RIE) mask in an Oxford PlasmaPro Cobra RIE. A plasma of 50 sccm C_4F_8 and Ar gases was used to etch $2.20 \mu\text{m}$ deep in 16:30 min. The remaining photoresist was removed by immersion in base piranha, rinsed in H_2O , and dried under a nitrogen gun. Finally, the wafer is cut into $24 \times 24 \text{ mm}^2$ substrates.

Infrared hemispherical reflection

The infrared hemispherical reflection measurements were conducted in a modified Bruker Vertex70 research-grade laboratory Fourier-transform infrared (FTIR) spectrometer at the University of Twente, as described in work by Hecker et al. [208] The Vertex70 is modified with an external, custom-made integrating sphere with a diffuse gold coating, with a Mercury Cadmium Telluride (MCT) infrared detector on top ($\lambda = 1 - 16.7 \mu\text{m}$). The sample is positioned at the south pole of the sphere, with a variable aperture of 20 mm. An external, high-power Globar source ($\lambda = 1 - 16.7 \mu\text{m}$) was used for high signal-to-noise measurements.

Measurements are taken at a wavenumber resolution of 8 cm^{-1} and repeated 8 times to average the noise. All measurements are normalized to the reflection of a diffuse or flat gold substrate, and the signal of an open sample port measurement is subtracted as background. The silica substrates were attached to the silicon substrate with immersion oil to avoid an air gap in between the substrates.

Visible to near-infrared hemispherical reflectance/transmittance

Hemispherical reflectance/transmittance measurements were conducted in the visible to near-infrared (NIR) wavelength ranges. An integrating sphere with a diffuse Teflon coating in reflection (transmission) configuration was used to capture all light reflecting from (transmitting through) the sample. An NKT SuperK Extreme EXU 6 supercontinuum laser was coupled into the integrating sphere, and the reflected (transmitted) light was measured with a grating spectrometer. In reflectance, the silica substrates were attached to the silicon substrate with immersion oil to avoid an air gap in between the substrates. The sample stacks were placed at the backside of the integrating sphere at an 8-degree angle from the optical path. In transmittance, only the silica substrates were placed in front of the integrating sphere.

The hemispherical reflectance/transmittance was measured over a wavelength range from 400 to 1562 nm in three intervals. In the visible (400-700 nm), the reflectance/transmittance was measured with 200 ms exposure time on a silicon CCD, using 150 grating lines per mm with a blaze of 500 nm. In the NIR (700-1050 and 1050-1562 nm), the exposure time was 1 second on an InGaAs detector, with 150 grating lines per mm and a blaze of 1200 nm. To exclude higher-order grating effects, all short-wavelength light was blocked, using a long-pass filter of 650 nm and 1050 nm for the 700-1050 nm and 1050-1562 nm wavelength range, respectively.

6

Application and validity of the effective medium approximation to the optical properties of nano-textured silicon coated with a dielectric layer

The emergence of nanotextures in photovoltaics has resulted in challenges associated with optical modeling. Whilst rigorous methods exist to accurately solve these textures, the computational effort required limits the scope of modeling applications. The effective medium approximation (EMA) is a potential alternative to provide rapid modeling results which can be easily integrated with ray-tracing of large complex structures. However, the validity of this technique is strongly dependent on the size of features relative to the wavelength of interest, making the application of EMA ambiguous for many situations. This paper aims to address this issue by comparing the simulated results between EMA and finite element methods for three randomly distributed silicon textures with and without a dielectric layer. Criteria for which the EMA approach is valid are proposed and generalized using ratios between root-mean-square roughness, correlation length and incident wavelength, making these limits broadly applicable, beyond that of just the nanotexture under specific solar spectrum regimes. The results in this chapter apply to random, isotropic textures under normal incident light. Based on the proposed criteria, the validity of different optical simulation techniques for a set of industrial photovoltaic textures is discussed. This analysis reveals a region within which neither geometric optics nor EMA are adequate for calculating the reflectivity of a textured surface, and hence FDTD or other new approaches are required.

This chapter is based on:

Application and validity of the effective medium approximation to the optical properties of nano-textured silicon coated with a dielectric layer

Tsun H. Fung¹, Tom Veecken², David Payne^{1,3}, Binesh Veettil^{1,3}, Albert Polman², and Malcolm Abbott¹

Optics Express **27**, pp. 38645-38660, 2019.

<https://doi.org/10.1364/OE.27.038645>

¹ School of Photovoltaic and Renewable Energy Engineering, University of New South Wales, Sydney, NSW, 2052, Australia

² Center for Nanophotonics, NWO-Institute AMOLF, Science Park 104, 1098 XG Amsterdam, The Netherlands

³ School of Engineering, Macquarie University, Sydney, NSW, 2109, Australia

Author contributions:

Tsun, David and Malcolm conceived the project. Tsun generated the artificial black silicon textures, performed the effective medium calculations, and wrote the original draft. Tom performed the FDTD simulations. Tsun and Tom performed the data analysis. Malcolm and Albert supervised the project. Tom and David reviewed and edited the manuscript. All authors provided feedback and contributed to the manuscript.

6.1 Introduction

Photovoltaics provides a significant market share of the world's electricity generation with a cumulative installed power over 500 GW by the end of 2018 [209]. Modeling is widely used in the industry to develop new technology, to optimize products and to predict the energy yield from large systems [210, 211]. Solving the wavelength dependence of light coupling and trapping in the cell, module and system (e.g. via ray-tracing) is one option being developed to provide more accurate results [212–214]. This approach relies on rapid techniques to solve the reflection, transmission and absorption at all the many optical interfaces between materials. This paper focuses on a specific aspect of this problem which is the interaction between the surface texture of a solar cell and the relevant wavelengths of light, particularly for the case where the texture contains nano-scaled features (e.g. black silicon). It examines the use of the effective medium approximation to simulate the solar cell front surface and compares the results to those determined via more rigorous techniques such as numerical Finite Difference Time Domain (FDTD) simulations which converge to exact solutions. The geometry studied is particularly relevant within the solar community to the optimization of black silicon textures and the detailed calculation of module operating temperatures [215, 216]. Its relevance extends to the more general development of nanotextures (particularly where they are coated with dielectric layers) for a broad range of applications [217–219].

Finite Difference Time Domain (FDTD) techniques are well known to simulate light propagation at sub-wavelength scales and provide exact solutions to Maxwell's equations. If done properly, this simulation method provides the most accurate optical simulation results. Several studies have applied FDTD to understand and model the optical behavior of nanotextured silicon [220–223]. In particular, Kroll et al. expanded such simulations with incoherent propagation within the silicon substrate in an attempt to simulate the absorption of the whole silicon wafer [222]. Due to the large simulation volume such simulations are computationally demanding and generally hard to apply to large areas. Another solution is to apply rigorous coupled wave analysis (RCWA) which is a semi-analytical method and ideal for studying scattering of periodic structures like grating devices [224]. The applicability of RCWA on studying nanotextured silicon has also been investigated and found to provide accurate solutions [223]. However, since typical nanotextured silicon is randomly distributed, a relatively large unit cell is required to capture all features in the simulation geometry. As a result, the wavelength range in that study was limited to a 100 nm bandwidth near the Si band edge in order to save computation power. This issue was further investigated by Tucher et al. where a field stitching method was applied to replace a large unit cell with several sub-cells and a field-averaging algorithm was used to smoothen the discontinuity in the overlapping regions [225]. However, there is still a restriction on the minimum size of the sub-cell which limits the computational advantage of that method.

Another challenge of rigorous optical simulation of industrial solar cells is the propagation of light through the bulk of the wafers ($\sim 180\ \mu\text{m}$ thick) and the interaction with the rear side of the wafers. One option to address the speed issue of both FDTD and RCWA is to derive a scattering matrix that describes the scattering efficiency for a discrete set of input and output angles. This can then be combined with ray-tracing to solve for light absorption in the thick wafer, a method also referred to as OPTOS [226] or AMF [227]. There are some situations where that approach has worked well [228, 229]. However, deriving the scattering matrix can still be computationally demanding and the solution space is limited to 1 dimension.

An alternative approach is to simply model the textured surface layer with optical material properties determined using an effective medium approximation (EMA) [230]. This analytical approach has previously been applied to simulate the reflection of silicon nanowires for

photovoltaic applications, where a single effective medium layer was used [231]. However, typical nanotextures for silicon solar cell applications have a gradual change in volume fraction which leads to an effective refractive index gradient rather than a single thin film [232]. This property was captured by a study where good agreement between EMA and RCWA was achieved in the infra-red region ($2\text{ }\mu\text{m}$ - $10\text{ }\mu\text{m}$) [229]. This has implications for modeling devices that operate in those regions, such as photodetectors. It is also relevant to more detailed solving of the operating temperature of silicon solar cells that parasitically absorb longer wavelengths of light leading to substrate heating and a reduction in cell efficiency. However, given the fact that the feature sizes of textured Si wafers are at or below the wavelength of the spectral band where light is absorbed in the solar cell, the validity of EMA for solar cell applications still requires further investigation.

Tang et al. investigated the reflectivity of one-dimensional surface profiles characterized by their root-mean-squared roughness (σ) and correlation length (τ) [233]. The reflectivity spectra were calculated by an exact approach based on the extinction theorem in the electromagnetic theory and compared to the geometric optics approximation where ray-tracing was used. Criteria for determining when geometric optics is a good approximation of the electromagnetic theory were proposed and generalized using ratios between σ , τ_L , and λ , making it applicable to textures of different size. In this work, we perform a similar analysis to investigate the validity of the effective medium approximation regarding its ability to predict the reflection and absorption of light in textured silicon.

In this chapter, we aim to: (1) outline a systematic approach for converting surface topography into appropriate effective medium layers (2) investigate the criteria for which EMA is a good approximation of exact electromagnetic theory models of the optical properties of nanotextured silicon, (3) apply EMA to model nanotextured silicon, both bare and with a conformal dielectric layer. The work does this for normal incident light and assesses agreement in terms of front surface reflection and absorption in the nanotexture.

6.2 Methods

Randomly distributed nano-scaled surfaces were computationally generated, and the optical properties were modelled by EMA and FDTD in the wavelength range of 300 nm to 2500 nm. We have assumed semi-infinite substrates to enable a direct comparison of FDTD and EMA models, focusing on the effect of front textures. Adding the effect of back-reflection would provide the same effect for both models and will not affect the conclusions. Furthermore, Sunlight has a coherence length of several 10s of microns, which is much larger than the considered feature sizes. As a result, only coherent treatment is considered in this chapter. In addition to the total front surface reflectance, two-dimensional cross-cuts of the electric field intensity distribution were recorded from the FDTD calculations, which assist in the discussion of the limitations of EMA for photovoltaic applications. We chose to use computer-generated surfaces because it is in practice very difficult to accurately measure the surface topography of nanotextures, and we would prefer to avoid the complication of additional experimental noise in determining the validity of the effective medium technique. It also avoids the question of how to fabricate a texture with the desired surface height distribution. The final section of this chapter includes some AFM measurements of typical solar cell textures. These measurements were made using Bruker Dimension ICON SPM. A diamond-like carbon-coated silicon probe (TESPD) with a nominal tip radius of 18nm was used for industrially acquired random pyramid texture and metal-assisted chemical texture. A minimum 5:1 high aspect ratio probe (TESPA-HAR) with a nominal tip radius of 10 nm was explicitly used for academically produced reactive-ion etched (RIE) textures. The preparation of the RIE textures were described in [234, 235].

6.2.1 Generation of random surfaces

Each surface morphology was created assuming a Gaussian distribution of heights specified by a set of targeted root-mean-square roughness (σ) and auto-correlation length (τ) using common definitions [236]. Both surface height distribution and correlation length of these surfaces were described by a Gaussian distribution. An open-source random surface generator was obtained and further modified to create the sets of homogeneous surfaces used in this study [237]. The shape of underlying features in each surface was created by producing numbers of sinusoidal waves with different frequencies. The actual values of σ and τ were confirmed by importing each surface into *Gwyddion*, a common open-source program for AFM data analysis, and using the software's surface statistics function to ensure that actual parameters are within 5nm of the targeted values [238]. Figure 6.1 shows the line profile of three textures studied in this chapter. Texture 1 has an effective slope index (σ/τ_L) of 3, which represents a more needle-like surface. Textures 2 and 3 have smaller effective slope index, representing more planar surfaces.

Figure 6.2 shows the diagram of “effective slope index versus wavelength-normalized roughness” proposed by Tang et al. The blue and green areas in the diagram represent geometries where electromagnetic theory can be approximated by geometric optics, with the green area being valid if only the specular component of total reflectance is concerned. The Textures 1, 2, and 3 examined in this chapter at different wavelengths were created with pairs of σ and τ_L that fall into the “electromagnetic region” for wavelengths in the range 300 - 1200 nm for which geometric optics will not work, as we previously confirmed for other experimentally produced photovoltaic nanotextures [239]. The orange region is the effective medium region proposed in this chapter (based on the results presented in Section 6.3.2), within which the total reflectance of textured silicon can be approximated by EMA.

In this study, the proposed criterion for EMA being valid is that the absolute difference in total reflectance between EMA and FDTD must be less than 2%. In this case, the mismatch between the two simulation approaches results in less than 1 mA/cm² difference in photon current between 300 nm - 1200 nm under the AM1.5G spectrum. It should be reiterated that the criterion proposed in this chapter only examines the total reflectance for normal incident light and its angular dependency is not within the scope of this study.

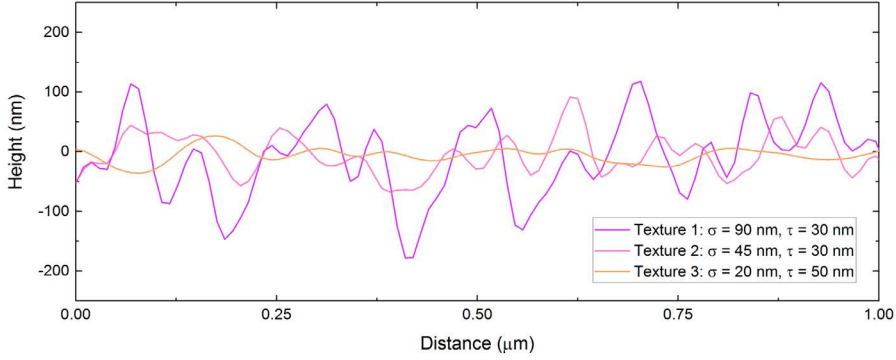


Figure 6.1: Line profiles for the artificially created Textures 1, 2 and 3.

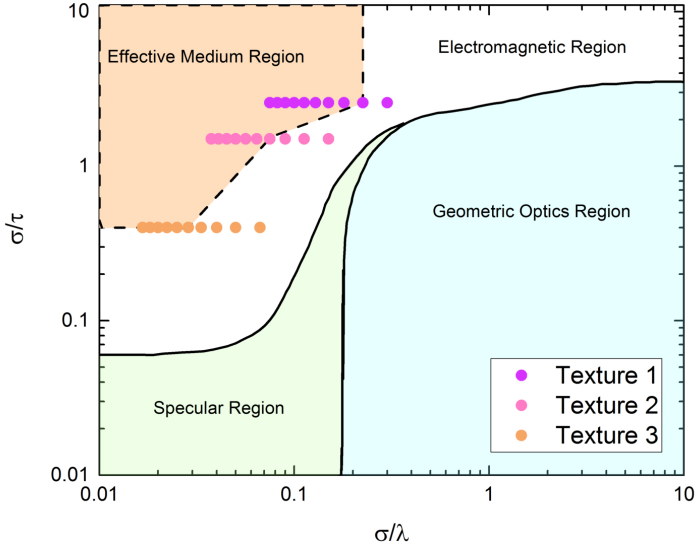


Figure 6.2: Diagram of effective slope index versus wavelength-normalized roughness after Tang et al. [233] with regions of specular reflection (green), geometric optics (blue), and the electrodynamic region. The effective medium region (orange) is proposed in this chapter. Each dot indicates one of the textures at a 100 nm wavelength interval between 300 and 1200 nm (right to left) for normal incident light.

6.2.2 Summary of EMA simulation

The created nanotextures were modeled as a stack of 20 thin films with each layer designated an effective index corresponding to the materials gradient from air to silicon (Fig. 6.3). This number of layers was chosen such that the reflectance does not change with a further increase in the number of layers and such that no interference fringes were observed. The effective medium method used to calculate the effective permittivity of each layer is described in Section 6.2.3, and the extraction of volume fraction of each element in each layer is described in Section 6.2.4. The calculated effective index of each layer was used in a transfer matrix model to calculate the effective specular reflectivity. Both EMA and FDTD models shared the same refractive index ($n + ik$), for silicon [74].

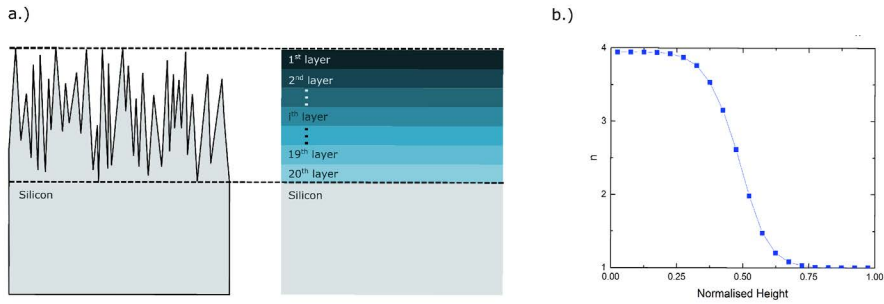


Figure 6.3: (a) Schematic diagram on the effective medium approach, where the nano-texture on the surface is modeled as an effective medium that consists of a stack of 20 thin films. (b) The real component of refractive index ($\lambda = 600$ nm) through the height of the effective medium, calculated by the Bruggeman effective medium model for a silicon surface with Gaussian height distribution in air.

6.2.3 Effective medium theory

Effective medium theory represents the optical properties of a complex composite by an effective homogenous medium. It has been successfully used to represent the effective optical properties of nanoparticles, porous silicon, mesocrystal and gratings [240–243]. Recently, it has also been applied to nanotextured silicon [229, 230].

Several different models have been developed with regards to calculating the optical properties of the mixed effective medium. The Maxwell-Garnett model is one of the most studied mixing formulae, originally derived for spherical inclusions in a host medium [244]. It works best for dilute composites due to its asymmetry property between the permittivity of host and inclusion [245]. Due to the same property, it cannot be generalized for modeling composite of three materials. As such, it is not applicable for modeling textured silicon in this chapter. We use the well-known Bruggeman mixing model, which, for a mixture of two dielectric media, states that

$$f_{Si} \left(\frac{\epsilon_{Si} - \epsilon_{BG}}{\epsilon_{Si} + 2\epsilon_{BG}} \right) + (1 - f_{Si}) \left(\frac{1 - \epsilon_{BG}}{1 + 2\epsilon_{BG}} \right) = 0, \quad (6.1)$$

with f_{Si} the volume fractions of Si and ϵ_{Si} and ϵ_{BG} the dielectric constants of Si and the modeled effective constant, respectively. This equation can be factorized into a second-order

polynomial [245, 246]

$$0 = A\epsilon_{BG}^2 + B\epsilon_{BG} + C, \quad (6.2)$$

where

$$A = -2 ; B = f_{Si}(2\epsilon_{Si} - 1) + (1 - f_{Si})(2\epsilon_{air} - \epsilon_{Si}) ; C = \epsilon_{Si}.$$

To model the effective permittivity of nanotextured silicon coated with a dielectric layer, the BG equation becomes

$$f_{Si}\left(\frac{\epsilon_{Si} - \epsilon_{BG}}{\epsilon_{Si} + 2\epsilon_{BG}}\right) + f_d\left(\frac{\epsilon_d - \epsilon_{BG}}{\epsilon_d + 2\epsilon_{BG}}\right) + (1 - f_{Si} - f_d)\left(\frac{1 - \epsilon_{BG}}{1 + 2\epsilon_{BG}}\right) = 0, \quad (6.3)$$

with f_d and ϵ_d the volume fractions of dielectric coating and dielectric constant of the coating, respectively. It can be factorized into a third-order polynomial

$$0 = D\epsilon_{BG}^3 + E\epsilon_{BG}^2 + F\epsilon_{BG} + G, \quad (6.4)$$

where

$$\begin{aligned} D &= -4, \\ E &= (6f_{Si} - 2)\epsilon_{Si} + (6f_d - 2)\epsilon_d + (4 - 6f_{Si} + 6f_d), \\ F &= (3\epsilon_{Si} + 3\epsilon_d - 1)\epsilon_{Si}\epsilon_d + (2 - 3f_d)\epsilon_{Si} + (2 - 3f_{Si})\epsilon_d, \\ G &= \epsilon_{Si}\epsilon_d. \end{aligned}$$

For both polynomials, only one root resulted in positive values for n and k . The other(s) resulted in negative numbers, which are discarded [245, 246].

6.2.4 Extraction of volume fraction for an individual element

Figure 6.4 shows the cumulative height distribution ($P(z)$) of Texture 1 extracted by *Gwyddion*. It is equivalent to the bearing area curve which gives the ratio of air to materials at any height (z), irrespective to the shape of the texture, number of materials, and randomness of the spatial distribution [236]. For a coated silicon surface, a 100 nm thick conformal layer was added on top of the generated texture. This is approximately equivalent to a directed deposition process. The addition of this layer causes the $P(z)$ to be shifted by 100 nm towards the positive z direction, such that

$$P'(z) = P(z + 100), \quad (6.5)$$

where $P'(z)$ is the cumulative height distribution of the passivated silicon surface. For the texture coated with dielectric, the volume fraction of silicon (v_{Si}) at height z is

$$v_{Si} = 1 - P(z), \quad (6.6)$$

the volume fraction of air (v_{air}) at height z is

$$v_{air} = P'(z), \quad (6.7)$$

and the volume fraction of dielectric layer (v_d) at height z is

$$v_d = 1 - P'(z) - P(z). \quad (6.8)$$

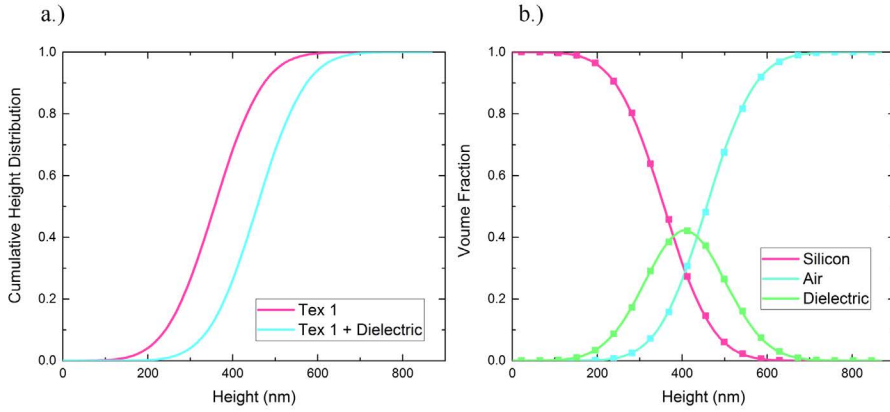


Figure 6.4: Cumulative height distribution of Texture 1 with and without dielectric (a) and volume fraction of each component in Texture 1 coated with dielectric (b).

6.2.5 Details of numerical FDTD calculation

The reflection and absorption spectra were calculated using finite-difference time-domain (FDTD) calculations performed in Lumerical FDTD Solutions [247]. The surface textures of $5 \times 5 \mu\text{m}$ were imported and placed in a simulation box of $5 \times 5 \times 1.4 \mu\text{m}$. For the calculations of textures with a dielectric coating, the same surface was copied and displaced in the lateral direction to mimic conformal coating of the Si texture. Periodic boundary conditions were employed in the surface texture plane, while perfectly matching layers (PMLs) were used in the lateral directions. A broadband plane wave source was employed under normal incidence propagating in the negative z -direction. To calculate the reflection from the texture, a power monitor was placed above the source; to calculate the absorption in the surface texture, two power monitors were placed at the beginning and end of the texture, respectively. To obtain the two-dimensional cross-cut of the electric field intensity distribution, a field monitor was placed in the x - z plane that recorded the electric field intensity of the propagating plane wave with 100 nm wavelength intervals. Mesh resolution convergence was found for a 3 nm mesh in all three dimensions, with conformal mesh refinement. The calculations were performed on a computer cluster, using 512 CPU's in parallel with 4GB RAM per CPU. To remain within the memory capacity, the calculations were carried out over two wavelength regimes: 300 - 1400 nm and 1400 - 2500 nm. To ensure identical optical properties for the materials in both wavelength regimes, the optical constants (n and k) were fitted with analytical functions over the full range (300 - 2500 nm) for both simulations. Literature values of the optical constants of Si were used [74]. The n and k values of the dielectric were set to equal 2 and 0, respectively, for all wavelengths.

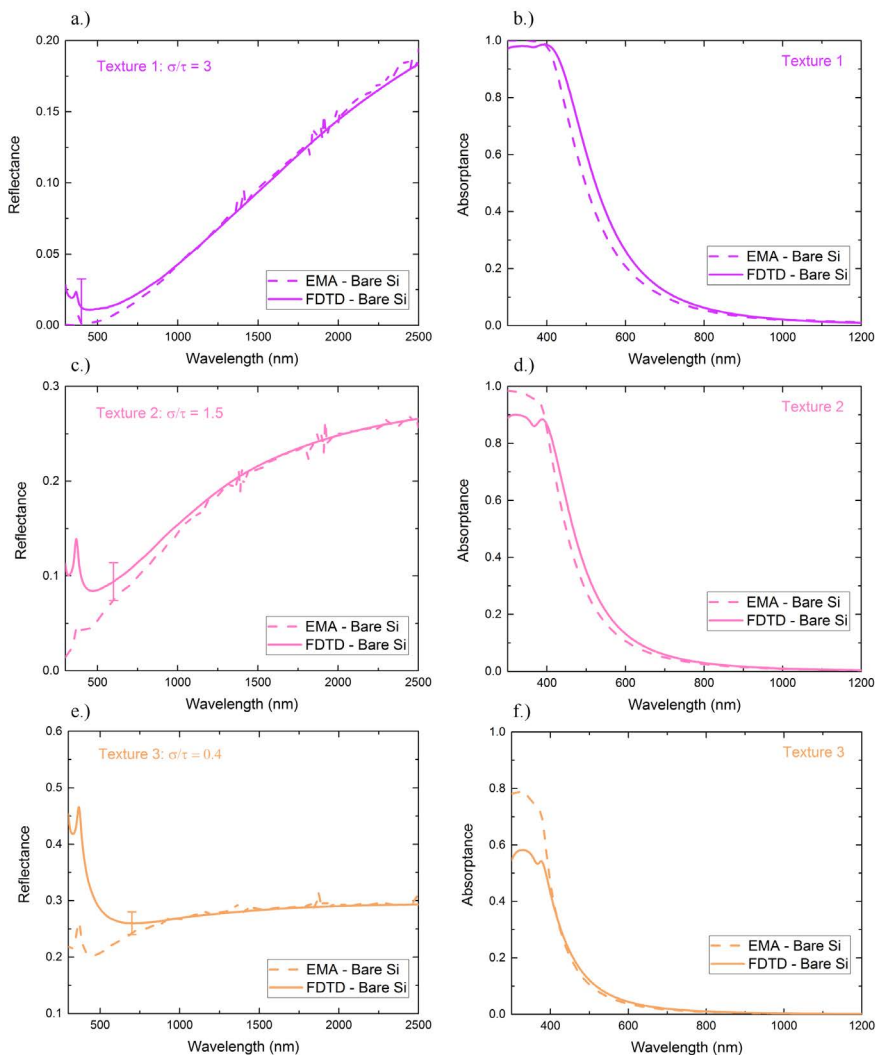


Figure 6.5: Simulated reflectance (a, c and e) and absorption (b, d and f) spectra for bare textured silicon, obtained by FDTD (solid lines) and EMA (dashed). The vertical bar shows $\pm 2\%$ absolute difference.

6.3 Results

6.3.1 Effective medium approximation for bare silicon

Figure 6.5 shows the reflectance and absorbance spectra of the bare silicon textures from the EMA model compared to the FDTD calculations. Excellent agreement is found for the simulated reflectance between the EMA model and FDTD calculations above 370 nm (Texture 1), 590 nm (Texture 2), and 700 nm (Texture 3), where the absolute difference in reflectance between the EMA model and FDTD calculations is less than 2% absolute (Fig. 6.6(a)). However, the simulated reflectance by EMA shows significant disagreement with FDTD in the short wavelength region for all textures, indicating that the EMA model is not valid within this region. As λ reduces, the σ/λ increases and the value of σ/λ beyond which deviation started to occur ($\sigma/\lambda_{critical}$) seems to depend on the value of effective slope index (σ/τ). In other words, the validity of EMA on textures with higher effective slope index extends to shorter wavelengths. In the short wavelength region, the EMA model consistently underestimates the reflectivity for all textures (Fig. 6.6(a)). The discrepancy between these models appears to be more significant when the effective slope index of the textures is smaller. The absolute difference in reflection at 300 nm between EMA and FDTD is 2% for Texture 1 and is as large as 20% for Texture 3. For a given volume fraction (e.g. $f_{air} = f_{Si} = 0.5$), the in-plane dimensions of individual elements in middle and deep layers is larger for planar texture (smaller effective slope index) as compared to that of more needle-like textures (larger effective slope index). As the individual elements get larger and closer to the incident wavelength, EMA starts to perform poorly.

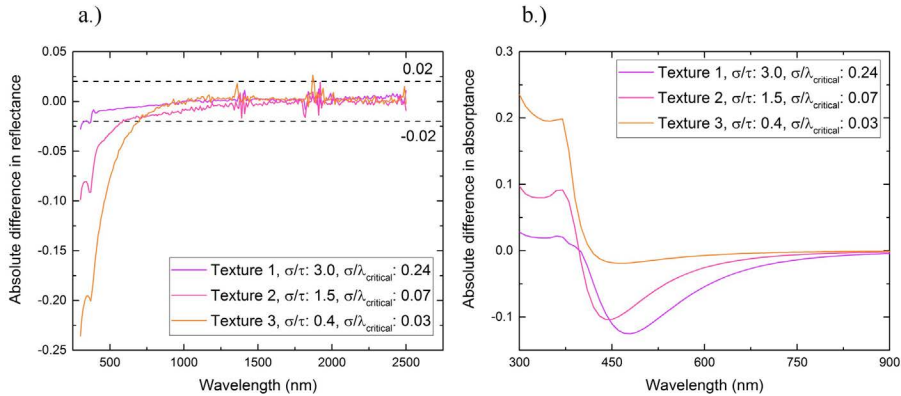


Figure 6.6: (a) Absolute difference in simulated reflectance between EMA and FDTD for $\lambda_{critical}$ represents the wavelength at which the absolute difference reaches 2%. (b) Absolute difference in simulated absorbance within the nanotexture between EMA and FDTD.

For all textures, the EMA model consistently overestimates the absorption for wavelengths less than 400 nm (Fig. 6.6(b)), which is related to the corresponding significant underestimation in the reflectivity at those wavelengths. For Texture 1, EMA underestimates the absorption within the nano-texture by up to 10% between 400 and 800 nm, while the simulated reflectance is also slightly underestimated in that wavelength range. The underestimation in absorption could be due to light scattering that is neglected in EMA, which would result in an underestimation of the optical path length within the nanotexture.

6.3.2 Electric field intensity distributions of light incident on the nanotexture

The electric field intensity distributions on all textures at 400 nm and 1000 nm (Fig. 6.7) provide insight into the deviation between EMA and FDTD. At 400 nm, a complex electric field intensity distribution is observed for all textures. We attribute this to strong resonance and multiple light scattering events from the textures, since the incident wavelength is similar to the feature size. The pattern observed in Fig. 6.7 is the result of interference between the plane wave and the scattered light. These prominent scattering effects are all accurately accounted for in the FDTD simulation. On the other hand, when the wavelength of the incident plane-wave increases to 1000 nm, there is no significant lateral disturbance in the electric field distribution. This indicates that scattering of light from these textures is negligible at 1000 nm and the reflection from these textures is mostly specular. The above results suggest that the discrepancy between EMA and FDTD present in Fig. 6.6 is due to the fact that near-field effects are not accounted for in the EMA model, which becomes prominent as the wavelength reduces. It is worth noting that a rather complex electric field intensity distribution was observed for Texture 1 at 400 nm, yet the total reflectance obtained with FDTD was low such that it was still within 2% absolute difference compared to EMA.

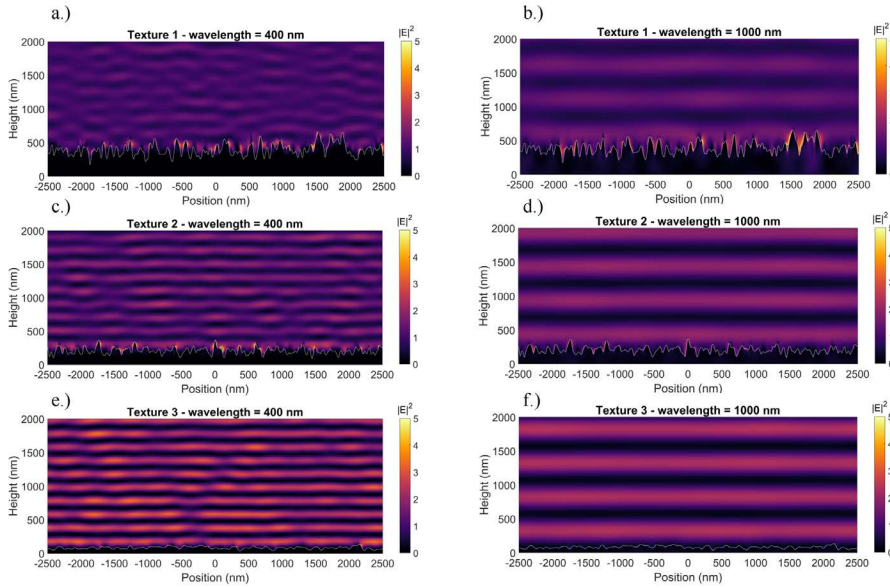


Figure 6.7: FDTD calculation of the electric field intensity distribution through a cross-section (highlighted by red curve) of the three bare silicon textures upon plane-wave illumination at a wavelength of 400 nm (a, c and e) and 1000 nm (b, d and f).

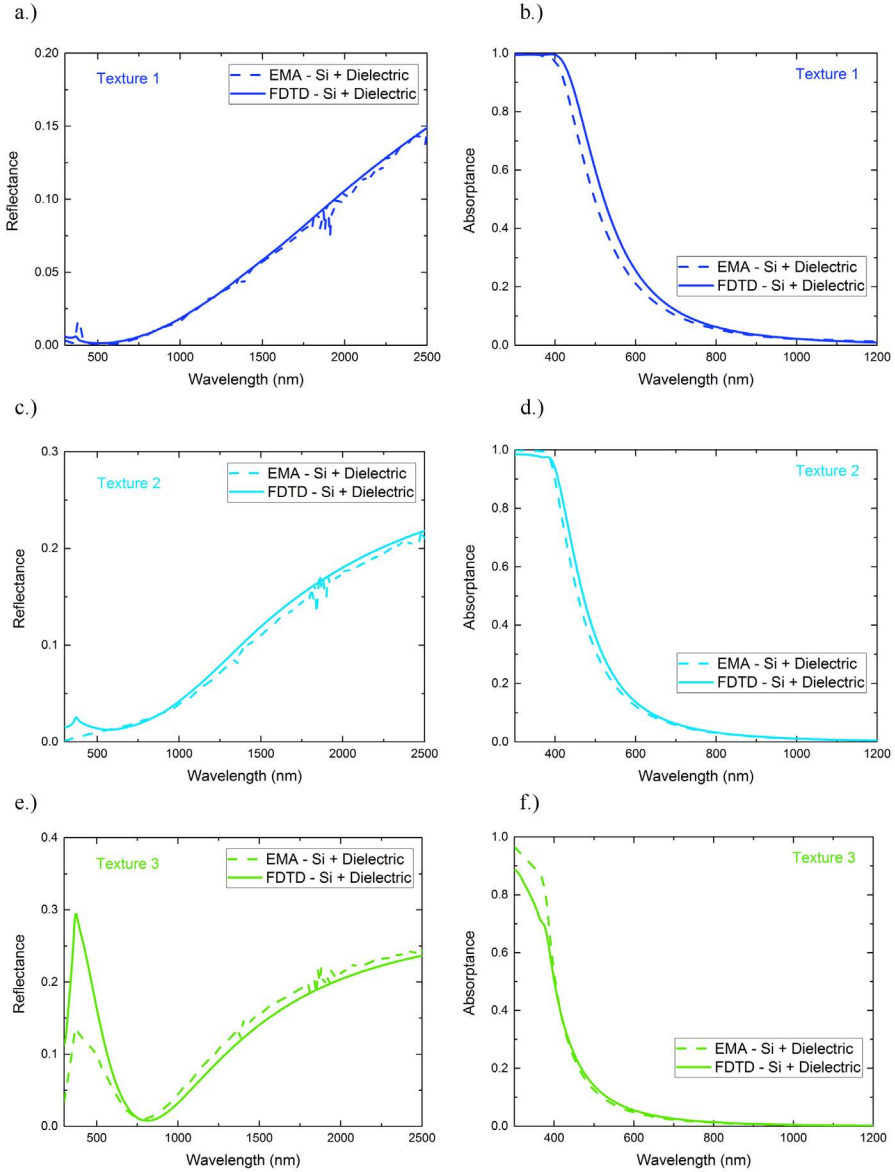


Figure 6.8: Simulated reflection (a, c and e) and absorption (b, d and f) within the texture for bare silicon coated with dielectric, obtained by FDTD (solid lines) and EMA (dashed).

6.3.3 Effective medium approximation for silicon coated with a dielectric

Figure 6.8 shows the reflection and absorption spectra of silicon conformally coated with a 100 nm thick dielectric layer from the EMA model compared to the FDTD calculations. The anti-reflection effect is clearly seen in the reduction in reflectance over the entire spectral range, compared to Fig. 6.5, with an interference minimum at 500 nm, 550 nm, and 800 nm, for Textures 1, 2, and 3, respectively. In this case, very good agreement in simulated reflectivity between the EMA model and FDTD calculations is achieved for the whole spectral range examined for Texture 1 and 2 with an absolute difference less than 2%, except in the region ($\lambda \approx 1900$ nm) where signal noise caused by the statistic involved in ray-tracing (Fig. 6.9(a)). This issue may be resolved by increasing the number of rays used in the Monte Carlo ray-tracing simulation. For Texture 3, the absolute difference from 750 nm and higher is less than 2% whilst it increases below 700 nm; the absolute difference reaches 15% at 380 nm. These results indicate the validity of the EMA model for AR-coated textured Si for small σ/λ . This enables EMA as a modeling technique to predict the optical properties of given nanotextures with a conformal dielectric coating. Similar to the case for the bare texture, very good agreement is observed for the absorption spectra in Fig. 6.8, with the largest deviation found for short wavelengths for Texture 3 (Fig. 6.9(b)).

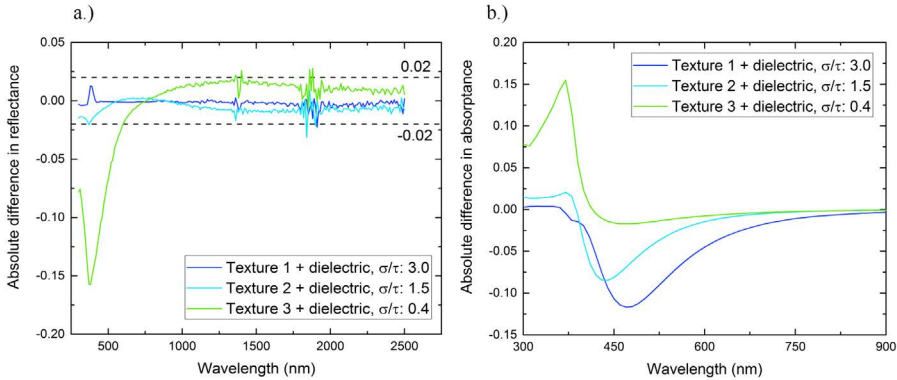


Figure 6.9: (a) Absolute difference in simulated reflectance between EMA and FDTD for Texture 1 to 3 coated with dielectric layer. The dashed lines indicate the 2% absolute difference. $\lambda_{critical}$ represents the wavelength at which the absolute difference reaches 2%. (b) Absolute difference in simulated absorbance within the nanotexture between EMA and FDTD.

6.3.4 Proposed criteria for approximating electromagnetic theory by the effective medium approximation

Figure 6.10 depicts the same data as shown in Fig. 6.2, but now both axes are wavelength-normalized, and diagonal lines correspond to σ/τ values. This representation reveals the influence of individual change in σ or τ relative to the wavelength. In addition to the specular, geometric-optics, and electromagnetic regions as taken from Tang et al., we define any texture as specular that has a roughness at least 100 times smaller than the wavelength. The EMT regions is proposed in this study and defined where the total simulated reflectance from EMA

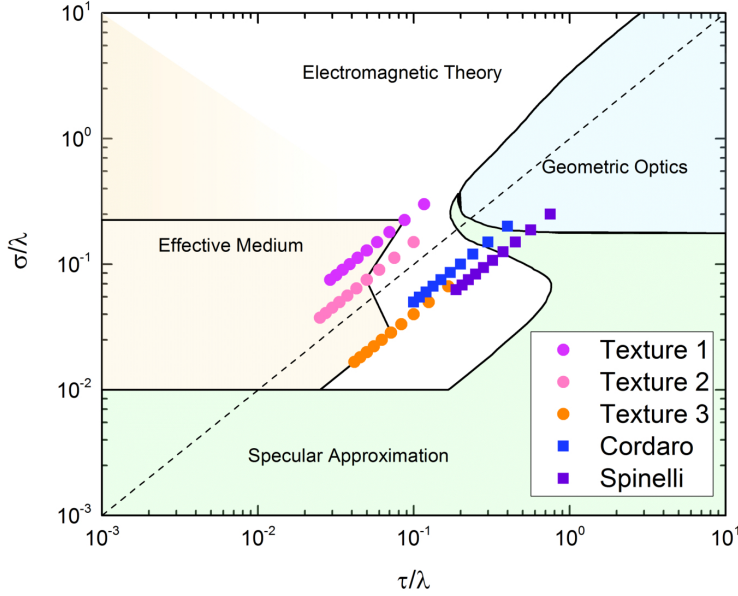


Figure 6.10: Diagram of wavelength-normalized roughness versus wavelength-normalized correlation length, with regions of specular reflection (green), geometric optics (green-blue), and the electrodynamic region (blue) as taken from Tang et al. (same data as in Fig. 2). The criteria proposed in this study are indicated in orange, where the total simulated reflectance from EMA is within 2% absolute difference to FDTD simulation for silicon textures. Each dot indicates one of the textures at a 100 nm wavelength interval between 300 and 1200 nm (right to left). The colored squares are taken from [24, 248], respectively. The diagonal dashed line depicts the $\sigma/\tau = 1$ line.

is within 2% absolute difference to FDTD simulation for silicon textures. The EMT fades to white, indicating a region that is out of scope of this study.

Alternative to the random structures considered in this chapter to achieve low reflection, ordered structures (silicon cylinders) that support Mie resonances can also be employed to achieve black silicon [24, 248–252]. Using the reported height, pitch and diameter, the σ and τ of these periodic silicon textures were calculated by using *Gwyddion* and analytical formulas. We find that these textures do not fall in the electromagnetic region (colored squares) at 550 nm (the middle of the visible spectrum) or lower. This indicates that the validity regions in this study are typical to random textures, and not valid for ordered/resonant structures.

The validity chart reveals a region within which neither geometric optics nor EMA are adequate for calculating the reflectivity of a textured surface, and where FDTD or other approaches are required. It is interesting to consider how this impacts the modeling of textures typically used in photovoltaics. Table 6.1 summarizes the surface characteristic of a variety of common photovoltaic textures based on reports in the literature and AFM measurements made as part of this chapter. For each texture, Table 6.1 provides the wavelength for normal incident light at which the boundaries of validity of EMA is crossed. The corresponding SEM images of these textures were shown in Fig. 6.11.

Table 6.1: Summary of surface characteristics and weighted reflectance between 300 nm – 950 nm for upright random pyramids (RPD), industrial metal-assisted chemical etching (MACE) and reactive-ion etching (RIE) and their regions of validity.

Texture	σ (nm)	τ (nm)	R _{weighted} (%)	GO valid max λ (μm)	Specular max λ (μm)	EMA ^a min λ (μm)
RPD	481	1213	0.119	2.5	4	17
MACE	146	322	0.198	0.9	1.1	5
Shallow RIE	52	55	0.104	N/A	N/A	1
Deep RIE	234	137	0.007	0.7	0.8	3

^aProposed in this work.

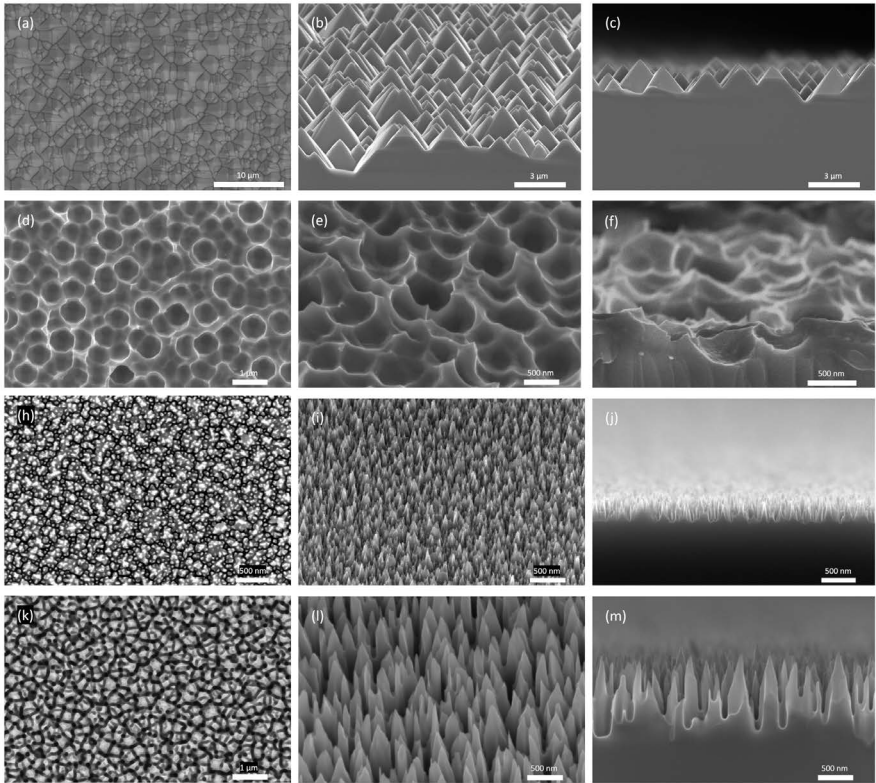


Figure 6.11: Top view, 45° and cross-sectional SEM images of random pyramid (a, b, and c), metal-assisted chemical etching (d, e, and f), shallow reactive-ion etching (h, i, and j) and deep reactive-ion etching (k, l, and m).

For macroscopic random pyramid texture, the geometric optics region applies for wavelengths below $2.5\text{ }\mu\text{m}$, which implies that 99% of the energy in AM1.5G spectrum can be accurately simulated by ray-tracing. Beyond 2500 nm , it crosses into the specular region, at which point the simulated results from ray-tracing become less accurate, at least when the angular distribution is of concern. The minimum wavelength for using EMA to model random pyramid is $17\text{ }\mu\text{m}$, which is beyond the interests in the applications of photovoltaics.

Metal-assisted chemical-etched (MACE) texture falls into the geometric optics region up to approximately 900 nm , beyond which it starts to cross into the specular region. This suggests that while the front surface reflectance of MACE may be accurately simulated by ray-tracing, the internal light rapping ($900\text{ nm} - 1200\text{ nm}$, where angular distribution is crucial) may not. As the MACE texture continuously reduces in size, this problem may become more significant in the future. Table 6.1 also suggests that the parasitic absorption ($1000\text{ nm} - 4000\text{ nm}$) of MACE textured silicon solar cells require rigorous solving. Nevertheless, the atmospheric window ($8\text{ }\mu\text{m} - 13\text{ }\mu\text{m}$ [253]) falls into the proposed effective medium region, which indicates that EMA can be used to rapidly simulate the optical properties of MACE textures when radiative heat loss is concerned [215, 253].

RIE-needles may form on a polished surface or a micro-textured surface [254, 255]; the former requires deep features to significantly reduce the front surface reflectance, whilst the later often requires shallower features for optimizing the electrical properties of the final device. Therefore, a vast range of surface characteristics are possible. Two options used in this chapter are shown in Table 6.1. Nevertheless, it can be observed that neither geometric nor effective medium approximation is fully valid for simulating any of these RIE textures within $300\text{ nm} - 1200\text{ nm}$, the wavelength range that is most relevant to solar cells. Like MACE texture, the atmospheric window of RIE textures falls into the effective medium region.

6.4 Conclusions

Rapid modeling of nanotextures can enable their integration into large and multi-variant simulations. This is particularly useful for the solar industry to optimize the front surface region and to determine the impact on a cell, module and system level. To enable this, the chapter presented here investigated the use of the effective medium approximation to model the optical properties of dielectric-coated nanotextures for photovoltaic applications. The validity of this approach was studied not just for a single specific texture, but as a function of feature size. Thus, allowing it to be applied to a broad range of textures. Randomly generated surfaces were used to allow the creation of specific size distributions and to avoid errors related to the topographical characterization of these surfaces. By comparing the reflection and absorption simulated via EMA and FDTD it identified a region of validity in which the agreement between the techniques for normal incident light was less than 2% absolute. This region was based on the results of three surfaces, further work could refine this further by including more surfaces and extending the analysis to include varied angles of incidence.

Plasma focused ion beam tomography for accurate characterization of black silicon validated by full-wave optical simulations

Black silicon (BSi) is a branch of processed silicon material whose surface is specially processed to a micro-/nanoscale structure, which can be used to achieve surfaces with ultra-low reflectance or ultra-high electrochemical reactivity. The diversity and complex surface structures of BSi make it challenging to commercialize BSi devices. Modeling and simulation are commonly used in the semiconductor industry to better understand the material properties, predict the device performance, and provide guidelines for optimizing fabrication parameters. The biggest challenge for BSi device modeling and simulation is obtaining accurate surface morphological data as input. In this work, we have compared the 3D models of the challenging BSi textures obtained by atomic force microscopy (AFM) and plasma focused ion beam (PFIB) tomography techniques. AFM is the most adopted surface topography characterization technique, in which a sharp tip on the end of the cantilever repeatedly contacts the surface. PFIB tomography is a technique that uses PFIB to sequentially remove the material layer by layer and uses scanning electron microscopy (SEM) to capture the specimen's cross-sectional features. In our previous work, we have optimized the PFIB tomography workflow towards the application of surface topography. In this work, we have comprehensively compared the 3D models obtained from both AFM and PFIB. Our results provide strong evidence that PFIB tomography is a better substitute to the AFM for highly roughened surface topographical characterization such as BSi, which provides surface 3D models with better reliability and consistency.

This chapter is based on:

Plasma focused ion beam tomography for accurate characterization of black silicon validated by full-wave optical simulations

Yu Zhang¹, Tom Veecken², Shaozhou Wang¹, Giuseppe Scardera¹, Malcolm Abbott¹, David Payne^{1,3}, Albert Polman², and Bram Hoex¹

Under review by Advanced Materials Technologies

¹ School of Photovoltaic and Renewable Energy Engineering, University of New South Wales, Sydney, NSW, 2052, Australia

² Center for Nanophotonics, NWO-Institute AMOLF, Science Park 104, 1098 XG Amsterdam, The Netherlands

³ School of Engineering, Macquarie University, Sydney, NSW, 2109, Australia

Author contributions:

Yu conducted the AFM and PFIB characterization, and wrote the original draft. Tom performed the FDTD simulations. Both Yu and Tom contributed to the data analysis, results discussion, review & edited the manuscript. David, Bram and Albert supervised this work, reviewed & edited the manuscript. Shaozhou, Giuseppe, and Malcolm contributed to different stages of conceptualization, methodology, reviewing & editing.

7.1 Introduction

Silicon is one of the most widely used materials in the semiconductor industry due to its abundance and stable chemical and mechanical structure. It has been widely used in various applications, such as chips and microchips in electronic devices, photodiodes, photodetectors, and photovoltaic devices. A particular branch of silicon material is black silicon (BSi), the surface of which is specially processed to create a micro-/nanoscale texture [219, 256]. As such, the optical performance of BSi is superior to the un-processed silicon wafer with a planar surface, with extremely high optical absorption and low reflectance achievable over a broad spectral range. However, due to the complex nature of the BSi surface structure, adapting the academic level BSi into a commercialized device is challenging. For example, BSi with an extremely high aspect ratio will present challenges for making acceptable screen-printed contacts as used in silicon solar cells [257]. Furthermore, the increased surface area can result in inferior surface passivation [258–260]. Therefore, the state-of-the-art commercialized BSi devices are typically compromised to a less aggressive surface structure with non-optimal optical properties [261, 262].

Semiconductor device fabrication involves multi-step physical and chemical manufacturing process sequences [263]. Each variable involved in multi-step processing could potentially bring uncertainties during manufacturing. As such, modeling and simulation are well-accepted concepts in the semiconductor industry. It provides guidelines for the optimal parameters for actual device fabrication and helps researchers to rapidly understand the new technology and its capability and economic potential. There are various commercially available simulation tools developed for the semiconductor industry. Simulation software packages, such as Sentaurus [264], are comprehensively designed to solve device performance, but they are computationally expensive. Other software that provides fast approximate simulation, such as SunSolve [265] usually focuses on one aspect of the device physics (such as the optical response) to enable efficient simulation and optimization towards a specific goal (such as optical absorption).

As BSi is a relatively new concept for the semiconductor industry, there are still many challenges for correctly simulating BSi device performance. For example, it is unknown how the nanotextured surface interacts with the pre- and post-manufacturing processes. For the PV industry, it is of great interest about how the enlarged surface area impacts the dopant diffusion for emitter formation, how the passivation layer interacts with the complex surface texturing, and how the near-surface damage produced during BSi fabrication would affect the final conversion efficiency of the solar cell. To establish an accurate BSi device performance simulation and a rapid modeling technique, it is vital that modeling of the material characteristics should be validated with the fundamental material properties.

The material characteristics of BSi that are considered most important, such as optical performance and surface electrochemical reactivity, are linked to its surface morphology, i.e., the shape and dimension of the nanostructure [219, 256, 266]. Nevertheless, it is challenging to probe the BSi surface properly [236, 267]. The most adopted surface topography characterization technique is atomic force microscopy (AFM), which measures the surface height data pixel by pixel with a scanning probe [268–270]. However, for BSi surfaces, the varied processing methods and processing parameters can result in various nanostructure shapes, such as needle-like structures, grooves, hollow-like structures, cone-like structures, etc. Limited by its working principle, AFM cannot detect structures that exceed the physical size of the scanning probe or micro-nano hybrid structures that exceed the oscillation limits of the cantilever. AFM may be applicable for only a few types of upright BSi whose surface structure is not too extreme. Moreover, it is incredibly challenging to avoid AFM imaging

artifacts when characterizing very rough surfaces. These artifacts can be induced by a non-ideal tip shape, tip bending, flexing, jumping effects, the adhesion forces forming between tip and sample, or non-optimal scan settings [271–273]. The constant tip-sample interaction during a highly roughened surface measurement can also degrade or contaminate the AFM probe tip. Without using additional alternate techniques such as SEM, it can be challenging to determine the correctness of the 3D model rendered from an AFM scan.

In this work, we compare the quality of 3D rendered models of BSi surface textures obtained from AFM and Plasma Focused Ion Beam (PFIB) tomography. We aim to evaluate the 3D models qualitatively and quantitatively by comparing the morphology with their SEM images, comparing the surface statistics, and evaluating the similarity by FDTD simulation. In our previous work, PFIB tomography was demonstrated as a potentially superior alternative for AFM, especially for probing complex structures such as a BSi surface [267]. Not only can PFIB tomography detect non-upright features that the AFM probe could not reach, but it also offers a less-biased 3D rendering model and enhanced consistency to avoid the AFM artifacts arising from the repetitive probe-sample interaction during the scanning process. However, in our previous work, the quality of the PFIB rendered 3D model was evaluated by visualizing and providing a simple comparison of surface statistics. The statistics, however, were not validated in any way with their correctness. To better evaluate the advantages of the PFIB 3D model over the AFM 3D model, this chapter focuses on quantitative evaluation, and the validation will be checked against simulation results.

In this work, the quality of the 3D model is evaluated by simulating the front surface reflectance. As there is no standard way of describing how accurate the topographical measurement was, the mismatch between the simulated reflectance and the measured reflectance can be used to describe the accuracy of the reconstructed 3D model. The varied processing methods and parameters for BSi fabrication result in various surface nanostructures, such as needle-like structures, grooves, hollow-like structures, cone-like structures, etc. The irregular shapes and sizes on the order of the wavelength make it challenging to predict the light-surface interaction, making the currently well-developed fast approximation methods (such as effective medium [230, 274] and geometric optics [233, 275]) not always valid for BSi textures. One of the most common tools to accurately calculate the front surface reflection is the finite-difference time-domain (FDTD) algorithm. Although it requires significantly more computational resources than the fast approximation methods, the FDTD simulation captures all light-matter interactions by solving Maxwell's equations. As such, simulated optical properties of BSi textures include resonant nanophotonic light-matter interactions that occur on length scales of the order of the wavelength [274]. Therefore, the FDTD technique bridges the first principle calculation with the experiment results [276]. Several previous studies have successfully applied FDTD to understand and model the optical behavior of nanotextured silicon [220–222]. Here, we use the convergence between the measured reflection (%R) and the FDTD simulated %R to evaluate the accuracy of the 3D model quantitatively. We found that the front surface reflectance curve simulated from two PFIB 3D models (RIE1 and RIE2) were in good agreement with the measured reflection. In contrast, the simulated reflectance based on the AFM 3D models shows a high inconsistency level. Our work provides strong evidence that the PFIB rendered 3D model can be used as a reliable simulation input for the FDTD algorithm to accurately model and predict the BSi wafer's front surface optical characteristics. In addition to the FDTD analysis, a thorough surface statistical comparison is also demonstrated. Some critical surface statistics will be reported for both the AFM 3D model and the PFIB 3D model, which will aid the development of a fast approximation method for BSi optical simulation [274, 277]. In addition, morphological parameters critical in the BSi electrical performance will also be compared

across the AFM 3D model and the PFIB 3D model, such as enhanced area factor and specific surface area [278].

In the future, the utility of such an accurate 3D rendered BSi model can be expanded for modeling other material fundamental properties, such as surface area related electrochemical reactivity, the pre- and/or post thin-film interaction during device manufacturing, etc. It can be further developed to predict the completed BSi device performance, such as fast optical simulation [239, 265, 277] or current-voltage simulation [279] of completed BSi device with the addition of surface deposition layers and encapsulation layers.

7.2 Experimental methodology

Two different BSi samples were used for this work, each with significantly different surface structures to evaluate the quality of the rendered 3D surface models. Both BSi samples were fabricated by reactive ion etching (RIE but under different fabrication conditions, which manifested different surface texturing finish). RIE1-BSi had relatively shallower and smaller groove-like features, while RIE2-BSi had relatively deeper inverted-hollow-like features. The 3D surface models for both samples were obtained from both PFIB tomography and AFM and were used as an input to the FDTD simulations. Three 3D surface models for both BSi samples were obtained: one from PFIB tomography, designated as RIE-PFIB, and two sets from AFM, designated as RIE-AFM-HQ (high quality) and RIE-AFM-LQ (low quality). Several critical surface-related statistics were then extracted to be used for the quantitative evaluation of the 3D model quality, including but not limited to the height distribution and the convergence of the FDTD simulated reflection to the measured reflection.

Sample information

Two plasma textured silicon surfaces were fabricated using different RIE tools to achieve distinct surface morphologies.

The RIE1-BSi texture was fabricated on a polished 4-inch round silicon wafer etched using an STS DRIE Pegasus tool for 16 minutes. The reactive gases used for this sample were O_2 (100 sccm) and SF_6 (70 sccm). The coil power was 3 kW.

The RIE2-BSi texture was fabricated on a polished 6-inch round silicon wafer using an SPTS RIE system. The maskless reactive ion etching was conducted at room temperature in an O_2 and SF_6 plasma for 16 minutes, with a gas flow ratio of $O_2:Sf_6 = 1:1$, chamber pressure of 24 mTorr, and 13.56 MHz radio-frequency power of 100 W.

Representative plan view and cross-sectional view SEM images of both RIE1 and RIE2 are shown in Figure 7.1. It can be seen that the RIE1-BSi texture is relatively shallower and shows smaller groove-like features. The depth of the texturing was around 400 nm, with a smooth transition from the peak to the bottom. The RIE2-BSi texture has comparatively deeper inverted-hollow-like features with a depth of around two microns and nearly vertical sidewalls connecting the upper and lower plateaus. The high aspect-ratio nature of the RIE2-BSi texture is likely to pose a challenge for AFM scanning characterization.

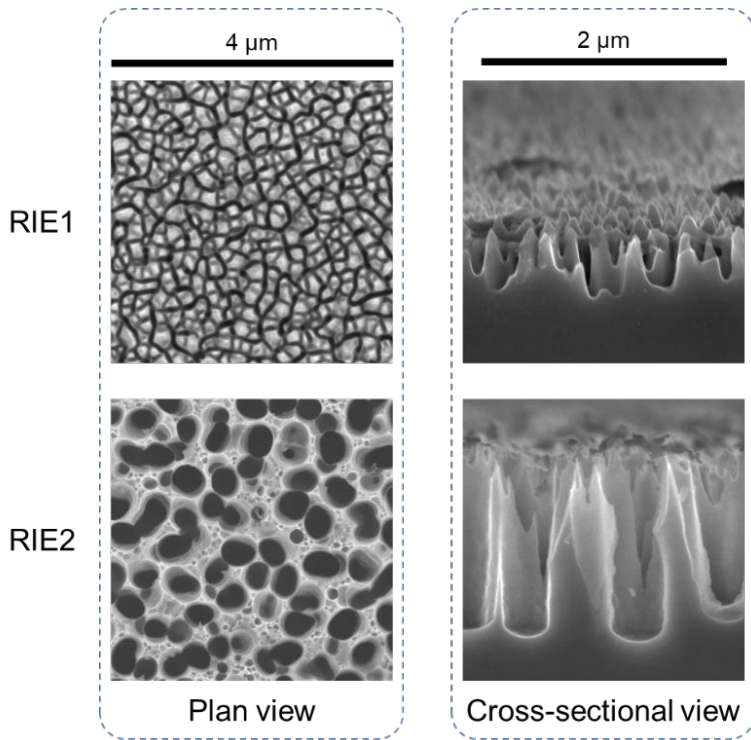


Figure 7.1: Plan view (left column) and cross-sectional view (right column) of RIE1 and RIE2, obtained using SEM.

Topographical characterization

AFM

Topographical characterization of both BSi-RIE1 and BSi-RIE2 was conducted by JEOL JSPM 5400 MkII Environmental Atomic Force Microscopy (AFM). Two sets of AFM scans were obtained for each sample, named AFM-HQ and AFM-LQ; these represent repeat measurements carried out with different AFM probes. HQ and LQ stand for “high quality” and “low quality”, respectively. AFM-LQ was considered a failed AFM attempt with visible artifacts were observed in the final 3D surface model. The probes used for RIE1-AFM-LQ were DDESP Bruker AFM probes, while TESPD Bruker AFM probes were used for RIE2-AFM-LQ. AFM-HQ was considered an acceptable AFM attempt with probe choice and settings optimized and tuned to minimize artifacts in the final 3D surface model. The probes used for both RIE1-AFM-HQ and RIE2-AFM-HQ were TESPD Bruker AFM probes. All the AFM scans were done in tapping mode over an area of 10 μm by 10 μm, with a scan-interval of 19.53 nm and a scan rate of 0.215 Hz. The tip velocity was tuned slightly around 4.30 μm/s to obtain optimal scan results.

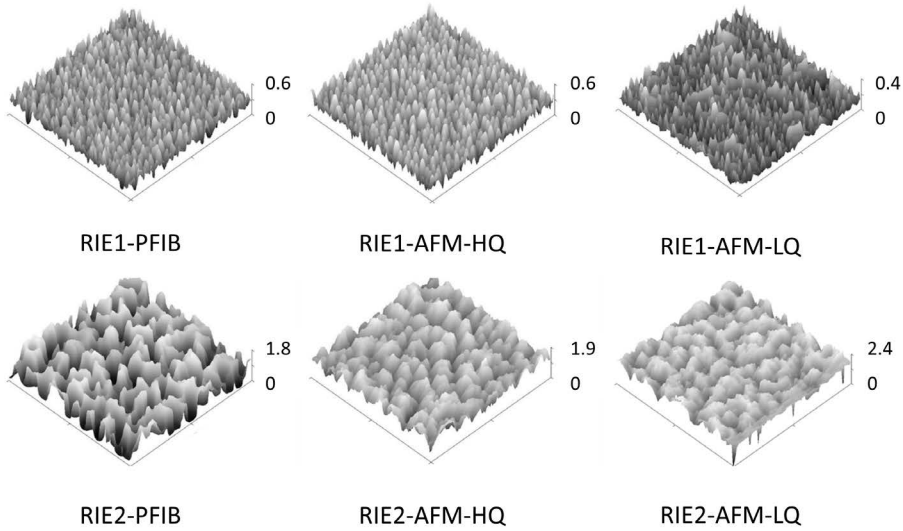


Figure 7.2: 3D surface models of the RIE1 and RIE2 samples obtained from (i) PFIB tomography, (ii) AFM-HQ, and (iii) AFM-LQ. Scans are $5 \times 5 \mu\text{m}$; height values on the z-axis are also in μm .

PFIB tomography

Topographical characterization of both BSi-RIE1 and BSi-RIE2 was also conducted by PFIB tomography. The method is described in our previously published work [280, 281]. 3D surface models of BSi-RIE1 and BSi-RIE2 obtained from PFIB tomography, AFM-HQ, and AFM-LQ are shown in Fig. 7.2.

Data comparison

Based on the working principle of PFIB-SEM tomography, the height distribution was extracted from each cross-sectional SEM image obtained during the slice-and-view process, which reveals the true cross-sectional morphology, ensuring minimized bias and high data accuracy.

After carefully choosing the AFM scanning probe and optimizing the probing parameters, the AFM-HQ scans for both RIE1-BSi and RIE2-BSi achieved similar results to their PFIB 3D model in some apparent surface statistics, regardless of whether their appearance was similar to the SEM image. In comparison, surface statistics of the AFM-LQ scans deviate significantly from RIE-AFM-HQ and the PFIB 3D model. In particular, the RIE1-AFM-LQ model appears to have multiple visible scan artifacts. The overall height was $0.2 \mu\text{m}$ shallower than the other two 3D models. For the RIE2-AFM-LQ model, due to the nature of the AFM working principle, it is difficult for the AFM probe to reach the bottom for such deep inverted-hollow-like BSi features. The AFM probe geometry restrained the detection of the bottom feature. Therefore, the depth of the structure at the artifact-free area appeared to be much shallower than the PFIB and AFM-HQ models.

Optical reflectance measurement

Optical characteristics were determined using a commercial PerkinElmer Lambda 1050 spectrophotometer to measure the wavelength-dependent total reflection (R_{Total}) and scattered Reflection ($R_{Scatter}$). Both were measured using a 150 mm integrating sphere, with the BSi specimen placed on the reflectance port (see Fig. 7.3). $R_{Scatter}$ was the measured diffuse reflectance with specular exclusion port un-plugged during the measurement. The incident beam was regulated into a 6 mm diameter circular beam by an adjustable iris. The measurement wavelength range was 250 nm - 1500 nm, with a step size of 5 nm. Due to the geometry of the accessory, the sample placed on the Reflectance Port was at an angle of 8 degrees relative to the incident beam during the reflectance measurement.

The R_{Total} and $R_{Scatter}$ were used for the calculation of specular reflectance ($R_{Specular}$) as defined in Equation (7.1):

$$R_{Specular} = R_{Total} - R_{Scatter}. \quad (7.1)$$

In addition, a double-side polished monocrystalline silicon wafer, with a thickness of 500 μm , was used as a reference reflectance standard. The measured reflectance was used to validate the optical constants of Si that were used as a simulation input.

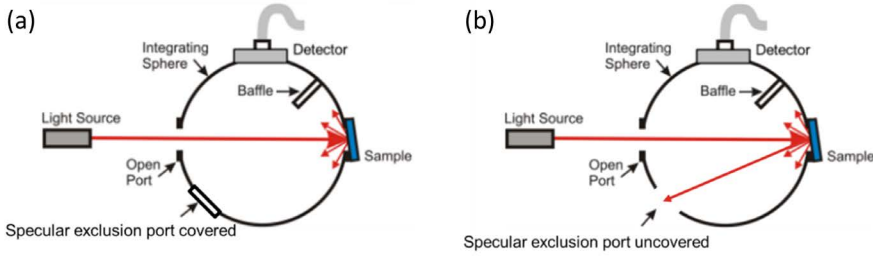


Figure 7.3: Measurement principle for (a) R_{Total} and (b) $R_{Scatter}$. The dimension of the specular exclusion port is roughly 33 mm².

Reflectance simulation method

Modeling of the %R was performed using the Ansys Lumerical FDTD simulation package [72]. The obtained 3D AFM and PFIB surface models were used as geometric inputs to define the unit cell of the silicon-air interface, and the optical constants of silicon were defined using values from the literature [74]. Periodic boundary conditions were employed along the surface, and perfectly matched layer (PML) boundary conditions in the out-of-plane direction. Diffraction from the unit cell periodicity is found to be negligible when the lateral unit cell size (5 μm by 5 μm) is much larger than the wavelength — this is not the case when a unit cell length of 1-3 μm is used, or if the surface texture is not (semi-)random. The input source was a broadband plane-wave (wavelengths spanning 200 - 1000 nm); separate simulations were performed for s- and p-polarizations and then averaged for comparison to the unpolarized experimental data. The plane wave was inserted at normal incidence instead of the experimental tilt of 8 degrees because the resulting simulated reflection is almost identical. Modeling at normal incidence allows for more robust simulation of all wavelengths in a single run, reducing the computational requirements.

A power monitor was positioned above the Si surface to collect the reflected light — this monitor in the near-field records the time-averaged electric field intensity, from which the simulated %R was determined. To differentiate between the specular and diffuse parts of %R, we used Lumerical's built-in far-field projection algorithm to obtain the calculated hemispherical reflection at a distance of 1 meter (Fig. 7.4). Analogous to the measurement, we calculated the intensity in the center of the hemisphere within 6.7 degrees from the normal to obtain the specular/diffuse %R. The Fraunhofer diffraction caused by the transform of the near-fields on the unit cell to the hemisphere in the far-field is assumed to be negligible for the comparison of specular and diffuse %R because the diffraction dip occurs beyond 15 degrees from the normal. The simulations were found to converge with a uniform mesh size of 5 nm in all directions, a distance of at least half the largest wavelength between the surface and the PML boundaries, and conformal mesh refinement.

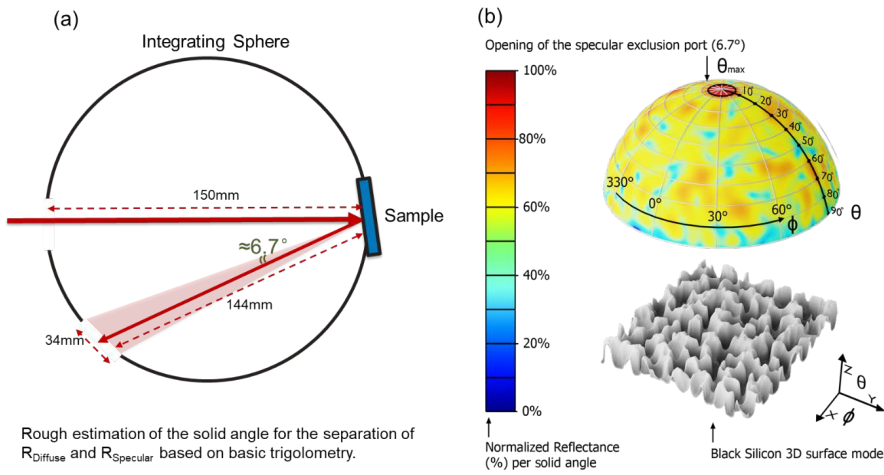


Figure 7.4: (a) Estimated solid angle for the separation of R_{Scatter} and R_{Specular} , to be used for the data analysis of the FDTD simulation results. The orientation and position of the BSi 3D model at the distance of $f = 144$ mm are indicated. (b) Illustration of a hemispherical far-field reflectance modeling of the BSi surface structure.

7.3 Results and discussion

Surface statistics of RIE1 and RIE2, extracted from 3D models

A direct comparison between the sample's SEM and their 3D models reconstructed by either PFIB or AFM is shown in Fig. 7.5; these images are all shown in plan-view. A qualitative comparison of these images can offer high-level insight into the accuracy of the models. The first impression from visual observation is that the PFIB models for both the BSi-RIE1 sample and the BSi-RIE2 sample retain the surface features revealed by SEM (groove-like for BSi-RIE1 and inverted-hollow-like for BSi-RIE2). In other words, the PFIB 3D models for both RIE1-BSi and RIE2-BSi show comparably better similarity than both AFM-HQ and AFM-LQ models. In contrast, both AFM reconstructed models are not similar to their corresponding SEM images.

In particular, the deep inverted-hollow-like BSi-RIE2 sample was considered too aggressive to the AFM probe geometry, and the resulting AFM models are severely tilted due to the contacting angle of the AFM probe. Interestingly, both AFM scans (AFM-HQ and AFM-LQ) for RIE2-BSi were obtained with identical probe and characterization settings used for the AFM scanning. Nevertheless, they still show significant statistical inconsistency because the RIE2 structure challenges the probe to operate under optimal conditions.

A discussion regarding differences in the surface statistics based on the reconstructed 3D models will be given. The height distribution of RIE1 3D models and RIE2 3D models are displayed in Fig. 7.6, where the X-axis represents the height values of each surface datapoint. The Y-axis represents the normalization of the density of the corresponding height value. The RIE1-PFIB and RIE1-AFM-HQ show similar height distributions (normal distribution), while the RIE1-AFM-LQ deviates significantly. For the RIE2-AFM-HQ and RIE2-AFM-LQ, the heights profiles are of similar shape. However, the peak location of the RIE2-AFM-HQ profile was $\sim 0.5\text{ }\mu\text{m}$ deeper than the RIE2-AFM-LQ profile. This difference might be because the AFM probe could reach a deeper level of the structure while probing the surface after careful optimization. In comparison, the PFIB profile shows double peaks, one at $\sim 0.4\text{ }\mu\text{m}$ depth and one at $\sim 1.7\text{ }\mu\text{m}$ depth. This profile matches what has been observed in the SEM: the deep inverted-hollow-like textures of RIE2 had two dominant plateaus features.

Some critical surface statistical parameters extracted from the 3D surface models are listed in Table 7.1. Using the PFIB 3D model as a reference, the percentage value in the bracket means how much the AFM 3D model extracted parameter deviated from the PFIB model.

The first parameter is the mean square roughness (RMS), which describes the irregularity of height data values. The reported RMS for RIE1-AFM-HQ and RIE1-PFIB were of comparable value, while the RMS of RIE2-AFM-HQ is only half that of RIE2-PFIB. This is because, unlike the BSi-RIE1, the BSi-RIE2 is too deep for the AFM probe-sample interaction. Therefore the resulting RIE2-AFM-HQ rendered 3D model is not as rough as the RIE2-PFIB model, with an RMS value of less than half of the RIE2-PFIB.

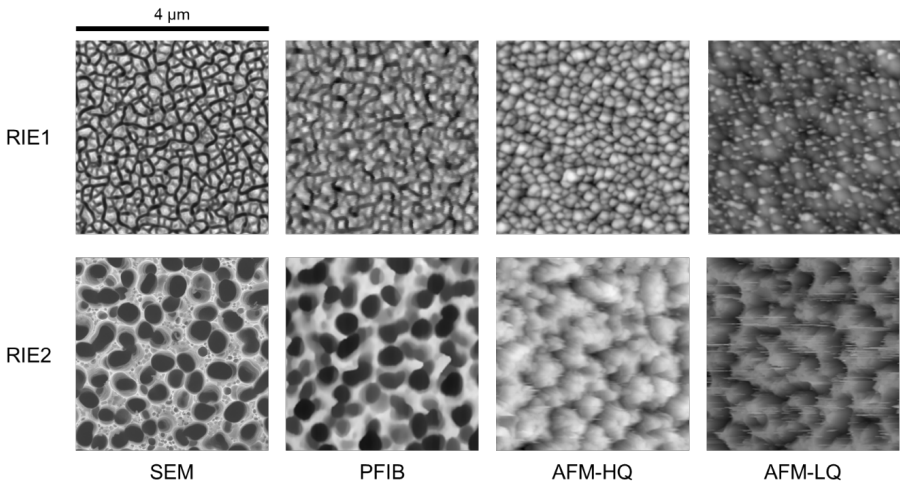


Figure 7.5: Direct comparison between the scanning electron microscopy images of the RIE1 and RIE2 samples and their 3D models reconstructed by PFIB, AFM-HQ, and AFM-LQ.

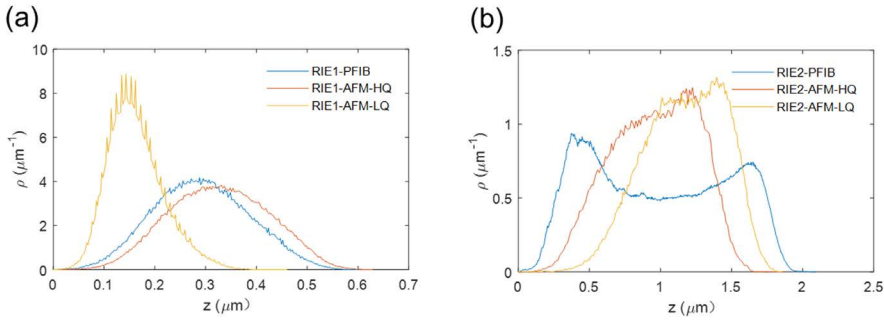


Figure 7.6: Height distribution of (a) RIE1 and (b) RIE2 extracted from PFIB and AFM models.

Another parameter, skewness (Ssk), describes the degree of bias of the roughness features (asperity). A symmetrical structure, relative to the mean plane, will have zero Ssk value. If the height distribution is skewed above the mean plane, Ssk will report a negative value and vice versa. As a comparison, RIE1-AFM-HQ and RIE1-PFIB are similar and have height distributions that are slightly skewed. However, the skewness of RIE2-AFM-HQ and RIE2-PFIB are of opposite sign, indicating their height distributions are inversely skewed.

The last two parameters, enhanced area factor (EAF) and specific surface area (SSA), describe the surface enlargement. The EAF describes the ratio of the total surface area to the projected planar area, which is most widely used in the literature. The SSA, defined as the ratio of the surface area to the volume of the underlying silicon nanofeature, was recently introduced to BSi in our previous work [278]. It is directly related to surface reactivity and found to be a better indicator of the surface chemical reaction rate [278]. Both BSi-RIE1 and BSi-RIE2 reported the highest EAF and SSA values from the PFIB 3D model. The SSA for the RIE1-AFM-HQ is reported to be 15.3% less than the RIE1-PFIB, while the SSA for the RIE2-AFM-HQ is 38.0% less than the RIE2-PFIB. As the SSA describes the ratio between the surface atoms to the internal atoms within the defined volume, the AFM-HQ model will report underestimated surface reactivity if used as simulation input.

Table 7.1: Critical surface statistical parameters for BSi-RIE1 and BSi-RIE2, extracted by 3D models of PFIB, AFM-HQ, and AFM-LQ.

	BSi-RIE1			BSi-RIE2		
	PFIB	AFM-HQ	AFM-LQ	PFIB	AFM-HQ	AFM-LQ
RMS	93.6	96.8 (3.4%)	54.8 (-41.5%)	487.2	279.5 (-42.6%)	296.9 (-39.1%)
Ssk	0.09	0.01	0.62	0.09	-0.30	-0.21
EAF	3.07	2.91 (-5.3%)	1.63 (-46.7%)	5.65	4.20 (-25.7%)	4.84 (-14.2%)
SSA	10.47	8.87 (-15.3%)	9.98 (-4.7%)	5.76	3.58 (-38.0%)	5.02 (-12.8%)

Simulated hemispherical reflectance

The FDTD simulated hemispherical reflectance results for both RIE1-PFIB and RIE2-PFIB are depicted in Fig. 7.7. As demonstrated in previous research, the reflectance spectrum for crystalline silicon exhibits two distinct peaks, E1 (~ 365 nm) and E2 (~ 275 nm) [282–284], which are correlated with silicon material quality, such as absorption coefficient [282, 285], refractive index [282, 285] and dielectric function [285, 286]. In particular, the E2 peak is highly correlated to surface etching. Therefore, our group’s previous work has extended the use of E1 and E2 peaks into a 2D mapping for surface texturing [287]. The FDTD simulation results show that the reflection for both RIE1 and RIE2 are well scattered at E1 and E2 peaks, which explains the root cause of the excellent optical behavior of BSi.

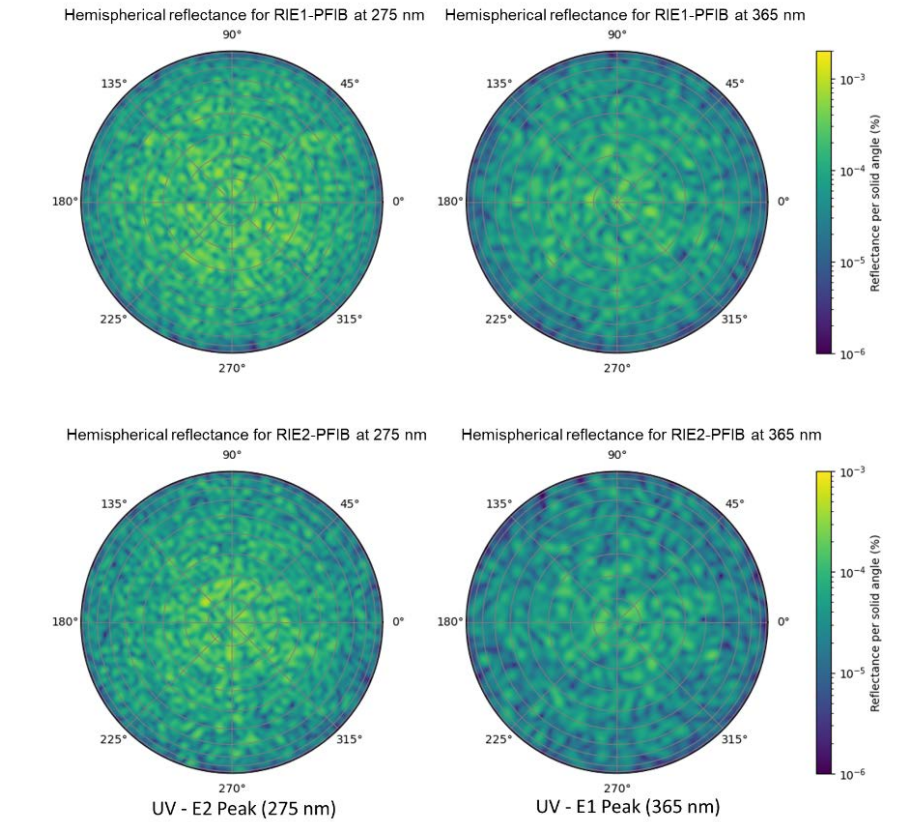


Figure 7.7: Simulated hemispherical reflectance of RIE1-PFIB (top row) and RIE2-PFIB (bottom row) at the E1 and E2 peaks.

Comparison of the measured reflectance data

The measured optical reflectance (%R) characteristics, including R_{Total} , $R_{Scatter}$ and $R_{Specular}$, are shown in Fig. 7.8 as the bold blue line. The comparison of %R results between RIE1 and RIE2 indicates that differences in the surface nanostructure morphology would impact the reflectance characteristics. The BSi-RIE2 sample was superior in light trapping and showed much-suppressed surface reflectance compared to the BSi-RIE1 sample.

To further evaluate the quality of the AFM 3D model and the PFIB 3D model, we use the convergence of the FDTD simulated reflection to the measured %R for quantitative evaluation.

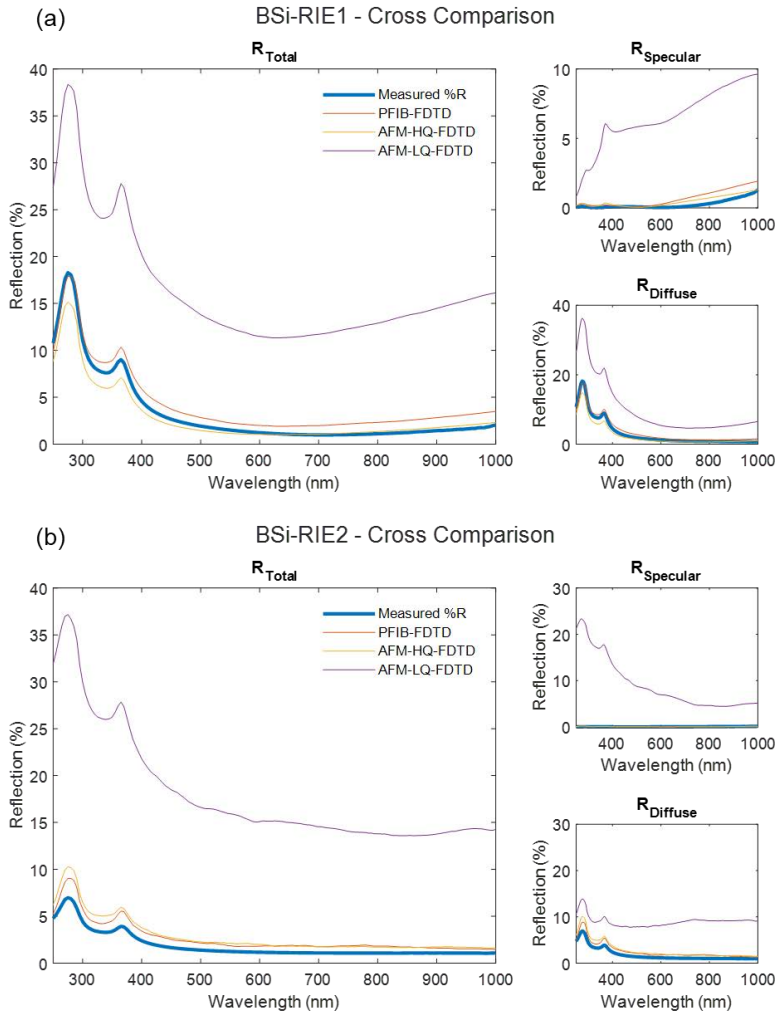


Figure 7.8: Cross comparison of R_{Total} , $R_{Scatter}$ and $R_{Specular}$ for (a) BSi-RIE1 and (b) BSi-RIE2.

The comparison between the measured %R and FDTD simulated reflectance based on the 3D surface model obtained by PFIB and AFM approaches are also shown in Fig. 7.8.

For RIE1, both PFIB-%R and AFM-HQ-%R are shown to be in good agreement with the measured %R. Surprisingly, for RIE2, the AFM-HQ-%R still agrees well with the measured %R, although differences in surface morphology can be observed visually and from the statistical results reported in Table 7.1. This suggests that the extra deep inverted-hollow feature, which is not detectable by the AFM probe, does not significantly contribute to the light trapping in this case. Therefore, the resulting FDTD simulated %R from the AFM-HQ model is about the same level as the PFIB model. The PFIB-FDTD of RIE1 is closer to the measured %R at the UV range, while the AFM-HQ-FDTD is closer to the measured %R at the VIS and NIR range.

The %R measurement settings had an incident beam angle of 8 degrees relative to the sample's zenith. However, the FDTD simulated %R was carried with a normal incident beam, as plane-wave simulation with a broad wavelength span and angled-incidence would drastically increase the computational cost. Such differences in the simulation settings may be the reason for the small mismatch between the PFIB/AFM-HQ simulated measured Reflection(%). However, other factors may also contribute to the simulation/measurement discrepancy, such as the difference between the simulation scale (on the order of square micrometers) to the measurement scale (on the order of square millimeters).

In contrast, the AFM-LQ-FDTD for both BSi-RIE1 and BSi-RIE2 drastically deviates from the measured R data. The surface morphology difference and statistical results also provide strong evidence that the 3D model does not accurately represent the true surface structure and characteristics of the actual BSi sample. Because AFM probing is highly sensitive to the experimental settings, there is a high potential that an erroneous surface model will be obtained. However, the surface rendered by PFIB tomography is based on the information extracted from the specimen's SEM images obtained during the slice-and-view, which can be directly checked against the bare specimen's cross-sectional SEM taken before the PFIB sampling. Our previous work described the PFIB sampling method in detail [267] and is less likely to obtain bias or artifacts when reconstructing the surface 3D model.

In addition to the reflectance line plots, the statistical convergence between the FDTD simulated reflectance and the measured reflectance is shown in Table 7.2. The root-mean-square-error (RMSE) (as defined in Equation (7.2)) was used for convergence evaluation, indicating how much in proportional the squared errors are between the FDTD simulated %R and the measured %R.

$$RMSE = \sqrt{\frac{\int (R_{FDTD} - R_{Measured})^2 d\lambda}{\int (R_{Measured})^2 d\lambda}} \quad (7.2)$$

From Table 7.2, we can see that the FDTD simulated %R for both the PFIB 3D model and the AFM-HQ 3D model were close to the measured %R data for Sample RIE1-BSi. The RMSE of RIE1-PFIB and RIE1-AFM-HQ were similar. For total reflectance, both PFIB and AFM-HQ were around 0.2, while the RMSE of RIE1-AFM-LQ was reported to be 2.6, which is around ten times higher than the other two. Table 7.2 also shows that the FDTD simulated data for the PFIB 3D model remains at the same level for Sample RIE2. At the same time, the AFM-LQ deviated drastically with an RMSE of 7.31 over the whole wavelength range, around twenty times greater than that of the RIE2-PFIB data.

Previously, it was reported that the ultraviolet (UV) reflectance behavior is particularly sensitive to surface nanoetching [287]. Therefore, a UV reflectance map is used to monitor the texturing variation quickly. Therefore, Table 7.2 also shows the deviation of FDTD simulated %R to the measured %R in the UV (250 nm to 400 nm) only range. In this range, the RMSE

Table 7.2: Statistic comparison of the FDTD simulated reflectance and the measured reflectance for sample RIE1 and RIE2, evaluated by RMSE.

	RIE1 RMSE			RIE2 RMSE		
	PFIB	AFM-LQ	AFM-HQ	PFIB	AFM-LQ	AFM-HQ
R_{Total} (250-1000 nm)	21.5%	260.4%	18.8%	38.3%	731.0%	51.6%
(250-400 nm)	9.0%	163.2%	18.6%	30.8%	557.7%	47.9%
$R_{Specular}$ (250-1000 nm)	127.7%	1633.4%	63.6%	110.9%	21972.3%	87.6%
(250-400 nm)	241.4%	6176.7%	289.1%	460.8%	83965.5%	3.9%
$R_{Scatter}$ (250-1000 nm)	14.4%	134.1%	20.5%	36.6%	318.3%	50.5%
(250-400 nm)	8.3%	77.0%	20.2%	28.7%	136.7%	46.2%

between the AFM-LQ %R to the measured %R for BSi-RIE1 is tenfold greater than the PFIB %R and AFM-HQ %R. In particular, the RMSE of AFM-LQ simulated $R_{Scatter}$ for BSi-RIE2 was nearly two hundred times higher than the PFIB simulated $R_{Scatter}$. This further supports the hypothesis that the BSi-RIE2 AFM-LQ 3D model poorly represents the true surface structure and corresponding optical performance.

Comparing the 3D models rendered from PFIB tomography and AFM, the PFIB 3D models qualitatively represent the sample's real morphology more accurately. By summarising the statistical results presented in Table 7.1, we found that the PFIB 3D model for both RIE samples reports a much higher surface roughness and area-to-volume ratio, which could be linked to a much greater chemical reaction rate. When referring to the FDTD simulated %R results presented in Table 7.2, it can be observed that PFIB 3D models, although showing just slight improvement towards the well-optimized AFM 3D model, were able to predict the %R accurately for both the RIE1 and RIE2 samples. This enables a more accurate prediction of the BSi material properties, especially when fully integrated into a final BSi device. The BSi devices has been widely used in multiple areas, such as photovoltaic applications [288, 289], photo-current sensors [290–294], photoelectrochemical devices [295–300], biosensors [301, 302], etc. Our work provides strong evidence that PFIB tomography is a better substitute to the AFM for surface topographical characterization, especially in probing highly roughened BSi surfaces. While PFIB is a destructive technique and may take longer than the conventional AFM approach, it has the benefit of consistent and easily validated results (by SEM). It can be used for extreme BSi surfaces with features such as vertical sidewalls or overhanging structures, which are not compatible with AFM probing. With the aid of PFIB tomography, the accurate BSi 3D models can be used to better model and simulate the BSi device performance.

7.4 Conclusion

This chapter compared various surface statistical parameters generated from PFIB 3D and AFM 3D models of BSi, which should correlate to the BSi surface optical and electrochemical performances. For a shallower textured surface with small groove-like features (RIE1), PFIB 3D model and AFM-HQ 3D model resulted in similar values for most surface profile parameters, such as RMS and Ssk, indicating that both surface models are in good agreement. However, the PFIB model reported a higher SSA value, which is a vital input parameter for predicting

the surface chemical reaction rates. For a more challenging deeper textured surface with inverted-hollow-like features (RIE2), the surface profile parameters from PFIB and AFM-HQ models deviate significantly, indicating that the reconstructed 3D surface generated from PFIB and AFM has different surface morphology. Similarly, the SSA value from PFIB is much higher than from the AFM-HQ model.

Even though surface topography statistics from the two models were proven to be dissimilar to each other, both PFIB and AFM-HQ show good convergence to measured %R when used as input parameters for FDTD front surface reflectance simulation. Both can be used to predict the optical performance of BSi accurately. By contrast, the AFM-LQ 3D modeled parameters deviate severely from the measured reflectance, tenfold greater than AFM-HQ to PFIB. In particular, the RMSE for RIE2-AFM-LQ in the UV range is as high as 83965.5%, indicating the data is significantly deviating from the measured %R.

In summary, AFM for BSi surface topographical characterization is highly dependent on the AFM probe selection and setting parameters, with significant potential for erroneous. PFIB 3D models are proven to be more accurate and consistent than the AFM-HQ models when used as model and simulation inputs. In the future, PFIB tomography, as a substitute for AFM surface probing technology, can further aid with developing and validating fast approximation methods for optical device simulation, such as effective medium and geometric optics, helping to reduce the computational cost for BSi device simulation.

Bibliography

- [1] J. Hecht, *City of Light: The Story of Fiber Optics*, revised ed. (Oxford University Press, 2004).
- [2] D. Bardell, *The Biologists' Forum: The invention of the microscope*, BIOS **75**, 78 (2004).
- [3] R. Feynman, R. Leighton, and M. Sands, *The Feynman Lectures on Physics*, Vol. 1, 50th ed. (Basic Books, 2011).
- [4] United Nations, *Policy Briefs in Support of the High-Level Political Forum Leveraging Energy Action for Advancing the Sustainable Development Goals*, (2021).
- [5] IEA, *Key World Energy Statistics*, Tech. Rep. (2021).
- [6] S. Chu, Y. Cui, and N. Liu, *The path towards sustainable energy*, Nature Materials **16**, 16 (2016).
- [7] B. Obama, *The irreversible momentum of clean energy*, Science **355**, 126 (2017).
- [8] J. Nelson, *The Physics of Solar Cells*, 1st ed. (World Scientific Publishing Co., 2003).
- [9] U. Wurfel, A. Cuevas, and P. Wurfel, *Charge carrier separation in solar cells*, IEEE Journal of Photovoltaics **5**, 461 (2015).
- [10] D. Goldsmith and T. Owen, *The Search For Life In The Universe*, 3rd ed. (University Science Books, 2001).
- [11] Subcommittee 09, *Standard Tables for Reference Solar Spectral Irradiances: Direct Normal and Hemispherical on 37° Tilted Surface*, in *Book of Standards Volume 14.04* (ASTM International, 2020).
- [12] W. Shockley and H. J. Queisser, *Detailed Balance Limit of Efficiency of p-n Junction Solar Cells*, Journal of Applied Physics **32**, 510 (1961).
- [13] A. Polman, M. Knight, E. C. Garnett, B. Ehrler, and W. C. Sinke, *Photovoltaic materials: Present efficiencies and future challenges*, Science **352**, 307 (2016).
- [14] U.S. Energy Information Administration, *Average Operating Heat Rate for Selected Energy Sources*, (2021).
- [15] W. C. Sinke, *Development of photovoltaic technologies for global impact*, Renewable Energy **138**, 911 (2019).
- [16] M. Yamaguchi, K.-H. Lee, P. Schygulla, F. Dimroth, T. Takamoto, R. Ozaki, K. Nakamura, N. Kojima, and Y. Ohshita, *Approaches for High-Efficiency III-V/Si Tandem Solar Cells*, Energy and Power Engineering **13**, 413 (2021).
- [17] E. C. Warmann, P. Espinet-Gonzalez, N. Vaidya, S. Loke, A. Naqavi, T. Vinogradova, M. Kelzenberg, C. Leclerc, E. Gdoutos, S. Pellegrino, and H. A. Atwater, *An ultralight concentrator photovoltaic system for space solar power harvesting*, Acta Astronautica **170**, 443 (2020).

- [18] ITRPV, *International technology roadmap for photovoltaic*, Tech. Rep. (2020).
- [19] J. S. Van Der Burgt and E. C. Garnett, *Nanophotonic Emission Control for Improved Photovoltaic Efficiency*, ACS Photonics **7**, 1589 (2020).
- [20] B. Ehrler, E. Alarcón-Lladó, S. W. Tabernig, T. Veeken, E. C. Garnett, and A. Polman, *Photovoltaics Reaching for the Shockley–Queisser Limit*, ACS Energy Letters **5**, 3029 (2020).
- [21] J. Perlin, *Let it shine* (New World Library, 2013).
- [22] M. A. Green, Y. Hishikawa, W. Warta, E. D. Dunlop, D. H. Levi, J. Hohl-Ebinger, and A. W. Ho-Baillie, *Solar cell efficiency tables (version 50)*, Progress in Photovoltaics: Research and Applications **25**, 668 (2017).
- [23] M. F. Ashby, P. J. Ferreira, and D. L. Schodek, *An Evolutionary Perspective*, in *Nanomaterials, Nanotechnologies and Design* (Elsevier, 2009) pp. 17–39.
- [24] A. Cordaro, J. Van De Groep, S. Raza, E. F. Pecora, F. Priolo, and M. L. Brongersma, *Antireflection High-Index Metasurfaces Combining Mie and Fabry–Pérot Resonances*, ACS Photonics **6**, 453 (2019).
- [25] G. Mie, *Beiträge zur Optik trüber Medien, speziell kolloidaler Metallösungen*, Annalen der Physik **330**, 377 (1908).
- [26] P. Spinelli, M. A. Verschuuren, and A. Polman, *Broadband omnidirectional antireflection coating based on subwavelength surface Mie resonators*, Nature Communications **3**, 692 (2012).
- [27] H. A. Atwater and A. Polman, *Plasmonics for improved photovoltaic devices*, Nature Materials **9**, 205 (2010).
- [28] M. A. van de Haar, R. Maas, B. Brenny, and A. Polman, *Surface plasmon polariton modes in coaxial metal-dielectric-metal waveguides*, New Journal of Physics **18**, 043016 (2016).
- [29] A. Polman and H. A. Atwater, *Photonic design principles for ultrahigh-efficiency photovoltaics*, Nature Materials **11**, 174 (2012).
- [30] A. I. Kuznetsov, A. E. Miroshnichenko, M. L. Brongersma, Y. S. Kivshar, and B. Luk'yanchuk, *Optically resonant dielectric nanostructures*, Science **354**, 846 (2016).
- [31] M. C. Van Lare and A. Polman, *Optimized Scattering Power Spectral Density of Photovoltaic Light-Trapping Patterns*, ACS Photonics **2**, 822 (2015).
- [32] E. C. Garnett, B. Ehrler, A. Polman, and E. Alarcon-Llado, *Photonics for Photovoltaics: Advances and Opportunities*, ACS Photonics **8**, 61 (2021).
- [33] IEA, *World Energy Outlook 2021*, (2021).
- [34] M. Kryszak and L. W. Wang, *The value of aesthetics in the BIPV roof products segment: a multiperspective study under European market conditions*, Energy Sources, Part A: Recovery, Utilization, and Environmental Effects (2020), 10.1080/15567036.2020.1807656.

- [35] T. E. Kuhn, C. Erban, M. Heinrich, J. Eisenlohr, F. Ensslen, and D. H. Neuhaus, *Review of technological design options for building integrated photovoltaics (BIPV)*, Energy and Buildings **231**, 110381 (2021).
- [36] V. Neder, S. L. Luxembourg, and A. Polman, *Efficient colored silicon solar modules using integrated resonant dielectric nanoscatterers*, Applied Physics Letters **111**, 073902 (2017).
- [37] B. Blasi, T. Kroyer, T. Kuhn, and O. Hohn, *The MorphoColor Concept for Colored Photovoltaic Modules*, IEEE Journal of Photovoltaics **11**, 1305 (2021).
- [38] G. Lozano, S. R. Rodriguez, M. A. Verschuuren, and J. Gómez Rivas, *Metallic nanostructures for efficient LED lighting*, Light: Science & Applications **5**, e16080 (2016).
- [39] E. Khaidarov, Z. Liu, R. Paniagua-Domínguez, S. T. Ha, V. Valuckas, X. Liang, Y. Akimov, P. Bai, C. E. Png, H. V. Demir, and A. I. Kuznetsov, *Control of LED Emission with Functional Dielectric Metasurfaces*, Laser and Photonics Reviews **14**, 1 (2020).
- [40] G. Lozano, D. J. Louwers, S. R. Rodríguez, S. Murai, O. T. Jansen, M. A. Verschuuren, and J. Gómez Rivas, *Plasmonics for solid-state lighting: enhanced excitation and directional emission of highly efficient light sources*, Light: Science & Applications **2**, e66 (2013).
- [41] F. Prins, D. K. Kim, J. Cui, E. De Leo, L. L. Spiegel, K. M. McPeak, and D. J. Norris, *Direct Patterning of Colloidal Quantum-Dot Thin Films for Enhanced and Spectrally Selective Out-Coupling of Emission*, Nano Letters **17**, 1319 (2017).
- [42] N. D. Bronstein, Y. Yao, L. Xu, E. O'Brien, A. S. Powers, V. E. Ferry, A. P. Alivisatos, and R. G. Nuzzo, *Quantum Dot Luminescent Concentrator Cavity Exhibiting 30-fold Concentration*, ACS Photonics **2**, 1576 (2015).
- [43] N. D. Bronstein, L. Li, L. Xu, Y. Yao, V. E. Ferry, A. P. Alivisatos, and R. G. Nuzzo, *Luminescent solar concentration with semiconductor nanorods and transfer-printed micro-silicon solar cells*, ACS Nano **8**, 44 (2014).
- [44] N. J. Thompson, M. W. B. Wilson, D. N. Congreve, P. R. Brown, J. M. Scherer, T. Bischof, M. Wu, N. Geva, M. Welborn, T. V. Voorhis, V. Bulović, M. G. Bawendi, and M. Baldo, *Energy harvesting of non-emissive triplet excitons in tetracene by emissive PbS nanocrystals*, Nature Materials **13**, 1039 (2014).
- [45] C. Ye, S. Chen, J. Liao, Y. S. Zhang, X. Wang, and Y. Song, *Efficiently Enhanced Triplet–Triplet Annihilation Upconversion Boosted by Multibandgaps Photonic Crystals*, The Journal of Physical Chemistry C **124**, 18482 (2020).
- [46] N. V. Hoang, A. Pereira, H. S. Nguyen, E. Drouard, B. Moine, T. Deschamps, R. Orobtcouk, A. Pillonnet, and C. Seassal, *Giant Enhancement of Luminescence Down-Shifting by a Doubly Resonant Rare-Earth-Doped Photonic Metastructure*, ACS Photonics **4**, 1705 (2017), arXiv:1303.4151 .
- [47] N. J. Davis, J. R. Allardice, J. Xiao, A. J. Petty, N. C. Greenham, J. E. Anthony, and A. Rao, *Singlet Fission and Triplet Transfer to PbS Quantum Dots in TIPS-Tetracene Carboxylic Acid Ligands*, Journal of Physical Chemistry Letters **9**, 1454 (2018).

- [48] H. Mertens, J. S. Biteen, H. A. Atwater, and A. Polman, *Polarization-Selective Plasmon-Enhanced Silicon Quantum-Dot Luminescence*, *Nano Letters* **6**, 2622 (2006).
- [49] H. Mertens and A. Polman, *Plasmon-enhanced erbium luminescence*, *Applied Physics Letters* **89**, 1 (2006).
- [50] A. G. Curto, G. Volpe, T. H. Taminiau, M. P. Kreuzer, R. Quidant, and N. F. van Hulst, *Unidirectional Emission of a Quantum Dot Coupled to a Nanoantenna*, *Science* **329**, 930 (2010).
- [51] T. Kosako, Y. Kadoya, and H. F. Hofmann, *Directional control of light by a nano-optical Yagi-Uda antenna*, *Nature Photonics* **4**, 312 (2010).
- [52] T. Coenen, F. Bernal Arango, A. Femius Koenderink, and A. Polman, *Directional emission from a single plasmonic scatterer*, *Nature Communications* **5**, 1 (2014).
- [53] T. Shegai, S. Chen, V. D. Miljković, G. Zengin, P. Johansson, and M. Käll, *A bimetallic nanoantenna for directional colour routing*, *Nature Communications* **2**, 481 (2011).
- [54] J. van de Groep and A. Polman, *Designing dielectric resonators on substrates: Combining magnetic and electric resonances*, *Optics Express* **21**, 26285 (2013).
- [55] I. Staude, A. E. Miroshnichenko, M. Decker, N. T. Fofang, S. Liu, E. Gonzales, J. Dominguez, T. S. Luk, D. N. Neshev, I. Brener, and Y. Kivshar, *Tailoring directional scattering through magnetic and electric resonances in subwavelength silicon nanodisks*, *ACS Nano* **7**, 7824 (2013).
- [56] Y. H. Fu, A. I. Kuznetsov, A. E. Miroshnichenko, Y. F. Yu, and B. Luk'yanchuk, *Directional visible light scattering by silicon nanoparticles*, *Nature Communications* **4**, 1527 (2013).
- [57] Y. Yang, A. E. Miroshnichenko, S. V. Kostinski, M. Odit, P. Kapitanova, M. Qiu, and Y. S. Kivshar, *Multimode directionality in all-dielectric metasurfaces*, *Physical Review B* **95**, 165426 (2017).
- [58] A. Capretti, A. Lesage, and T. Gregorkiewicz, *Integrating Quantum Dots and Dielectric Mie Resonators: A Hierarchical Metamaterial Inheriting the Best of Both*, *ACS Photonics* **4**, 2187 (2017).
- [59] A. F. Cihan, A. G. Curto, S. Raza, P. G. Kik, and M. L. Brongersma, *Silicon Mie resonators for highly directional light emission from monolayer MoS₂*, *Nature Photonics* **12**, 284 (2018).
- [60] I. Staude, V. V. Khardikov, N. T. Fofang, S. Liu, M. Decker, D. N. Neshev, T. S. Luk, I. Brener, and Y. S. Kivshar, *Shaping Photoluminescence Spectra with Magnetolectric Resonances in All-Dielectric Nanoparticles*, *ACS Photonics* **2**, 172 (2015).
- [61] A. Vaskin, S. Liu, S. Addamane, P. P. Vabishchevich, Y. Yang, G. Balarishnan, M. B. Sinclair, T. Pertsch, I. Brener, and I. Staude, *Manipulation of quantum dot emission with semiconductor metasurfaces exhibiting magnetic quadrupole resonances*, *Optics Express* **29**, 5567 (2021).
- [62] S. Murai, G. W. Castellanos, T. V. Raziman, A. G. Curto, and J. G. Rivas, *Enhanced Light Emission by Magnetic and Electric Resonances in Dielectric Metasurfaces*, *Advanced Optical Materials* **8**, 1902024 (2020).

- [63] H. Agrawal and E. C. Garnett, *Nanocube Imprint Lithography*, ACS Nano **14**, 11009 (2020).
- [64] A. Gopal, K. Hoshino, and X. Zhang, *Nano-stamping of quantum dot based inorganic light emitting devices*, in *2009 IEEE/LEOS International Conference on Optical MEMS and Nanophotonics*, Figure 4 (IEEE, 2009) pp. 85–86.
- [65] M. K. Choi, J. Yang, K. Kang, D. C. Kim, C. Choi, C. Park, S. J. Kim, S. I. Chae, T. H. Kim, J. H. Kim, T. Hyeon, and D. H. Kim, *Wearable red-green-blue quantum dot light-emitting diode array using high-resolution intaglio transfer printing*, Nature Communications **6**, 1 (2015).
- [66] T. H. Kim, K. S. Cho, E. K. Lee, S. J. Lee, J. Chae, J. W. Kim, D. H. Kim, J. Y. Kwon, G. Amaratunga, S. Y. Lee, B. L. Choi, Y. Kuk, J. M. Kim, and K. Kim, *Full-colour quantum dot displays fabricated by transfer printing*, Nature Photonics **5**, 176 (2011).
- [67] S. Oh, S. K. Park, J. H. Kim, I. Cho, H. J. Kim, and S. Y. Park, *Patterned Taping: A High-Efficiency Soft Lithographic Method for Universal Thin Film Patterning*, ACS Nano **10**, 3478 (2016).
- [68] L. Novotny and B. Hecht, *Principles of Nano-Optics*, 2nd ed. (Cambridge University Press, Cambridge, 2012).
- [69] E. Snoeks, A. Lagendijk, and A. Polman, *Measuring and Modifying the Spontaneous Emission Rate of Erbium near an Interface*, Physical Review Letters **74**, 2459 (1995).
- [70] K. Drexhage, *Influence of a dielectric interface on fluorescence decay time*, Journal of Luminescence **1-2**, 693 (1970).
- [71] A. B. Evlyukhin, T. Fischer, C. Reinhardt, and B. N. Chichkov, *Optical theorem and multipole scattering of light by arbitrarily shaped nanoparticles*, Physical Review B **94**, 1 (2016).
- [72] ANSYS Lumerical, *FDTD Solutions*, (2022).
- [73] J. Yang, J. P. Hugonin, and P. Lalanne, *Near-to-Far Field Transformations for Radiative and Guided Waves*, ACS Photonics **3**, 395 (2016).
- [74] E. D. Palik, *Handbook of Optical Constants of Solids*, 1st ed., Vol. 1 (Academic Press, 1997).
- [75] G. J. Brakenhoff, K. Visscher, and H. T. M. van der Voort, *Size and Shape of The Confocal Spot: Control and Relation to 3D Imaging and Image Processing*, in *Handbook of Biological Confocal Microscopy* (Springer US, Boston, MA, 1990) pp. 87–91.
- [76] Wolfram, *Mathematica*, (2020).
- [77] BP, *BP Statistical Review of World Energy*, Tech. Rep. (2019).
- [78] Enerdata, *Global Energy Statistical Yearbook*, (2019).
- [79] M. Meir, *IEA EBC Annex 58*, Tech. Rep. (IEA Solar Heating and Cooling Programme, 2019).

- [80] R. J. Yang and P. X. Zou, *Building integrated photovoltaics (BIPV): costs, benefits, risks, barriers and improvement strategy*, International Journal of Construction Management **16**, 39 (2016).
- [81] R. R. Lunt and V. Bulovic, *Transparent, near-infrared organic photovoltaic solar cells for window and energy-scavenging applications*, Applied Physics Letters **98**, 113305 (2011).
- [82] C. J. Traverse, R. Pandey, M. C. Barr, and R. R. Lunt, *Emergence of highly transparent photovoltaics for distributed applications*, Nature Energy **2**, 849 (2017).
- [83] A. A. Husain, W. Z. W. Hasan, S. Shafie, M. N. Hamidon, and S. S. Pandey, *A review of transparent solar photovoltaic technologies*, Renewable and Sustainable Energy Reviews **94**, 779 (2018).
- [84] C. Lamnatou and D. Chemisana, *Solar radiation manipulations and their role in greenhouse claddings: Fluorescent solar concentrators, photoselective and other materials*, Renewable and Sustainable Energy Reviews **27**, 175 (2013).
- [85] W. H. Weber and J. Lambe, *Luminescent greenhouse collector for solar radiation*, Applied Optics **15**, 2299 (1976).
- [86] C. Corrado, S. W. Leow, M. Osborn, I. Carbone, K. Hellier, M. Short, G. Alers, and S. A. Carter, *Power generation study of luminescent solar concentrator greenhouse*, Journal of Renewable and Sustainable Energy **8**, 043502 (2016).
- [87] M. E. Loik, S. A. Carter, G. Alers, C. E. Wade, D. Shugar, C. Corrado, D. Jokerst, and C. Kitayama, *Wavelength-Selective Solar Photovoltaic Systems: Powering Greenhouses for Plant Growth at the Food-Energy-Water Nexus*, Earth's Future **5**, 1044 (2017).
- [88] E. Cuce, D. Harjunowibowo, and P. M. Cuce, *Renewable and sustainable energy saving strategies for greenhouse systems: A comprehensive review*, Renewable and Sustainable Energy Reviews **64**, 34 (2016).
- [89] R. Fu, D. Feldman, R. Margolis, M. Woodhouse, K. Ardani, R. Fu, D. Feldman, R. Margolis, M. Woodhouse, and K. Ardani, *NREL Technical Report*, Tech. Rep. (National Renewable Energy Laboratory, 2018).
- [90] W. Shurcliff and C. R. Jones, *The Trapping of Fluorescent Light Produced within Objects of High Geometrical Symmetry*, Journal of the Optical Society of America **39**, 912 (1949).
- [91] E. Yablonovitch, *Thermodynamics of the fluorescent planar concentrator*, Journal of the Optical Society of America **70**, 1362 (1980).
- [92] A. Rabl, *Comparison of solar concentrators*, Solar Energy **18**, 93 (1976).
- [93] M. G. Debije and V. A. Rajkumar, *Direct versus indirect illumination of a prototype luminescent solar concentrator*, Solar Energy **122**, 334 (2015).
- [94] Y. Li, Y. Sun, and Y. Zhang, *Luminescent solar concentrators performing under different light conditions*, Solar Energy **188**, 1248 (2019).
- [95] V. A. Rajkumar, C. Weijers, and M. G. Debije, *Distribution of absorbed heat in luminescent solar concentrator lightguides and effect on temperatures of mounted photovoltaic cells*, Renewable Energy **80**, 308 (2015).

- [96] A. Reinders, R. Kishore, L. Slooff, and W. Eggink, *Luminescent solar concentrator photovoltaic designs*, (2018).
- [97] P. Moraitis, G. van Leeuwen, and W. van Sark, *Visual appearance of nanocrystal-based luminescent solar concentrators*, *Materials* **16** (2019), 10.3390/ma12060885.
- [98] F. Meinardi, F. Bruni, and S. Brovelli, *Luminescent solar concentrators for building-integrated photovoltaics*, *Nature Reviews Materials* **2**, 1 (2017).
- [99] A. Reinders, M. G. Debije, and A. Rosemann, *Measured Efficiency of a Luminescent Solar Concentrator PV Module Called Leaf Roof*, *IEEE Journal of Photovoltaics* **7**, 1663 (2017).
- [100] J. A. H. P. Sol, G. H. Timmermans, A. J. van Breugel, A. P. H. J. Schenning, and M. G. Debije, *Multistate Luminescent Solar Concentrator “Smart” Windows*, *Advanced Energy Materials* **8**, 1702922 (2018).
- [101] K. Wu, H. Li, and V. I. Klimov, *Tandem luminescent solar concentrators based on engineered quantum dots*, *Nature Photonics* **12**, 105 (2018).
- [102] D. R. Needell, O. Ilic, C. R. Bukowsky, Z. Nett, L. Xu, J. He, H. Bauser, B. G. Lee, J. F. Geisz, R. G. Nuzzo, A. P. Alivisatos, and H. A. Atwater, *Design Criteria for Micro-Optical Tandem Luminescent Solar Concentrators*, *IEEE Journal of Photovoltaics* **8**, 1560 (2018).
- [103] D. R. Needell, Z. Nett, O. Ilic, C. R. Bukowsky, J. He, L. Xu, R. G. Nuzzo, B. G. Lee, J. F. Geisz, A. P. Alivisatos, and H. A. Atwater, *Micro-optical Tandem Luminescent Solar Concentrator*, in *2017 IEEE 44th Photovoltaic Specialist Conference (PVSC)* (IEEE, 2017) pp. 1737–1740.
- [104] D. R. Needell, C. R. Bukowsky, S. Darbe, H. Bauser, O. Ilic, and H. A. Atwater, *Spectrally Matched Quantum Dot Photoluminescence in GaAs-Si Tandem Luminescent Solar Concentrators*, *IEEE Journal of Photovoltaics* **9**, 1 (2019).
- [105] M. M. Lunardi, D. R. Needell, H. Bauser, M. Phelan, H. A. Atwater, and R. Corkish, *Life Cycle Assessment of tandem LSC-Si devices*, *Energy* **181**, 1 (2019).
- [106] M. G. Debije and P. P. C. Verbunt, *Thirty Years of Luminescent Solar Concentrator Research: Solar Energy for the Built Environment*, *Advanced Energy Materials* **2**, 12 (2012).
- [107] A. Goetzberger and W. Greube, *Solar energy conversion with fluorescent collectors*, *Applied Physics* **14**, 123 (1977).
- [108] C. Tummeltshammer, A. Taylor, A. Kenyon, and I. Papakonstantinou, *Losses in luminescent solar concentrators unveiled*, *Solar Energy Materials and Solar Cells* **144**, 40 (2016).
- [109] A. R. Burgers, L. H. Slooff, R. Kinderman, and J. M. van Roosmalen, *Modeling of Luminescent Concentrators by Ray-tracing*, in *Proceedings of Twentieth European Photovoltaic Solar Energy Conference* (2005) pp. 394–397.
- [110] B. Rowan, L. Wilson, and B. Richards, *Advanced Material Concepts for Luminescent Solar Concentrators*, *IEEE Journal of Selected Topics in Quantum Electronics* **14**, 1312 (2008).

- [111] A. L. Martínez and D. Gómez, *Design, fabrication, and characterization of a luminescent solar concentrator with optimized optical concentration through minimization of optical losses*, Journal of Photonics for Energy **6**, 045504 (2016).
- [112] Z. Krumer, W. G. van Sark, R. E. Schropp, and C. de Mello Donegá, *Compensation of self-absorption losses in luminescent solar concentrators by increasing luminophore concentration*, Solar Energy Materials and Solar Cells **167**, 133 (2017).
- [113] A. Kerrouche, D. Hardy, D. Ross, and B. Richards, *Luminescent solar concentrators: From experimental validation of 3D ray-tracing simulations to coloured stained-glass windows for BIPV*, Solar Energy Materials and Solar Cells **122**, 99 (2014).
- [114] R. Connell, C. Pinnell, and V. E. Ferry, *Designing spectrally-selective mirrors for use in luminescent solar concentrators*, Journal of Optics **20**, 024009 (2018).
- [115] L. H. Slooff, E. E. Bende, A. R. Burgers, T. Budel, M. Pravettoni, R. P. Kenny, E. D. Dunlop, and A. Büchtemann, *A Luminescent Solar Concentrator with 7.1% power conversion efficiency*, Physica Status Solidi - Rapid Research Letters **2**, 257 (2008).
- [116] M. G. Debije, R. C. Evans, and G. Griffini, *Laboratory protocols for measuring and reporting the performance of luminescent solar concentrators*, Energy & Environmental Science **14**, 293 (2021).
- [117] L. Xu, Y. Yao, N. D. Bronstein, L. Li, A. P. Alivisatos, and R. G. Nuzzo, *Enhanced Photon Collection in Luminescent Solar Concentrators with Distributed Bragg Reflectors*, ACS Photonics **3**, 278 (2016).
- [118] D. K. G. de Boer, D. J. Broer, M. G. Debije, W. Keur, A. Meijerink, C. R. Ronda, and P. P. C. Verbunt, *Progress in phosphors and filters for luminescent solar concentrators*, Optics Express **20**, A395 (2012).
- [119] D. K. G. de Boer, C.-W. Lin, M. P. Giesbers, H. J. Cornelissen, M. G. Debije, P. P. C. Verbunt, and D. J. Broer, *Polarization-independent filters for luminescent solar concentrators*, Applied Physics Letters **98**, 021111 (2011).
- [120] C. Tummeltshammer, A. Taylor, A. J. Kenyon, and I. Papakonstantinou, *Homeotropic alignment and Förster resonance energy transfer: The way to a brighter luminescent solar concentrator*, Journal of Applied Physics **116**, 173103 (2014).
- [121] M. G. Debije, *Solar Energy Collectors with Tunable Transmission*, Advanced Functional Materials **20**, 1498 (2010).
- [122] C. L. Mulder, P. D. Reusswig, A. P. Beyler, H. Kim, C. Rotschild, and M. A. Baldo, *Dye alignment in luminescent solar concentrators: II Horizontal alignment for energy harvesting in linear polarizers*, Optics Express **18**, A91 (2010).
- [123] H. C. Bauser, C. R. Bukowsky, M. Phelan, W. Weigand, D. R. Needell, Z. C. Holman, and H. A. Atwater, *Photonic Crystal Waveguides for >90% Light Trapping Efficiency in Luminescent Solar Concentrators*, ACS Photonics **7**, 2122 (2020).
- [124] P. P. C. Verbunt, C. Sánchez-Somolinos, D. J. Broer, and M. G. Debije, *Anisotropic light emissions in luminescent solar concentrators—isotropic systems*, Optics Express **21**, A485 (2013).

- [125] P. P. C. Verbunt, T. M. de Jong, D. K. de Boer, D. J. Broer, and M. G. Debije, *Anisotropic light emission from aligned luminophores*, The European Physical Journal Applied Physics **67**, 10201 (2014).
- [126] P. P. C. Verbunt, A. Kaiser, K. Hermans, C. W. M. Bastiaansen, D. J. Broer, and M. G. Debije, *Controlling Light Emission in Luminescent Solar Concentrators Through Use of Dye Molecules Aligned in a Planar Manner by Liquid Crystals*, Advanced Functional Materials **19**, 2714 (2009).
- [127] P. Moraitis, D. K. G. de Boer, P. T. Prins, C. de Mello Donegá, K. Neyts, and W. G. J. H. M. van Sark, *Should Anisotropic Emission or Reabsorption of Nanoparticle Luminophores Be Optimized for Increasing Luminescent Solar Concentrator Efficiency?* Solar RRL **4**, 2000279 (2020).
- [128] D. A. Hanifi, N. D. Bronstein, B. A. Koscher, Z. Nett, J. K. Swabeck, K. Takano, A. M. Schwartzberg, L. Maserati, K. Vandewal, Y. van de Burgt, A. Salleo, and A. P. Alivisatos, *Redefining near-unity luminescence in quantum dots with photothermal threshold quantum yield*, Science **363**, 1199 (2019).
- [129] H. Fang, C. Battaglia, C. Carraro, S. Nemsak, B. Ozdol, J. S. Kang, H. A. Bechtel, S. B. Desai, F. Kronast, A. A. Unal, G. Conti, C. Conlon, G. K. Palsson, M. C. Martin, A. M. Minor, C. S. Fadley, E. Yablonovitch, R. Maboudian, and A. Javey, *Strong interlayer coupling in van der Waals heterostructures built from single-layer chalcogenides*, Proceedings of the National Academy of Sciences **111**, 6198 (2014).
- [130] M. A. Steiner, J. F. Geisz, I. García, D. J. Friedman, A. Duda, and S. R. Kurtz, *Optical enhancement of the open-circuit voltage in high quality GaAs solar cells*, Journal of Applied Physics **113**, 123109 (2013).
- [131] M. A. Green, *Radiative efficiency of state-of-the-art photovoltaic cells*, Progress in Photovoltaics: Research and Applications **20**, 472 (2012).
- [132] S. Sandhu, Z. Yu, and S. Fan, *Detailed balance analysis of nanophotonic solar cells*, Optics Express **21**, 1209 (2013).
- [133] L. H. Slooff, R. Kinderman, A. R. Burgers, A. Büchtemann, R. Danz, T. B. Meyer, A. J. Chatten, D. Farrell, K. W. J. Barnham, and J. A. M. van Roosmalen, *The luminescent concentrator illuminated*, in *Proceedings of SPIE, Photonics for Solar Energy Systems*, Vol. 6197 (2006) p. 61970K.
- [134] U. Rau, F. Einsele, and G. C. Glaeser, *Efficiency limits of photovoltaic fluorescent collectors*, Applied Physics Letters **87**, 171101 (2005).
- [135] G. C. Glaeser and U. Rau, *Collection and conversion properties of photovoltaic fluorescent collectors with photonic band stop filters*, in *Photonics for Solar Energy Systems*, Vol. 6197 (2006) p. 61970L.
- [136] D. Şahin, B. İlhan, and D. F. Kelley, *Monte-Carlo simulations of light propagation in luminescent solar concentrators based on semiconductor nanoparticles*, Journal of Applied Physics **110**, 033108 (2011).

- [137] S. Sadeghi, R. Melikov, H. Bahmani Jalali, O. Karatum, S. B. Srivastava, D. Conkar, E. N. Firat-Karalar, and S. Nizamoglu, *Ecofriendly and Efficient Luminescent Solar Concentrators Based on Fluorescent Proteins*, ACS Applied Materials & Interfaces **11**, 8710 (2019).
- [138] A. H. Smets, K. Jäger, O. Isabella, R. A. van Swaaij, and M. Zeman, *Solar Energy: The Physics and Engineering of Photovoltaic Conversion, Technologies and Systems* (UIT Cambridge Ltd., 2016).
- [139] Enerdata, *Global Energy Statistical Yearbook*, (2021).
- [140] O. Almora, D. Baran, G. C. Bazan, C. Berger, C. I. Cabrera, K. R. Catchpole, S. Erten-Ela, F. Guo, J. Hauch, A. W. Ho-Baillie, T. J. Jacobsson, R. A. Janssen, T. Kirchartz, N. Kopidakis, Y. Li, M. A. Loi, R. R. Lunt, X. Mathew, M. D. McGehee, J. Min, D. B. Mitzi, M. K. Nazeeruddin, J. Nelson, A. F. Nogueira, U. W. Paetzold, N. G. Park, B. P. Rand, U. Rau, H. J. Snaith, E. Unger, L. Vaillant-Roca, H. L. Yip, and C. J. Brabec, *Device Performance of Emerging Photovoltaic Materials (Version 1)*, Advanced Energy Materials **11**, 2002774 (2021).
- [141] M. R. Bergren, N. S. Makarov, K. Ramasamy, A. Jackson, R. Guglielmetti, and H. McDaniel, *High-Performance CuInS₂ Quantum Dot Laminated Glass Luminescent Solar Concentrators for Windows*, ACS Energy Letters **3**, 520 (2018).
- [142] A. Renny, C. Yang, R. Anthony, and R. R. Lunt, *Luminescent Solar Concentrator Paintings: Connecting Art and Energy*, Journal of Chemical Education **95**, 1161 (2018).
- [143] E. Mengelkamp, B. Notheisen, C. Beer, D. Dauer, and C. Weinhardt, *A blockchain-based smart grid: towards sustainable local energy markets*, Computer Science - Research and Development **33**, 207 (2018).
- [144] C. Yang, D. Liu, M. Bates, M. C. Barr, and R. R. Lunt, *How to Accurately Report Transparent Solar Cells*, Joule **3**, 1803 (2019).
- [145] J. S. Van Der Burgt, D. R. Needell, T. Veeken, A. Polman, E. C. Garnett, and H. A. Atwater, *Unlocking Higher Power Efficiencies in Luminescent Solar Concentrators through Anisotropic Luminophore Emission*, ACS Applied Materials and Interfaces **13**, 40742 (2021).
- [146] G. Smestad, H. Ries, R. Winston, and E. Yablonovitch, *The thermodynamic limits of light concentrators*, Solar Energy Materials **21**, 99 (1990).
- [147] F. Meinardi, S. Ehrenberg, L. Dharmo, F. Carulli, M. Mauri, F. Bruni, R. Simonutti, U. Kortshagen, and S. Brovelli, *Highly efficient luminescent solar concentrators based on earth-Abundant indirect-bandgap silicon quantum dots*, Nature Photonics **11**, 177 (2017).
- [148] K. E. Knowles, T. B. Kilburn, D. G. Alzate, S. McDowall, and D. R. Gamelin, *Bright CuInS₂/CdS nanocrystal phosphors for high-gain full-spectrum luminescent solar concentrators*, Chemical Communications **51**, 9129 (2015).
- [149] J. Roncali, *Luminescent Solar Collectors: Quo Vadis?* Advanced Energy Materials **10**, 2001907 (2020).

- [150] G. C. Heres, L. M. Einhaus, and R. Saive, *Analytical Model for the Performance of a Free-Space Luminescent Solar Concentrator*, in *2021 IEEE 48th Photovoltaic Specialists Conference (PVSC)* (IEEE, 2021) pp. 1027–1029.
- [151] L. R. Bradshaw, K. E. Knowles, S. McDowall, and D. R. Gamelin, *Nanocrystals for Luminescent Solar Concentrators*, *Nano Letters* **15**, 1315 (2015).
- [152] M. Fisher, D. Farrell, M. Zanella, A. Lupi, P. N. Stavrinou, and A. J. Chatten, *Utilizing vertically aligned CdSe/CdS nanorods within a luminescent solar concentrator*, *Applied Physics Letters* **106**, 3 (2015).
- [153] A. Vaskin, R. Kolkowski, A. F. Koenderink, and I. Staude, *Light-emitting metasurfaces*, *Nanophotonics* **8**, 1151 (2019).
- [154] A. G. Curto, T. H. Taminiau, G. Volpe, M. P. Kreuzer, R. Quidant, and N. F. van Hulst, *Multipolar radiation of quantum emitters with nanowire optical antennas*, *Nature Communications* **4**, 1750 (2013).
- [155] S. R. K. Rodriguez, F. B. Arango, T. P. Steinbusch, M. A. Verschuuren, A. F. Koenderink, and J. G. Rivas, *Breaking the Symmetry of Forward-Backward Light Emission with Localized and Collective Magnetoelectric Resonances in Arrays of Pyramid-Shaped Aluminum Nanoparticles*, *Physical Review Letters* **113**, 247401 (2014).
- [156] I. Staude, T. Pertsch, and Y. S. Kivshar, *All-Dielectric Resonant Meta-Optics Lightens up*, *ACS Photonics* **6**, 802 (2019).
- [157] M. Peter, A. Hildebrandt, C. Schlickriede, K. Gharib, T. Zentgraf, J. Förstner, and S. Linden, *Directional Emission from Dielectric Leaky-Wave Nanoantennas*, *Nano Letters* **17**, 4178 (2017).
- [158] A. Vaskin, S. Mashhadi, M. Steinert, K. E. Chong, D. Keene, S. Nanz, A. Abass, E. Rusak, D. Y. Choi, I. Fernandez-Corbaton, T. Pertsch, C. Rockstuhl, M. A. Noginov, Y. S. Kivshar, D. N. Neshev, N. Noginova, and I. Staude, *Manipulation of Magnetic Dipole Emission from Eu 3+ with Mie-Resonant Dielectric Metasurfaces*, *Nano Letters* **19**, 1015 (2019).
- [159] N. E. Watkins, J. Guan, B. T. Diroll, K. R. Williams, R. D. Schaller, and T. W. Odom, *Surface Normal Lasing from CdSe Nanoplatelets Coupled to Aluminum Plasmonic Nanoparticle Lattices*, *The Journal of Physical Chemistry C* **125**, 19874 (2021).
- [160] M. Aellen, A. A. Rossinelli, R. C. Keitel, R. Brechbühler, F. V. Antolinez, S. G. Rodrigo, J. Cui, and D. J. Norris, *Role of Gain in Fabry-Pérot Surface Plasmon Polariton Lasers*, *ACS Photonics* **9**, 630 (2022).
- [161] M. Wu, L. Ding, R. P. Sabatini, L. K. Sagar, G. Bappi, R. Paniagua-Domínguez, E. H. Sargent, and A. I. Kuznetsov, *Bound State in the Continuum in Nanoantenna-Coupled Slab Waveguide Enables Low-Threshold Quantum-Dot Lasing*, *Nano Letters* **21**, 9754 (2021).
- [162] T. Veeken, B. Daiber, H. Agrawal, M. Aarts, E. Alarcón-Lladó, E. C. Garnett, B. Ehrler, J. van de Groep, and A. Polman, *Directional quantum dot emission by soft-stamping on silicon Mie resonators*, *Nanoscale Advances* **4**, 1088 (2022).

- [163] A. A. Rossinelli, H. Rojo, A. S. Mule, M. Aellen, A. Cocina, E. De Leo, R. Schäublin, and D. J. Norris, *Compositional Grading for Efficient and Narrowband Emission in CdSe-Based Core/Shell Nanoplatelets*, Chemistry of Materials **31**, 9567 (2019).
- [164] J. van de Groep and A. Polman, *Designing dielectric resonators on substrates: Combining magnetic and electric resonances*, Optics Express **21**, 26285 (2013).
- [165] S. Ha, R. Janissen, Y. Y. Ussembayev, M. M. Van Oene, B. Solano, and N. H. Dekker, *Tunable top-down fabrication and functional surface coating of single-crystal titanium dioxide nanostructures and nanoparticles*, Nanoscale **8**, 10739 (2016).
- [166] J. Van De Groep, P. Spinelli, and A. Polman, *Single-Step Soft-Imprinted Large-Area Nanopatterned Antireflection Coating*, Nano Letters **15**, 4223 (2015).
- [167] V. Liu and S. Fan, *S4 : A free electromagnetic solver for layered periodic structures*, Computer Physics Communications **183**, 2233 (2012).
- [168] I. Sersic, C. Tuambilangana, and A. Femius Koenderink, *Fourier microscopy of single plasmonic scatterers*, New Journal of Physics **13**, 083019 (2011).
- [169] A. Richter, M. Hermle, and S. W. Glunz, *Reassessment of the limiting efficiency for crystalline silicon solar cells*, IEEE Journal of Photovoltaics **3**, 1184 (2013).
- [170] K. Yoshikawa, H. Kawasaki, W. Yoshida, T. Irie, K. Konishi, K. Nakano, T. Uto, D. Adachi, M. Kanematsu, H. Uzu, and K. Yamamoto, *Silicon heterojunction solar cell with interdigitated back contacts for a photoconversion efficiency over 26%*, Nature Energy **2**, 17032 (2017).
- [171] J. G. Ingersoll, *Simplified calculation of solar cell temperatures in terrestrial photovoltaic arrays*, Journal of Solar Energy Engineering, Transactions of the ASME **108**, 95 (1986).
- [172] O. Dupré, R. Vaillon, and M. A. Green, *Thermal Behavior of Photovoltaic Devices*, 1st ed. (Springer International Publishing, 2017) p. 130.
- [173] E. Skoplaki and J. A. Palyvos, *On the temperature dependence of photovoltaic module electrical performance: A review of efficiency/power correlations*, Solar Energy **83**, 614 (2009).
- [174] C. R. Osterwald and T. J. McMahon, *History of accelerated and qualification testing of terrestrial photovoltaic modules: A literature review*, Progress in Photovoltaics: Research and Applications **17**, 11 (2009).
- [175] D. H. Otth and R. G. Ross, *Assessing Photovoltaic Module Degradation and Lifetime From Long Term Environmental Tests*, in *29th Institute of Environmental Sciences Technical Meeting* (Los Angeles, CA, 1983) pp. 121–126.
- [176] M. Kumar and A. Kumar, *Performance assessment and degradation analysis of solar photovoltaic technologies: A review*, Renewable and Sustainable Energy Reviews **78**, 554 (2017).
- [177] S. Fan and W. Li, *Photonics and thermodynamics concepts in radiative cooling*, Nature Photonics (2022), 10.1038/s41566-021-00921-9.

- [178] D. Beysens, I. Milimouk, V. Nikolayev, M. Muselli, and J. Marcillat, *Using radiative cooling to condense atmospheric vapor: A study to improve water yield*, Journal of Hydrology **276**, 1 (2003).
- [179] D. Zhao, X. Yin, J. Xu, G. Tan, and R. Yang, *Radiative sky cooling-assisted thermoelectric cooling system for building applications*, Energy **190**, 116322 (2020).
- [180] A. P. Raman, M. A. Anoma, L. Zhu, E. Rephaeli, and S. Fan, *Passive radiative cooling below ambient air temperature under direct sunlight*, Nature **515**, 540 (2014).
- [181] W. Li, Y. Shi, K. Chen, L. Zhu, and S. Fan, *A Comprehensive Photonic Approach for Solar Cell Cooling*, ACS Photonics **4**, 774 (2017).
- [182] M. Zahir and M. Benlattar, *Design of radiative cooler based on porous TiO₂ for improving solar cells' performance*, Applied Optics **60**, 445 (2021).
- [183] G. Perrakis, A. C. Tasolamprou, G. Kenanakis, E. N. Economou, S. Tzortzakis, and M. Kafesaki, *Combined nano and micro structuring for enhanced radiative cooling and efficiency of photovoltaic cells*, Scientific Reports **11**, 1 (2021).
- [184] J. Jaramillo-Fernandez, G. L. Whitworth, J. A. Pariente, A. Blanco, P. D. Garcia, C. Lopez, and C. M. Sotomayor-Torres, *A Self-Assembled 2D Thermofunctional Material for Radiative Cooling*, Small **15**, 1 (2019).
- [185] L. Long, Y. Yang, and L. Wang, *Simultaneously enhanced solar absorption and radiative cooling with thin silica micro-grating coatings for silicon solar cells*, Solar Energy Materials and Solar Cells **197**, 19 (2019).
- [186] E. Lee and T. Luo, *Black body-like radiative cooling for flexible thin-film solar cells*, Solar Energy Materials and Solar Cells **194**, 222 (2019).
- [187] L. Zhu, A. Raman, K. X. Wang, M. A. Anoma, and S. Fan, *Radiative cooling of solar cells*, Optica **1**, 32 (2014).
- [188] L. Zhu, A. P. Raman, and S. Fan, *Radiative cooling of solar absorbers using a visibly transparent photonic crystal thermal blackbody*, Proceedings of the National Academy of Sciences **112**, 12282 (2015).
- [189] M. Gao, Y. Xia, R. Li, Z. Zhang, Y. He, C. Zhang, L. Chen, L. Qi, Y. Si, Q. Zhang, and Y. Zheng, *The design of near-perfect spectrum-selective mirror based on photonic structures for passive cooling of silicon solar cells*, Nanomaterials **10**, 1 (2020).
- [190] B. Zhao, M. Hu, X. Ao, Q. Xuan, and G. Pei, *Comprehensive photonic approach for diurnal photovoltaic and nocturnal radiative cooling*, Solar Energy Materials and Solar Cells **178**, 266 (2018).
- [191] Q. Zhai and Q. Zhu, *Radiative cooling film with self-cleaning function*, Solar Energy Materials and Solar Cells **228**, 111117 (2021).
- [192] G. Chen, Y. Wang, J. Qiu, J. Cao, Y. Zou, S. Wang, J. Ouyang, D. Jia, and Y. Zhou, *A visibly transparent radiative cooling film with self-cleaning function produced by solution processing*, Journal of Materials Science and Technology **90**, 76 (2021).

- [193] C. Ziming, W. Fuqiang, G. Dayang, L. Huaxu, and S. Yong, *Low-cost radiative cooling blade coating with ultrahigh visible light transmittance and emission within an "atmospheric window"*, Solar Energy Materials and Solar Cells **213**, 110563 (2020).
- [194] R. Kitamura, L. Pilon, and M. Jonasz, *Optical constants of silica glass from extreme ultraviolet to far infrared at near room temperature*, Applied Optics **46**, 8118 (2007).
- [195] S. Kruk and Y. Kivshar, *Functional Meta-Optics and Nanophotonics Governed by Mie Resonances*, ACS Photonics **4**, 2638 (2017).
- [196] A. F. Koenderink, A. Alù, and A. Polman, *Nanophotonics: Shrinking light-based technology*, Science **348**, 516 (2015).
- [197] C. Van Lare, F. Lenzmann, M. A. Verschuuren, and A. Polman, *Dielectric Scattering Patterns for Efficient Light Trapping in Thin-Film Solar Cells*, Nano Letters **15**, 4846 (2015).
- [198] R. Alaei, R. Filter, D. Lehr, F. Lederer, and C. Rockstuhl, *A generalized Kerker condition for highly directive nanoantennas*, Optics Letters **40**, 2645 (2015).
- [199] W. Liu and Y. S. Kivshar, *Generalized Kerker effects in nanophotonics and meta-optics [Invited]*, Optics Express **26**, 13085 (2018).
- [200] A. C. Overvig, S. A. Mann, and A. Alù, *Thermal Metasurfaces: Complete Emission Control by Combining Local and Nonlocal Light-Matter Interactions*, Physical Review X **11**, 21050 (2021).
- [201] R. Carminati and J.-J. Greffet, *Near-Field Effects in Spatial Coherence of Thermal Sources*, Physical Review Letters **82**, 1660 (1999).
- [202] S. Hava and M. Auslender, *Theoretical dependence of infrared absorption in bulk-doped silicon on carrier concentration*, Applied Optics **32**, 1122 (1993).
- [203] E. Hecht, *Optics*, 4th ed. (Addison Wesley, 2002).
- [204] S. D. Lord, *A New Software Tool for Computing Earth's Atmospheric Transmission of Near- and Far-Infrared Radiation*, NASA Technical Memorandum 103957 (1992).
- [205] Gemini Observatory, *Infrared Atmospheric Transmission Spectra*, (2022).
- [206] S. J. Byrnes, *Multilayer optical calculations*, (2016), arXiv:1603.02720 .
- [207] R. L. Olmon, B. Slovick, T. W. Johnson, D. Shelton, S.-H. Oh, G. D. Boreman, and M. B. Raschke, *Optical dielectric function of gold*, Physical Review B **86**, 235147 (2012).
- [208] C. Hecker, S. Hook, M. van der Meijde, W. Bakker, H. van Werff, H. Wilbrink, F. van Ruitenbeek, B. de Smeth, and F. van der Meer, *Thermal infrared spectrometer for earth science remote sensing applications-instrument modifications and measurement procedures*, Sensors **11**, 10981 (2011).
- [209] ITRPV, *International technology roadmap for photovoltaic*, 10th ed. (VDMA Photovoltaic Equipment, 2019).

- [210] S. A. Pelaez, C. Deline, S. M. MacAlpine, B. Marion, J. S. Stein, and R. K. Kostuk, *Comparison of Bifacial Solar Irradiance Model Predictions With Field Validation*, IEEE Journal of Photovoltaics **9**, 82 (2019).
- [211] G. T. Klise and J. S. Stein, *Sandia National Laboratories*, Tech. Rep. December (Sandia National Laboratories (SNL), Albuquerque, NM, and Livermore, CA (United States), 2009).
- [212] M. Abbott, K. McIntosh, B. Sudbury, J. Meydbray, T. H. Fung, M. Umair Khan, Y. Zhang, S. Zou, X. Wang, G. Xing, G. Scardera, and D. Payne, *Annual energy yield analysis of solar cell technology*, in *Conference Record of the IEEE Photovoltaic Specialists Conference* (IEEE, 2019) pp. 3046–3050.
- [213] M. R. Vogt, T. Gewohn, K. Bothe, C. Schinke, and R. Brendel, *Impact of Using Spectrally Resolved Ground Albedo Data for Performance Simulations of Bifacial Modules*, in *Proc. 35th European Photovoltaic Solar Energy Conference and Exhibition*, 35 (2018) pp. 1011–1016.
- [214] C. K. Lo, Y. S. Lim, and F. A. Rahman, *New integrated simulation tool for the optimum design of bifacial solar panel with reflectors on a specific site*, Renewable Energy **81**, 293 (2015).
- [215] R. Couderc, M. Amara, and M. Lemiti, *In-Depth Analysis of Heat Generation in Silicon Solar Cells*, IEEE Journal of Photovoltaics **6**, 1123 (2016).
- [216] A. Riverola, A. Mellor, D. Alonso Alvarez, L. Ferre Llin, I. Guarracino, C. Markides, D. Paul, D. Chemisana, and N. Ekins-Daukes, *Mid-infrared emissivity of crystalline silicon solar cells*, Solar Energy Materials and Solar Cells **174**, 607 (2018).
- [217] M. Steglich, M. Zilk, A. Bingel, C. Patzig, T. Käsebier, F. Schrempel, E.-B. Kley, and A. Tünnermann, *A normal-incidence PtSi photoemissive detector with black silicon light-trapping*, Journal of Applied Physics **114**, 183102 (2013).
- [218] M. Steglich, M. Oehme, T. Käsebier, M. Zilk, K. Kosteck, E.-B. Kley, J. Schulze, and A. Tünnermann, *Ge-on-Si photodiode with black silicon boosted responsivity*, Applied Physics Letters **107**, 051103 (2015).
- [219] J. Lv, T. Zhang, P. Zhang, Y. Zhao, and S. Li, *Review Application of Nanostructured Black Silicon*, Nanoscale Research Letters **13**, 110 (2018).
- [220] M. Steglich, T. Käsebier, M. Zilk, T. Pertsch, E.-B. Kley, and A. Tünnermann, *The structural and optical properties of black silicon by inductively coupled plasma reactive ion etching*, Journal of Applied Physics **116**, 173503 (2014).
- [221] S. Ma, S. Liu, Q. Xu, J. Xu, R. Lu, Y. Liu, and Z. Zhong, *A theoretical study on the optical properties of black silicon*, AIP Advances **8**, 035010 (2018).
- [222] M. Kroll, T. Käsebier, M. Otto, R. Salzer, R. Wehrspohn, E.-B. Kley, A. Tünnermann, and T. Pertsch, *Optical modeling of needle like silicon surfaces produced by an ICP-RIE process*, in *Proceedings of SPIE, Photonics for Solar Energy Systems III*, Vol. 7725 (2010) p. 772505.

- [223] A. J. Bett, J. Eisenlohr, O. Höhn, P. Repo, H. Savin, B. Bläsi, and J. C. Goldschmidt, *Wave optical simulation of the light trapping properties of black silicon surface textures*, Optics Express **24**, A434 (2016).
- [224] M. G. Moharam, T. K. Gaylord, E. B. Grann, and D. A. Pommet, *Formulation for stable and efficient implementation of the rigorous coupled-wave analysis of binary gratings*, Journal of the Optical Society of America A **12**, 1068 (1995).
- [225] N. Tucher, H. T. Gebrewold, and B. Bläsi, *Field stitching approach for the wave optical modeling of black silicon structures*, Optics Express **26**, A937 (2018).
- [226] N. Tucher, J. Eisenlohr, P. Kiefel, O. Höhn, H. Hauser, M. Peters, C. Müller, J. C. Goldschmidt, and B. Bläsi, *3D optical simulation formalism OPTOS for textured silicon solar cells*, Optics Express **23**, A1720 (2015).
- [227] Y. Li, Y. Chen, Z. Ouyang, and A. Lennon, *Angular matrix framework for light trapping analysis of solar cells*, Optics Express **23**, A1707 (2015).
- [228] J. Eisenlohr, N. Tucher, H. Hauser, M. Graf, J. Benick, B. Bläsi, J. C. Goldschmidt, and M. Hermle, *Efficiency increase of crystalline silicon solar cells with nanoimprinted rear side gratings for enhanced light trapping*, Solar Energy Materials and Solar Cells **155**, 288 (2016).
- [229] A. A. Elsayed, Y. M. Sabry, F. Marty, T. Bourouina, and D. Khalil, *Optical modeling of black silicon using an effective medium/multi-layer approach*, Optics Express **26**, 13443 (2018).
- [230] S. Chattopadhyay, Y. Huang, Y. Jen, A. Ganguly, K. Chen, and L. Chen, *Anti-reflecting and photonic nanostructures*, Materials Science and Engineering: R: Reports **69**, 1 (2010).
- [231] T. Rahman and S. A. Boden, *Optical Modeling of Black Silicon for Solar Cells Using Effective Index Techniques*, IEEE Journal of Photovoltaics **7**, 1556 (2017).
- [232] M. Otto, M. Algasinger, H. Branz, B. Gesemann, T. Gimpel, K. Fücksel, T. Käsebier, S. Kontermann, S. Koynov, X. Li, V. Naumann, J. Oh, A. N. Sprafke, J. Ziegler, M. Zilk, and R. B. Wehrspohn, *Black Silicon Photovoltaics*, Advanced Optical Materials **3**, 147 (2015).
- [233] K. Tang, R. A. Dimenna, and R. O. Buckius, *Regions of validity of the geometric optics approximation for angular scattering from very rough surfaces*, International Journal of Heat and Mass Transfer **40**, 49 (1996).
- [234] M. M. Plakhotnyuk, M. Gaudig, R. S. Davidsen, J. M. Lindhard, J. Hirsch, D. Lausch, M. S. Schmidt, E. Stamate, and O. Hansen, *Low surface damage dry etched black silicon*, Journal of Applied Physics **122**, 143101 (2017).
- [235] P. Repo, J. Benick, G. von Gastrow, V. Vähänissi, F. D. Heinz, J. Schön, M. C. Schubert, and H. Savin, *Passivation of black silicon boron emitters with atomic layer deposited aluminum oxide*, Physica Status Solidi - Rapid Research Letters **7**, 950 (2013).
- [236] B. Bhushan, *Surface roughness analysis and measurement techniques*, in *Modern Tribology Handbook*, edited by T. Inc and Francis (CRC Press, 2000) Chap. 2.2.2.4, p. 1760.

- [237] D. Bergstrom, *Computer program: Rough surface generation and analysis*, (2012).
- [238] D. Nečas and P. Klapetek, *Gwyddion: an open-source software for SPM data analysis*, *Open Physics* **10**, 181 (2012).
- [239] D. Payne, M. Abbott, A. L. Claville, Y. Zeng, T. H. Fung, K. McIntosh, J. C. Campa, R. Davidson, M. Plakhotnyuk, and D. Bagnall, *Rapid optical modelling of plasma textured silicon*, in *Proceedings of the IEEE EUPVSEC 2017*, 33 (2017) pp. 897–901.
- [240] M. Khardani, M. Bouaïcha, and B. Bessaïs, *Bruggeman effective medium approach for modelling optical properties of porous silicon: Comparison with experiment*, *Physica Status Solidi (C) Current Topics in Solid State Physics* **4**, 1986 (2007).
- [241] B. C. Bergner, T. A. Germer, and T. J. Suleski, *Effective medium approximations for modeling optical reflectance from gratings with rough edges*, *Journal of the Optical Society of America A* **27**, 1083 (2010).
- [242] Y. Battie, A. En Naciri, W. Chamorro, and D. Horwat, *Generalized Effective Medium Theory to Extract the Optical Properties of Two-Dimensional Nonspherical Metallic Nanoparticle Layers*, *The Journal of Physical Chemistry C* **118**, 4899 (2014).
- [243] O. Zhuromskyy, *Applicability of Effective Medium Approximations to Modelling of Mesocrystal Optical Properties*, *Crystals* **7**, 1 (2016).
- [244] J. Maxwell Garnett, *XII. Colours in metal glasses and in metallic films*, *Philosophical Transactions of the Royal Society A* **203**, 385 (1904).
- [245] V. A. Markel, *Introduction to the Maxwell Garnett approximation: tutorial*, *Journal of the Optical Society of America A* **33**, 1244 (2016).
- [246] J. Humlicek, *Ellipsometry at the Nanoscale*, edited by M. Losurdo and K. Hingerl (Springer Berlin Heidelberg, Berlin, Heidelberg, 2013) pp. 145–178.
- [247] ANSYS Lumerical, *FDTD Solutions*, (2018).
- [248] P. Spinelli, M. A. Verschuuren, and A. Polman, *Broadband omnidirectional antireflection coating based on subwavelength surface Mie resonators*, *Nature Communications* **3**, 1 (2012).
- [249] J. Zhu, Z. Yu, G. F. Burkhardt, C. M. Hsu, S. T. Connor, Y. Xu, Q. Wang, M. McGehee, S. Fan, and Y. Cui, *Optical absorption enhancement in amorphous silicon nanowire and nanocone arrays*, *Nano Letters* **9**, 279 (2009).
- [250] S. Jeong, M. D. McGehee, and Y. Cui, *All-back-contact ultra-thin silicon nanocone solar cells with 13.7% power conversion efficiency*, *Nature Communications* **4**, 2950 (2013).
- [251] E. F. Pecora, A. Cordaro, P. G. Kik, and M. L. Brongersma, *Broadband Antireflection Coatings Employing Multiresonant Dielectric Metasurfaces*, *ACS Photonics* **5**, 4456 (2018).
- [252] Y. Wang, N. Lu, H. Xu, G. Shi, M. Xu, X. Lin, H. Li, W. Wang, D. Qi, Y. Lu, and L. Chi, *Biomimetic corrugated silicon nanocone arrays for self-cleaning antireflection coatings*, *Nano Research* **3**, 520 (2010).

- [253] M. M. Hossain and M. Gu, *Radiative Cooling: Principles, Progress, and Potentials*, Advanced Science **3**, 1500360 (2016).
- [254] P. Repo, A. Haarahiltunen, L. Sainiemi, M. Yli-Koski, H. Talvitie, M. C. Schubert, and H. Savin, *Effective Passivation of Black Silicon Surfaces by Atomic Layer Deposition*, IEEE Journal of Photovoltaics **3**, 90 (2013).
- [255] A. Ingenito, O. Isabella, and M. Zeman, *Nano-cones on micro-pyramids: modulated surface textures for maximal spectral response and high-efficiency solar cells*, Progress in Photovoltaics: Research and Applications **23**, 1649 (2015).
- [256] X. Liu, P. R. Coxon, M. Peters, B. Hoex, J. M. Cole, and D. J. Fray, *Black silicon: fabrication methods, properties and solar energy applications*, Energy Environ. Sci. **7**, 3223 (2014).
- [257] Y. Xia, B. Liu, J. Liu, Z. Shen, and C. Li, *A novel method to produce black silicon for solar cells*, Solar Energy **85**, 1574 (2011).
- [258] R. Bilyalov, R. Lüdemann, W. Wettling, L. Stalmans, J. Poortmans, J. Nijs, L. Schirone, G. Sotgiu, S. Strehlke, and C. Lévy-Clément, *Multicrystalline silicon solar cells with porous silicon emitter*, Solar Energy Materials and Solar Cells **60**, 391 (2000).
- [259] M. B. Rabha, W. Dimassi, M. Bouaïcha, H. Ezzaouia, and B. Bessaïs, *Laser-beam-induced current mapping evaluation of porous silicon-based passivation in polycrystalline silicon solar cells*, Solar Energy **83**, 721 (2009).
- [260] T. Pasanen, V. Vähänissi, N. Theut, and H. Savin, *Surface passivation of black silicon phosphorus emitters with atomic layer deposited SiO₂/Al₂O₃ stacks*, Energy Procedia **124**, 307 (2017).
- [261] J. Wu, H. Wu, X. Chen, Z. Yao, D. Zhang, S. Su, M. Zhang, F. Jiang, and G. Xing, *21.4% efficiency bifacial multi-Si PERC cells and 410W modules*, in 2019 IEEE 46th Photovoltaic Specialists Conference (PVSC), 199 (IEEE, 2019) pp. 1466–1470.
- [262] M. U. Khan, G. Scardera, S. Zou, D. Zhang, and M. Abbott, *The Role of Metal-Catalyzed Chemical Etching Black Silicon in the Reduction of Light- and Elevated Temperature-Induced Degradation in P-Type Multicrystalline Wafers*, IEEE Journal of Photovoltaics **11**, 627 (2021).
- [263] F. Shimura, *Semiconductor silicon crystal technology*, 1st ed., Vol. 26 (Academic Press, 1989).
- [264] I. Synopsys, *Sentaurus Device - An advanced multidimensional (1D/2D/3D) device simulator*, (2021).
- [265] PV-Lighthouse, *SunSolve™*, (2019).
- [266] K. Füchsel, M. Kroll, M. Otto, M. Steglich, A. Bingel, T. Käsebier, R. B. Wehrspohn, E.-B. Kley, T. Pertsch, and A. Tünnermann, *Black Silicon Photovoltaics*, in *Photon Management in Solar Cells*, Vol. 3 (Wiley-VCH Verlag GmbH & Co. KGaA, Weinheim, Germany, 2015) pp. 117–151.
- [267] Y. Zhang, C. Kong, R. S. Davidsen, G. Scardera, L. Duan, K. T. Khoo, D. N. Payne, B. Hoex, and M. Abbott, *3D characterisation using plasma FIB-SEM: A large-area tomography technique for complex surfaces like black silicon*, Ultramicroscopy **218**, 113084 (2020).

- [268] F. J. Giessibl, *Advances in atomic force microscopy*, Reviews of Modern Physics **75**, 949 (2003).
- [269] N. Jalili and K. Laxminarayana, *A review of atomic force microscopy imaging systems: application to molecular metrology and biological sciences*, Mechatronics **14**, 907 (2004).
- [270] D. Sarid, *Review of scanning force microscopy*, Journal of Vacuum Science & Technology B: Microelectronics and Nanometer Structures **9**, 431 (1991).
- [271] E. Ukraintsev, A. Kromka, H. Kozak, Z. Reme, and B. Rezek, *Artifacts in Atomic Force Microscopy of Biological Samples*, in *Atomic Force Microscopy Investigations into Biology - From Cell to Protein* (InTech, 2012).
- [272] J. I. Paredes, A. Martinez-Alonso, and J. M. D. Tascon, *Adhesion artefacts in atomic force microscopy imaging*, Journal of Microscopy **200**, 109 (2000).
- [273] U. D. Schwarz, H. Haefke, P. Reimann, and H.-J. Güntherodt, *Tip artefacts in scanning force microscopy*, Journal of Microscopy **173**, 183 (1994).
- [274] T. H. Fung, T. Veeken, D. Payne, B. Veetil, A. Polman, and M. Abbott, *Application and validity of the effective medium approximation to the optical properties of nano-textured silicon coated with a dielectric layer*, Optics Express **27**, 38645 (2019).
- [275] T. H. Fung, M. U. Khan, Y. Zhang, N. J. Western, D. N. R. Payne, K. R. McIntosh, and M. D. Abbott, *Improved Ray Tracing on Random Pyramid Texture via Application of Phong Scattering*, IEEE Journal of Photovoltaics **9**, 591 (2019).
- [276] Y. Ge, F. Zhao, L. Wang, and X. Wang, *A novel perspective on the design of thermochromic VO₂ films: Combining ab initio calculations with FDTD simulations*, Surface and Coatings Technology **402**, 126493 (2020).
- [277] D. Payne, T. H. Fung, M. U. Khan, J. Cruz-Campa, K. McIntosh, and M. Abbott, *Understanding the optics of industrial black silicon*, in *AIP Conference Proceedings*, Vol. 1999 (2018) p. 050007.
- [278] G. Scardera, S. Wang, Y. Zhang, M. U. Khan, S. Zou, D. Zhang, R. S. Davidsen, O. Hansen, L. Mai, D. N. R. Payne, B. Hoex, and M. D. Abbott, *On the Enhanced Phosphorus Doping of Nanotextured Black Silicon*, IEEE Journal of Photovoltaics **11**, 298 (2021).
- [279] A. Fell, K. C. Fong, K. R. McIntosh, E. Franklin, and A. W. Blakers, *3-D Simulation of Interdigitated-Back-Contact Silicon Solar Cells With Quokka Including Perimeter Losses*, IEEE Journal of Photovoltaics **4**, 1040 (2014).
- [280] Y. Zhang, D. N. R. Payne, C. Kong, M. U. Khan, T. H. Fung, R. S. Davidsen, O. Hansen, G. Scardera, M. D. Abbott, and B. Hoex, *Advanced Characterisation of Black Silicon Surface Topography with 3D PFIB-SEM*, in *2019 IEEE 46th Photovoltaic Specialists Conference (PVSC)* (IEEE, Chicago, 2019) pp. 0825–0828.
- [281] Y. Zhang, C. Kong, G. Scardera, M. Abbott, D. N. Payne, and B. Hoex, *Large volume tomography using plasma FIB-SEM: A comprehensive case study on black silicon*, Ultramicroscopy **233**, 113458 (2022).
- [282] H. R. Philipp and E. A. Taft, *Optical Constants of Silicon in the Region 1 to 10 eV*, Physical Review **120**, 37 (1960).

- [283] M. A. Green, *Self-consistent optical parameters of intrinsic silicon at 300K including temperature coefficients*, Solar Energy Materials and Solar Cells **92**, 1305 (2008).
- [284] M. Welkowsky and R. Braunstein, *Interband Transitions and Exciton Effects in Semiconductors*, Physical Review B **5**, 497 (1972).
- [285] G. Jellison, *Optical functions of GaAs, GaP, and Ge determined by two-channel polarization modulation ellipsometry*, Optical Materials **1**, 151 (1992).
- [286] W. Theiß, *Optical properties of porous silicon*, Surface Science Reports **29**, 91 (1997).
- [287] G. Scardera, D. Payne, M. Khan, Y. Zhang, A. Soeriyadi, S. Zou, D. Zhang, R. Davidsen, O. Hansen, B. Hoex, and M. Abbott, *Silicon Nanotexture Surface Area Mapping Using Ultraviolet Reflectance*, IEEE Journal of Photovoltaics **11**, 1291 (2021).
- [288] H.-C. Yuan, V. E. Yost, M. R. Page, P. Stradins, D. L. Meier, and H. M. Branz, *Efficient black silicon solar cell with a density-graded nanoporous surface: Optical properties, performance limitations, and design rules*, Applied Physics Letters **95**, 123501 (2009).
- [289] H. M. Branz, V. E. Yost, S. Ward, K. M. Jones, B. To, and P. Stradins, *Nanostructured black silicon and the optical reflectance of graded-density surfaces*, Applied Physics Letters **94**, 231121 (2009).
- [290] F. Patolsky, G. Zheng, and C. M. Lieber, *Nanowire sensors for medicine and the life sciences*, Nanomedicine **1**, 51 (2006).
- [291] F. Patolsky, B. P. Timko, G. Zheng, and C. M. Lieber, *Nanowire-Based Nanoelectronic Devices in the Life Sciences*, MRS Bulletin **32**, 142 (2007).
- [292] M. J. Schmand, D. Henseler, R. Grazioso, N. Zhang, and M. S. Andreaco, *Patent: Medical Imaging with Black Silicon Photodetector*, (2010).
- [293] M. U. Pralle, J. E. Carey, H. Homayoon, S. Alie, J. Sickler, X. Li, J. Jiang, D. Miller, C. Palsule, and J. McKee, *Black silicon enhanced photodetectors: a path to IR CMOS*, in *Infrared Technology and Applications XXXVI*, Vol. 7660, edited by B. F. Andresen, G. F. Fulop, and P. R. Norton (2010) p. 76600N.
- [294] G. Seniutinas, G. Gervinskas, R. Verma, B. D. Gupta, F. Lapierre, P. R. Stoddart, F. Clark, S. L. McArthur, and S. Juodkazis, *Versatile SERS sensing based on black silicon*, Optics Express **23**, 6763 (2015).
- [295] A. P. Goodey, S. M. Eichfeld, K.-k. Lew, J. M. Redwing, and T. E. Mallouk, *Silicon Nanowire Array Photoelectrochemical Cells*, Journal of the American Chemical Society **129**, 12344 (2007).
- [296] J. R. Szczech and S. Jin, *Nanostructured silicon for high capacity lithium battery anodes*, Energy Environ. Sci. **4**, 56 (2011).
- [297] J. Oh, T. G. Deutsch, H.-C. Yuan, and H. M. Branz, *Nanoporous black silicon photocathode for H₂ production by photoelectrochemical water splitting*, Energy & Environmental Science **4**, 1690 (2011).
- [298] I. Oh, J. Kye, and S. Hwang, *Enhanced Photoelectrochemical Hydrogen Production from Silicon Nanowire Array Photocathode*, Nano Letters **12**, 298 (2012).

-
- [299] R. Carter, S. Chatterjee, E. Gordon, K. Share, W. R. Erwin, A. P. Cohn, R. Bardhan, and C. L. Pint, *Corrosion resistant three-dimensional nanotextured silicon for water photo-oxidation*, *Nanoscale* **7**, 16755 (2015).
- [300] Y. Yu, Z. Zhang, X. Yin, A. Kvit, Q. Liao, Z. Kang, X. Yan, Y. Zhang, and X. Wang, *Enhanced photoelectrochemical efficiency and stability using a conformal TiO₂ film on a black silicon photoanode*, *Nature Energy* **2**, 17045 (2017).
- [301] Y.-L. Deng and Y.-J. Juang, *Black silicon SERS substrate: Effect of surface morphology on SERS detection and application of single algal cell analysis*, *Biosensors and Bioelectronics* **53**, 37 (2014).
- [302] E. P. Ivanova, J. Hasan, H. K. Webb, G. Gervinskas, S. Juodkazis, V. K. Truong, A. H. Wu, R. N. Lamb, V. A. Baulin, G. S. Watson, J. A. Watson, D. E. Mainwaring, and R. J. Crawford, *Bactericidal activity of black silicon*, *Nature Communications* **4**, 2838 (2013).

List of Publications

Related to this thesis

1. B. Ehrler, E. Alarcón-Lladó, S.W. Tabernig, T. Veeken, E.C. Garnett, and A. Polman, *Photovoltaics reaching for the Shockley–Queisser limit*, ACS Energy Letters **5**, pp. 3029–3033, 2020. (**Chapter 1**)
2. T. Veeken, B. Daiber, H. Agrawal, M. Aarts, E. Alarcón-Lladó, E.C. Garnett, B. Ehrler, J. van de Groep, and A. Polman, *Directional quantum dot emission by soft-stamping on silicon Mie resonators*, Nanoscale Advances **4**, pp. 1088–1097, 2020. (**Chapter 2**)
3. J.S. van der Burg*, D.R. Needell*, T. Veeken*, A. Polman, E.C. Garnett, and H.A. Atwater, *Unlocking higher power efficiencies in luminescent solar concentrators through anisotropic luminophore emission*, ACS Applied Materials and Interfaces **13**, pp. 40742–40753, 2021. (**Chapter 3**)
4. T. Veeken, K. Orbons, N. de Gaay Fortman, A.A. Rossinelli, D.J. Norris, A.F. Koenderink, and A. Polman, *Anisotropic luminophore emission for enhanced light trapping in luminescent solar concentrators*, in preparation. (**Chapter 4**)
5. E. Akerboom*, T. Veeken*, C. Hecker, J. van de Groep, and A. Polman, *Passive radiative cooling of silicon solar modules with silica microcylinder arrays*, in preparation. (**Chapter 5**)
6. T.H. Fung, T. Veeken, D. Payne, B. Veettil, A. Polman, and M. Abbott, *Application and validity of the effective medium approximation to the optical properties of nano-textured silicon coated with a dielectric layer*, Optics Express **27**, pp. 38645–38660, 2019. (**Chapter 6**)
7. Y. Zhang, T. Veeken, S. Wang, G. Scardera, M. Abbott, D. Payne, A. Polman, and B. Hoex, *Plasma focused ion beam tomography for accurate characterization of black silicon validated by full-wave optical simulation*, under review by Advanced Materials Technologies, 2022. (**Chapter 7**)

* These authors contributed equally.

Other

8. L. Polak, T. Veeken, J. Houtkamp, M.J. Slaman, S.M. Kars, J.H. Rector, and R.J. Wijngaarden, *Two-step sputter-hydrothermal synthesis of NaTaO₃ thin films*, Thin Solid Films, **603**, pp. 413–417, 2016.
9. N. Tavakoli, W. Kim, T. Veeken, D. Poorten, L. Guniat, A. Rudra, A. Fontcuberta i Morral, E. Alarcon-Llado, *Coloured and semi-transparent nanowire-based solar cells for building integrated photovoltaics*, Preprint at <http://arxiv.org/abs/2107.09465>, 2021.

Summary

Light is an amazing phenomenon. It plays a central role in our modern society, ranging from electrical lighting to fiber-optic communication systems and mobile/computer displays to lasers. We use light to see the world around us, to study the smallest organisms with microscopes and the largest objects in the universe with telescopes. In addition, light can be a source of energy. Light from the sun provides more than 9000 times the amount of global primary energy supply our modern society generates. In the transition towards a world powered by renewable energy, photovoltaic energy conversion will play a key role, harvesting the nearly inexhaustible power that the sun provides. Photovoltaics (PV) is a mature technology that has seen decades of research and technological advances, which resulted in exponential growth of the installed capacity and exponential decline of the price of solar power generation. Two key challenges remain to be overcome to enable large-scale energy supply by PV: i) the further cost-reduction of solar electricity and ii) the integration of PV into our buildings, landscapes, and infrastructure.

In Chapter 1, we outline these two challenges in more detail. We start by investigating the potential of solar energy generation. We continue by quantifying the limits of photovoltaic energy conversion and comparing them to the current record-efficiency solar cells. Then, we discuss the role that photonics can play in PV. We conclude with a motivation to the thesis, discussing the two key challenges listed above.

In the remainder of this thesis, we investigate the photonic control over absorption and emission of light in photovoltaic systems to address these two challenges. In the first part (Chapters 2-4), we provide a fundamental description of nanophotonic structures to control the angular distribution of emission by dipole-like emitters. This has applications in, for example, up- and down-conversion schemes for photovoltaics and luminescent solar concentrators. In the second part (Chapters 5-7), we investigate photonic structures to enhance infrared emission for radiative cooling and surface textures for anti-reflection in silicon solar cells.

Up- and down-conversion schemes are designed to improve the conversion efficiency of photovoltaic systems. The absorption efficiency of the converted light in the solar cell is determined by the angular emission profile. Thus, controlling the direction of emission is of great importance to the efficiency. In Chapter 2, we introduce the use of Si nanocylinders to control the angular emission of CdSeTe/ZnS core-shell quantum dots (QDs). The Mie-like multipolar resonances in the cylinders can be tuned by changing their size, which influences the local density of optical states (LDOS) for the QDs placed on top of the cylinders. We treat the QDs as dipole-like emitters and use finite-difference time-domain (FDTD) simulations to optimize the cylinder dimensions for enhanced upward- or downward emission. QDs centered on a 400 nm diameter nanocylinder surface show 98% emission directionality into the Si substrate. Alternatively, for homogeneous ensembles placed over the nanocylinder top-surface, the upward emission is enhanced 10-fold for 150 nm diameter cylinders. Then, we demonstrate a novel soft-stamping method to selectively print a homogeneous layer of QDs on top of an array of Si nanocylinders. Experimental PL intensity measurements corroborate the simulated trends with cylinder diameter. PL lifetime measurements reflect well the variations of the LDOS at the QD position due to coupling to the resonant cylinders. These results demonstrate that the soft imprint technique provides a unique manner to directly integrate optical emitters with nanostructures. This can enable the application of

nanophotonic structures in up- and down-conversion schemes for improved photovoltaics, or other optoelectronic devices such as light-emitting diodes (LEDs) or displays. This chapter also serves as the introduction to the next two chapters, where we study anisotropic emission for photovoltaic luminescent solar concentrators.

Building-integrated photovoltaic (BIPV) technologies integrate photovoltaic energy generation into the design of semi-transparent and opaque building envelopes. The photovoltaic luminescent solar concentrator (LSC) is an example of such a technology and offers the potential for low-cost, passive concentration of direct and diffuse light. Despite decades of research, the conversion efficiency for luminescent concentrator modules has fallen far short of that achievable by geometric concentrators. Recent advances in the photoluminescence quantum yield (PLQY) of semiconductor luminophores could significantly reduce parasitic losses, but efficient light trapping remains elusive to achieve high conversion efficiency LSCs. Anisotropically-emitting nanophotonic structures could enable a significant step forward in efficiency. In Chapter 3, we employ Monte Carlo ray-trace modeling to evaluate the conversion efficiency of LSCs using anisotropic luminophore emission, as a function of PLQY, luminophore concentration, and geometric gain. By spanning the full LSC parameter space, we define a roadmap towards high LSC conversion efficiency. To calculate the conversion efficiency from ray-tracing results, we derive an analytical function for the dark radiative current of an LSC. Design parameters are provided for optimized LSCs with practical geometrical gains of 10. We conclude that conversion efficiencies beyond 28% are achievable if strong anisotropic luminophore emission is combined with high PLQY. This analysis reveals that for high luminescent solar concentrator performance, light trapping is equally important to the luminophore PLQY.

After investigating the potential of light trapping for LSCs, now we demonstrate anisotropic luminophore emission to enhance light trapping in the LSC waveguide in Chapter 4. By embedding semiconductor nanoplatelet emitters into high-index TiO_2 nanocylinders, we alter their angular emission profile to increase emission into the angular range for total internal reflection (TIR). We explain the control over emission directionality by a combination of Mie-like multipolar resonances in the individual nanocylinders and the interaction with the lattice. We model the TiO_2 nanocylinder array as a photonic crystal (PhC) and identify the PhC waveguide modes as a function of the lattice pitch and wavelength. By increasing the pitch, we move the dominant PhC waveguide modes into the TIR angular range at the luminophore emission wavelength (650 nm). Angle-resolved photoluminescence measurements were performed on fabricated nanocylinders arrays to capture the angular emission profiles. By optimizing the cylinder shape and lattice spacing, we show an increase in light trapping from 75% (isotropic emission) to 83.5%. These results complement the results shown in Chapter 2, demonstrating nanophotonic emission control for photovoltaics and optoelectronic devices in general.

In the second part of the thesis, we study photonic structures for radiative cooling and anti-reflection of (silicon) solar cells. In Chapter 5, we investigate the use of passive radiative cooling (PRC) to dissipate excess heat from a silicon solar cell into or through the earth's atmosphere. To achieve a lower operating temperature, which is beneficial for both the efficiency and operating lifetime of a silicon solar cell, we make use of its spontaneous emission of infrared (IR) thermal radiation. The main challenge is to enhance PRC while simultaneously retaining transparency for sunlight above the silicon bandgap. We design and fabricate a hexagonal array of microcylinders that can be integrated into the top surface of the solar cell module glass. We use FDTD simulations to optimize the geometry to enhance emission in the IR wavelength range. Multipolar Mie-like resonances in the cylinders are shown to reduce reflection in the IR, which results in enhanced IR emissivity. Using integrating

sphere spectroscopy, we measure the reflection of the silica cylinder array for IR as well as visible to near-infrared wavelengths. The results in the IR compare very well to the simulated results, while we retain transparency for light with energy above the silicon bandgap. The fabricated microstructure increased the average emissivity between $\lambda = 7.5 - 16 \mu\text{m}$ from 84.3% to 97.7%. With this design procedure, a PRC structure can be obtained for any photovoltaic device, with or without module glass encapsulation, or any other outdoor device that benefits from a lower operating temperature.

Complementary to light management of IR light, we investigate nanotextures for improved anti-reflection of light with energy above the bandgap. The emergence of these nanotextures in silicon solar cells has resulted in challenges associated with optical modeling. Whilst rigorous methods exist to accurately model black silicon (BSi) textures, the computational effort required limits the scope of modeling applications. In Chapter 6, we model three BSi nanotextures, each with a distinct random geometry, with an effective medium approximation (EMA). We validate the use of the EMA with full-wave optical simulations. We propose criteria for the validity of different optical simulation techniques based on a set of industrial photovoltaic textures. This analysis reveals a region within which neither geometric optics nor the EMA are adequate for calculating the reflectivity of a textured surface, and hence full-wave optical simulations are required. Even though we studied specific BSi textures for visible to near-infrared wavelengths, the proposed criteria are broadly applicable. We based the limits only on the root-mean-square roughness and correlation length, both normalized to the wavelength of the incident light, making them applicable to any surface texture.

Modeling and simulation of surface textures are commonly used in the PV industry to better understand the material properties, predict the device performance, and provide guidelines for optimizing fabrication parameters. Obtaining an accurate and reliable surface morphology of the BSi texture is one of the key challenges to achieving accurate models. In Chapter 7, we investigate the reliability and consistency of BSi texture characterization. We compare 3D models of complex BSi textures obtained by atomic force microscopy (AFM) and plasma focused ion beam (PFIB) tomography techniques. Hemispherical reflection measurement results are compared to full-wave optical simulated results to test the reliability and consistency of the tomography models. Our results provide evidence that PFIB tomography is more reliable and consistent at characterizing highly roughened BSi textures than AFM tomography.

Overall, this thesis provides new insights into several light management strategies to improve photovoltaic systems. Based on a fundamental understanding of the interaction between resonant photonic nanostructures and luminophores, we demonstrate control over the direction of emission. These insights and results pave the way for more efficient up- and down-conversion schemes and luminescent solar concentrators, specifically for photovoltaic applications. Similarly, we study the interaction of light with silicon solar cells to improve the emission of excess thermal energy and reduce reflection losses. We employ full-wave simulations to accurately predict this interaction at the scale of the wavelength of light to enable optimization of the surface textures. Many of these insights are also applicable to other optoelectronic devices such as photodetectors, light-emitting diodes, and displays.

Samenvatting

Fotonische controle over licht absorptie en straling in fotonische systemen

Licht is een wonderlijk fenomeen. Het speelt een centrale rol in onze moderne samenleving, variërend van elektrische verlichting tot glasvezelcommunicatiesystemen en mobiele/computer schermen tot lasers. We gebruiken licht om de wereld om ons heen te zien, om de kleinste organismen te bestuderen met microscopen en de grootste objecten in het heelal waar te nemen met telescopen. Daarnaast kan licht een bron van energie zijn. Licht van de zon levert meer dan 9000 keer de hoeveelheid primaire energie die onze moderne samenleving opwekt. Bij de overgang naar een wereld die wordt aangedreven door hernieuwbare energie, zal fotonische energieopwekking een sleutelrol spelen, waarbij de bijna onuitputtelijke energie die de zon levert wordt geoogst door fotonische systemen zoals zonnepanelen. Fotonische energieopwekking, Photonics (PV) in het Engels, is een volwassen technologie die tientallen jaren van onderzoek en technologische vooruitgang heeft doorgemaakt, wat heeft geleid tot een exponentiële groei van de geïnstalleerde capaciteit en een exponentiële daling van de prijs van zonne-energie. Er moeten nog twee belangrijke uitdagingen worden overwonnen om grootschalige energievoorziening door PV mogelijk te maken: i) de verdere kostenverlaging van zonne-elektriciteit en ii) de integratie van PV in onze gebouwen, landschappen en infrastructuur.

In Hoofdstuk 1 schetsen we deze twee uitdagingen in meer detail. We beginnen met het onderzoeken van het potentieel van zonne-energieopwekking. We gaan verder met het kwantificeren van de limieten van photonics en vergelijken deze met de huidige recordrendement zonnecellen. Vervolgens bespreken we de rol die fotonica kan spelen bij PV. We sluiten af met een motivatie voor het proefschrift en bespreken de twee belangrijkste uitdagingen die hierboven zijn opgesomd.

In de rest van dit proefschrift onderzoeken we de fotonische controle over absorptie en straling van licht in fotonische systemen om deze twee uitdagingen aan te pakken. In het eerste deel (Hoofdstukken 2-4) geven we een fundamentele beschrijving van nanofotonische structuren om de hoekverdeling van straling door dipoolachtige emitters te controleren. Dit heeft toepassingen in bijvoorbeeld foton-conversieschema's voor fotonische systemen, en voor luminescente zonneconcentratoren. In het tweede deel (Hoofdstukken 5-7), onderzoeken we fotonische structuren ter verbetering van de infraroodstraling voor stralingskoeling en oppervlaktestructuren voor antireflectie in siliciumzonnecellen.

Deel één

Het spectrum van de zon bevat licht met veel verschillende golflengtes, variërend van ultra-violet (hogere energie) naar zichtbaar tot infrarood (lagere energie). Figuur 1.1a *op blz. 5* laat de intensiteit van het zonnespectrum zien als functie van de golflengte (zwart) en hoeveel daarvan maximaal benut kan worden door een enkele zonnecel (oranje). Een enkele zonnecel kan theoretisch maximaal 33,7% van het zonlicht omzetten in elektriciteit, hoewel het record in de praktijk op 29,2% ligt. Het rendement wordt voornamelijk gelimiteerd doordat infrarood licht te weinig energie heeft (hoge golflengtes, rechts van het oranje oppervlak) en dus geen elektriciteit kan opwekken, en doordat ultra-violet en zichtbaar licht meer energie heeft dan de zonnecel kan gebruiken (boven het oranje oppervlak). De positie van de oranje lijn markeert de 'bandgap' van de zonnecel, de minimale energie (maximale golflengte) die licht nodig heeft om omgezet te kunnen worden in elektrische stroom. De bandgap verschilt per materiaal en bepaalt het maximale rendement — Figuur 1.2a *op blz. 7* laat het theoretische rendement per bandgap zien, en de behaalde records voor zonnecellen van verschillende materialen.

Om het rendement te verhogen van zonnecellen te verhogen, kunnen twee of meer zonnecellen op elkaar gelegd worden. Figuur 1.1b *op blz. 5* laat zien dat drie zonnecellen met verschillende bandgaps (blauw, groen en rood) ieder een ander gedeelte van het zonnespectrum omzetten. Tezamen verhoogt dit het maximum rendement naar 51,6%, maar maakt het tot nu toe altijd moeilijker en veel duurder om te fabriceren.

Foton-conversieschema's zijn een alternatieve manier om het theoretisch rendement van een zonnecel te verhogen; zie Figuur 1.3d ter illustratie *op blz. 11*. Hierin worden bijvoorbeeld twee lage-energie fotonen (minder energie dan de bandgap) omgezet in één hoge-energie foton (rood naar blauw), zodat die wel omgezet kan worden in elektriciteit. Andersom kan een hoge-energie foton gesplitst worden (blauw naar rood) in twee of meer lage-energie fotonen (met minstens de energie van de bandgap), zodat er meer elektriciteit opgewekt wordt.

Een materiaal waarin foton-conversie plaatsvindt moet eerst zonlicht absorberen, en daarna het geconverteerde licht weer uitzenden. Dat zal echter niet automatisch alleen richting de zonnecel uitgezonden worden. Daarom is het van belang om de richting te kunnen controleren waarin licht wordt uitgezonden. In Hoofdstukken 2, 3 en 4 demonstreren we hoe we nanofotonica gebruiken om de stralingsrichting te controleren van lichtgevende deeltjes.

Foton-conversieschema's zijn ontworpen om het rendement van fotonvoltaïsche systemen te verbeteren. Het absorptierendement van het omgezette licht in de zonnecel wordt bepaald door het hoek-afhankelijke stralingsprofiel. Het beheersen van de stralingsrichting is dus van groot belang voor het rendement. In Hoofdstuk 2 introduceren we het gebruik van silicium (Si) nanocilinders om de hoekafhankelijke straling van CdSeTe/ZnS kwantumdeeltjes (KD's) te regelen. De Mie-achtige multipolaire resonanties in de cilinders kunnen worden afgestemd door hun grootte te veranderen, wat de lokale dichtheid van optische toestanden (LDOS) beïnvloedt voor de KD's die bovenop de cilinders zijn geplaatst. We modelleren de KD's als dipoolachtige emitters en gebruiken FDTD-simulaties (finite-difference time-domain) om de cilinderdimensies te optimaliseren voor verbeterde opwaartse of neerwaartse straling. KD's gecentreerd op een oppervlak van een nanocilinder met een diameter van 400 nm stralen 98%

neerwaards het Si-substraat in. Daarentegen, homogene ensembles die over het bovenoppervlak van de nanocilinder zijn geplaatst met een diameter van 150 nm, vertonen 10 keer meer opwaardse straling. Vervolgens demonstreren we een nieuwe zachte stempelmethode om selectief een homogene laag KD's op een reeks Si-nanocilinders te stampen. Experimentele fotoluminescentie (PL) intensiteitsmetingen bevestigen de gesimuleerde trends als functie van de cilinderdiameter. PL-levensduurmetingen weerspiegelen goed de variaties van de LDOS op de KD-positie als gevolg van koppeling aan de resonanties. Deze resultaten tonen aan dat de zachte stempeltechniek een unieke manier biedt om lichtgevendende deeltjes zoals kwantumdeeltjes direct te integreren met nanostructuren. Dit kan de toepassing van nanofotonische structuren mogelijk maken in foton-conversieschema's voor fotonvoltaïsche systemen of andere opto-elektronische apparaten zoals light-emitting diodes (LED's) of displays. Dit hoofdstuk dient ook als inleiding op de volgende twee hoofdstukken, waar we anisotrope straling bestuderen voor fotonvoltaïsche luminescente zonneconcentratoren.

Gebouwegeïntegreerde fotonvoltaïsche (BIPV) technologieën integreren fotonvoltaïsche energieopwekking in het ontwerp van semi-transparante en ondoorzichtige componenten van de gebouwde omgeving. De fotonvoltaïsche luminescente zonneconcentrator (LSC) is een voorbeeld van een dergelijke technologie en biedt de mogelijkheid voor goedkope, passieve concentratie van direct en diffuus licht. Ondanks tientallen jaren van onderzoek, is het rendement van LSC's ver achtergebleven bij dat van geometrische concentrators. Recente ontwikkelingen in het fotoluminescentie-rendement (PLQY) van halfgeleider luminoforen (lichtgevendende deeltjes) zouden de verliezen aanzienlijk kunnen verminderen, maar even goed is efficiënte lichtopsluiting in het systeem nodig voor LSC's met een hoog rendement. Anisotroop stralende nanofotonische structuren zouden een belangrijke stap voorwaarts in rendement kunnen betekenen. In Hoofdstuk 3 gebruiken we Monte Carlo ray-trace modellering om het rendement van LSC's te evalueren met behulp van anisotrope luminofoorstraling, als een functie van PLQY, luminofoorconcentratie en geometrische versterking. Door alle LSC parameters te beschouwen, definiëren we een routekaart naar hoge-rendement LSC's. Om het rendement uit raytracing-resultaten te berekenen, leiden we een analytische functie af voor de donkerstroom van een LSC. Ontwerpparameters worden bepaald voor geoptimaliseerde LSC's met praktische geometrische concentratie van 10. We concluderen dat rendementen van meer dan 28% haalbaar zijn als sterke anisotrope luminofoorstraling wordt gecombineerd met hoge PLQY. Deze analyse laat zien dat voor hoge LSC rendementen, lichtopsluiting even belangrijk is als de PLQY.

Nadat we het potentieel van lichtopsluiting voor LSC's hebben onderzocht, demonstreren we nu anisotrope luminofoorstraling om de lichtopsluiting in de LSC-golfgeleider te verbeteren in Hoofdstuk 4. Door halfgeleider kwantumdeeltjes in te bedden in TiO_2 nanocilinders met een hoge brekingsindex, veranderen we hun hoekafhankelijke stralingsprofiel om de straling in het hoekbereik voor totale interne reflectie (TIR) te vergroten. We verklaren de controle over stralingsrichting door een combinatie van Mie-achtige multipolaire resonanties in de individuele nanocilinders en de interactie met het rooster. We modelleren het TiO_2 nanocilinder-rooster als een fotonisch kristal (FC) en identificeren de FC-golfgeleidermodi als een functie van de roosterafstand en golflengte. Door de roosterafstand te vergroten, verplaatsen we de dominante FC-golfgeleidermodi naar het TIR-hoekbereik bij de luminofoorstralinggolflengte (650 nm). Hoek-opgeloste fotoluminescentiemetingen werden uitgevoerd op gefabriceerde nanocilinders-arrays om de hoekafhankelijke stralingsprofielen te meten. Door de cilindervorm en de roosterafstand te optimaliseren, laten we een toename in lichtopsluiting zien van 75% (isotrope stralingsverdeling) naar 83,5%. Deze resultaten zijn een aanvulling op de resultaten die worden getoond in Hoofdstuk 2.

Deel twee

De zonnepanelen die we op de Nederlandse daken zien zijn voornamelijk gemaakt van silicium (Si). Silicium kennen we vooral als bestandsdeel in zand en glas in de vorm van siliciumoxide (SiO_2). In de typische zonnecel wordt juist kristallijn Si gebruikt om zonlicht om te zetten naar elektriciteit. Naast elektriciteit wordt een groot gedeelte van het inkomende zonlicht omgezet in warmte, waardoor de temperatuur op kan lopen tot boven de 60 graden Celsius. Het rendement van een silicium zonnecel wordt minder met oplopende temperatuur, en ook de levensduur verslechtert. In Hoofdstuk 5 kijken we daarom naar een manier om een zonnecel passief te koelen (zonder dat dat energie kost) met fotonische structuren.

Om zonlicht om te kunnen zetten naar elektriciteit, moet het licht wel in de zonnecel terecht komen. Om de absorptie van licht in de zonnecel te maximaliseren, moet de reflectie minimaal worden (hier beschouwen we een zonnecel met een metalen achterkant die geen licht doorlaat). Oppervlaktetexturen kunnen de reflectie verminderen en ook de lichtopsluiting in de zonnecel verbeteren. In Hoofdstukken 6 en 7 onderzoeken we hoe oppervlaktetexturen beter en/of sneller gemodelleerd en gekarakteriseerd kunnen worden. Dit draagt bij aan het ontwerp en de fabricage van (silicium) zonnecellen met lagere reflectie en betere consistentie van de gefabriceerde (nano)structuren.

In het tweede deel van het proefschrift bestuderen we fotonische structuren voor stralingskoeling en antireflectie van (silicium) zonnecellen. In Hoofdstuk 5 onderzoeken we het gebruik van passieve stralingskoeling (PSK) om overtollige warmte van een silicium zonnecel van de aarde naar of door de atmosfeer af te voeren. Om een lagere temperatuur te bereiken, wat gunstig is voor zowel het rendement als de levensduur van een silicium zonnecel, maken we gebruik van de spontane straling van infrarood (IR) warmtestraling. De belangrijkste uitdaging is om PSK te verbeteren en tegelijkertijd de transparantie voor zonlicht boven de silicium bandgap te behouden. We ontwerpen en fabriceren een zeshoekig rooster van microcilinders die kunnen worden geïntegreerd in het bovenoppervlak van het glas van een zonnepaneel. We gebruiken FDTD-simulaties om de geometrie te optimaliseren om de straling in het IR-golflengtebereik te verbeteren. Van multipolaire Mie-achtige resonanties in de cilinders is aangetoond dat ze reflectie in het IR verminderen, wat resulteert in een verbeterde IR-straling. Met behulp van integrerende bolspectroscopie meten we de reflectie van het silica cilinderrooster voor IR en voor zichtbare tot nabij-infrarode golflengten. De resultaten in het IR komen goed overeen met de gesimuleerde resultaten, terwijl we transparantie behouden voor licht met energie boven de silicium bandgap. De gefabriceerde microstructuur verhoogt de gemiddelde straling tussen $\lambda = 7,5 - 16 \mu\text{m}$ van 84,3% tot 97,7%. Met deze ontwerpprocedure kan een PSK-structuur worden verkregen voor elk fotovoltaïsch systeem, met of zonder een omsluiting van glas, of elk ander apparaat dat in de open lucht staat en profiteert van een lagere temperatuur.

Als aanvulling op het management van IR-licht, onderzoeken we nanotexturen voor verbeterde antireflectie van licht met energie boven de bandgap. De opkomst van deze nanotexturen in silicium zonnecellen heeft geleid tot uitdagingen in verband met optische modellering. Hoewel er rigoureuze methoden bestaan om de texturen van zwart silicium (zSi) nauwkeurig te modelleren, beperkt de vereiste rekenkracht de modelleringstoepassingen. In Hoofdstuk 6 modelleren we drie zSi-nanotexturen, elk met een aparte willekeurige geometrie, met een effectieve-stof benadering. We valideren het gebruik van de effectieve-stof benadering met lichtgolf simulaties. We stellen criteria voor de validiteit van verschillende optische

simulatietechnieken voor op basis van een reeks industriële fotonische texturen. Deze analyse onthult een gebied waarbinnen noch geometrische optica noch de effectieve-stof benadering geschikt zijn voor het berekenen van de reflectiviteit van een gestructureerd oppervlak, en daarom zijn lichtgolf simulaties vereist. Hoewel we specifieke zSi-texturen hebben bestudeerd voor zichtbare tot nabij-infrarode golflengten, zijn de voorgestelde criteria breed toepasbaar. We hebben de limieten alleen gebaseerd op de ruwheid en correlatielengte van de textuur, beide genormaliseerd naar de golflengte van het invallende licht, waardoor ze toepasbaar zijn op elke oppervlakte-textuur.

Modellering en simulatie van oppervlaktestructuren worden vaak gebruikt in de zonnecelindustrie om de materiaaleigenschappen beter te begrijpen, de prestaties van het apparaat te voorspellen en richtlijnen te geven voor het optimaliseren van fabricageparameters. Het verkrijgen van een nauwkeurige en betrouwbare oppervlaktestructuur van de zSi-textuur is een van de belangrijkste uitdagingen voor het verkrijgen van nauwkeurige modellen. In Hoofdstuk 7 onderzoeken we de betrouwbaarheid en consistentie van zSi-textuurkarakterisering. We vergelijken 3D-modellen van complexe zSi-texturen verkregen door atoomkrachtmicroscopie (AFM) en plasmagerichte ionenstraal (PFIB) technieken. Hemisferische-reflectie meetresultaten worden vergeleken met lichtgolf gesimuleerde resultaten om de betrouwbaarheid en consistentie van de textuurmodellen te testen. Onze resultaten leveren bewijs dat PFIB betrouwbaarder en consistent is in het karakteriseren van sterk opgeruwde zSi-texturen dan AFM.

Als geheel biedt dit proefschrift nieuwe inzichten om fotonische systemen te verbeteren door middel van verschillende fotonische controle over licht. Op basis van een fundamenteel begrip van de interactie tussen resonante fotonische nanostructuren en luminoforen, demonstren we controle over de richting van straling. Deze inzichten en resultaten dragen bij aan de ontwikkeling van efficiëntere foton-conversieschema's en luminescente zonneconcentratoren, specifiek voor fotonische toepassingen. Verder bestuderen we de interactie van licht met silicium zonnecellen om de straling van overtollige thermische energie te verbeteren en reflectieverliezen te verminderen. We gebruiken lichtgolf simulaties om deze interactie nauwkeurig te voorspellen op de schaal van de golflengte van het licht om optimalisatie van de oppervlakte-texturen mogelijk te maken. Veel van deze inzichten zijn ook toepasbaar op andere opto-elektronische apparaten zoals fotodetectoren, lichtgevende dioden en displays.

Acknowledgements

The job of a PhD student as a junior researcher is oftentimes called a quite personal endeavor: you have to take responsibility for your own projects. Nevertheless, this thesis is certainly not a completely personal achievement. Every person that accompanied me on this journey in one way or another has contributed to this final product. Colleagues, friends, and family, thank you so much, my experience of the PhD life has been shaped by your companionship, which I am forever grateful for!

First of all, I want to thank my parents. **Mamma**, *ik kan niet in woorden uit-drukken hoe gelukkig ik ben met alles wat ik van jou geleerd heb, jouw opvoeding heeft mij gemaakt tot wie ik nu ben. Ik heb ontzettend veel bewondering voor alles wat jij doet en over hebt voor de familie, hoe je iedereen verbonden en betrokken houdt.* **Pappa**, *wat bijzonder dat jij altijd achter me staat, altijd voor me klaar staat met hulp of raad. Net als mamma inspireer je mij mijn eigen leven te leven. Ik hou ontzettend van jullie en kijk uit naar de schatten die ons in het verschiet liggen!*

Second, the rest of my family. **Tim**, *bedankt dat je mijn grootste broer bent. Jij laat zien dat een echt grootse man ook een gevoelige man is. Ik heb enorm genoten van onze (telefoon)gesprekken de afgelopen jaren en hoop dat er nog heel veel bij komen :) Ook ben ik enorm trots dat jij naast me staat met de verdediging!* **Nicole**, *dankjewel voor je smile :) Jouw inzet voor anderen is echt bijzonder, evenals hoe je onderdeel bent geworden van onze familie. Heel fijn dat ik altijd welkom ben bij jullie, ik kijk uit naar de volgende G&T.* **Jeroen**, *bedankt voor alle belevenissen, alle (board)games, vakanties, het samen verbouwen van ons huis, en alles er tussenin. Jij hebt me de afgelopen jaren altijd gesteund, naar me geluisterd, en me een veilige plek geboden. Ik kan niet wachten op alle komende avonturen, te beginnen met de verdediging :)* **Sophie**, *bedankt dat je m'n part time huisgenoot was in Noord, voor je kookkunsten en de gezelligheid.* **Lieve Raven**, *bedankt dat je in onze familie bent gevlogen!* **Joost**, *wat ben jij een fijne broer, zo anders als ik en toch ook weer niet. Bedankt dat je echt altijd zo heerlijk kookt, de hoeksteen van de familie. Wat we samen hebben beleefd voelt als een geweldig fundament waar we op kunnen blijven bouwen. Ik ben heel blij dat je de afgelopen jaren op hetzelfde level bent gekomen als Jeroen en ik, en ik heb veel zin in de levels die nog komen!* **Romy**, *stoere zus, bedankt dat je altijd blij bent als we elkaar weer zien. Jij maakt altijd je eigen keuzes, zelfs als dat geen makkelijke of mainstream keuzes zijn, wat ik heel inspirered vind.* **Phong**, *bedankt voor alle tech-praat :)* **Opa**, *als er iemand stoer is dan bent u het wel! Heel inspirerend hoe u van het leven geniet.* **Oma**, *bedankt voor het delen van uw wijsheid en uw oprecht interesse. Ik ben heel gelukkig dat u samen met Opa er altijd voor ons bent geweest, zonder ooit een moeilijk of lelijk woord!* **Maud**, *thank you for becoming dinosaurs together. Het afgelopen jaar was geweldig; ongelofelijk en toch ook vertrouwd. Je geeft me een heel warm en zeker gevoel, en ik kijk enorm uit naar wat er verder op ons pad komt!*

Albert, thank you for being a fantastic (PhD) advisor. I've had the pleasure of working with you for close to 6 years now, and while I was already enjoying your supervision as a master student in the first year, I've only come to appreciate you more over time, as a group leader and as a person. You stand out as a group leader in obvious ways: I can't imagine a PhD student that wouldn't be happy with a group leader that organizes a week-long lab tour visiting fellow research groups. But you also stand out in less obvious or at least less public

ways: you show honest interest in our lives and share about your personal life, you join us for coffee, lunch and tea breaks or drinks after work, and you invite us into your home for parties or take us for summer night boat trips through the Amsterdam canals. Also, covid hasn't been easy for at least the social part of the group, and you put a lot of effort into keeping us connected. This you do in a natural way, but nevertheless it is vital to the group dynamic and what enabled me to complete this thesis. *Bedankt voor alles en meer!*

Jorik, thank you for being such an inspiring co-promotor. From the very beginning of my AMOLF time, your PhD thesis work inspired me and importantly taught me about Mie-like resonances in nanostructures. During the few times that we met when you were at Stanford, you were always eager to help me and share your insights and technical solutions. Then later, when you came back to Amsterdam, you helped with finishing the story of chapter 2 with discussions and manuscript edits. I've learned a great deal from your input, also on chapter 5 and the rest of the thesis, and feel I have improved my writing because of that. Besides all that you taught me, it is also a pleasure to work with you. As I see it, you combine the ability to teach without sounding condescending, the ability to create a collaborative atmosphere, and the ability to ensure I am taking responsibility with confidence.

Dear committee, thank you for the time and effort you are putting into my PhD defense. **Peter**, thank you for putting so much trust in me as a teaching assistant. **Erik**, thank you for always asking interesting questions, to my own presentations and those of others, inspiring us all to do the same. It has been great to directly work with you, which resulted in two publications that are now part of this thesis, and since recently on the PerFORM KIC project. You're always kind and make me feel like an equal, which is a highly valued asset as a group leader. **Wim**, thank you for inspiring me and so many other people to work on photovoltaics. *Het voelt altijd heel bemoedigend om met jou te praten, zowel door je positieve visie voor zonne-energie als hoe je mij als jonge onderzoeker motiveert.* **Isabelle**, I am very happy that you have accepted to be in my PhD committee because much of this thesis has been influenced and shaped by work. **Rebecca**, thank you for showing that it is certainly possible to keep practical applications and circumstances in mind when conducting fundamental research.

Photonic Materials group, you are the best, a true Dream Team! First, I would like to thank my tutors, the postdocs of the group. **Mark**, thank you for teaching me how to do research. In only a few months, you showed me (by example) how to take responsibility for your own research while also collaborating with and helping others, the importance of conducting and understanding reference simulations or measurements, and how to foster the social aspects of the group, the gezelligheid. And of course, thank you for all the beautiful pictures! **Sophie**, thank you for showing me how fun and exciting research is, and that you don't have to be an expert to ask good and relevant questions. The times on the (Veldhoven) dance floor I'll never forget :) **Nick**, thanks for the endless times you helped with my theory questions, I've learned so much from all the discussions. Your enthusiasm for science is really contagious, I hope you keep that attitude forever! **Daniël**, thank you for so much valuable (research) advice in just a few months! **Kelly**, I really admire your work-discipline and enjoyed your little jokes a lot, random or not. To be honest, I'm a little sad that we didn't get to spend more time together due to covid, so I hope you're making up for those (lonely) times in California now. On the bright side, we've laughed a lot during live and online game nights :)

Then, I would like to specifically thank Verena, Magda, and Andrea, with whom I shared (almost) the entire PhD journey. **Verena**, amazing how you always made sure the group was an inclusive place, made sure that everyone felt they were a part of it. When you just started as a PhD student and I as a master student, you treated me (and all the other master students,

PhD students, or postdocs that followed) like equals. Also, I really admire how you make clever jokes but are never mean. **Magda**, thank you for sharing the AMOLF master-PhD experience, I've enjoyed it a lot to see you become the confident researcher you are now. Besides the occasional somewhat-dark, Kelly-type joke, you never say anything bad about anyone, which I think is one of the best habits to have. **Andrea**, thank you for making sure that our research time was supplemented with sufficient social time. Your honest realism is contagious, and your ability to call bullshit or tell me I'm being too serious very appreciated (at least by me). I'm also very thankful that you're always available for any discussion or question. The fact that you often directly cut to the chase shows what a great researcher you are — my honest opinion. Also, thank you for inviting us to Catania for a perfect trip, I'll never forget it!

Next, all the other master and PhD students that are and have been part of the group. **Stefan**, even though you've spent two years down under, I feel that we have made quite some memories. We saw a lot of football matches together and had a lot of fun on the trips to Catania, Berlin, and Switzerland. You never seem to stress much (over work) and are always available to discuss, making it great to work with you. **Matthias**, what's up? — peace :) You're a super nice and funny guy, inspiring me to make/play more (silly) jokes. Some people might say you're not that organized, but I think you have complete control over the important stuff, which is much more useful than micromanaging everything. I really enjoyed all the lecture style group meeting presentations you gave and the tech-talk. Peace out. **Nika**, thank you for being so concerned with the welfare of me and the rest of the group. I really admire your capacity to bask in the joyful moments and cheer other people on. Also, your organization of the Switzerland lab-tour was just spot-on! **Evelijn**, thank you for such a fruitful and fun year of teamwork. *Ik heb heel erg genoten van ons PRC avontuur, van alle online meetings tot aan de trips naar Twente. Overleggen en samenwerken kun jij super goed, en tegelijkertijd neem je daarnaast zelf het heft in handen. Dat zijn precies de eigenschappen die een goede PhD student nodig heeft, dus jouw thesis wordt zeker een succes, en ik ben blij dat we zo nog collega's zijn :)* **Cyrian**, thanks for making the California trip so much fun! **Joris**, it was a blast to be colleagues for 10 months with a friend. Even though we're quite different people, we share our enthusiasm for solving problems and boardgames. **Kyra**, thank you for working together on such a interesting topic, for your insightful and critical thinking, and for presenting the LSC story with such beautiful drawings. **Floris**, thanks for making sure all the breaks were filled with laughter, and for all the drinks and football games after work. **Marnix**, thank you for teaching us about carrier dynamics. **Heleen**, thank you for making all the coffee and lunch breaks so enjoyable, either with fun or serious talk. **Daphne**, very inspiring how you took on a master project outside of your comfort zone and made it a success. Also, thank you for teaching us to talk proper English ;) **Hannah**, thank you for organizing the Switzerland lab-tour, I'll never forget it!

Finally, I'd like to thank the Polman group alumni for their advice and tutoring. **Toon**, you are one of the most dependable people that I know and its a true asset to the group that you remain affiliated. You helped me decide when I was contemplating a PhD position in Albert's group, and helped with many other things throughout the years. Besides that, you've probably inspired me the most by your work as a researcher that bridges the fundamental science of AMOLF to applied science. **Benjamin B.**, thank you for staying in touch with the group and for the times we ended up on the dance floor, you rock! **Ruben**, thank you for all the invaluable WITec advice and the discussions during the GRC conference.

I have also had an incredible team of colleagues working besides me in other groups at AMOLF. First, I would like to thank those that were involved in making the projects described in this thesis a success. **Bruno**, our collaboration started immediately on the first day of my

PhD and I've learned a lot from our discussions. **Esther**, thank you for being so supportive to all young researchers at AMOLF. **Femius**, thank you for all your valuable remarks and questions during colloquia and poster sessions. Also, many thanks for your insight into the experimental LSC chapter, thanks to the S4 simulations you set up I got to the beautiful result on the cover. **Benjamin D.**, I feel very lucky that you were the first colleague to collaborate with for such a long time. We have explored the project that is now chapter 2 of this thesis together, where you've shown me how to combine each other's expertise and identify where more help is needed. Thank you for teaching me by example, and being such a nice guy along the way! **Harshal**, thank you for all the lab work we did together, I learned a lot about chemistry, and for always thinking towards solutions. **Mark A.**, thank you for teaching me how to perform AFM measurements while you were so busy with your own thesis. **Julia**, I'm super happy that we happened to be having similar research questions in mind, and that we worked on a collaborative project as a result. *Het is heel fijn om samen te werken met jou, onze brainstorm sessies waren heel effectief, vervolgens had je in no-time weer overzicht gecreëerd en kwam je alles na wat je beloofde. Ook ben je een geweldige luisteraar en ben ik blij met alle gezellige en diepgaande gesprekken. Ik kijk uit naar de volgende bbq :)* **Nasim**, thank you for always sharing your warmth and happiness with those around you. I'm very glad we have been working together for so long, you certainly and sincerely made AMOLF a happier place. **Nelson**, thank you for measuring the beautiful Fourier images together that now feature this cover. *Je werkt heel rustig en gestaag, waardoor je heel veel overzicht en inzicht verwerft en het fijn is om samen te werken!*

Besides the colleagues that directly helped me with my PhD work, there were many more that supported me indirectly. **Sven**, thank you for all the times you beat me with squash, and for all the interesting discussions we had before and after. **Lucie**, thank you for being such a sweet person and putting all your efforts into renewable energy (research). **Silvia**, thanks for being so thoughtful and kind when we have a chat. **Alex**, thanks for teaching me about computers, hydrogen technology, and other tech (you know your stuff), and for taking over some of my duties without ever complaining. **Eitan**, I really admire how positive and happy to always are, or at least seem :) Furthermore, thanks to **Hongyu, Susan, Sarah, Gianluca, Imme, Moritz S., Jeroen, Yorick, Daphne, Ilan, Deba, Rene, Roel, Jesse, Jente, Francesca, Mees, Wiebke, Ewold, Said, Wim N.**, and those that I'm forgetting here!

There have also been a lot of colleagues that left AMOLF before me, but very much determined the culture in which I have been happy to work. Thank you for the many coffee/tea/lunch breaks, the epic pv events such as Christmas/Easter lunches and AMOLF outings, colloquia and poster sessions, and for creating/sustaining a sense of community. **Jenny**, thank you for always sharing your happiness and smile with the people around you, and for being such a good listener. **Lukas**, I really admire how you always take the time to connect with everyone and are so generous with sharing your ideas and help. **Robin**, you're one of the most friendly people I know; combined with your smart humor it's very fun to be around you. **Isabelle**, thanks for all the dancing! **Loreta**, thanks for sharing the incredible summer school week in Austria. Also many thanks to **John, Sander, Sebastian, Gede, Parisa**, and **Moritz F., Ruslan, Annemarie, Marco V., Giorgio, Hugo**, and **Christian**.

The success of AMOLF is very much the result of the excellent support in several departments of the institute. The in-house expertise and the cooperation of the support staff is truly exceptional, and I would like to thank all staff sincerely for their effort. As a junior researcher I've felt literally supported by technical and personal support, I've never felt alone, but which I'm very grateful for! Specifically, I would like to thank the people that directly supported my personal research efforts. **Dion**, *bedankt dat je altijd overal mee wilt helpen*,

dat je het altijd leuk vindt om een oplossing te vinden voor waar ik dan ook mee aanklop, en dat je alles zo positief aanvliegt. Floortje, bedankt dat altijd zo veel lol maakt en tegelijkertijd alles op rolletjes laat lopen. Hans, bedankt voor de inspiratie te genieten van het onderzoek en de techniek op AMOLF te begrijpen, en dat je me veel te dikke lagen TiO_2 hebt laten opdampen in de E-flex. Dmitri, Bob, en Igor, bedankt dat jullie altijd voor mij en iedereen klaar staan en tegelijk de cleanroom zo'n gezellige plek maken. Hincó, Marc, Petra, Grace, Clyde, Rutger, Gerben, en alle support staff die ik nu vergeet, bedankt voor al jullie hulp de afgelopen jaren, jullie zijn goud waard!

This thesis is the result of many successful collaborations with colleagues all around the world, whom I would like to thank dearly. **Harry**, thank you for inspiring me and so many others with your vision. Your passion for science is contagious and your work on renewable energy a true inspiration. **David Ne.**, I have enjoyed our brainstorming and discussions tremendously. You are so good in expressing your thought, both in words and writing, and your figure-making skills are astounding — thank you for making our paper such a beauty! **John, David P., Malcolm, YoYo, and Bram**, thank you for such a fruitful collaboration from across the world. **Aurelio and David No.**, thank you for trusting me with your nanocrystals! **Chris**, thanks for inviting Evelijn and me to Twente, without you we would never have come to these beautiful results! **Rinke, Jan, and Leo**, thank you for introducing me to scientific research when I was only just a bachelor student, I have felt very welcome and taken seriously. **Qitong**, thank you for taking the time to teach me about multipole decompositions. **Maarten**, *bedankt voor de leuke gesprekken bij de Sunday en AMOLF poster sessies.*

Finally, I would like to thank my friends for joining me along this PhD journey. **Jonas**, we already met a couple months before my academic journey even began, and you have been grooming and advising and tutoring and inspiring me ever since. Your passion for renewable energy has sparked mine, you welcomed me into the Physics study association, and your invitation to join Extensus made my study life so much richer. *Je bent een goede vriend en ik ben heel benieuwd waar onze (duurzame) wegen verder heen zullen leiden. Ilse*, thank you for sharing the Amsterdam study experience for so many years. *Ik heb het heel leuk gevonden bijna alle vakken samen met jou te volgen, we zaten zo op een lijn met onze keuzes en interesses. Zonder jou was het niet hetzelfde geweest!* **Kees**, thank you for teaching me physics theory when I thought I understood but actually didn't. *Jij bent een van de slimste mensen die ik ken, en zeker de slimste uit ons studiejaar, maar nog belangrijker heel aardig, oprecht, en gezellig!* **Jorick**, thanks for making life, and thus also our study time, a party! *Jouw positiviteit is aanstekelijk en het is heerlijk dat je overal wel een mening over of idee voor hebt. Ik zal nooit vergeten hoe we Jiskefet - Stiften speelden aan de bar bij Aik :p* **Daan**, you're never easily convinced, which makes discussions either interesting or refreshing or both :p *Bedankt dat je me elektrodynamica hielp begrijpen en de diners van genoeg humor voorzag.*

Everybody that was part of the study associations **Aik and Extensus**, thank you shaping my studies leading up to this PhD work. In particular, I would like to thank: **Ada**, *bedankt dat je altijd met scherp inzicht en verfrissende opvattingen komt, en we nooit uitgepraat lijken te raken. Ruben*, *dankjewel dat je er altijd was op de (gala-)dansvloer, en voor de (droge) humor tijdens vergaderingen en biertjes. Maartje*, *dankjewel dat je er was toen ik dit avontuur richting zonnel-onderzoek startte, en alle andere mooie/leuke belevenissen. Laura*, *bedankt dat je altijd zo betrokken bent, zelfs als we elkaar een tijd niet gezien hebben, en voor je heerlijke diners tijdens vergaderingen. Floris*, *thanks voor alle gesprekken over tech en (levens-)filosofie, echt knap/leuk/interessant hoe scherp jij kunt observeren. Yarah*, *bedankt voor alle spelletjesavonden, Aik trips, en borrelavonden. Lotus*, *bedankt dat je zo'n prachtig mens bent,*

Acknowledgements

*altijd open en gezellig en blij :) **Romy D.**, dankjewel voor alle bordspellen die ik van je geleerd heb, voor de lesdagen die we samen gedaan hebben, en voor de persoonlijke gesprekken :) Tot slot, **Sanne**, bedankt voor de geweldige Istanbul trip en conferentie, en voor je gezelligheid elke week.*

“Fall in love with some activity, and do it! Nobody ever figures out what life is all about, and it doesn’t matter. Explore the world. Nearly everything is really interesting if you go into it deeply enough. Work as hard and as much as you want to on the things you like to do the best. Don’t think about what you want to be, but what you want to do. Keep up some kind of a minimum with other things so that society doesn’t stop you from doing anything at all.”

— Richard P. Feynman

“Remember to look up at the stars and not down at your feet. Try to make sense of what you see and wonder about what makes the universe exist. Be curious. And however difficult life may seem, there is always something you can do and succeed at. It matters that you don’t just give up.”

— Stephen Hawking

“The measure of intelligence is the ability to change.”

— Albert Einstein

Curriculum Vitae

Personal Information

Thomas (Tom) P N Veeken

tomveeken@gmail.com
[linkedin.com/in/tomveeken](https://www.linkedin.com/in/tomveeken)

1991 Born in Alkmaar, The Netherlands



Education

2010 Atheneum (high school) and Vrije School (Waldorf) diplomas
Adriaan Roland Holtschool, Bergen (NH), The Netherlands

SEPT. 2011 Bachelor of Science (Hons) in Physics and Astronomy
- JULY 2014 VU University Amsterdam, The Netherlands
Thesis Development of very sensitive hydrogen detection instruments
Supervisor Dr. R. Wijngaarden

SEPT. 2014 Master of Science in Advanced Matter & Energy Physics
- AUGUST 2017 Joint degree VU University Amsterdam & University of Amsterdam, The Netherlands
Thesis Spectrum-splitting concepts for parallel-stacked tandem solar cells
Supervisor Prof.dr. Albert Polman

SEPT. 2017 Ph.D. in Physics
- MARCH 2022 from University of Amsterdam, The Netherlands
Research at NWO-Institute AMOLF, Amsterdam, The Netherlands
Thesis Photonic control over light absorption and emission in photovoltaics
Promotor Prof.dr. Albert Polman
Copromotor Dr. Jorik van de Groep